Rotary (redox) reactor-based oxy combustion chemical looping power cycles for CO_2 capture: analysis and optimization

by

Chukwunwike Ogbonnia Iloeje

MSc. Mechanical Engineering
Massachusetts Institute of Technology, 2011

Submitted to the Department of Mechanical Engineering in partial fulfillment of the requirements for the degree of

Doctor of Philosophy

at the

MASSACHUSETTS INSTITUTE OF TECHNOLOGY
JUNE 2016

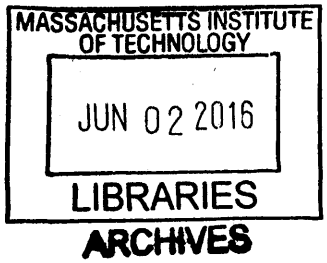

Signature redacted

Signature of Author: _____

Department of Mechanical Engineering
May 19, 2016

Signature redacted

Certified by: _____

Prof. Ahmed Ghoniem
Ronald C. Crane (1972) Professor
Thesis Supervisor

Signature redacted

Accepted by: _____

Rohan Abeyaratne
Chairman, Department Committee on Graduate Students

Rotary (redox) reactor-based oxy combustion chemical looping power cycles for CO_2 capture: analysis and optimization

by

Chukwunwike Ogbonnia Iloeje

Submitted to the Department of Mechanical Engineering on May 19, 2016 in partial fulfillment of the requirements for the degree of Doctor of Philosophy in Mechanical Engineering

Abstract:

A number of CO_2 capture-enabled power generation technologies have been proposed to address the negative environmental impact of CO_2 emission. An important barrier to adopting these technologies is the associated energy and economic penalties. Chemical-looping (CLC) is an oxy-combustion technology that can significantly lower such penalties, utilizing a redox process to eliminate the need for an air separation unit and enable better energy integration. Conventional CLC employs two separate reactors, with metal oxide particles circulating pneumatically in-between, leading to significant irreversibility associated with reactor temperature difference. A rotary reactor, on the other hand, maintains near-thermal equilibrium between the two stages by thermally coupling channels undergoing oxidation and reduction.

In this thesis, a multiscale analysis for assessing the integration of the rotary CLC reactor technology in power generation systems is presented. This approach employs a sequence of models that successively increase the resolution of the rotary reactor representation, ranging from interacting thermal reservoirs to higher fidelity quasi-steady state models, in order to assess the efficiency potential and perform a robust optimization of the integrated system. Analytical thermodynamic availability and ideal cycles are used to demonstrate the positive impact of reactor thermal coupling on system efficiency. Next, detailed process flowsheet models in which the rotary reactor is modeled as a set of interacting equilibrium reactors are used to validate the analytical model results, identify best cycle configurations and perform preliminary parametric analysis for

relating system specifications with performance. In order to capture important feedback interaction between the reactor and the system while maintaining computational efficiency, an intermediate fidelity model is developed, retaining finite rate surface kinetics and internal heat transfer within the reactor. This model is integrated with a detailed system model and used for optimization, parametric analysis and characterization of the relative techno-economic performance of different oxygen carrier options for thermal plants integrated with the rotary CLC reactor.

Results show that thermal coupling in the redox process increases the efficiency by up to 2% points for combined, recuperative and hybrid cycles. The studies also show that the thermal efficiency is a function of the reactor purge steam demand, which depends on the reactivity of the oxygen carrier. While purge steam constitutes a monotonic parasitic loss for the combined cycle, for recuperative and hybrid cycles, it raises the efficiency as long as the steam demand is less than a threshold value. This relationship between reactivity and system efficiency provides a useful selection criteria for the oxygen carrier material. Optimization results based on efficiency and levelized cost of electricity (LCOE) identify nickel-based oxygen carriers as the most suitable for the rotary reactor because its high reactivity ensures low steam demand and reactor cost. Compared to nickel, maximum efficiency and minimum LCOE are respectively 7% lower and 40% higher for a copper-based system; iron-based systems have 4% higher maximum efficiency and 7% higher minimum LCOE. This study also showed that optimal efficiency generally has an inverse profile to that for the optimized LCOE.

Acknowledgements

First, I would like to thank Prof. Ahmed Ghoniem for playing the role of guide, mentor and, of course, Thesis advisor, throughout my stay here at MIT. I am grateful for the freedom he allowed me in research direction, and for demanding very high standards from my work. He really made MIT a great learning experience for me and I owe him much of what I have become.

I would also like to express my gratitude to Randall Field for being a great support and research mentor, and especially for helping me navigate through the initial stages of my research career. I am grateful for the interest he has shown in my work, and for the valuable feedback I have received over the years.

Thanks to Prof. Paul Barton for being part of my PhD Thesis committee, for his useful feedback, and for connecting me with resources that helped with aspects of my research. I am also grateful to Prof. Kripa Varanasi for being on my PhD Thesis committee and for his interest and valuable feedback.

This work would not have been possible without help from Zhenlong Zhao, my colleague on the CLC project. He has been a great - and unforgiving - sounding board for my ideas, and was an outstanding resource when I needed to figure out new directions at some of the difficult stages of this research. I also want to thank Harry Watson for making time to discuss some modeling challenges related to this work.

A big thanks to all my friends in the RGD lab: Cristina, Kushal and Addison, who were my quals buddies; to Sofiene, Richie, Akhilesh, Nadim, George and Christos, who made it their mission to ensure that all work and all play made life interesting for Nwike; Xiaoyu and Katherine, co-founders of the now defunct B-Squad, and Elysia for being the anti-role model for the squad. Special thanks to Katherine for being the unofficial editor-in-chief of this thesis, and for ensuring that someone outside my committee actually read my thesis – not many PhD graduates can boast of this! I guess I cannot list everyone, but I do appreciate the experience of being part of this group in my two stays at MIT.

I did have a great time working on a couple of initiatives with amazing people here at MIT. A shout out to the bridgeInitiative team: Duby, Tunde, and Chibueze; and to the ImpactLabs team:

Mureji, Joy and Tunde. I would also like to thank Julia Reynolds-Cuellar from MIT-Africa Initiative for supporting us throughout these projects and the MIT D-Lab for simply being one of the coolest resources available on campus. Many thanks to Leslie Regan and Lorraine for their support throughout my stay here.

I would not forget Paul B. and Jimmy K. for our refreshing 'weekly' lunch discussions, ranging from simple things like changing the world, to more complicated issues like changing baby diapers. Next I would like to thank my family for their unconditional love and support, and really for making all this possible: Mum, Dad, Ada and her hobby, Chukwudi; Neme, Chinenye, Bobby, Kevin, Dave, Tunji, Chuks, Obum, Uchenna, Amarachi, everyone (it's a really big family). Special recognition goes to Meso and Muna, for making me a PhD uncle (without my permission, though).

Finally, I would like to recognize the financial contribution from the MASDAR Institute of Science and Technology and the King Abdullah University of Science and Technology (KAUST) investigator award, which has supported this thesis research.

Contents

List of Figures

List of Tables

1. Introduction

1.1. CLC concept

Concerns about the environmental impact of CO_2 emissions have led to the development of technologies that enable CO_2 capture from thermal power plants. Two important barriers to the large-scale adoption of carbon capture are the efficiency and cost penalties associated with these technologies. Compared to alternative carbon capture options, chemical looping combustion (CLC) is one of the most promising technologies with the potential for lowering the efficiency and cost barriers. It utilizes a chemical intermediate (oxygen carrier) to transfer oxygen from an oxidizing stream (usually air) to a separate reducing stream (fuel). This set-up allows fuel to be burned completely while avoiding mixing of the two streams [1]–[3]. The two-step CLC redox reaction scheme is represented in Figure 1-1 and equations 1.1 & 1.2. In the first step, the reduced oxygen carrier reacts with oxygen in air to yield the metal oxide according to equation 1.1. The product gas stream from this step consists primarily of nitrogen and depleted oxygen.

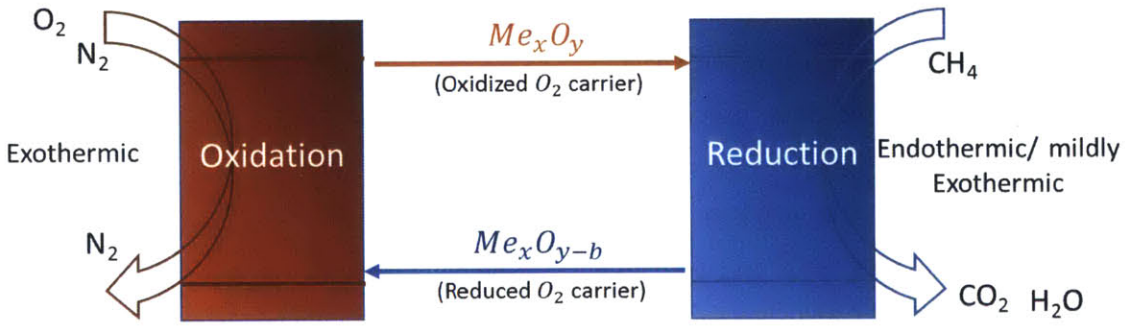

Figure 1-1: General reaction scheme for a CLC process

In the second step, the oxidized carrier comes in contact with the fuel stream and is reduced, producing CO_2 and H_2O as shown in equation 1.2. In this way, the overall CLC process produces separate air and CO_2/H_2O streams. The H_2O can easily be condensed out, providing a CO_2 stream

ready for transport and storage or enhanced oil recovery. Combining reactions 1.1 and 1.2 yields equation 1.3, which is equivalent to the net combustion reaction of the fuel with oxygen.

$$(2n + m - p)Me_xO_{y-b} + b\left(n + \frac{m}{2} - \frac{p}{2}\right)O_2 \rightarrow (2n + m - p)Me_xO_y \quad (1.1)$$

$$(2n + m - p)Me_xO_y + bC_nH_{2m}O_p \rightarrow (2n + m - p)Me_xO_{y-b} + bnCO_2 + bmH_2O \quad (1.2)$$

$$C_nH_{2m}O_p + \left(n + \frac{m}{2} - \frac{p}{2}\right)O_2 \rightarrow nCO_2 + mH_2O \quad (1.3)$$

Typical oxygen carrier materials used in CLC reactors include nickel, copper, iron, manganese and cobalt [3]–[7].

The earliest applications of the chemical looping concept were driven by the need to develop processes for obtaining specific chemical products. One of the first commercial scale CLC applications was the steam-iron process for hydrogen production developed by Howard Lane [8] at the turn of the 20th century. The steam-iron process was used to generate hydrogen from coal gas and steam using iron oxide as the chemical intermediate in an indirect reaction scheme. This process was however displaced when natural gas supplanted coal gas as the preferred raw material for hydrogen production [2]. Later, Lewis and Gilliland [9], [10] proposed a CO_2 production process for use in beverage industries based on the chemical looping concept, with copper oxides and iron oxides as the oxygen carriers. They were the first to introduce the idea of two interconnected fluidized bed reactors with the oxygen carrier solids circulating between them. More recent applications for chemical looping combustion have been directed towards fuel and energy conversion systems. This shift in chemical looping application was prompted first by the objective of increasing the efficiency of energy conversion systems, then subsequently, by the need to respond to the growing concern about the environmental impact of CO_2 emissions.

CLC design in energy conversion systems realizes complete fuel conversion through a set of intermediate-reactions which reduce reaction exergy losses and improve emissions control while capturing the CO_2 produced in the combustion reaction. Consequently, this design eliminates the need for additional CO_2 separation equipment and the associated energy penalty, leading to higher thermal efficiency than most alternative technologies [11]–[16]. The idea of applying the chemical looping concept to energy conversion systems, specifically for power generation, was originally

suggested by Ritcher and Knoche [1], who proposed it as a solution to minimizing exergy loss and improve the thermal efficiency of power plants. Ishida et al. subsequently proposed CLC for CO_2 capture from combustion plants [12], [17]. For either application, the CLC redox reactions produce two high temperature streams; an oxygen-depleted air stream and a CO_2-rich exhaust stream, each of which can be used independently to generate power.

1.2. CLC reactor designs

A number of reactor designs have been proposed for the CLC redox process. The most common design is the circulating fluid bed reactor, which consists of separate oxidation and reduction reactors, with oxygen carrier particles circulating pneumatically between the two reactors [3], [18], [19]. This design is shown schematically in Figure 1-2. Thus, the oxygen carrier is successively oxidized in the oxidation reactor and reduced in the reduction reactor in a continuous cycle. A cyclone and a loop seal are used to separate the oxygen carrier particles from the gas streams. These particles are selected based on suitable thermo-physical and kinetic properties (e.g., reactivity, oxygen carrying capacity, thermal and physical stability and resistance to agglomeration and attrition), as well as economic considerations. Major limitations of this reactor configuration include a large pressure drop due mostly to particle fluidization, difficulty in maintaining particle circulation at high temperature and pressures, attrition from particle friction, cyclic thermal stresses, agglomeration, particle entrainment and lower CO_2 separation efficiency [18], [20]. Yet from a system efficiency perspective, the most important shortcoming is the significant irreversibility associated with the temperature difference between the oxidation and reduction reactors, particularly when the reduction reaction is endothermic.

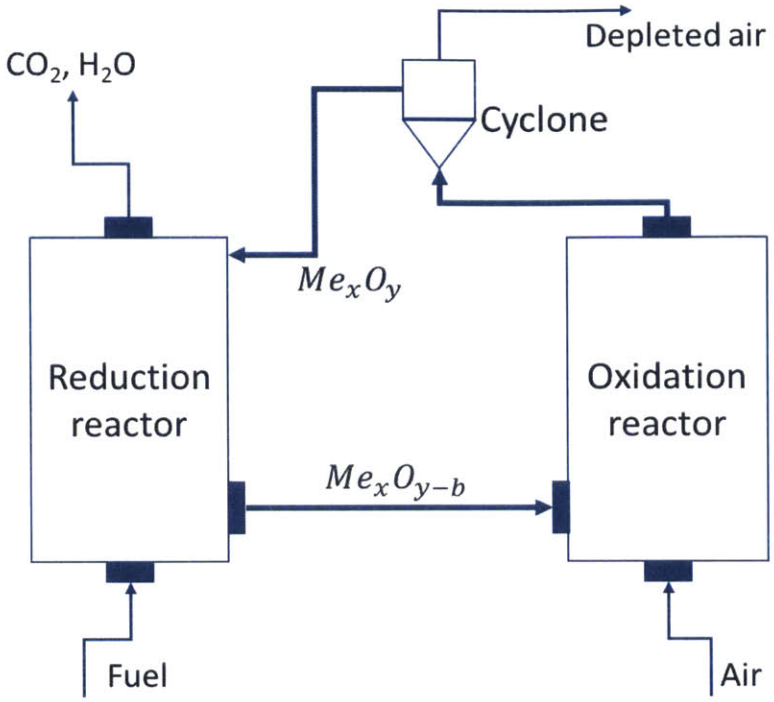

Figure 1-2: Schematic diagram of a traditional fluid bed CLC reactor

Other CLC reactor designs have also been proposed, including the moving bed reactor [2], [21] and the fixed packed-bed reactor [22], [23]. In the fixed packed bed setup, the reactor is alternately exposed to reducing and oxidizing conditions via periodic switching of the air and fuel feed streams. This design requires at least two reactors in parallel to ensure continuous exhaust gas supply to the downstream power island. A variation of this design is the SCOT reactor proposed by Chakravarthy et al. [24]. This design consists of at least one pair of packed bed reactors integrated with a system of heat engines interacting with the two reactors, as well as one or more heat pumps. This setup attempts to ensure that the oxidation and reduction reactors operate as close as possible to their respective equilibrium temperatures. The internal heat engine is required to transfer heat from the reactor in the oxidation phase to the reactor in the endothermic reduction phase when the temperature of the solid oxygen carriers start falling below the reduction equilibrium reaction temperature. The heat pump transfers heat to the oxidation reactor when the reaction heat release is insufficient to raise the temperature of the oxygen carrier to the equilibrium (or maximum) oxidation temperature. This setup enables the reactor to utilize a wider range of oxygen carriers but faces the practical challenge of incorporating an internal heat engine. To

overcome the technical challenges related to high temperature gas switching inherent in the fixed bed designs, Dahl & Hakonsen et al. proposed the rotating packed-bed reactor [25], [26]. This reactor consists of a doughnut shaped, fixed oxygen carrier bed that rotates between four fixed gas feed sectors on the top face – air sector, fuel sector and two purging sectors to prevent air/fuel mixing. The gas streams flow radially outwards through the bed while reacting with the oxygen carrier. These designs overcome particle circulation challenges but still contend with temperature swings between the reduction and the oxidation cycles. This temperature swing increases reactor entropy generation, especially for oxygen carriers with endothermic reduction reactions.

1.3. The thermally coupled rotary reactor

The rotary reactor design proposed by Zhao et al. [4], [27]–[29], has the potential to overcome these limitations. This design consists of a solid rotating wheel and stationary inlet and exit chambers, as shown in Figure 1-3a. The inlet chamber is divided into four sectors - fuel, air, and two purging sectors - while the outlet chamber is split into two zones - the air zone, which coincides with the air and air purge sectors, and the fuel zone, which merges the fuel and fuel purge sectors. The rotating wheel consists of a matrix of micro-channels with the oxygen carrier coated or impregnated on the inner walls of the channels (Figure 1-3b). The channel wall is composed of a dense structural substrate layer and a porous oxygen carrier layer. As the wheel rotates, each micro-channel passes successively through the four sectors: the fuel sector, where fuel reduces the oxygen carrier via an endothermic or mildly exothermic reaction; the fuel purge sector, where steam sweeps out the exhaust gas from the channel; the air sector, where oxygen carrier is oxidized exothermically in an air/oxidizing stream; and the air purge sector, where steam flushes out the air prior to re-entering the fuel sector. The combined fuel and fuel purge sector streams leave via the fuel zone while the air and air purge sector streams leave from the air zone.

During cyclic operation, the solid wheel also acts as a thermal energy storage medium to transfer the reaction heat between the gas streams and to provide internal thermal coupling between all the sectors in the reactor. The bulk support layer, usually made of high thermal capacity and conductivity material like boron nitride, provides this thermal integration. Thermodynamically, this internal thermal coupling can be conceptualized as series of heat exchangers transferring heat

across an infinitesimal temperature difference between the air and the fuel reactors at each location along the length of the reactor. This means that at any axial location, the temperature is uniform in the radial and circumferential directions. Consequently, the reduction reactions take place at essentially the same temperature as the oxidation reaction and the exhaust gases leave the air and fuel zones at nearly the same temperature. The thermal performance of the rotary reactor based on simulation results by Zhao et al. [29] is shown in Figure 1-3c and 1.3d. It is evident in these figures that the circumferential temperature variation is small, with a maximum value of less than 30K in the lower part of the reactor and less than 2K at the reactor exit. This effective thermal coupling between the four reactor sectors is possible because the bulk support layer forms a continuous heat conduction path, avoiding the solid-gas-solid and solid-solid contact resistances that limit alternative reactor designs.

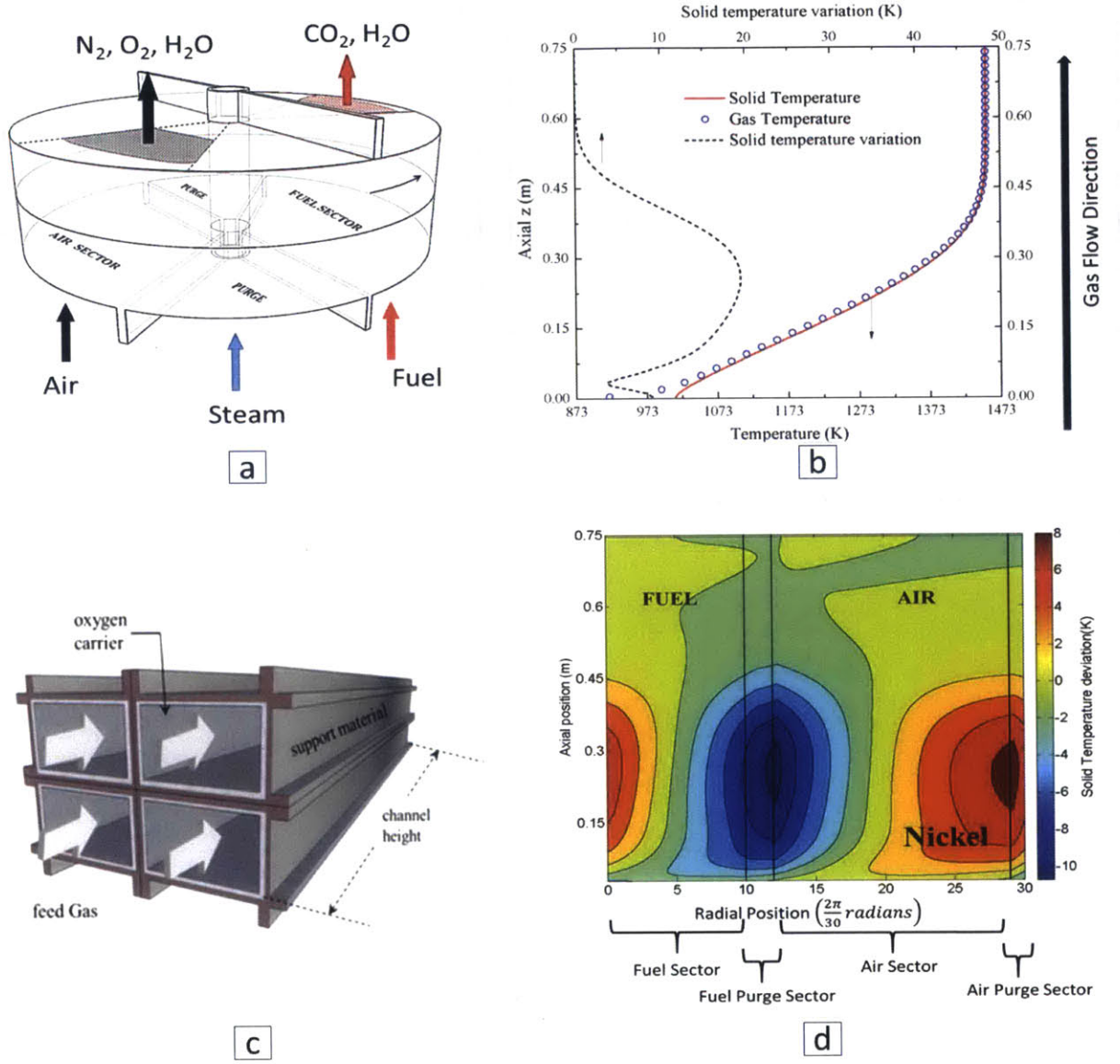

Figure 1-3: Rotary CLC reactor geometry and thermal performance.
(a) The reactor showing inlet sectors, exit zones and rotating drum; (b) Reactor channel structure with the oxygen carrier coated on the inner walls of the channels; (c) Axial temperature profile in reactor channel (d) Solid temperature variation across the reactor sectors for a nickel-based rotary reactor. [27], [29]

1.4. Chemical looping combustion-based energy conversion systems

The application of chemical looping concept to energy conversion systems was a bio-inspired strategy initially proposed by Ritcher and Knoche [1]. It was premised on the idea that combustion

entropy generation can be reduced by replacing the direct, uncontrolled reaction of oxygen and fuel with a series of more controlled, intermediate reactions, akin to what is observed in biological processes. These intermediate steps can be designed to minimize exergy losses by improving the reversibility of the heat transfer process in the combustor. Ritcher and Knoche illustrated this concept with a three reservoir model, representing the exothermic oxidation reaction as the hot reservoir, and the endothermic reduction reaction and environment as cold reservoirs. This concept is schematically visualized in Figure 1-4.

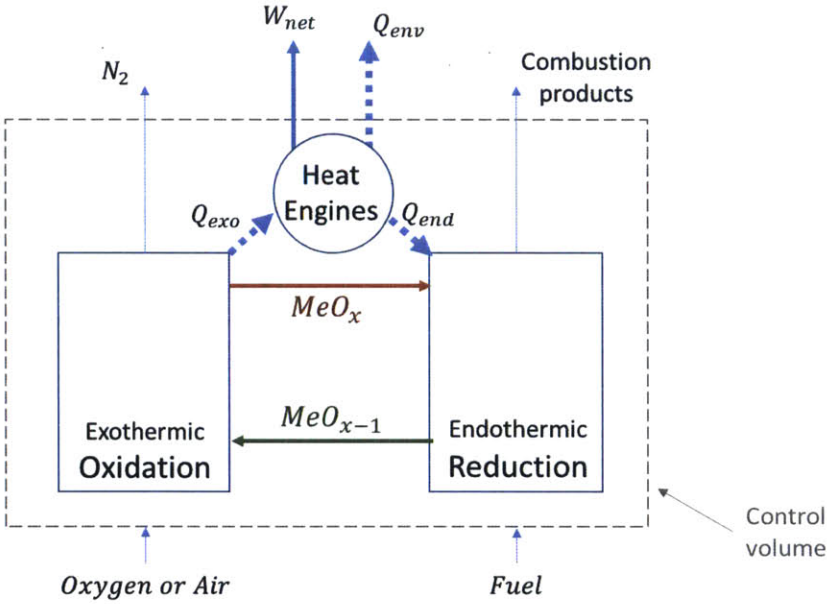

Figure 1-4: Theoretical concept for CLC in energy conversion systems.
Ref: [1]

In this setup, a series of heat engines is installed to produce work while reversibly exchanging heat between the three reservoirs. Theoretically, such a system would produce more work since the reversible heat transfer between the reactors reduces exergy loss and increases the availability of the system. While installing a heat engine between the two reactors is a challenging prospect, the possibility of keeping the air and fuel streams separate is of interest to researchers because it enables CO_2 capture from the thermal plant [17].

A unique feature of CLC energy conversion systems is that there are two high temperature streams exiting the reactors, each of which can be used in different power generation arrangements. Therefore, there are up to n^2 possible configurations for producing power (compared to n for a conventional system), as shown in Figure 1-5. The challenge, then, is to select an optimal combination of possible cycle configurations that maximizes CLC system performance.

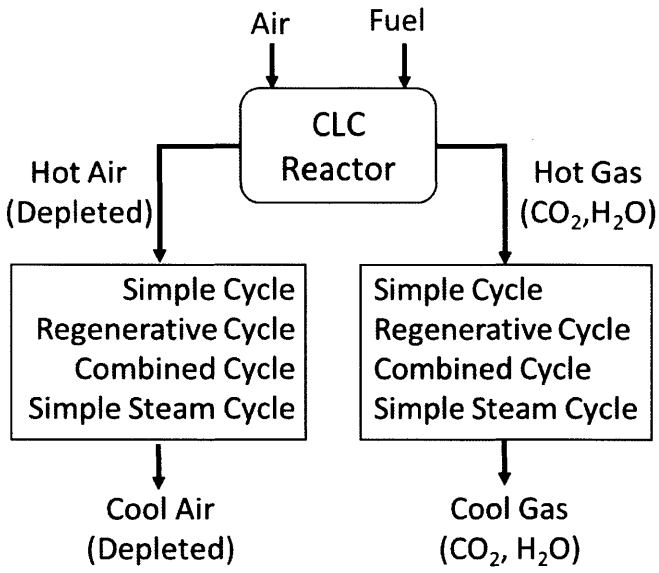

Figure 1-5: Possible energy conversion system configurations for CLC.

The following sections in this chapter will present a brief summary of CLC cycle configurations that have been studied in literature. Performance analysis of these proposed cycles show that CLC-based systems can achieve higher thermal efficiencies than most alternative carbon-capture enabled technologies, with reported efficiencies ranging from 48% to 58% [11]–[14], [17], [30], [31]. Most of these studies focused on demonstrating that integrating CLC into power generation systems reduces the exergy loss in the reactor compared to conventional combustors. However, lower reactor exergy loss does not necessarily translate into higher thermal efficiency. In fact, introducing CLC often leads to an efficiency penalty [32]. One reason for this apparent counter-intuitive observation is that the efficiency of thermal plants is ultimately a function of the temperature of the reactor exhaust streams. Therefore, lower fuel-side exhaust temperatures in CLC systems with endothermic reduction reactions penalizes efficiency relative to a conventional

combustor. Moreover, the overall availability of a power plant is also influenced by other components besides the reactor. However, CLC-based systems remain attractive because they outperform conventional systems when the energetic cost of CO_2 capture is taken into account.

1.4.1. Simple (Brayton) CLC cycle

This configuration employs one or two simple Brayton cycles; one for the air-side reactor and the other with the fuel-side reactor. Since the Brayton cycle is a low efficiency design, it has not really be considered as a viable option for CLC systems. Researchers have focused more on recuperative cycles, which are essentially Brayton cycles modified to include heat integration.

1.4.2. Recuperative CLC cycles

In this modified Brayton cycle, the enthalpy of the exhaust streams leaving each turbine is used to preheat the feed streams. An implementation proposed by Ishida et al. [17] also includes a saturator heat-integrated with the compressor intercoolers, as shown in Figure 1-6.

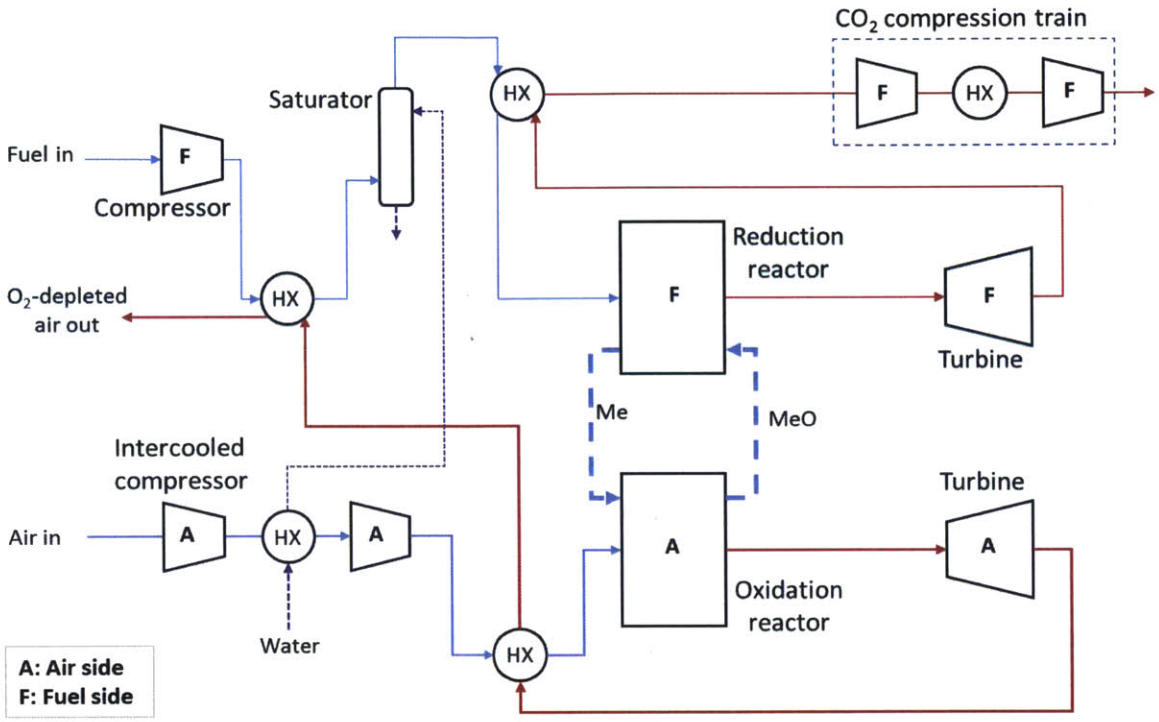

Figure 1-6: Schematic diagram of a recuperative CLC cycle.
Ref: [17]

In this cycle, the gaseous fuel is compressed to system pressure, saturated, and then preheated by the exhaust gas stream before entering the reduction reactor, where it reduces the metal oxide. The fuel reactor exhaust is first expanded in the turbine, then used to preheat the inlet fuel stream before proceeding to the CO_2 compression train. The air side follows a similar process. The compressor intercoolers are used to preheat the water supplied to the saturator. Combining preheating and saturation has the advantage of increasing the degree of utilization of the low temperature heat sources, as well as the net power output of the turbine. Ishida reported an efficiency of around 50.2% for a pressure ratio of 20 and maximum TIT of 1200C. A modified version of this system with the saturator on the air side yielded a 55% efficiency (both do not include CO_2 compression cost). Brandvoll [16] reported an efficiency of 51.3% for a similar configuration at compressor ratio of 18, including the cost of CO_2 compression.

1.4.3. Simple CLC steam cycles

In a simple CLC steam cycle, the exhaust stream enthalpies from both reactors are used to generate steam in a heat recovery steam generator (HRSG). The steam drives turbines to produce power. A simple CLC steam cycle layout proposed by Naqvi et al. [33] is represented schematically in Figure 1-7.

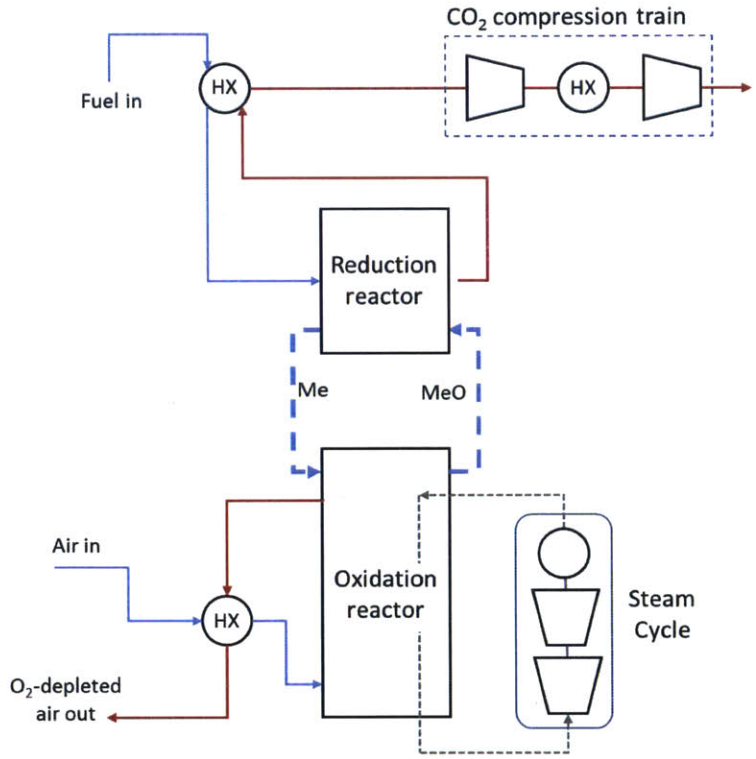

Figure 1-7: Schematic diagram of a simple CLC steam cycle.
Ref: [33]

In this setup, the steam generation takes place in the oxidation reactor in tubes fitted to the reactor walls (like in conventional 'water wall' furnaces) and the thermal energy in the exhaust streams is used to preheat the inlet stream. On the fuel-side, the reactor exhaust is simply used to preheat the feed fuel stream before proceeding to the CO_2 compression unit. This ambient pressure system has a thermal efficiency of around 40.1% with CO_2 compression to 200bar. Brandvoll [16] also reported an efficiency of about 40.4% for a similar system setup.

1.4.4. CLC combined cycle

The CLC combined cycle configuration has received the most interest from researchers because of its potential for high electrical efficiency, as well as the extensive industry experience in building and operating combined cycle plants. The layout is similar to that of conventional combined cycle, except that the CLC reactors have two separate exhaust streams. In the layout proposed by Naqvi et al. [14], [33], the air-side exhaust is first expanded in a turbine, then used to generate steam for a bottoming steam cycle while the fuel-side exhaust is first expanded in the fuel turbine, then used to preheat the fuel feed stream. This is essentially a hybrid configuration with a recuperative cycle on the fuel side and a combined cycle on the air side. The schematic diagram is shown in Figure 1-8.

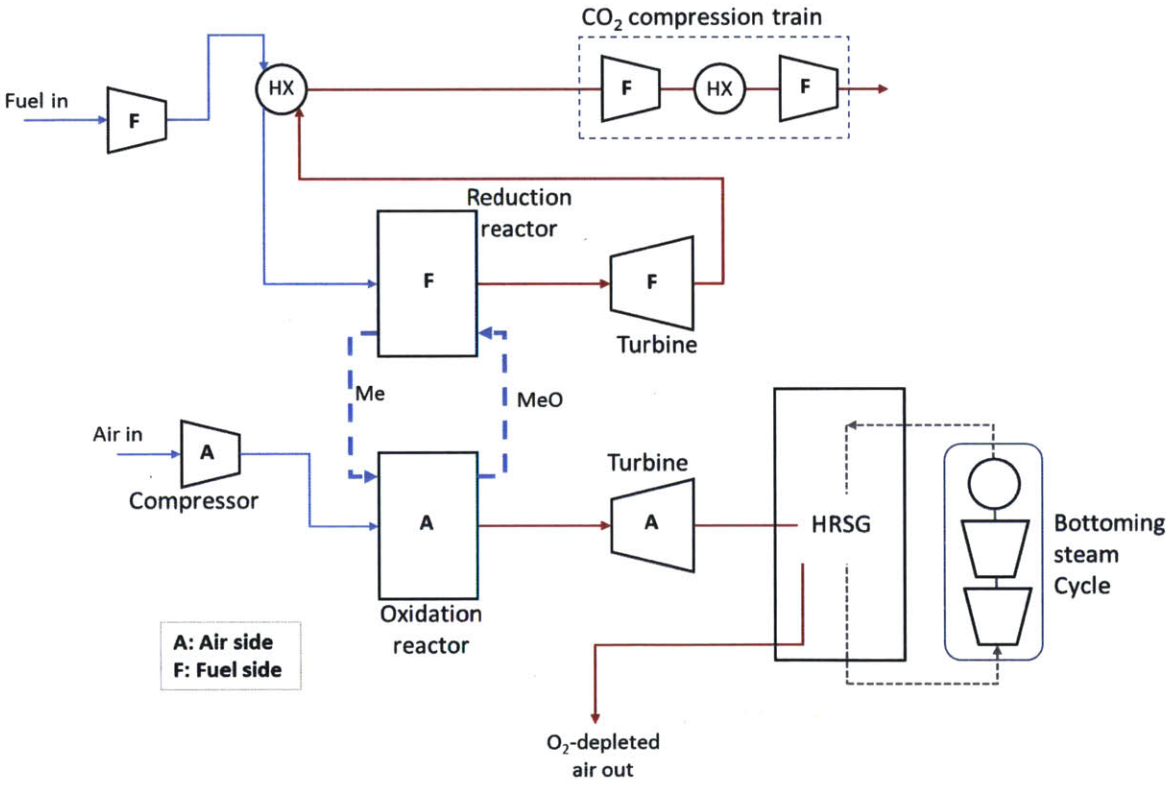

Figure 1-8: Schematic diagram of a CLC combined (hybrid) cycle.
Ref: [33]

A modification to this layout is the combined-reheat cycle proposed by Naqvi et al. [14] which incorporates partial expansion and reheat of the reactor exhaust streams, as shown in Figure 1-9. It achieves this by making use of two or more reactors in series, operating at different pressures. Introducing reheat increases the specific work output from the system since the reheat increases the average turbine inlet temperature.

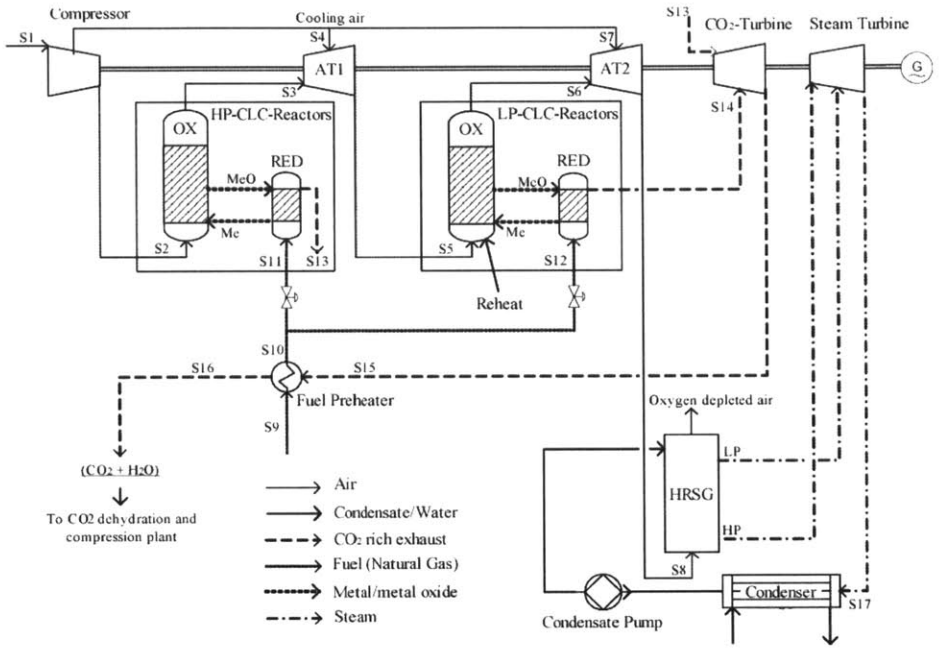

Figure 1-9: Schematic diagram of a Combined-reheat CLC cycle.
Ref: [14]

The reported efficiency for combined cycle CLC systems ranged from 48.5% to 52% [14], [15], [30], [31], [33]. The combined-reheat system was shown to improve efficiency by about 1% point [14] up to 53%, but the added cost and complexity might outweigh the performance benefits. Note that the differences in reported efficiencies have a lot to do with differences in modeling assumptions, and cycle layout and exhaust CO_2 compression pressure.

1.4.5. Partial capture systems

Partial capture systems refer to a category of cycle designs that propose a tradeoff between CO_2 capture and performance. The idea is to reduce the efficiency penalty associated with CO_2 capture by trading-off on the CO_2 capture efficiency of the system. Two interesting proposals of this

concept are the sorbent energy transfer system (SETS) of Yu et al. [32] and the CLC combined cycle with supplementary firing of Consonni et al. [31]. These designs regulate the temperature of the oxidation reactor, allowing it to operate closer to the equilibrium reaction temperature of the reduction reaction. Reactor temperature regulation minimizes heat transfer entropy generation, while firing raises the turbine inlet temperature, increasing the cycle net power output.

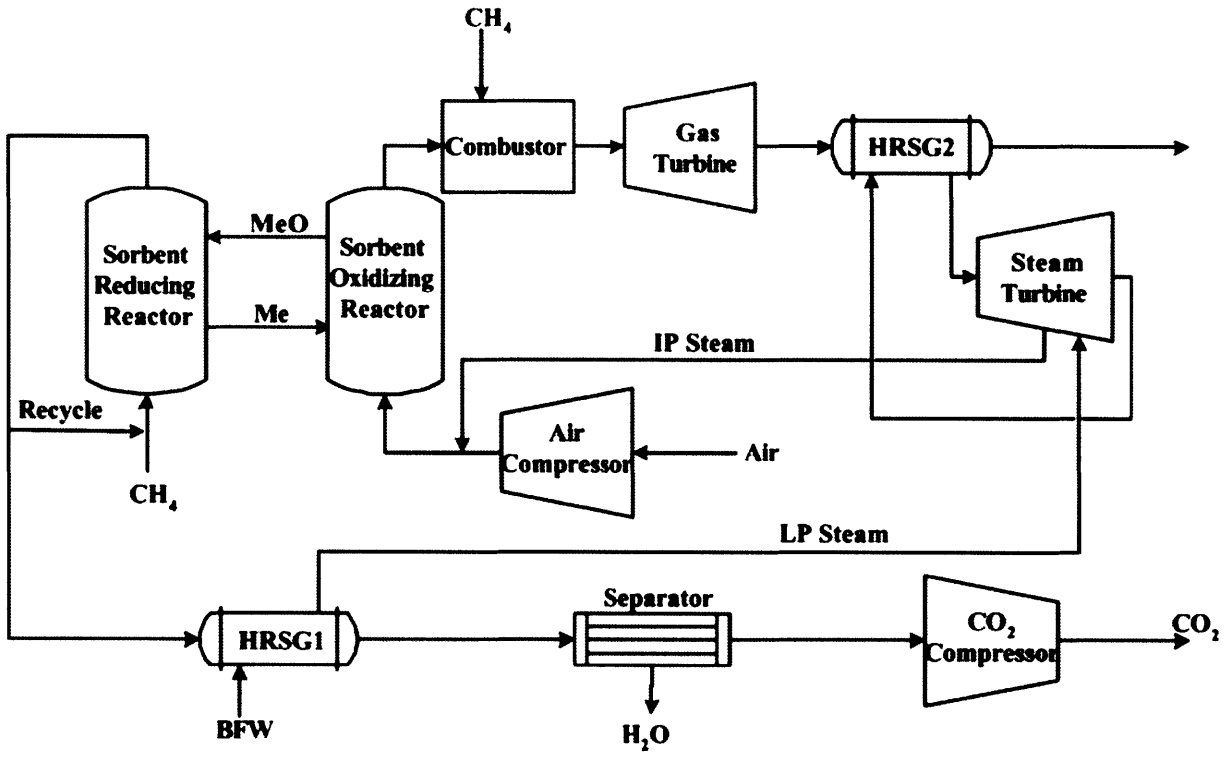

Figure 1-10: Schematic diagram of the sorbent energy transfer system (SETS).
Ref: [32]

Figure 1-10 shows a schematic diagram of the SETS process. The fuel stream is combined with some recycled gas stream and fed into the reducing reactor where the fuel reduces the metal oxide, producing CO_2 and H_2O. Part of this CO_2-rich product stream is recycled to the fuel reactor to control carbon deposition and the rest is used to generate low pressure steam for the steam cycle, before proceeding to the CO_2 compression train. On the air side, the inlet air stream is compressed, mixed with some intermediate pressure steam (to maintain gas turbine design flow rate in a retrofitted plant) and fed to the oxidation reactor. The oxygen-depleted oxidation reactor exhaust proceeds to a supplementary combustor where it directly reacts with additional fuel, increasing the enthalpy of the turbine inlet stream. The turbine exhaust stream is used to generate high pressure

steam for the steam turbine cycle. The cycle efficiency for the SETS process is about 53%, with 50% CO_2 capture, compared to about 56% for an equivalent conventional combined cycle without CO_2 capture. The supplementary firing system of Consonni et al. has a similar layout to the SETS process. Like the SETS layout, it introduces a combustor downstream of the oxidation reactor. However, there is no steam injection to the inlet air stream. Simulation results showed that by increasing the turbine inlet temperature from 1050C to 1200C, supplementary firing increased efficiency from 48% to about 52% with 50% CO_2 capture.

1.4.6. CLC systems for alternative fuels

The results presented so far were for natural gas-fired cycles. However, there have been studies for CLC-based thermal plants using other fuels. One interesting study in this category is the methanol-fired CLC combined cycle system of Zhang et al. [34] shown in Figure 1-11.

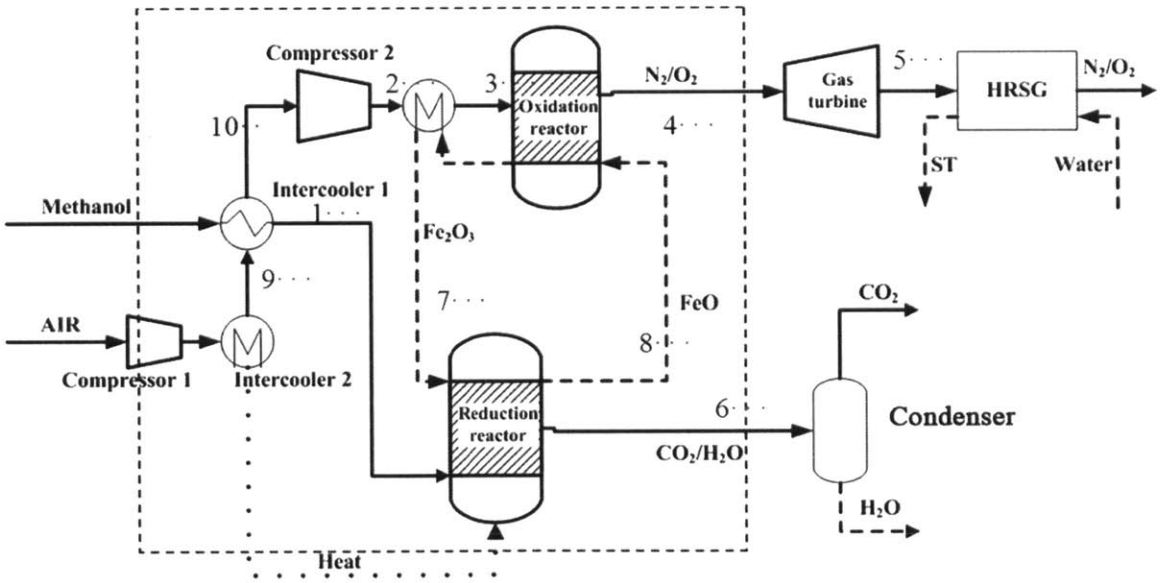

Figure 1-11: Schematic diagram of a CLC methanol-based cycle.
Ref: [34]

This configuration takes advantage of the fact that the equilibrium temperature of the reaction between the metal oxide and methanol is around 100-200C. Therefore, low temperature thermal

sources (e.g., compressor intercooling) can be used to provide the required thermal energy in the reactor. There is also energy saved since the methanol is a liquid at ambient temperature and can therefore be pumped to system pressure, avoiding gas compression. Zhang et al. reported an efficiency of 56.8% for this system. However, this value does not factor in the penalty from CO_2 compression. Moreover, the reported efficiency will be further downgraded if the energy requirement for methanol production is taken into account. For example, given that methanol production efficiency from coal and methane are typically less than 70% [35], the effective cycle efficiency could drop to the 40% range. There is also the challenge of implementing gas-solid heat exchange between the metal oxides leaving the oxidation reactor and the inlet air feed stream.

1.4.7. Energy conversion systems for solid fuels

The use of CLC for solid fuel applications is motivated by the availability and comparative cost advantage of these solid fuels compared to gaseous fuels. Typical solid fuels that can be used in CLC systems include coal, petroleum coke and biomass. The use of CLC in solid fuel combustion for power is particularly relevant given the abundance of coal and other solid fuel, and in light of the anticipated restrictions in CO_2 emission. Three main CLC designs have been proposed for handling solid fuels: 1) integrated gasification CLC combined cycles (IG-CLC-CC) with a separate gasifier and an air separation unit; 2) IG-CLC-CC with the gasifier embedded within the oxidation reactor; and 3) the coal-direct CLC system (CDCLC). These three options are illustrated in Figure 1-12, Figure 1-13 and Figure 1-14 respectively.

The configuration in Figure 1-12 includes a traditional gasifier upstream of the reduction reactor, with oxygen supplied from an air separation unit [2], [36]. The product syngas is supplied to the reduction reactor and the rest of the cycle is like a typical configuration for gaseous fuels. The drawback of using the air separation unit (ASU) is that it constitutes a significant parasitic energy demand which can be up to 15% of gross power output [36], [37]. An alternative design, shown in Figure 1-13, has the gasifier embedded within the oxidation reactor. For this setup, the energy of the endothermic gasification process is provided by the exothermic oxidation reaction [37]. This design does away with the ASU but introduces the challenge of managing heat transfer between the oxidation reactor and the gasifier.

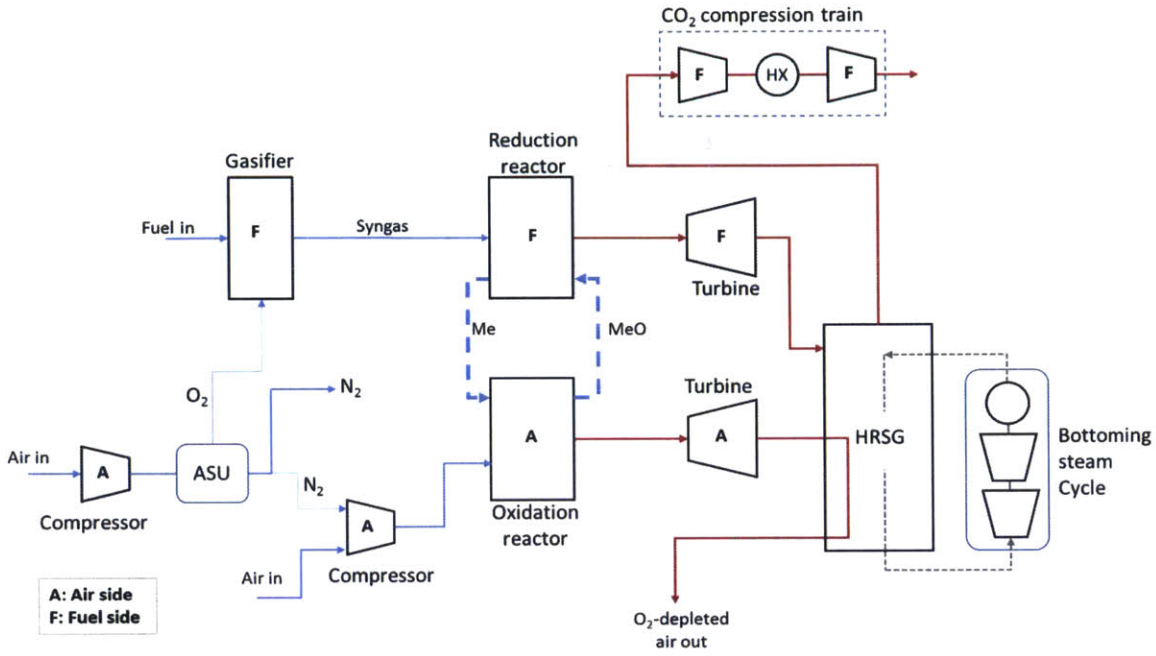

Figure 1-12: Schematic diagram of the IG-CLC-CC with ASU.

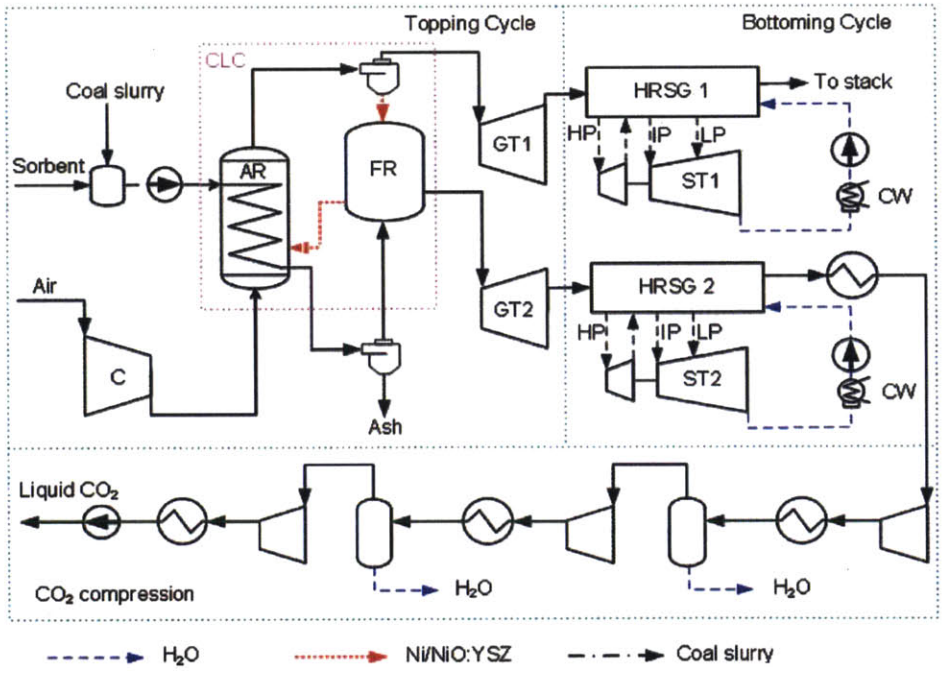

Figure 1-13: Schematic diagram of IG-CLC-CC with an embedded gasifier.
Ref: [37]

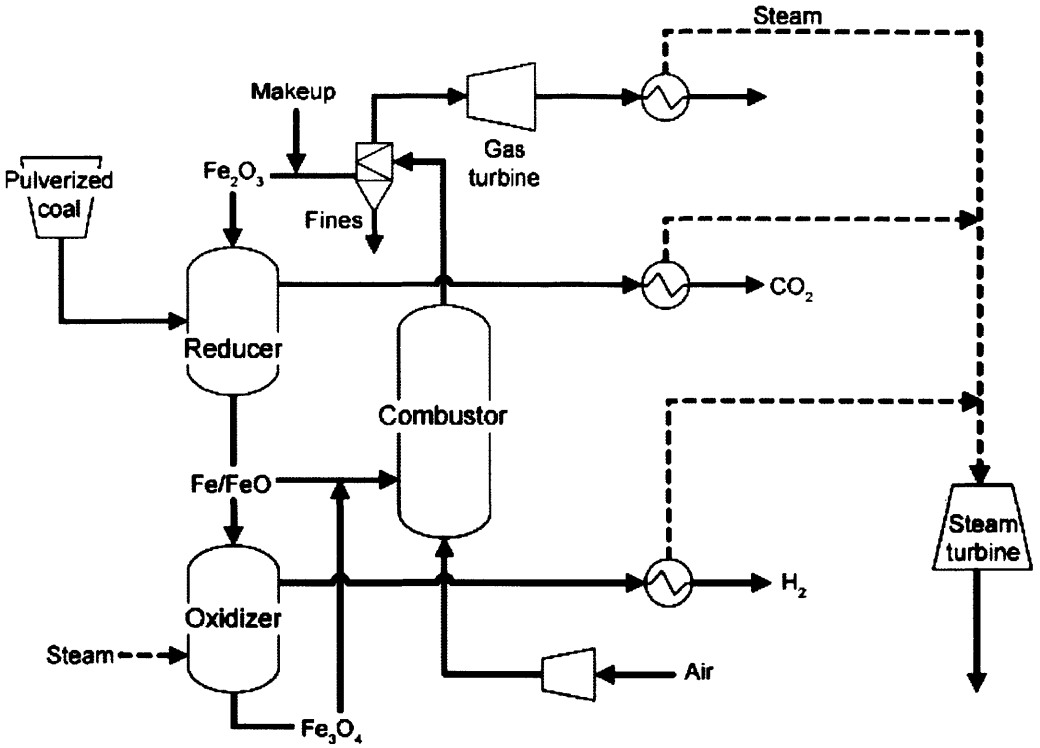

Figure 1-14: Schematic diagram of the (CDCL), a direct solid conversion system. Ref: [38]

The coal direct system of Figure 1-14 has a reduction reactor (reducer) and one or more oxidation reactors (oxidizer and combustor) [38]. The 'oxidizer' reactor is used only for combined hydrogen-electricity applications. Coal is directly oxidized by the oxygen carrier in the reducer to produce CO_2. The reduced oxygen carrier leaving this reactor is split in two; one part goes to the oxidizer where reaction with steam produces hydrogen. The other part proceeds to the combustor where it is oxidized via an exothermic reaction with the compressed air stream. The oxygen-depleted exhaust stream is expanded for power in a gas turbine. The three hot exhaust streams from the turbine, reducer and oxidizer are used to generate steam for the bottoming steam cycle. In general, direct solid fuel conversion systems do away with the gasifier and ASU and therefore promises to be a more efficient option.

Fan et al. reported a cycle efficiency of about 36.5% for the IG-CLC-CC (Fe-based) system with an ASU, compared to about 50% for the coal direct system based on process simulation results [38]. The difference in performance is mostly due to the elimination of the ASU for the coal direct system, as well as the conversion inefficiencies associated with gasification. For the IG-CLC-CC

system with an embedded gasifier, Xiang et al. showed simulation results in the range of 43-45%, depending on the turbine inlet temperature and the specified CO_2 capture efficiency [37]. Similar to Fan et al, Rezvani et al. presented cycle efficiency results of 34-35% for the IG-CLC-CC integrated with an ASU, with CO_2 compression up to 110 bar [36]. They also proposed a double stage IG-CLC-CC system configuration which can be used to optimally regulate the temperatures in the reactors, preventing the occurrence high temperature zones caused by heat transfer and mixing inefficiencies. This way, a more uniform temperature can be maintained in the reactors, enhancing combustion efficiency. In this concept (shown in Figure 1-15), the syngas from the gasifier is distributed between the two fuel reactors and exhaust gas streams from all the reactors are used to generate power in a gas turbine, and subsequently to generate steam in the HRSG for the bottoming steam cycle. The efficiency of this double stage concept was 36.1 – 36.6%, almost two percentage points higher than the single stage case. The underlying principle is the same as that for the combined-reheat cycle of Naqvi et al. [14] for natural gas fired plants.

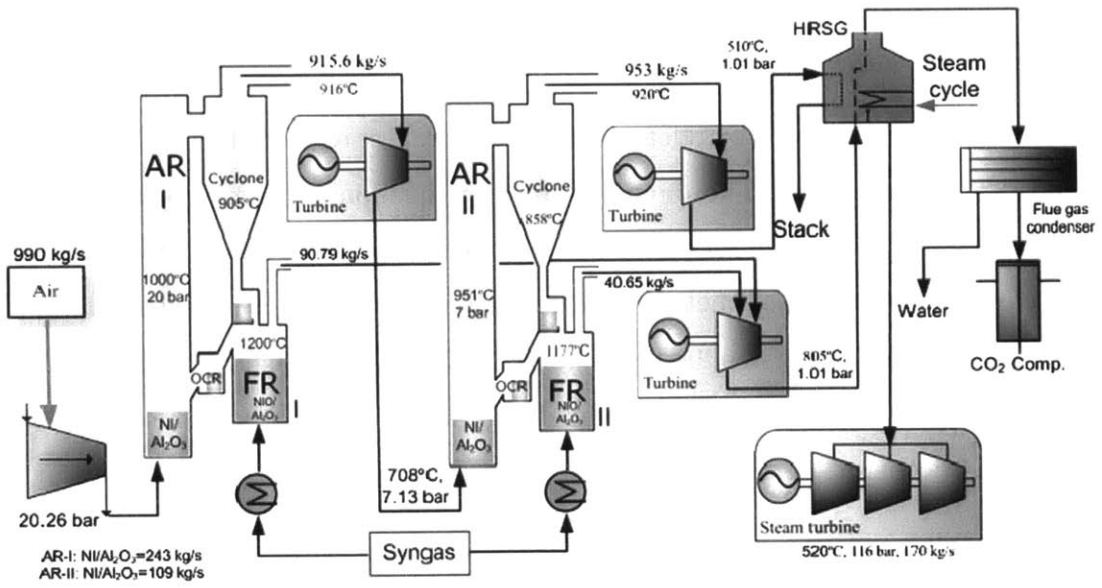

Figure 1-15: Double stage IG-CLC-CC system (ASU not shown).
Ref: [36]

1.4.8. Other CLC conversion applications

Besides energy conversion applications, CLC has also be proposed for a range of alternative applications, including fuel reforming for syngas or hydrogen production, combined reforming and electricity generation applications, and air separation [3], [39], [40].

1.4.9. Cycle layout concepts for the rotary reactor

For the specific case of the rotary reactor, an important design problem is to figure out an appropriate layout as well as reactor dimensions for the proposed power plant. Replacing a conventional gas-fired plant with a rotary reactor-based power plant will necessitate a rearrangement of the power island, given the significant geometric differences between the rotary reactor and the gas turbine combustor. Based on a reference reactor geometry and thermal size, the scaling relationship between the thermal and geometric size of the rotary reactor can be expressed as follows:

$$MW_{thermal} \propto (N * D^2 * L) \tag{1.4}$$

Where $MW_{thermal}$ = thermal energy release rate in reactor, D = reactor diameter, N = number of reactors and L = reactor length. The three variables in equation 1.4 represent the 3 degrees of freedom at the designer's disposal for determining the plant layout. To illustrate with an example, consider a reference $1MW_{thermal}$ nickel-based reactor of approximately 1m diameter and 0.5m height. Suppose the plan is to design the layout for a $200MW_{thermal}$ plant. Assuming that to meet certain structural and pressure drop criteria, the design target for the reactor height is set at 1m. Then equation 1.4 becomes:

$$\left(\frac{200}{1}\right) = \left(\frac{1}{0.5}\right)\left(\frac{N}{1}\right)\left(\frac{D}{1}\right)^2 \tag{1.5}$$

This means that any combination of NxD that satisfy equation 1.5 can be selected. From among the possible options encapsulated in equation 1.5, possible options include a single reactor of 10m diameter ($N = 1$; $D = 10$); or perhaps four 5m diameter reactors ($N = 4$; $D = 5$). Having determined the reactor size to number ratio, the next issue to consider is the reactor to turbine ratio. For the recuperative cycle, at least a pair of turbines is required to deal with the fuel and air-side

exhaust streams. Continuing with the example with four, $50MW_{thermal}$ reactors, the designer can adopt a modular approach to matching the total plant thermal size by stacking reactor-turbine modules in series, such that you have a pair of small turbines for each reactor, as illustrated in Figure 1-16. Alternatively, he or she could select two turbines that take the combined exhaust flows from the four reactors, as shown in Figure 1-17.

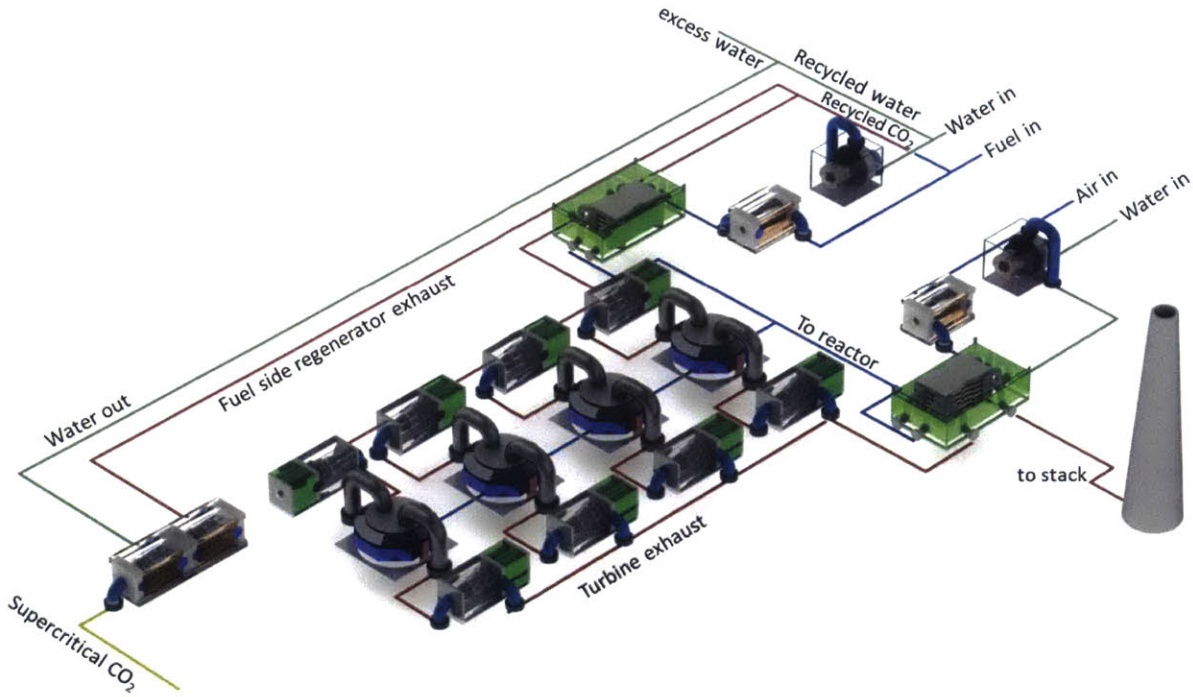

Figure 1-16: A modular recuperative CLC cycle layout with rector-turbine pairs in series.

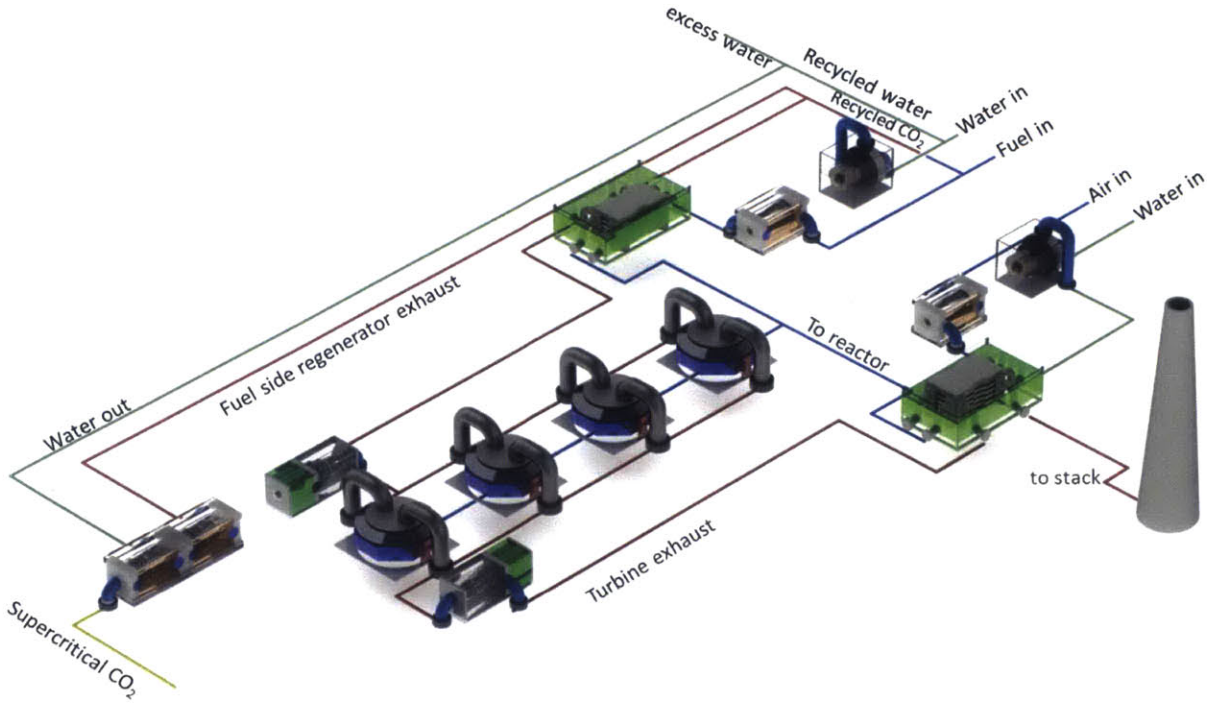

Figure 1-17: A modular recuperative CLC cycle layout with rectors in series and one turbine set.

These are just a few of a myriad of possible layout configurations for the rotary reactor-based recuperative power plant. They are used here simply to illustrate some of the design questions that need to be dealt with for these kind of systems. Important factors that must be considered in deciding on an optimal layout include the resulting cost, space requirements and technical challentges inherent in each design.

1.5. Thesis motivation & methodology

There has been some effort in analyzing and modeling CLC-based energy conversion systems, covering both fundamental thermodynamic analysis and more detailed process modeling. Ritcher and Knoche [1] made use of ideal thermodynamic availability models to provide the fundamental thermodynamic basis for CLC energy conversion system design and performance. This approach

was taken up and expanded by McGlashan and Chakravarthy [24], [41] to further characterize the key features, thermal characteristics and ideal performance limits of these systems.

However, the bulk of CLC system level studies have concentrated on more detailed process flowsheet development for use in cycle analysis. These studies all face the challenge of choosing an appropriate model for representing the CLC reactor in the integrated system. Most of them employ equilibrium reaction models or simple energy conservation models, usually implemented in standard or custom flowsheet modeling tools [11]–[15], [30], [31], [42]–[46]. Though this is a generally useful approach for system level modeling, its main limitation is that in using a very simplified reactor model, it fails to capture important feedback interactions between the CLC reactor and the rest of the system. To address this limitation, a few studies have integrated the system level model with a detailed dynamic model of the CLC reactor [42], [43]. Although this captures the reactor-system interactions more accurately, it dramatically increases the computational cost of system modeling. What appears to be missing is a strategy that directly integrates the system level model with a reactor model of appropriate intermediate complexity. Such a strategy allows for a detailed analysis of the integrated system and accurately represent important feedback interaction between the reactor and the overall system.

This thesis presents a unified, multiscale approach for adequately assessing the integration of the rotary reactor CLC technology in energy conversion systems. It develops a framework composed of models that capture, in increasing detail, the characteristics of the integrated system, as shown in Figure 1-18. The simplest form uses the concept of thermodynamic availability to model the system while the reactor is represented by interacting reservoirs. At the other end of the spectrum, detailed cycle models are used for system representation and these are integrated with a higher resolution reactor model derived by reducing the detailed dynamic rotary reactor model of Zhao et al. [29]. The reduced fidelity reactor model combines sufficiently accurate reactor representation with significantly lower computational costs. This feature makes it ideal for use in the integrated system analysis because it provides sufficient resolution to capture the nature and impact of reactor-system feedback interactions on optimal design and performance.

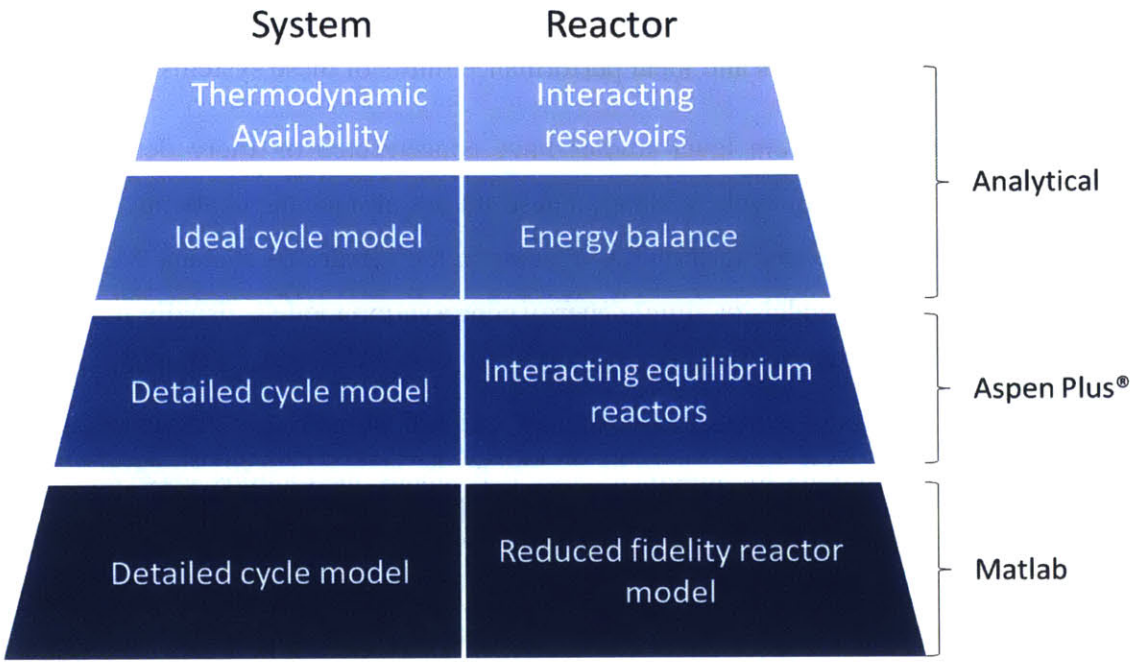

Figure 1-18: Multilevel framework for the integrated CLC system analysis in this thesis.

The availability and ideal cycle models comprise analytical formulations that represent high level trends and theoretical performance bounds for generic, thermally-coupled CLC-based systems. The Aspen Plus® flowsheet models are used for more realistic representations of the integrated system and are applied in comparative analysis and preliminary sensitivity studies of cycle configurations based on the thermally-coupled rotary reactor. The integrated Matlab model captures the relationship between oxygen carrier properties, reactor design and system specifications and is used for simultaneous optimization of the integrated system.

1.6. Thesis structure

The analysis in this thesis is presented in five chapters. Chapter 2 investigates the integration of the thermally coupled CLC reactor with a power generation cycle, and demonstrates the impact of reactor thermal coupling for a recuperative cycle. Chapter 3 extends this analysis to alternative configurations with the two-pronged objective of validating the thermal coupling effect for alternative cycle configurations and identifying suitable cycles for these reactors. Chapter 4 presents the formulation, validation and analysis of a reduced fidelity model for the rotary reactor.

In Chapter 5, this reduced fidelity reactor model is incorporated into the system model and used for optimization and parametric analysis of the integrated system. Finally, Chapter 6 develops an economic model for the optimization and comparative analysis of rotary reactor-based systems using selected oxygen carrier materials.

2. Thermodynamic analysis of thermally coupled CLC power plants

2.1. Introduction

As discussed in chapter 1, during the cyclic operation of the rotary reactor, the solid wheel, which is made of a high thermal capacity and conductivity material like boron nitride, provides internal thermal coupling between all the different sectors in the reactor. A natural consequence of this feature is that the exhaust stream from the oxidation reactor leaves at the same temperature as that from the reduction reactor. This state of thermal coupling in CLC configurations that maintains equilibrium between the fuel and air reactors, creating equal fuel and airside exhaust stream temperatures, will be referred to as thermally balanced reactor operation.

This chapter investigates the integration of a thermally coupled CLC reactor with a power generation cycle, using the rotary reactor as a case study. It presents an analysis of the impact of the thermal coupling on the performance of a CLC energy conversion system in three stages, outlined in Sections 2.2 - 2.4. In Section 2.2, a theoretical availability model, following the approach used by Ritcher and Knoche [1], Chakravarthy et al. [24] and McGlashan [41], is used to develop a functional relationship between efficiency and the temperatures of the oxidation and reduction reactors. This formulation is then used to frame the discussion on the relationship between reactor thermal balance and the availability of practical CLC systems, taking into account relevant thermodynamic and material limitations. For this stage, the CLC reactor is modeled as a pair of interacting thermal reservoirs.

Next, the idealizing assumptions are relaxed to accommodate the limitations imposed by specific cycle configurations. Section 2.3 makes use of an ideal thermodynamic model of a recuperative CLC cycle for this purpose. The expression for the recuperative CLC cycle efficiency as a function of the ratio of reactor temperatures is used to define the relationship between reactor thermal balance and optimal system efficiency. The discussion in this section also covers the implication of thermodynamic and material limitations of practical CLC systems in the context of thermally

balanced or imbalanced CLC reactor designs. Here, the CLC reactor is modeled by taking an energy balance around a control volume with heat input equal in magnitude to the reaction enthalpy.

In section 2.4, the thermodynamic idealizations are further relaxed and a higher fidelity Aspen Plus® model of the recuperative CLC cycle introduced in Section 2.3 is developed. This model provides a more realistic representation of a practical CLC energy conversion system, capturing the effects of the configurational constraints of a specific cycle. The simulation results are used to validate the conclusions of the previous sections and to quantify the thermal efficiency advantage that results from thermally balanced reactor operation. The Aspen Plus® model is also used to carry out a parametric analysis on the recuperative CLC cycle to determine the impact of key design/operating parameters on system thermal efficiency. Here, the CLC reactor is modeled as a pair of interacting equilibrium reactors with coupled thermal and material exchange.

2.2. Theoretical availability analysis

The theoretical availability of a Chemical Looping Combustion (CLC) energy conversion system provides valuable insight into its efficiency potential [47]. One of the major arguments in favor of CLC is that it achieves complete fuel conversion through a staged reaction process that improves system availability by reducing exergy destruction in the reactor [2], [13], [38]. Therefore, the analysis in this section will derive expressions for availability as a function of reactor temperatures to investigate the impact of reactor thermal coupling on CLC system performance. Note that the following discussion presents conceptual scenarios that broadly define the feasible operating window for CLC energy conversion systems.

In an ideal CLC energy conversion system, all processes have to be reversible. Approaching this reversible limit implies minimizing the entropy generation associated with heat transfer and chemical reaction. To minimize reaction entropy generation, the reaction process should be isothermal and should take place at the equilibrium temperature of the reaction. This equilibrium temperature is determined by setting the change in Gibbs free energy to zero in the classical chemical thermodynamic relation [41], [48]:

$$\Delta G_{rxn} = 0 = \Delta H_{rxn} - T_{eq}\Delta S_{rxn} \quad (2.1)$$

ΔG_{rxn} is the reaction Gibbs free energy, ΔH_{rxn} is the reaction enthalpy, ΔS_{rxn} is the reaction entropy and T_{eq} is the reaction equilibrium temperature. For CLC processes, the oxidation reaction is exothermic ($\Delta H_{ox} > 0$). The reduction reaction is typically endothermic ($\Delta H_{red} > 0$), but could be exothermic. In either case, the sum of the two enthalpies, evaluated at the corresponding reactor temperatures, gives the overall reaction enthalpy (ΔH). The enthalpy of reaction depends on the oxygen carrier type as well as the fuel; take nickel from Table 2.1 for example, the reduction reaction with methane is endothermic while that with hydrogen is mildly exothermic.

Table 2.1: CLC Reaction property data for selected oxygen carriers

a) Oxidation properties

Oxygen Carrier	**$T_{melting}$ (K)**	**Reaction**	**ΔH_0 (kJ/mol)**	**Teq (K)**
Ni/NiO	1728	$O_2 + 2Ni = 2NiO$	−479	2542
Cu/CuO	1358	$O_2 + 2Cu = 2CuO$	−312	1676
Fe_3O_4/ Fe_2O_3	1811	$O_2 + 4Fe_3O_4 = 6Fe_2O_3$	-464	1751
Mn_3O_4 / Mn_2O_3	1161	$O_2 + 4Mn_3O_4 = 6Mn_2O_3$	−190	1153

b) Reduction properties

Oxygen Carrier	**$T_{melting}$ (K)**	**Reaction**	**Teq (K)**	**ΔH_0 (kJ/mol)**
Ni/NiO	1728	$CH_4 + 4NiO = CO_2 + 2H_2O + 4Ni$	420	156
		$H_2 + NiO = Ni + H_2O$	−43	−2
Cu/CuO	1358	$CH_4 + 4CuO = CO_2 + 2H_2O + 4Cu$	-489	−179
		$H_2 + CuO = Cu + H_2O$	−1771	−86
Fe_3O_4/ Fe_2O_3	1811	$CH_4 + 12Fe_2O_3 = CO_2 + 2H_2O + 8Fe_3O_4$	241	126
		$H_2 + 3Fe_2O_3 = 2Fe_3O_4 + H_2O$	−109	−10
Mn_3O_4 / Mn_2O_3	1161	$CH_4 + 12Mn_2O_3 = CO_2 + 2H_2O + 8Mn_3O_4$	−1302	−422
		$H_2 + 3Mn_2O_3 = 2Mn_3O_4 + H_2O$	−3864	−147

The oxidation reaction usually occurs at a higher temperature than the reduction reaction. When the reduction reaction is endothermic, the oxidation reaction provides the deficit heat required to sustain this reaction. Modeling the reactors as isothermal heat reservoirs, it is theoretically possible to install a reversible engine (or series of engines) that extracts additional work while interacting with the two reservoirs and the environment [1]. This idealized concept proposed by Ritcher and Knoche was subsequently expanded on by McGlashan [41] and Chakravarthy et al. [24] and will serve as the framework for the discussion in this section.

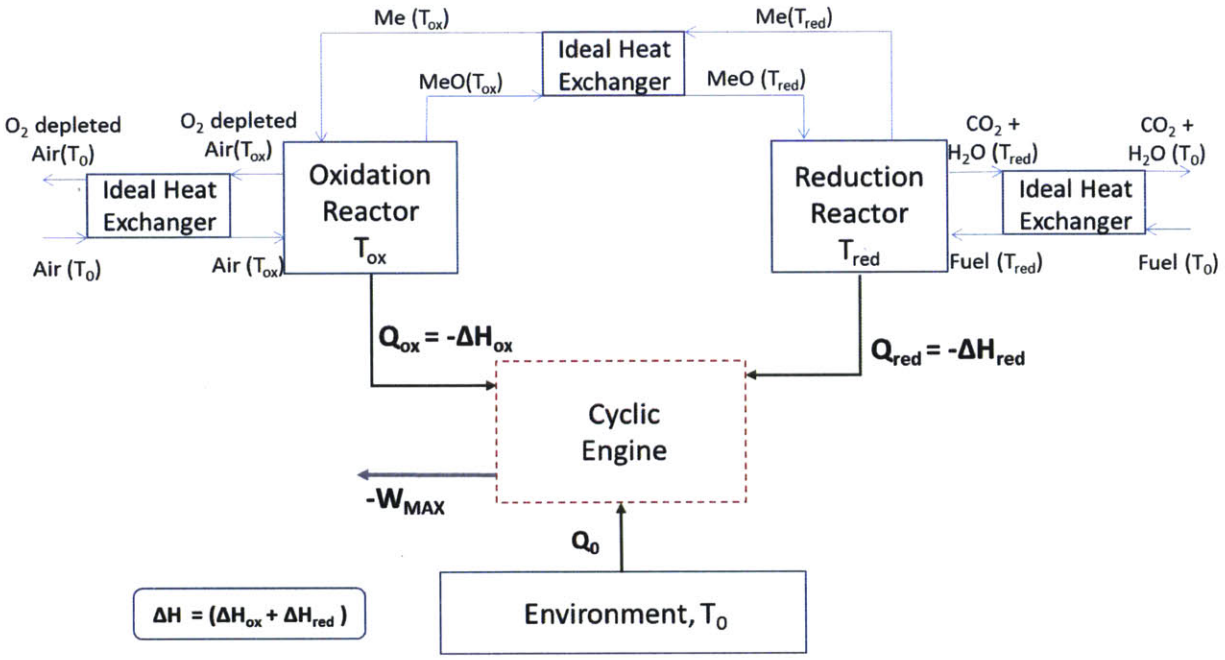

Figure 2-1: Ideal generic CLC system.

Figure 2-1 shows an idealized representation of a generic CLC system that consists of an ideal cyclic engine interacting with the oxidation reactor, the reduction reactor and the environment. This setup assumes that the three counter-flow heat exchangers have balanced flows and maintain only an infinitesimal temperature difference between the hot and cold streams. If the reduction reaction is exothermic, the heat release from both reactors is delivered directly to the engine to produce work. For an endothermic reduction reaction, the heat engine transfers some of the heat

from the oxidation reactor to sustain the reduction reaction while producing work. In all cases, both reactors are isothermal and will be treated as thermal reservoirs in the following analysis.

For a system with exothermic reduction reaction, applying the first and second laws of thermodynamics to the cyclic engine control volume gives

$$-W_{MAX} = |\Delta H|\left(1 - \left(\frac{T_0}{T_{ox}}\right)\right) - |\Delta H_{red}|\left(\frac{T_0}{T_{ox}}\left(\frac{T_{ox}-T_{red}}{T_{red}}\right)\right) \quad (2.2)$$

The same approach for a system with endothermic reduction reaction gives

$$-W_{MAX} = |\Delta H|\left(1 - \left(\frac{T_0}{T_{ox}}\right)\right) + |\Delta H_{red}|\left(\frac{T_0}{T_{ox}}\left(\frac{T_{ox}-T_{red}}{T_{red}}\right)\right) \quad (2.3)$$

Where T_{ox} is the oxidation reaction temperature, T_{red} is the reduction reaction temperature, T_0 is the environment temperature, ΔH_{red} is the reduction reaction enthalpy, ΔH_{ox} is the oxidation reaction enthalpy, $-W_{MAX}$ is the net work output of the system and the net reaction enthalpy, ΔH is the sum of the oxidation and the reduction reaction enthalpies, given by $\Delta H = \Delta H_{ox} + \Delta H_{red}$. The derivation for equations 2.2 and 2.3 can be found in Appendix 2A. The first term on the right hand side in both expressions is equivalent to the work output of a Carnot engine operating between two reservoirs at the temperature of the oxidation reactor and the environment. The second term constitutes an additional component that modifies the overall system availability, depending on the temperature difference between the two reactors ($\frac{T_{ox}-T_{red}}{T_{red}}$). In order to analyze the contribution of this second term to CLC system work output, scenarios for exothermic and endothermic reduction reactions will be considered. Except when stated otherwise, the following analysis assumes that T_{ox} is fixed at its thermodynamic upper bound, given by the equilibrium temperature of the oxidation reaction defined in equation 2.1 [24], [41]. T_{red} is free to take any value within the feasible range for the respective exothermic or endothermic reactions. The equilibrium reduction reaction temperature defines the lower bound for this range. For the endothermic reduction reaction, the oxidation reaction temperature defines the upper bound.

2.2.1. Scenario 1: exothermic reduction reaction

Here, $\Delta H_{red} < 0$ while $\Delta S_{red} > 0$, and equation 2.1 provides an infeasible negative equilibrium temperature that defines the lower bound. Therefore, theoretically, the reduction reaction temperature can take any value above this lower bound [24]. When $T_{red} \leq T_{ox}$, maximizing work output corresponds to minimizing the temperature difference between both reactors, and the maximum availability corresponds to the situation where $T_{ox} = T_{red}$, in which case equation 2.2 becomes

$$-W_{MAX} = |\Delta H|\left(1 - \left(\frac{T_0}{T_{ox}}\right)\right) \tag{2.4}$$

Equation 2.4 defines the availability for the thermally balanced CLC system. Notice that the expression is equivalent to that of an ideal heat engine operating between the oxidation reactor temperature and the environment temperature.

If $T_{red} \geq T_{ox}$, and T_{ox} is fixed at the equilibrium oxidation temperature, then equation 2.2 suggests that work output increases with increasing difference between the reactor temperatures. In the limit when $T_{red} \gg T_{ox}$, equation 2.2 simplifies to equation 2.5

$$-W_{MAX} = |\Delta H| - \left(\frac{T_E}{T_{ox}}(|\Delta H_{ox}|)\right) \tag{2.5}$$

In CLC setups with $T_{red} > T_{ox}$, if the oxidation reactor is at its equilibrium temperature, then the oxygen carrier leaving the fuel reactor has to be cooled down before the oxidation reaction can proceed. For circulating reactors, this could mean increasing the oxidation reactor residence time to accommodate both the cooling and the reaction phases, or introducing either a heat exchanger or a reformer in-between the two reactors. For packed/fixed bed reactors, one option is to increase oxidation residence time to accommodate cooling and reaction. Another is to have successive reduction and reforming phases in the fuel reactor before switching on the oxidizing stream. These adjustments introduce additional complexity to reactor design and operational management. However, in practical CLC systems, the maximum reactor temperature is usually constrained below the equilibrium oxidation temperature by the properties of the oxygen carrier, the turbine

inlet material or the material of the heat recovery steam generator (HRSG). These material temperature limits impose a more stringent upper bound than the oxidation reactor temperature. Consequently, consistent with the conclusion by Chakravarthy et al. [24], T_{red} can only be as high as the feasible T_{ox} and the maximum work output is obtained at this condition. The expression for the maximum work output for this condition is the same as in equation 2.4.

2.2.2. Scenario 2: endothermic reduction reaction

Here, $\Delta H_{red} > 0$ and $\Delta S_{red} > 0$, and the equilibrium temperature determined from equation 2.1 defines the thermodynamic lower bound for this reaction. Equation 2.3 suggests that maximizing availability corresponds to maximizing the temperature difference between the two reactors. Thus, maximum work should be obtained when T_{red} is equal to the equilibrium reduction temperature, which is the minimum thermodynamically feasible value [24], [41]. This scenario, however, has serious practical challenges. For one, it requires an engine that extracts additional work while transferring heat from the oxidation to the reduction reactor. Realizing such a setup in a real CLC installation may be prohibitively complex. One proposal by McGlashan [41] is the high temperature Rankine cycle using metal vapor working fluid, with the oxidation and reduction reactors serving respectively as the boiler and condenser. A steam cycle that uses the condensing metal vapor as heat source could also be added when the heat of condensation is larger than the endothermic enthalpy of reaction. There is, however, the difficulty of finding adequate high temperature materials and managing effective heat transfer involving both gas and solid phase components.

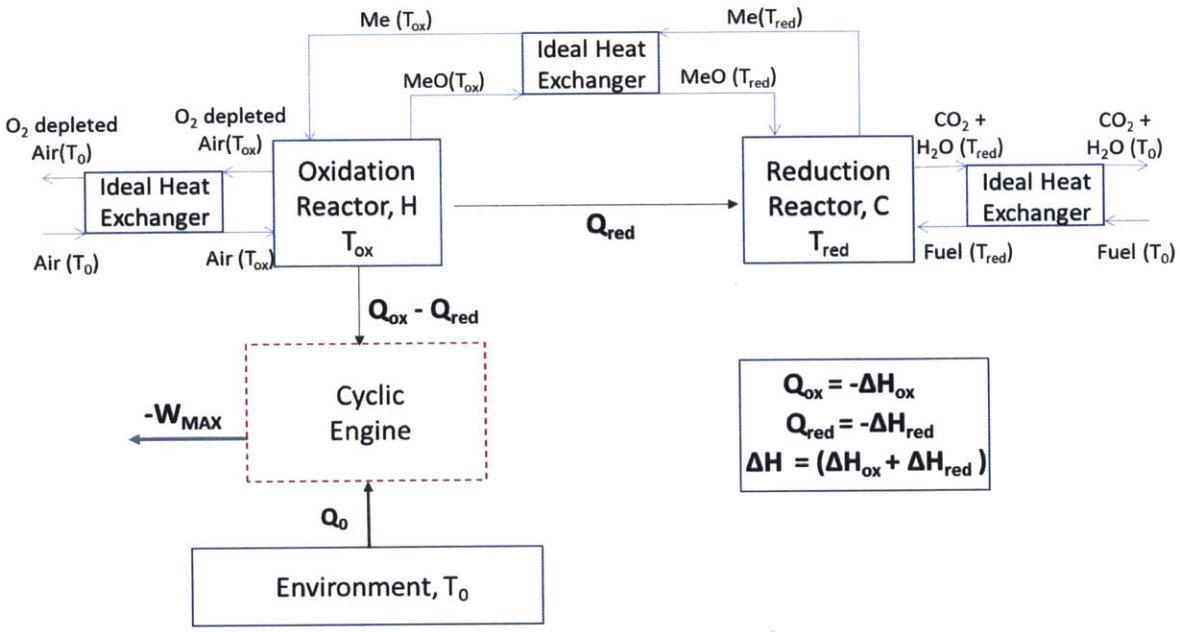

Figure 2-2: Ideal generic CLC system with direct reactor heat transfer.

The thermodynamics of an actual design r configuration. This direct heat transfer also results in increased entropy generation, which can be reduced using thermally coupled reactors to minimize the reactor temperature difference.

Kinetic considerations also play an important role in determining the optimal operating conditions for the reduction reactor. Lower temperatures result in slower kinetics, requiring longer residence times in the reactor. This means larger reactors and higher costs. For this reason, higher temperatures are required to speed up kinetics and favor products formation. Consequently, the reduction reactor temperature should be as high as possible, with the optimal scenario achieved when $T_{ox} = T_{red}$. To summarize, for a CLC setup with endothermic reduction reaction, practical considerations currently exclude the feasibility of installing an engine between the two reactors to extract additional work while reaction kinetics support high reduction reactor temperatures. The optimal operating condition therefore corresponds to the case where the two reactors are in thermal equilibrium. Table 2.2 summarizes the key conclusions from this section.

Table 2.2: Summary table for availability analysis

Reduction Reaction	**Condition for Maximum Efficiency**	
	Thermodynamic Constraints only	Thermodynamic and material constraints
Endothermic	$\boldsymbol{T_{red} < T_{ox}}$ $T_{ox} = T_{equilibrium}\,(oxidation)$ $T_{red} = T_{equilibrium}(reduction)$	$\boldsymbol{T_{red} = T_{ox}}$ $T_{ox} = T_{max}$
Exothermic	$\boldsymbol{T_{red} > T_{ox}}$ $T_{ox} = T_{equilibrium}\,(oxidation)$ $T_{red} \gg T_{equilibrium}(reduction)$	$\boldsymbol{T_{red} = T_{ox}}$ $T_{ox} = T_{max}$

T_{max} is the maximum temperature imposed by either oxygen carrier melting point or turbine inlet temperature.

2.3. Thermodynamic analysis for idealized cycles

Section 2.2 used theoretical availability models with Carnot-type engines to analyze the performance limits of CLC systems. This section extends the theoretical analysis to a specific cycle configuration, in this case, an ideal recuperative (Brayton) CLC cycle. A sketch of the recuperative CLC cycle is shown in Figure 2-3a, while the corresponding T-S diagram is represented in Figure 2-3b. This cycle includes a compressor, a combustor, a turbine and a recuperative heat exchanger on both the fuel and the air side (denoted by the subscripts 'f' and 'a' respectively). On either side, the process path comprises of isentropic compression (1-2), inlet stream preheating in the recuperator (2-3), constant pressure combustion (3-4), isentropic expansion (4-5) and exhaust heat recovery in the recuperator (5-6). The broken line represents the cooling process of the exhaust discharged into the ambient environment. The following analysis assumes that the inlet air and fuel are at ambient temperature and pressure, the heat exchangers are ideal, the thermal capacity (mc_p) of the air-side and fuel-side streams are constant and independent of temperature or pressure, the fuel flow rate $(m_f)$is fixed and therefore, the net heat release (Q) in the reactor is constant. The CLC reactor in Figure 2-3a comprises both the oxidation and the reduction reactors. Since the control volume is placed around the reactor, it only captures the net heat release, represented by Q, and does not make a distinction between endothermic or exothermic reduction reactions. The air and fuel-side pressure ratios are equal and the turbines and compressors are

isentropic. Work (W) and Heat (Q) are defined as positive into the control volume, the air-side reactor exhaust temperature is fixed and the air flow rate (m_a) is varied to control the fuel side reactor exhaust temperature. The thermodynamic process for this recuperative cycle is shown in Figure 2-3b. Applying energy conservation on the airside and fuel-side components of the recuperative system in Figure 2-3 gives

$$W_{Net_a} = m_a c_{pa} T_0 \left(\pi^{\alpha} - \frac{T_{ox}}{T_0}\right)(1 - \pi^{-\alpha}) \tag{2.6}$$

$$W_{Net_f} = m_f c_{pf} T_0 \left(\pi^{\alpha} - \frac{T_{red}}{T_0}\right)(1 - \pi^{-\alpha}) \tag{2.7}$$

Energy balance on the reactor gives

$$Q = -\Delta H = (m_f c_{pf} T_{red} + m_a c_{pa} T_{ox})(1 - \pi^{-\alpha}) \tag{2.8}$$

T_{ox} is the oxidation reactor temperature, T_{red} is the reduction reactor temperature, T_0 is the ambient temperature, W_{Net_a} is the net-work output from the air-side cycle, W_{Net_f} is the net-work output from the fuel-side cycle, $Q(-\Delta H)$ is the net reaction enthalpy, m_f is the fuel-side mass flow rate, m_a is the air-side mass flow rate, c_{pf} is the fuel stream specific heat capacity, c_{pa} is the air stream specific heat capacity, and π is the compressor pressure ratio.

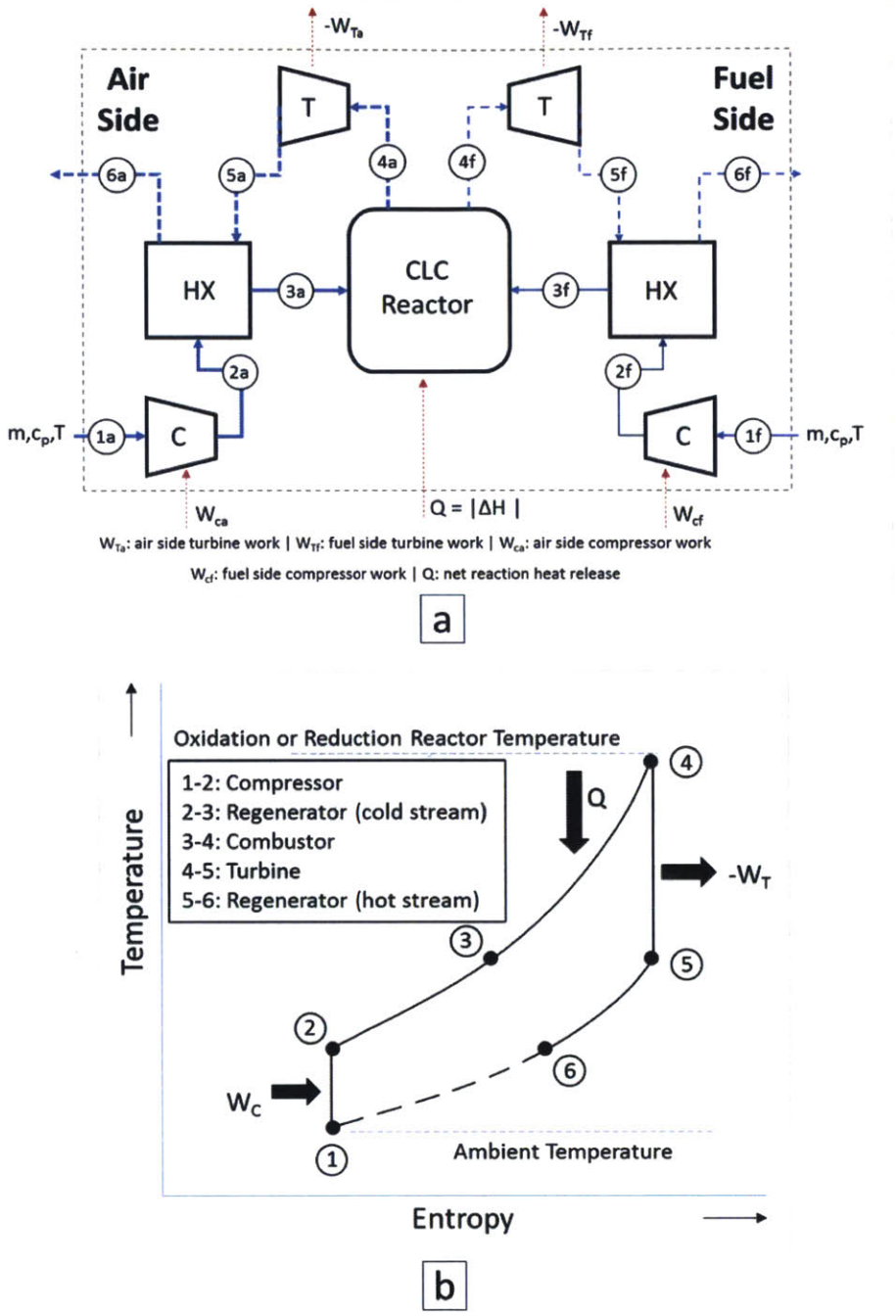

Figure 2-3: Ideal recuperative CLC cycle.
(a) Cycle layout; (b) Temperature-entropy (T-S) diagram. The path 1-2-3-4-5-6 represents the process on either the fuel side or the air side.

Combining equations 2.6, 2.7 and 2.8, one can arrive at an explicit expression for efficiency as a function of reactor temperatures:

$$\eta = 1 - \frac{T_0(m_f c_{pf} + m_a c_{pa})(\pi^{\alpha})}{(m_f c_{pf} T_{red} + m_a c_{pa} T_{ox})} \tag{2.9}$$

η is the cycle efficiency (See Appendix 2B for details of the derivation). Now consider the following cases:

Thermally balanced reactors: the oxidation and reduction reactors are in thermal equilibrium ($T_{ox} = T_{red}$): Substituting $T_{ox} = T_{red}$ into equation 2.9, the resulting expression for the efficiency of the system is given in equation 2.10. Note that this is the same expression for a conventional (ideal) recuperative Brayton cycle operating over the same temperature range and pressure ratio:

$$\eta_{thermal} = 1 - \frac{(\pi^{\alpha})}{\left(\frac{T_{ox}}{T_0}\right)} \tag{2.10}$$

Thermal imbalanced reactors: the oxidation and reduction reactors are not in thermal equilibrium ($T_{ox} \neq T_{red}$) : The relationship between m_a and T_{red} means that equation 2.9 has only one degree of freedom. Thus, efficiency can be expressed solely in terms of either of these variables. Therefore, substituting for m_a from equation 2.8 into equation 2.9 and rearranging, the following expression for efficiency is obtained:

$$\eta = 1 - \frac{\left(\left(\frac{Q}{(1-\pi^{-\alpha})c_{pa}T_{ox}}\right)c_{pa}\pi^{\alpha}\right) + (m_f c_{pf}\pi^{\alpha})}{\left(\left(\frac{Q}{(1-\pi^{-\alpha})c_{pa}T_{ox}}\right)c_{pa}\frac{T_{ox}}{T_0}\right)} + \frac{\left(\left(\frac{m_f c_{pf}}{c_{pa}}\right)\pi^{\alpha}\right)}{\left(\left(\frac{Q}{(1-\pi^{-\alpha})c_{pa}T_{ox}}\right)\frac{T_{ox}}{T_0}\right)}\left(\frac{T_{red}}{T_{ox}}\right)$$

$$= 1 - \Psi_1 + \Psi_2\left(\frac{T_{red}}{T_{ox}}\right) \tag{2.11}$$

Ψ_1 *and* Ψ_2 are positive constants (see Appendix 2B). Thus the derivative of the cycle efficiency with respect to the reactor temperature ratio is a positive constant and given by

$$\frac{\partial\eta}{\partial\left(\frac{T_{red}}{T_{ox}}\right)} = \frac{\left(\left(\frac{m_f c_{pf}}{c_{pa}}\right)\pi^{\alpha}\right)}{\left(\left(\frac{Q}{(1-\pi^{-\alpha})c_{pa}T_{ox}}\right)\frac{T_{ox}}{T_0}\right)} = \Psi_2 \tag{2.12}$$

Equation 2.11 shows that the efficiency for the recuperative CLC system is positively correlated to the reduction/oxidation reactor temperature ratio and maximizing efficiency corresponds to

increasing the reduction reactor temperature relative to the oxidation reactor temperature. The derivative of the efficiency with respect to the reduction/oxidation reactor temperature ratio shows that the slope of a graph of efficiency with respect to this ratio is a positive constant (equation 2.12).

For an endothermic reduction reaction, in line with the discussion from Section 2.2, the oxidation reactor temperature constrains the maximum system temperature since heat needs to be transferred from the oxidation to the reduction reaction. Equation 2.11 shows that increasing the reduction reactor temperature translates to an increase in efficiency. Therefore the maximum efficiency corresponds to the thermally balanced case where $T_{red} = T_{ox}$ and the resulting expression for efficiency is given in equation 2.10. For an exothermic reduction reaction, equation 2.11 shows that maximum efficiency also corresponds to the thermally balanced case for all values of T_{red} less than or equal to the equilibrium temperature of the oxidation reaction. If $T_{red} > T_{ox}$ and T_{ox} is fixed at its equilibrium temperature, then from equation 2.11, a thermally imbalanced reactor configuration would result in higher efficiency. However, temperature limitations imposed by thermal properties of the oxygen carriers or turbine material typically define a stricter upper bound for the feasible operating temperature than the oxidation equilibrium temperature. Therefore, T_{red} can only be as high as the feasible T_{ox}, and the operating efficiency limit for this case in practical systems will also correspond to the efficiency defined in equation 2.10.

Table 2.3: Summary table for idealized (recuperative CLC) cycle analysis

Reduction Reaction	**Condition for Maximum Efficiency**	
	Thermodynamic Constraints only	Thermodynamic and material constraints
Endothermic	$\boldsymbol{T_{red} = T_{ox}}$ $T_{ox} = T_{equilibrium}\ (oxidation)$ $T_{red} > T_{equilibrium}(reduction)$	$\boldsymbol{T_{red} = T_{ox}}$ $T_{ox} = T_{max}$
Exothermic	$\boldsymbol{T_{red} > T_{ox}}$ $T_{ox} = T_{equilibrium}\ (oxidation)$ $T_{red} \gg T_{equilibrium}(reduction)$	$\boldsymbol{T_{red} = T_{ox}}$ $T_{ox} = T_{max}$

T_{max} is the maximum temperature imposed by either oxygen carrier melting point or turbine inlet temperature.

In summary, the foregoing analysis has made use of an ideal configuration-specific model to develop an expression for efficiency defined in terms of the reduction/oxidation reactor temperature ratio. Using this expression, and incorporating some knowledge of oxygen carrier properties, as well as process and material constraints, it was shown that the highest efficiency is obtained when both reactors are in thermal equilibrium. Table 2.3 summarizes the key conclusions from this section.

2.4. Detailed thermodynamic analysis

In sections 2.2 and 2.3, , it was shown that when CLC material and power cycle practical limitations are taken into account, thermally balanced CLC reactor designs have a greater efficiency potential when integrated with idealized power cycles. In this section, a higher fidelity model of the recuperative CLC cycle is developed in Aspen Plus®. This model is used to assess the conclusions about the effect of reactor thermal coupling from the previous sections.

2.4.1. Model development and methodology

2.4.1.1. Cycle description

Figure 2-4 presents a schematic of the Aspen Plus® flow sheet for the rotary CLC recuperative cycle. On the air side, the inlet air is first compressed, then preheated in the recuperator before proceeding to the rotary reactor, where it reacts exothermically with the oxygen carrier. Compression with intercooling is utilized. The reactor exit is divided into two zones; the air zone and the fuel zone. The air zone exhaust is a mixture of oxygen-depleted air and steam from the air and air purge sectors respectively. The fuel zone exhaust contains the combustion products from the fuel sector (CO_2 and H_2O) and steam from the fuel purge sector. The air zone exhaust is expanded for power in the air-side turbine. The turbine exhaust is subsequently used for heat recovery in the air-side recuperator before being discharged to the atmosphere. The fuel side follows an identical process up till the recuperator. Some of the CO_2 from the cool recuperator exhaust stream is recycled to the fuel inlet where it serves as carrier gas/diluent for the fuel. The

remaining CO_2 stream is prepared for sequestration by compressing it up to 110 bars in the CO_2 compression unit. This unit delivers staged compression with intercooling, which also enables the condensation and removal of water vapor from the CO_2 stream. The recuperators are also used to generate purge steam for the air and fuel sectors.

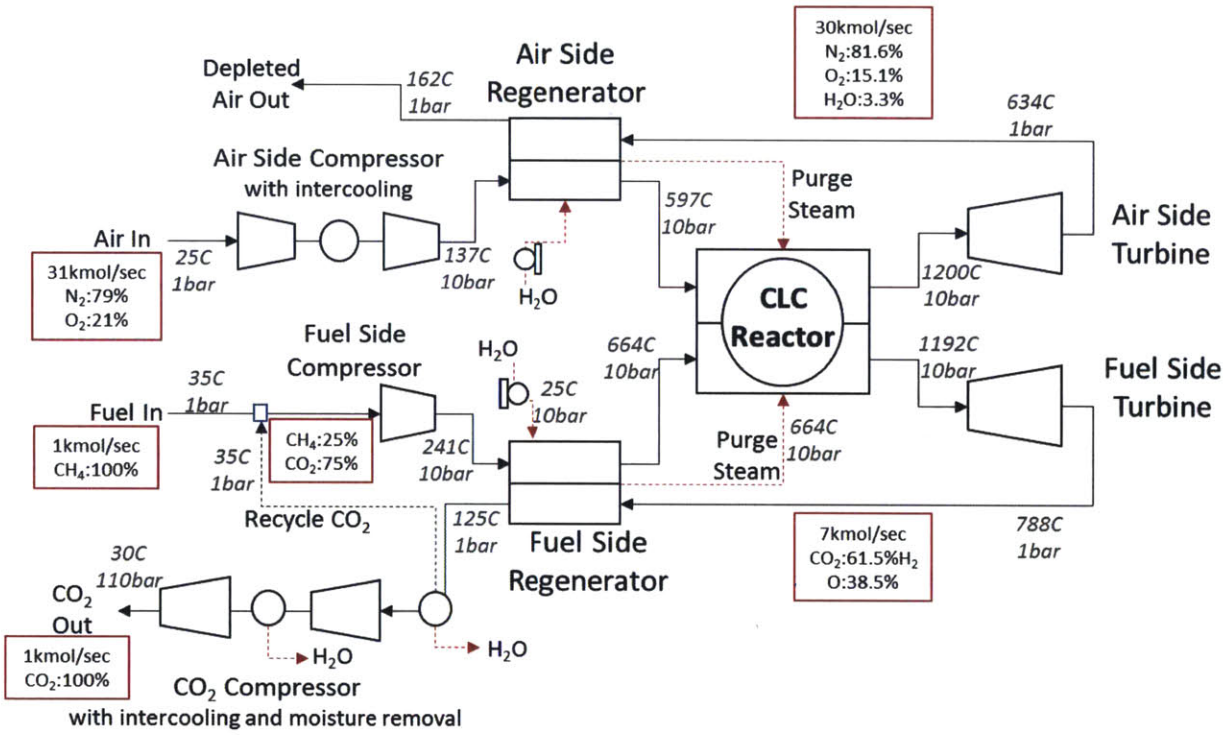

Figure 2-4: Schematic of the flow sheet layout for the recuperative CLC cycle. (With base case temperature/pressure/flow/composition data).

2.4.1.2. Rotary reactor model

The rotary reactor design and operation is described in detail in [4], [27]–[29]. It is essentially a solid wheel with a matrix of micro channels. The solid wheel enables internal thermal coupling, absorbing, transferring and releasing heat as required to ensure that at each point along the reactor axial direction, the different reactor sectors are thermally equilibrated. At the reactor exit, the air and fuel streams are mixed with the corresponding purge steam streams, creating just two separate exhaust streams. Therefore, based on thermodynamic considerations, the key feature of the rotary

reactor design is the internal heat transfer/thermal coupling that maintains the oxidation and reduction reactors in thermal equilibrium [28], [29]. Therefore, to develop a steady state model of this reactor in Aspen Plus®, two operating requirements need to be satisfied. First is that the reactors be at the same temperature or nearly so. The second is that the oxidation reactor exhaust comprise of depleted air and air purge steam while the reduction reactor exhaust contain the combustion products and the fuel purge steam. To simulate this reactor in Aspen Plus®, the setup in Figure 2-5 is used. Two interconnected reactor blocks represent the oxidation and reduction reactors. The oxygen carrier and support material circulate between the reactors, and split blocks are used to model gas-solid separation. For this model, nickel is used as the oxygen carrier, boron nitride as the support material and CH_4 as fuel. Since the fuel flow rate is fixed, Ni/CH_4 ratio is set at a fixed value above the stoichiometric amount required for complete conversion of the fuel. The reactors are simulated using the RGibbs model, which determines product phase and composition by minimizing Gibbs free energy. For the sensitivity studies, the oxidation reactor temperature is varied by varying the inlet air flow rate while the reduction reactor temperature is controlled by varying the solid support material circulation rate. To satisfy the second rotary reactor operating requirement, each purge steam is fed directly into the corresponding reactor. This modeling strategy does not reflect the physical design of the rotary reactor since the rotary reactor has no circulating particles. Nevertheless, it captures the objective of representing the thermal coupling in the rotary reactor.

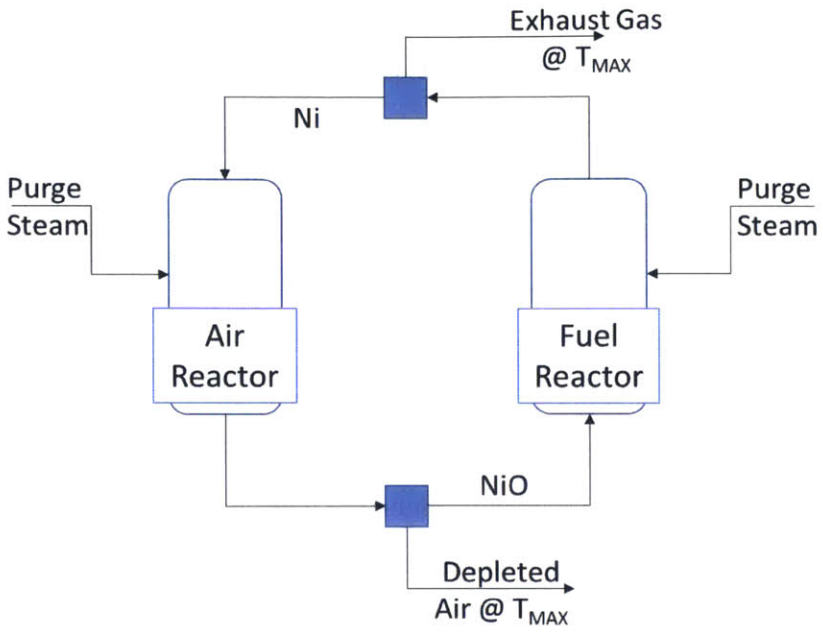

Figure 2-5: CLC reactor setup in Aspen®.

2.4.1.3. Model specifications

The modeling assumptions and specifications used in developing the base case rotary reactor Aspen Plus® system models are summarized in Table 2.4 and Table 2.5. For the reactor model, nickel is chosen as the oxygen carrier with boron nitride as the support material. The base case reactor temperature was set at 1200C because it is in the same temperature range as used in a number of earlier studies [12]–[15], [31]. The oxidation reactor temperature is defined as a design specification target and is controlled by varying the inlet air flow rate. The reduction reactor temperature is controlled by varying the boron nitride circulation rate. A base case compressor ratio of 10 is used but is varied between 2 and 20 for the parametric studies. Pressure drop in the reactor is neglected since the value is very small for the rotary reactor [27]. The CO_2 compression unit uses staged compression with intercooling to deliver supercritical CO_2 at 110 bars and 30C to an external CO_2 pipeline. Moisture is removed in the intercoolers during the compression process.

Table 2.4: General specifications for base case model

Item	Units	Value
General		
Oxidation reactor temperature	C	1200
Ambient temperature	C	25
Reactor/operating pressure	bar	10
Ambient pressure	bar	1
Gas compressor isentropic efficiency	%	90
Gas turbine isentropic efficiency	%	90
Sequestration co_2 compression pressure	bar	110
Recuperative heat exchanger minimum pinch	C	25
Oxygen Carrier (MeO / Me)	Nickel oxide/nickel (NiO / Ni)	
Bulk layer (inert solid) material	Boron nitride (BN)	
Inlet streams		
Fuel type		Methane
Inlet fuel flow rate	kmol/sec (kg/sec)	1 (16.04)
Lower heating value (LHV) fuel	MJ/kg	50
Inlet air N_2 composition	fraction	0.79
Inlet air O_2 composition	fraction	0.21
Recycled CO_2 / CH_4 composition in inlet stream	ratio	3 : 1
Oxygen carrier (Ni+NiO) / fuel (CH_4) mole ratio	ratio	6 : 1
Fuel side purge steam	kmol/sec	0.5
Air side purge steam	kmol/sec	1
Variable design/operating parameters		
Inlet air flow rate	Varied to control the oxidation reactor temperature	
Boron nitride (bulk support material) circulation rate	Varied to control reduction reactor temperature	

Table 2.5: Design strategy

Specification	Strategy
Air side compressor intercooling	Yes
Fuel side compressor intercooling	No
Exhaust heat recovery	After air/fuel-side compressors
Oxidation reactor purge steam source	Fuel side recuperator
Reduction reactor purge steam source	Fuel side recuperator

2.4.1.4. Temperature ratio study

In sections 2.2 and 2.3, simple thermodynamic models of specific cycles were used to show that the efficiency of most CLC configurations is a function of the reactor temperature ratio, $\frac{T_{red}}{T_{ox}}$, and that under the typical conditions that apply to realistic systems, the highest efficiency was obtained in reactors when $\frac{T_{red}}{T_{ox}} = 1$. This study examines the sensitivity of cycle efficiency to this ratio by varying the reduction reactor temperature from around 800C to the fixed oxidation reactor temperature of 1200C. All other design and operating specifications are as indicated in Table 2.4 and Table 2.5.

2.4.2. Results

2.4.2.1. Reactor temperature ratio study

Figure 2-6 compares the efficiency of a thermally balanced and a thermally imbalanced recuperative CLC cycles at base case conditions. The results show about 54% efficiency for the thermally balanced reactor compared to 52% for the imbalanced design. A work breakdown plot is shown in Figure 2-7 to provide some insight into why this is the case. Compared to the thermally imbalanced case, thermally balanced reactor operation is characterized by a higher reduction reactor temperature, which reduces the airflow required for temperature regulation. The higher reduction reactor temperature leads to increased fuel-side turbine output, while the lower air flow rate reduces both the turbine output and the compressor power requirement on the air side, such

that the overall effect is a smaller net reduction in air-side work output. A close examination of the component contributions to the net system work output shows that the increase in fuel-side turbine output is larger than the corresponding decrease on the air side. Consequently, the net effect of thermally balanced reactor operation is an increase in system efficiency. Therefore, maintaining the reactors in thermal equilibrium increases the availability of the fuel-side reactor exhaust stream, leading to higher turbine output and a net increase in system efficiency. Figure 2-8 relates the ratio of reduction-to-oxidation reactor temperatures, $\frac{T_{red}}{T_{ox}}$, to the cycle efficiency for the recuperative cycle at different compressor pressure ratios. For each case, efficiency is shown to be a linear function of this ratio, and the slope of the graph is constant as shown in equation 2.13.

$$\frac{\Delta\eta}{\Delta\left(\frac{T_{red}}{T_{ox}}\right)} = \text{Constant}, \left(\frac{T_{red-equilibrium}}{T_{ox}} \leq \frac{T_{red}}{T_{ox}} \leq 1\right) \tag{2.13}$$

Equation 2.13, arrived at from the Aspen Plus® model results, is equivalent to equation 2.12 obtained using the ideal recuperative CLC cycle model. Consequently, these results corroborate the conclusion from sections 2.2 and 2.3 that thermally balanced reactors are ideal for maximizing system efficiency. Cycle efficiencies reported in literature for reactor configurations with different degrees of thermal imbalance (T_{red} ranging from 800C to 1100C), methane fuel and complete CO_2 separation range from 47 – 53.5 % [11], [14], [15], [31] for combined cycle CLC systems. Ishida et al. [12] and Brandvoll et al. [30] reported efficiencies of 53% and 54% respectively for nickel-based humid air CLC cycles (accounting for CO_2 compression). The configuration presented by Brandvoll et al. includes a solid-to-gas heat exchanger between the oxidation and reduction reactors to increase the temperature of the fuel reactor exhaust stream and consequently minimize reactor exergy loss. In the absence of internal thermal coupling, installing a heat exchanger between the two reactors is a good option for improving system availability, though implementing it currently remains technically challenging.

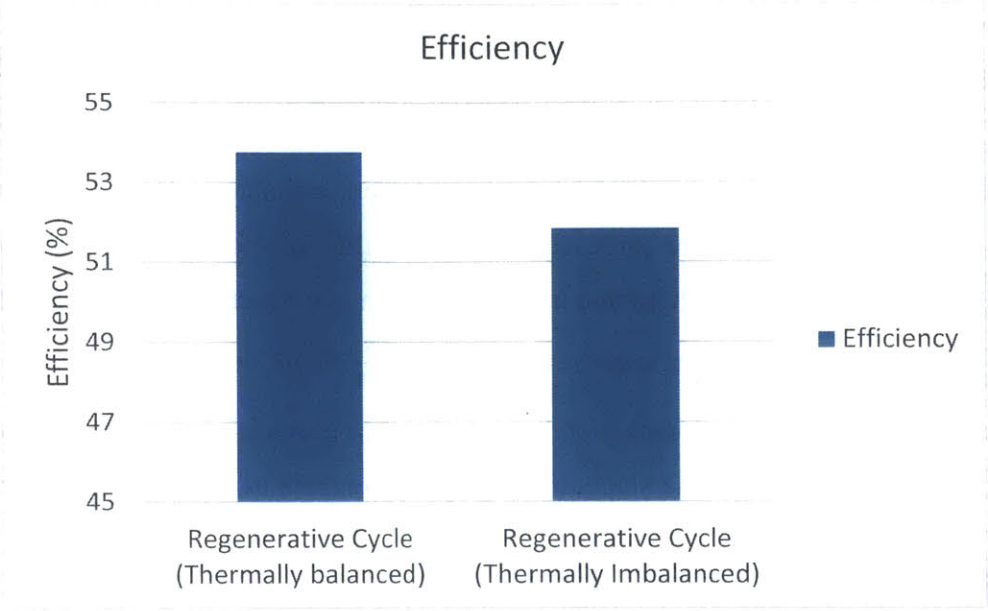

Figure 2-6: Base case efficiency plots illustrating impact of thermal balance. Thermally balanced reactor operation increases efficiency.
$pressure\ ratio = 10$ | $Thermal\ balance: T_{ox} = T_{red} = 1200C$ | $Thermal\ imbalance: T_{ox} = 1200C, T_{red} = 800C$

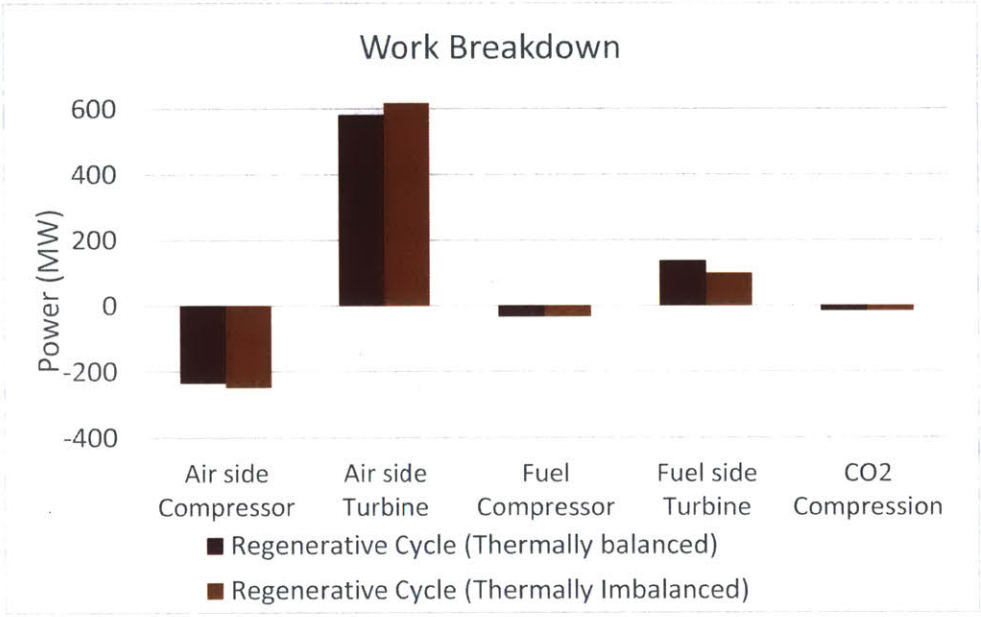

Figure 2-7: Breakdown of contributions to net power output. Reactor thermal coupling leads to increased availability of the hotter fuel exhaust stream, as seen by comparing the fuel-side turbine work.
$pressure\ ratio = 10$ | $Thermal\ balance: T_{ox} = T_{red} = 1200C$ | $Thermal\ imbalance: T_{ox} = 1200C, T_{red} = 800C$

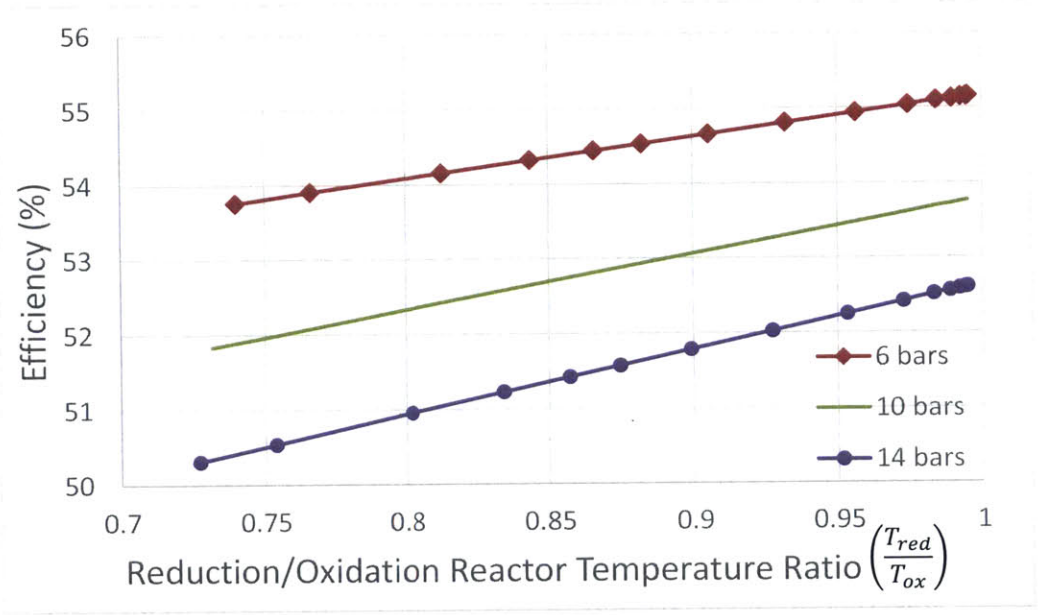

Figure 2-8: Efficiency vs reactor temperature ratio.
Cycle thermal efficiency is a linear function of the reduction/oxidation reactor temperature ratio for the recuperative CLC cycle and maximum efficiency corresponds to thermally balanced reactor operation$\left(\frac{T_{red}}{T_{ox}} = 1\right)$.

2.4.2.2. Pressure sensitivity

The operating pressure has a significant impact on the efficiency of rotary CLC reactor systems. Figure 2-9 shows the variation of efficiency with pressure for the recuperative cycle configuration. The plot shows a negative proportionality between efficiency and the cycle pressure ratio, (π), consistent with the expression in equation 2.10. The efficiency peaks at $\pi = 3$, with a value of about 56%. Compressor intercooling is partly responsible for this high efficiency value. It reduces the compression power requirement, and the lower temperature stream leaving the compressor can then recover more heat from the exhaust gas in the recuperator. This maximum efficiency value is clearly higher than efficiencies reported for different CH_4-fueled CLC cycle configurations (admitting differences in modeling assumptions), favoring its selection for CLC power generation. Nevertheless, lower pressures imply higher volumetric gas flow rates, which in turn require larger recuperators and reactors, and may lead to higher costs. A detailed economic evaluation will need to be carried out to more appropriately determine the optimal efficiency/cost trade-off for this configuration.

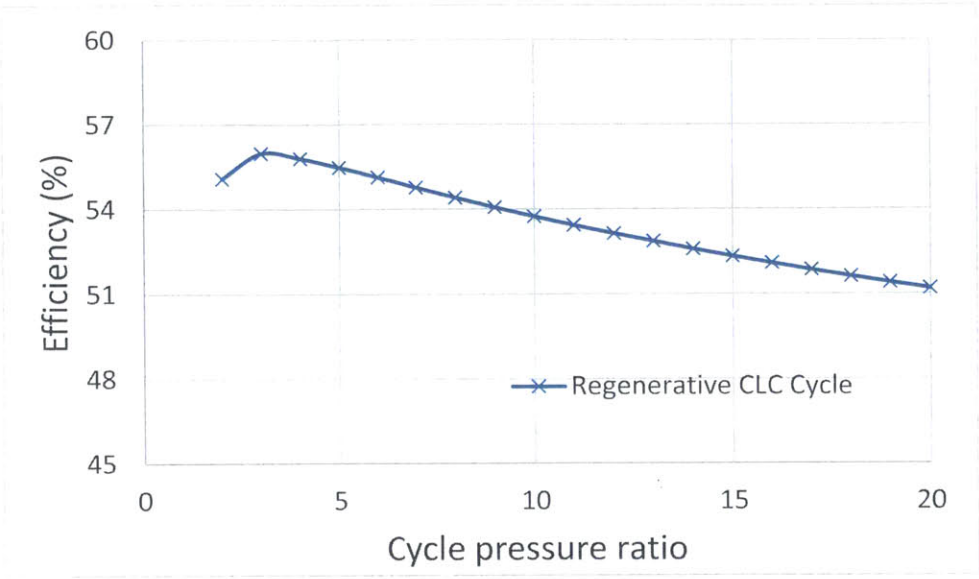

Figure 2-9: Impact of pressure ratio on efficiency for recuperative CLC cycle.

2.4.2.3. CO_2 fraction sensitivity

Recycled CO_2 is normally used as the carrier gas for the fuel which is supplied to the reactor. This sensitivity study examines the impact of feed stream CO_2 fraction on system efficiency by varying CO_2 recycle ratio. In fluid bed CLC designs, feed stream CO_2 fraction is determined mainly by fluidization requirements in the fuel reactor. Since fluidization is not relevant for the rotary reactor, the results from this study could provide an alternative criteria for determining an optimal diluent fraction. The effect of varying the CO_2 fraction in the fuel supply stream on efficiency is shown in Figure 2-10.

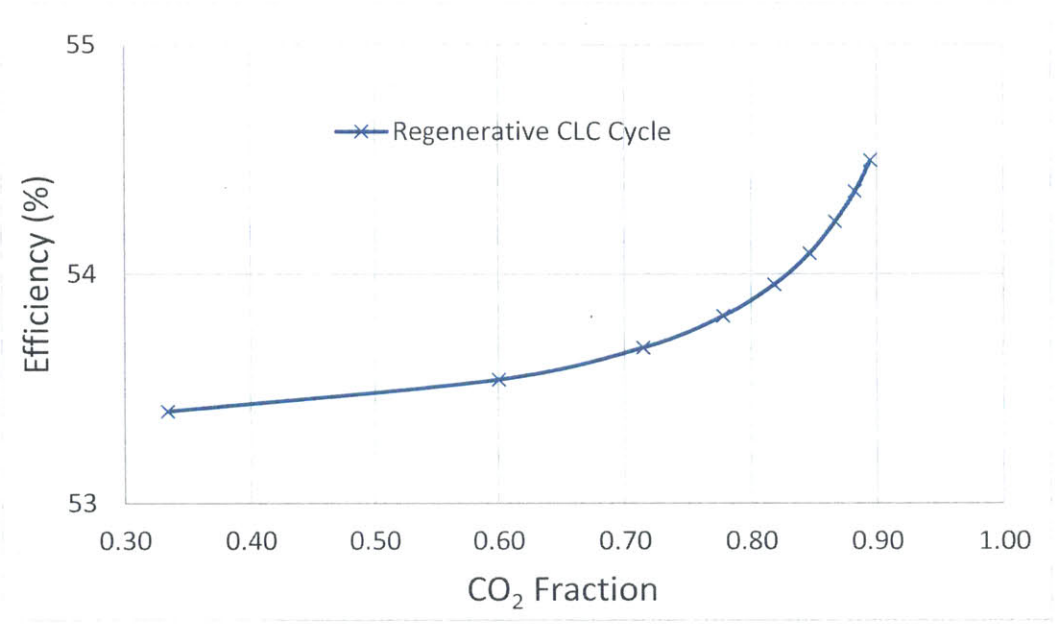

Figure 2-10: Impact of feed stream CO_2 fraction on efficiency.
Results obtained at compressor ratio of 10.

For the recuperative CLC cycle, higher CO_2 fraction increases cycle efficiency at the selected base case pressure ratio. Since the fuel-side stream leaves the recuperator at a higher temperature than the air side, a mole increase in CO_2 results in approximately a mole drop in Air flow requirement for reactor temperature regulation. The resulting net compressor/turbine work for one mole of the CO_2 is larger than the net for an equivalent mole of air for the current operating condition, which is why there is a resulting positive contribution to net power output as CO_2 fraction increases. The optimal fraction will have to be determined from a tradeoff between efficiency and reactor cost.

2.4.2.4. Multivariable parametric study

This study identifies the optimal efficiency region in the space defined by varied design/operating parameter pairs and visualizes the results on surface plots. The parameters considered are operating pressure, CO_2 fraction and turbine inlet temperature (TIT). Figure 2-11 presents the relationship between efficiency, pressure ratio (π) and TIT. For the recuperative CLC cycle, efficiency has an inverse relationship with pressure, independent of TIT. The peak value for TIT of 1000C is 51% at $\pi = 3$. This peak pressure ratio does not change much, moving only to 4 at 1400C; the efficiency

at this point is 60%. In Figure 2-12, efficiency is seen to increase monotonically with CO_2 fraction for the entire TIT range at pressure ratio of 10. However, efficiency is shown to be a much stronger function of TIT than CO_2 fraction. Figure 2-13 presents an interesting result. At higher pressure ratios, efficiency increases with CO_2 fraction, with up to 1.5% increase at $\pi = 15$ when CO_2 fraction is varied from 0.33 to 0.92. The slope of the efficiency/CO_2 fraction curve however decreases continuously till around $\pi = 4$, where it flips and becomes negative. Thus, in the 2-4 pressure ratio range, lower fractions give higher efficiency. In summary, for the recuperative CLC cycle, the optimal operating region is in the low pressure, low CO_2 fraction and high TIT region. Table 2.6 summarizes the key results from the preceding parametric analysis. The directions of the arrows represent the slopes of the efficiency/parameter curve; upward arrows indicate a positive correlation while downward pointing arrows represent a negative correlation. The results of this study could provide useful input into subsequent optimization studies.

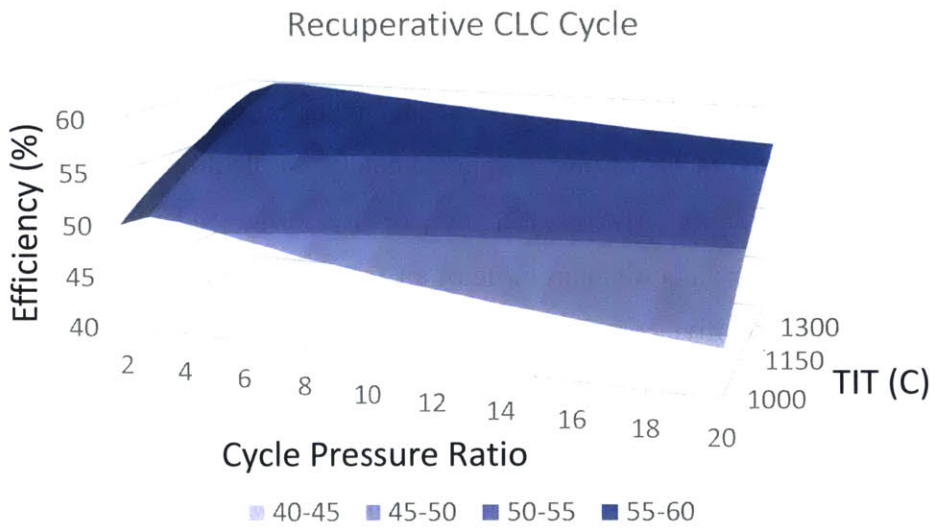

Figure 2-11: Pressure/TIT multivariable analysis result.
Optimal conditions in the low pressure and high TIT region for the recuperative CLC cycle.

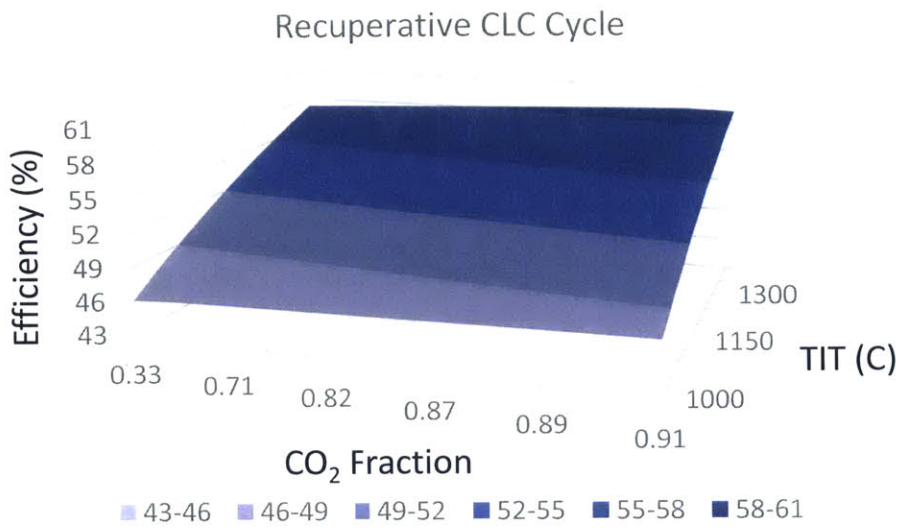

Figure 2-12: CO_2 fraction/TIT multivariable analysis result.
Optimal conditions in the high CO_2 fraction and high TIT region for the recuperative CLC cycle. Results were obtained at pressure ratio of 10.

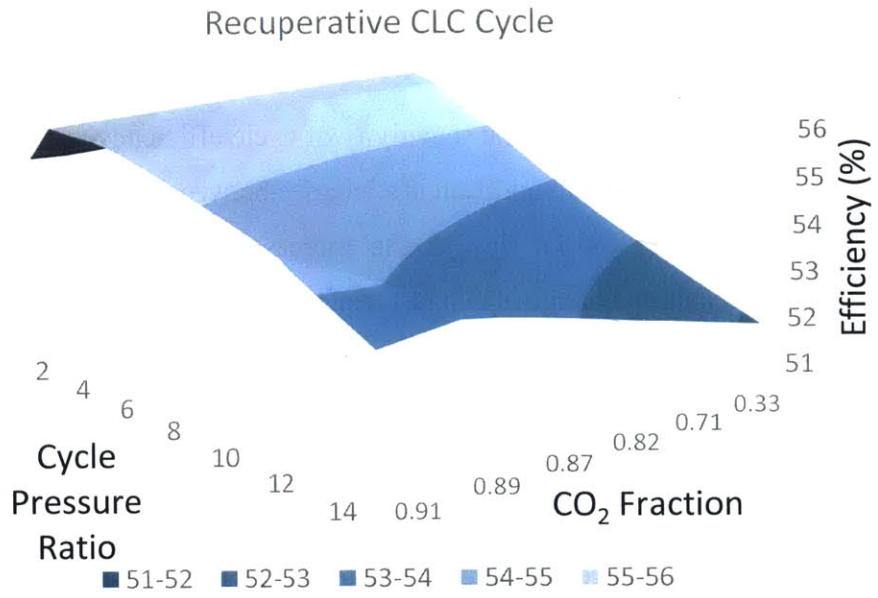

Figure 2-13: CO_2 fraction/Pressure multivariable analysis result.
Efficiency is positively correlated with CO_2 fraction at very low pressures but the trend reverses at higher operating pressures. Optimal operating condition in the low pressure and low CO_2 fraction region.

Table 2.6: Summary of parametric analysis results

Relation	**Low TIT**	**High TIT**
Efficiency/Pressure*	↓	↓
Efficiency/CO_2 Fraction	↑	↑
Relation	**Low Pressure**	**High Pressure**
Efficiency/TIT	↑	↑
Efficiency/CO_2 Fraction	↓	↑
Relation	**Low CO_2 Fraction**	**High CO_2 Fraction**
Efficiency/Pressure	↓	↓
Efficiency/TIT	↑	↑

*efficiency increases with decreasing pressure up to a maximum value, beyond which it decreases

2.4.2.5. Steam generation sensitivity

Figure 2-14 and Figure 2-15 illustrate the sensitivity of cycle efficiency to the required amount of purge steam. The net effect of steam addition is a balance between the energetic cost of producing steam, the additional power output due to the increased reactor exhaust flow and the net contribution from the resulting change in exhaust heat recovery. Figure 2-14 and Figure 2-15 show that the impact on efficiency depends on the amount of steam required, the cycle pressure ratio and the turbine inlet temperature. In general, steam generation constitutes a net positive benefit for the recuperative cycle for low steam requirement. In this range, in addition to increasing the gross exhaust enthalpy, steam generation improves exhaust heat recovery and minimizes losses to the environment. In the higher range (between 2-3 times fuel flow), the cost of steam generation becomes the dominant contribution and negatively impacts efficiency. For the rotary reactor, purge steam requirement depends on a number of factors, including reactor temperature, oxygen carrier material and operating pressure. Therefore, optimizing purge steam requirement is an important consideration in designing reactors for integration with energy conversion systems.

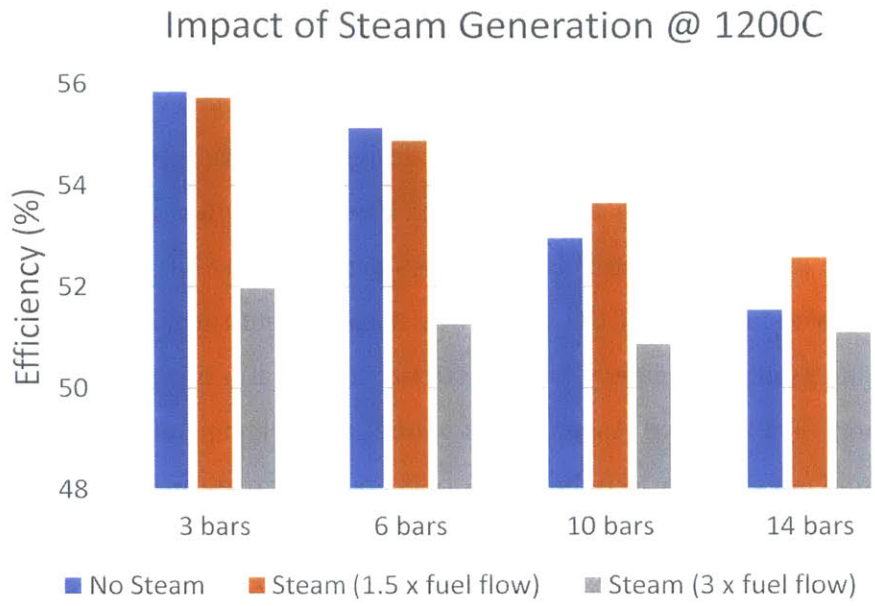

Figure 2-14: Impact of purge steam demand on efficiency.
The effect of purge steam generation on efficiency is mostly a balance between steam generation energy penalty and additional work output from larger exhaust flow.

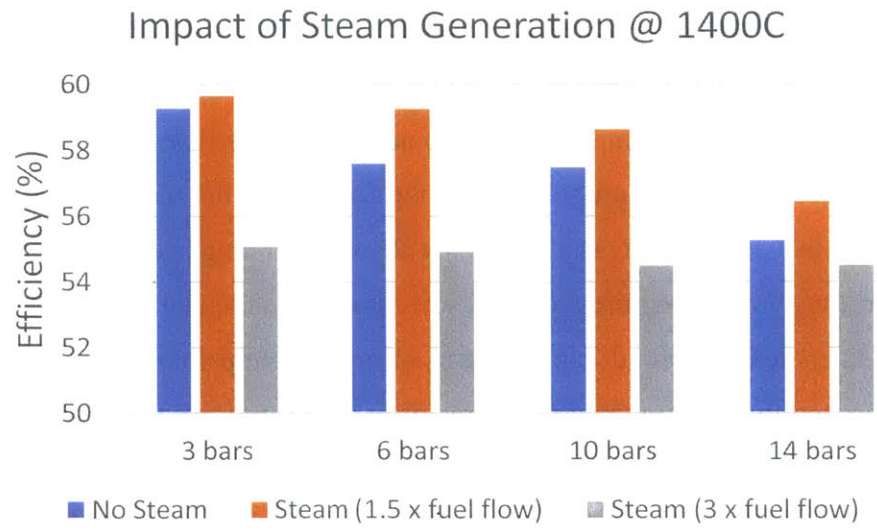

Figure 2-15: Impact of purge steam demand on efficiency.
The effect of purge steam generation on efficiency is mostly a balance between steam generation energy penalty and additional work output from larger exhaust flow. This balance is also a function of TIT and required steam flow rate.

2.5. Summary

Starting with a generic availability model, then moving on to a specific ideal thermodynamic model and subsequently, a more rigorous Aspen flow sheet model, this chapter has made the case for the advantage of thermally coupled CLC reactor designs for power generation. The availability model was used to show that given typical oxygen carrier properties and material constraints, optimal performance can be obtained if both reactors are maintained in thermal equilibrium. An idealized model of a recuperative CLC cycle was used to confirm this conclusion as well as demonstrate that the system efficiency is proportional to the ratio of the reduction-to-oxidation reactor temperatures. The detailed Aspen Plus® model of the recuperative CLC cycle confirms this relationship, and goes further to indicate up to 2% point increase in efficiency resulting from thermally balanced reactor operation in a recuperative CLC cycle. The results from the Aspen Model also indicate that this efficiency advantage derives mainly from the increased availability in the reduction reactor exhaust stream. These results suggest that recuperative power cycles integrated with thermally coupled reactor designs have a distinct performance advantage, making the rotary CLC reactor design ideal for integration with thermal power plants.

Thermally balanced operation can be approached in traditional fluid bed reactors for oxygen carriers with endothermic reduction reaction, but will require extremely high particle flow rates. Larger oxygen carrier flow rates proportionally increase the size of the reactor, the parasitic power demand and other operational complexities associated with particle circulation. Alternative designs like the packed bed reactor proposed by Noorman [22] or the thermally balanced version of the SCOT process by Chakravarthy et al. [24] as well as the moving bed reactor [25] are possible options. However, these would require a careful selection of the oxygen carriers, a high inert bed material loading to increase thermal capacity and minimize temperature swings, and fast feed cycling. Increasing bed material loading might result in a non-uniform temperature profile along the reactor due to solid-solid and solid-gas-solid interfacial heat transfer resistances; rapid cycling could inhibit CO_2 separation. The rotary reactor design is well suited for thermally balanced operation. The high thermal capacity and conductivity of the bulk support layer provides the thermal equilibration between the fuel and air sectors along the reactor axial direction. This makes the rotary reactor design ideal for maximizing system efficiency.

2.6. Appendices

2.6.1. Appendix 2A

Applying the first and second laws of thermodynamics to the Carnot engine for the ideal CLC setup in Figure 2-1, the maximum work that can be extracted from the system is obtained as follows:

1st Law

$$Q_{ox} + Q_{red} + Q_0 + W_{MAX} = 0 \tag{2-A1}$$

2nd Law

$$\frac{Q_{ox}}{T_{ox}} + \frac{Q_{red}}{T_{red}} + \frac{Q_0}{T_0} = 0 \tag{2-A2}$$

Solving equations 2-A1 and 2-A2, the maximum work output from the system is given by

$$-W_{MAX} = Q_{ox}\left(1 - \left(\frac{T_0}{T_{ox}}\right)\right) + Q_{red}\left(1 - \left(\frac{T_0}{T_{red}}\right)\right) \tag{2-A3}$$

But

$$Q_{ox} = Q - Q_{red} \tag{2-A4}$$

Substituting into equation 2-A3 and rearranging, gives:

$$-W_{MAX} = (Q - Q_{red})\left(1 - \left(\frac{T_0}{T_{ox}}\right)\right) + Q_{red}\left(1 - \left(\frac{T_0}{T_{red}}\right)\right) \tag{2-A5}$$

$$-W_{MAX} = Q\left(1 - \left(\frac{T_0}{T_{ox}}\right)\right) - Q_{red}\left(\frac{T_0}{T_{ox}}\left(\frac{T_{ox} - T_{red}}{T_{red}}\right)\right) \tag{2-A6}$$

Case 1: Exothermic Reduction Reaction, Exothermic Oxidation Reaction

$$Q_{red} = |\Delta H_{red}| \tag{2-A7}$$

$$-W_{MAX} = |\Delta H|\left(1 - \left(\frac{T_0}{T_{ox}}\right)\right) - |\Delta H_{red}|\left(\frac{T_0}{T_{ox}}\left(\frac{T_{ox} - T_{red}}{T_{red}}\right)\right) \tag{2-A8}$$

Case 2: Endothermic Reduction Reaction, Exothermic Oxidation Reaction

$$Q_{red} = -|\Delta H_{red}| \quad \text{(2-A9)}$$

$$-W_{MAX} = |\Delta H|\left(1 - \left(\frac{T_0}{T_{ox}}\right)\right) + |\Delta H_{red}|\left(\frac{T_0}{T_{ox}}\left(\frac{T_{ox} - T_{red}}{T_{red}}\right)\right) \quad \text{(2-A10)}$$

2.6.2. Appendix 2B

This simplified analysis will consider an ideal recuperative cycle configuration for a CLC system.

Symbol Definitions

$$T_0 = T_{1f} = T_{1a} \quad \text{(i)}$$

$$T_{ox} = T_{4a} \quad \text{(ii)}$$

$$T_{red} = T_{4f} \quad \text{(iii)}$$

$$\pi = \frac{P_2}{P_1} \quad \text{(iv)}$$

$$\alpha = \frac{\left(\frac{c_p}{c_v}\right) - 1}{\left(\frac{c_p}{c_v}\right)} \quad \text{(v)}$$

$$m_i c_{pi} = constant, i = 1, \ldots n \quad \text{(vi)}$$

Applying the laws of thermodynamics on each of the components (compressors, turbines, heat exchangers and reactor) and taking into account the preceding assumptions leads to the following formulation:

Air side Compressor:

$$T_{2a} = T_0(\pi^{\alpha}) \quad \text{(2-B1)}$$

$$W_{ca} = m_a c_{pa} T_0(\pi^{\alpha} - 1) \quad \text{(2-B2)}$$

Air side Turbine:

$$T_{5a} = T_{4a}(\pi^{-\alpha}) = T_{ox}(\pi^{-\alpha}) \quad \text{(2-B3)}$$

$$W_{Ta} = m_a c_{pa} T_{ox}(\pi^{-\alpha} - 1) \quad \text{(2-B4)}$$

Air side Heat Exchanger

$$T_{3a} = T_{5a} = T_{ox}(\pi^{-\alpha}) \quad \text{(2-B5)}$$

Fuel side Compressor:

$$T_{2f} = T_0(\pi^{\alpha}) \quad \text{(2-B6)}$$

$$W_{cf} = m_f c_{pf} T_0(\pi^{\alpha} - 1) \quad \text{(2-B7)}$$

Fuel side Turbine:

$$T_{5f} = T_{4f}(\pi^{-\alpha}) = T_{red}(\pi^{-\alpha}) \quad \text{(2-B8)}$$

$$W_{Tf} = m_f c_{pf} T_{red}(\pi^{-\alpha} - 1) \quad \text{(2-B9)}$$

Fuel side Heat Exchanger

$$T_{3f} = T_{5f} = T_{red}(\pi^{-\alpha}) \quad \text{(2-B10)}$$

CLC Reactor

$$Q = -\Delta H = (m_f c_{pf} T_{red} + m_a c_{pa} T_{ox})(1 - \pi^{-\alpha}) \quad \text{(2-B11)}$$

Since air mass flow rate is used to control reduction reactor side exit temperature, the expression for mass flow rate is derived and expressed as:

$$m_a = \left(\frac{Q}{(1-\pi^{-\alpha}) c_{pa} T_{ox}} - \left(\frac{m_f c_{pf}}{c_{pa}} \right) \left(\frac{T_{red}}{T_{ox}} \right) \right) \quad \text{(2-B12)}$$

$$W_{Net_a} = W_{Ta} + W_{ca} = m_a c_{pa} T_0 \left(\pi^{\alpha} - \frac{T_{ox}}{T_0} \right)(1 - \pi^{-\alpha}) \quad \text{(2-B13)}$$

$$W_{Net_f} = W_{Tf} + W_{cf} = m_f c_{pf} T_0 \left(\pi^{\alpha} - \frac{T_{red}}{T_0} \right)(1 - \pi^{-\alpha}) \quad \text{(2-B14)}$$

The efficiency for the system is given by

$$\eta = -\frac{W_{Net_a} + W_{Net_f}}{Q} \quad \text{(2-B15)}$$

$$\eta = 1 - \frac{(m_f c_{pf} + m_a c_{pa})(\pi^{\alpha})}{\left(m_f c_{pf} \left(\frac{T_{red}}{T_0} \right) + m_a c_{pa} \left(\frac{T_{ox}}{T_0} \right) \right)} \quad \text{(2-B16)}$$

Case 1: Oxidation and reduction reactor in thermal equilibrium $\left(\left(\frac{T_{red}}{T_{ox}} \right) = 1 \right)$

Therefore, equation 2-B16 reduces to

$$\eta = 1 - \frac{(\pi^{\alpha})}{\left(\frac{T_{ox}}{T_0}\right)} \tag{2-B17}$$

Case 2: oxidation and reduction reactor not in thermal equilibrium $\left(\left(\frac{T_{red}}{T_{ox}}\right) \neq 1\right)$

From equation 2-B12, the mass flow rate is a linear function of $\left(\frac{T_{red}}{T_{ox}}\right)$ and can be written as

$$m_a = \left(\Psi_1 - \Psi_2 \left(\frac{T_{red}}{T_{ox}}\right)\right) \tag{2-B18}$$

Where

$$\Psi_1 = \left(\frac{Q}{(1-\pi^{-\alpha})c_{pa}T_{ox}}\right) = constant \tag{2-B19}$$

$$\Psi_2 = \left(\left(\frac{m_f c_{pf}}{c_{pa}}\right)\right) = constant \tag{2-B20}$$

Substituting (2-B18) into (2-B16) and rearranging:

$$\eta = 1 - \frac{\left(\left(\frac{Q}{(1-\pi^{-\alpha})c_{pa}T_{ox}}\right)c_{pa}\pi^{\alpha}\right)+(m_f c_{pf}\pi^{\alpha})}{\left(\left(\frac{Q}{(1-\pi^{-\alpha})c_{pa}T_{ox}}\right)c_{pa}\frac{T_{ox}}{T_0}\right)} + \frac{\left(\left(\frac{m_f c_{pf}}{c_{pa}}\right)\pi^{\alpha}\right)}{\left(\left(\frac{Q}{(1-\pi^{-\alpha})c_{pa}T_{ox}}\right)\frac{T_{ox}}{T_0}\right)}\left(\frac{T_{red}}{T_{ox}}\right)$$

$$\eta = 1 - \Psi_1 + \Psi_2 \left(\frac{T_{red}}{T_{ox}}\right) \tag{2-B21}$$

Where

$$\Psi_1 = \frac{\left(\left(\frac{Q}{(1-\pi^{-\alpha})c_{pa}T_{ox}}\right)c_{pa}\pi^{\alpha}\right)+(m_f c_{pf}\pi^{\alpha})}{\left(\left(\frac{Q}{(1-\pi^{-\alpha})c_{pa}T_{ox}}\right)c_{pa}\frac{T_{ox}}{T_0}\right)} = constant \tag{2-B22}$$

$$\Psi_2 = \frac{\left(\left(\frac{m_f c_{pf}}{c_{pa}}\right)\pi^{\alpha}\right)}{\left(\left(\frac{Q}{(1-\pi^{-\alpha})c_{pa}T_{ox}}\right)\frac{T_{ox}}{T_0}\right)} = constant \tag{2-B23}$$

3. Efficient cycles for thermally coupled CLC reactor-based power plants

3.1. Introduction

In chapter 2, theoretical availability concepts, together with ideal and detailed recuperative CLC cycle models, were used to demonstrate that under practical operating conditions, the internal thermal coupling in the rotary reactor increases cycle thermal efficiency. The analysis showed an increase of up to 2% points for the recuperative CLC cycle. This chapter extends this analysis to alternative configurations with the two-pronged objective of validating the thermal coupling effect for alternative cycle configurations and identifying suitable cycles for thermally coupled reactors. Section 3.2 makes use of analytical thermodynamic models of the simple Brayton, Steam and Combined CLC cycles to study the impact of reactor thermal coupling on thermal efficiency. In section 3.3, the same analysis is carried out using higher fidelity Aspen Plus® models of the same cycles. Hybrid combined, steam and recuperative cycles are also included in the analysis and the results are used to validate the conclusions from section 3.2, as well as identify cycle configurations suitable for integration with the rotary reactor. Next, section 3.4 makes use of parametric studies to compare the sensitivity of the selected cycle configurations to design and operating parameters like pressure ratio, reactor outlet temperature (turbine inlet temperature), diluent (CO_2) fraction and purge steam generation. The results from this phase of the study are used to identify the key operating parameters, map out the optimal operating conditions for each configuration, and define criteria for selecting from among the different cycle options. Though focused on the rotary reactor, the results of this study will also be applicable to any other thermally coupled CLC reactor design.

3.2. Analytical thermodynamic CLC power cycle models

In chapter 2, an ideal recuperative CLC cycle model was used to develop a functional relationship between cycle thermal efficiency and the reactor temperatures. This functional relationship was

used to demonstrate a positive correlation between cycle thermal efficiency and reactor temperature ratio of the form

$$\eta = 1 - \Psi_3 + \Psi_4 \left(\frac{T_{red}}{T_{ox}}\right) \tag{3.1}$$

Ψ_3 *and* Ψ_4 are positive constants, T_{red} is the reduction reactor temperature, T_{ox} is the oxidation reactor temperature and η is the cycle thermal efficiency. Equation 3.1 was used to demonstrate the advantage of thermally balanced redox reactors ($T_{red} = T_{ox}$) over thermally imbalanced designs ($T_{red} < T_{ox}$) for the recuperative cycle. Given that each cycle configuration has unique features that could introduce specific constraints on the maximum cycle thermal efficiency, the same analysis is extended here to other cycles using analytical models of the Brayton, Steam and combined CLC cycles. For each of these ideal configurations, the expression for efficiency is determined by applying energy balance to subcomponents, then back-substituting all the known variables into the equation

$$\eta = -\frac{Net\ Work\ Output}{Reaction\ Heat\ Input} \tag{3.2}$$

3.2.1. Assumptions

Idealizing assumptions simplify analysis and make it possible to quantify and compare important trends without the need to precisely predict the performance of real life systems. To account for the effect of irreversibilities in the system, some 2nd law efficiencies are included to partially relax these idealizations. The following are general assumptions used in the model formulation:

I. Air and fuel inlet temperatures are equal to ambient temperature
II. Thermal capacity (mc_p) for air and fuel-side streams are constant and independent of temperature
III. Fuel flow rate is fixed ($m_f = constant$)
IV. Heat release (equal to net enthalpy of reaction) in the reactor is constant
V. Air side and fuel-side pressure ratios are equal ($\pi_a = \pi_f = \pi$)
VI. Air flow rate (m_a) varies to control fuel exit temperature from the reactor
VII. Work (W) and Heat (Q) are defined as positive into the control volume

VIII. For the steam and combined cycles, exhaust gas leaves the heat recovery steam generator (HRSG) at ambient temperature

IX. Steam cycle low temperature reservoir is at ambient temperature (T_1)

X. Steam engine 2nd law efficiency is defined as a function of HRSG steam-exit to gas-inlet temperature ratio (see Appendices B and C)

XI. Compressors and turbines have specified isentropic efficiency

3.2.2. Simple (Brayton) CLC cycle

A schematic representation of the simple Brayton CLC cycle is shown in Figure 3-1. Applying the laws of thermodynamics to the air-side components, fuel-side components and the reactor, and substituting into equation 3.2 gives

$$\eta = -\frac{W_{Ba} + W_{Bf}}{Q}$$

$$= \Psi_1 - \Psi_2 \Omega \left(1 - \left(\frac{T_{red}}{T_{ox}}\right)\right) \qquad (3.3)$$

where $\Psi_1 = \frac{\pi^{\alpha}-1}{\pi^{\alpha}}\left(\frac{\beta_a \eta_T \eta_c - \pi^{\alpha}}{\beta_a \eta_c - \pi^{\alpha} + 1 - \eta_c}\right)$; $\Psi_2 = \frac{\pi^{\alpha}-1}{Q\eta_c \pi^{\alpha}}\left(\frac{m_f c_{pf} T_1 \beta_a}{\beta_a \eta_c - \pi^{\alpha} + 1 - \eta_c}\right)$; $\Omega = \left(\eta_T \eta_c (1 - \eta_c) + \eta_c \pi^{\alpha}(1 - \eta_T)\right)$; W_{Ba} and W_{Bf} are the work output of the air and fuel-side Brayton cycles respectively; π is the compressor pressure ratio, $\left(\frac{P_2}{P_1}\right)$, m_f is the fuel mass flow rate, c_{pf} is the fuel specific heat capacity at constant pressure, c_{vf} is the fuel specific heat capacity at constant volume, η_c is the compressor isentropic efficiency, η_T is the turbine isentropic efficiency, T_1 is the ambient temperature, T_{red} is the reduction reactor temperature , T_{ox} is the oxidation reactor temperature, β_a is the ratio of the oxidation reactor temperature to ambient temperature $\left(\frac{T_{ox}}{T_1}\right)$, $\alpha = \frac{\left(\frac{c_{pf}}{c_{vf}}\right)-1}{\left(\frac{c_{pf}}{c_{vf}}\right)}$ and Q is the net reaction heat release (see Appendix 3-A for derivation). Equation 3.3 shows that efficiency is positively correlated with reduction/oxidation reactor temperature ratio. Discounting compressor and turbine irreversibilities ($\eta_c = \eta_T = 1$), equation 3.3 reduces to the classical form, which is independent of the reactor temperature ratio

$$\eta = 1 - \pi^{-\alpha} \tag{3.4}$$

Equation 3.4 suggests that for an ideal Brayton CLC cycle with isentropic compressors and turbines, cycle efficiency is independent of reactor thermal balance. The dependence arises when irreversibilities are taken into account. This dependence is visualized in Figure 3-2 by plotting the efficiency from equation 3.3 against the reduction/oxidation reactor temperature ratio. For this plot, $T_{ox} = 1473K$, $T_1 = 300K$, $m_f = 1kg/sec$, $c_{pf} = 2.22x10^3\, J/kg$, $\eta_T = \eta_c = 0.8$, $\pi = 8{,}10\ and\ 12$, $\alpha = 0.2336$ and $LHV = 45x10^6\, J/kg$ and $Q = m_f * LHV$. The lower bound for each plot is defined such that $T_{red} > T_1\pi^{\alpha}$. The plot area is divided into three sections covering the range of values of T_{red} considered. The plot shows a linear relationship with a constant positive slope. Now consider the following scenarios:

Exothermic reduction reaction: For an exothermic reduction reaction, assuming there are no material constraints on the temperature of the reduction reactor, the region to the right of B ($T_{red} > T_{ox}$), defines the optimal cycle efficiency. However, as discussed in chapter 2, the maximum reduction reactor temperature is often limited by oxygen carrier material thermal properties or turbine inlet temperature (TIT) limit such that it cannot be higher than the oxidation reactor temperature. In such a case, the oxidation and reduction reactor temperatures become equal and the optimal efficiency corresponds to the thermally balanced case defined by line B.

Endothermic reduction reaction: For an endothermic reduction reaction, the reduction reactor temperature cannot be greater than the oxidation reactor temperature without requiring an external heat source; so the feasible reduction reactor temperature lies in the region to the left of B in Figure 3-2 and maximum efficiency also corresponds to the thermally balanced operating point at B.

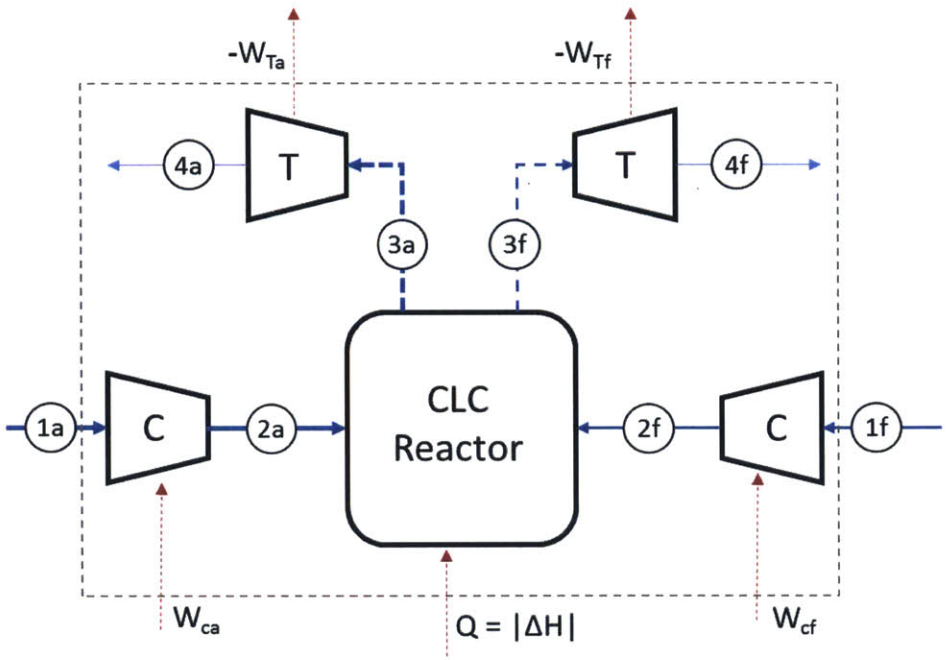

Figure 3-1: Simple (Brayton) CLC cycle.

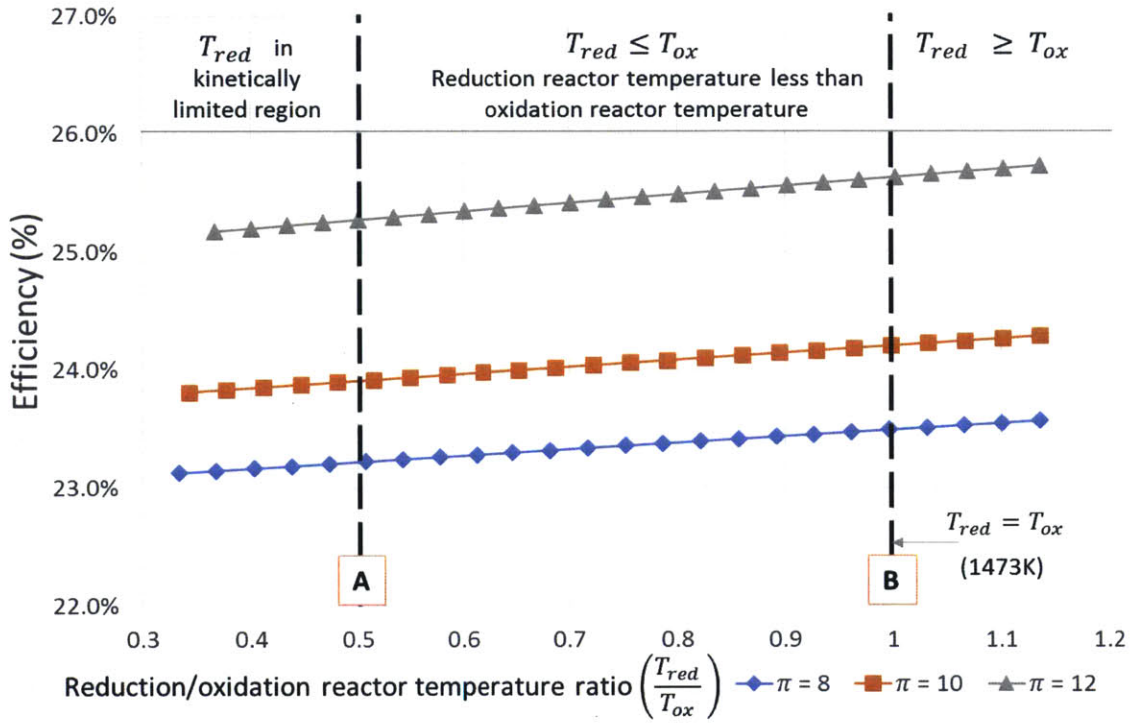

Figure 3-2: Impact of reactor thermal balance on efficiency for a Simple Brayton CLC cycle.

3.2.3. Simple steam CLC cycle

Figure 3-3a shows a schematic of a simple CLC steam cycle. The steam engine is modeled as an ideal engine extracting work from the exhaust gas stream as it cools to ambient conditions as shown in Figure 3-3b. The actual work output is obtained by applying a 2nd law efficiency to the work output from this steam engine (see Appendix 3B). Applying the laws of thermodynamics on the reactor, the air and the fuel-side steam cycles gives the following expression for efficiency

$$\eta = -\frac{W_{Sa} + W_{Sf}}{Q}$$

$$= \eta_{2sa}\left(1 - \frac{\ln(\beta_a)}{\beta_a - 1}\right) + \frac{m_f c_{pf} T_1}{Q}\left(\beta_a \frac{T_{red}}{T_{ox}} - 1\right)\left(\eta_{2sf}\left(1 - \frac{\ln\left(\beta_a \frac{T_{red}}{T_{ox}}\right)}{\beta_a \frac{T_{red}}{T_{ox}} - 1}\right) - \eta_{2sa}\left(1 - \frac{\ln(\beta_a)}{\beta_a - 1}\right)\right) \tag{3.5}$$

W_{Sa} and W_{Sf} are the work output of the air and fuel-side steam cycles respectively; η_{2sa} is the air-side steam cycle second law efficiency; η_{2sf} is the fuel-side steam cycle second law efficiency and all the other terms are as described in section 3.2.2. η_{2sa} and η_{2sf} are approximate 2nd law efficiencies defined as

$$\eta_{2sa} = \frac{\varepsilon\beta_a - 1}{\varepsilon(\beta_a - 1)} \tag{3.6}$$

$$\eta_{2sf} = \frac{\varepsilon\beta_a\left(\frac{T_{red}}{T_{ox}}\right) - 1}{\varepsilon\left(\beta_a\left(\frac{T_{red}}{T_{ox}}\right) - 1\right)} \tag{3.7}$$

Here, ε is the ratio of the HRSG steam exit to hot gas inlet temperature (see Appendix B for details). Assuming $\eta_{2sa} = \eta_{2sf} = 1$, equation 3.5 reduces to

$$\eta = 1 - \frac{Ln\beta_a}{\beta_a - 1} + \left(\frac{m_f c_{pf} T_1}{Q}\right)\left(\frac{\beta_a Ln\beta_a}{\beta_a - 1}\left(\left(\frac{T_{red}}{T_{ox}}\right) - 1\right) - Ln\left(\frac{T_{red}}{T_{ox}}\right)\right) \tag{3.8}$$

Figure 3-4 is obtained by plotting efficiency from equation 3.5 against the reduction/oxidation reactor temperature ratio. The parameter values used are the same as those for the Brayton cycle; ε is assumed to be 0.75 and the lower bound for $\frac{T_{red}}{T_{ox}}$ is defined such that $T_{red} > T_1$.

Exothermic reduction reaction: Assuming no material constraints on the temperature of the reduction reactor, efficiency is maximized in the region to the right of B in Figure 3-4 where $T_{red} > T_{ox}$. However, in practical conditions where oxygen carrier or HRSG material thermal properties impose stricter bounds on the maximum temperature, the optimal efficiency will correspond to the thermally balanced case defined by line B.

Endothermic reduction reaction: Since an endothermic reduction reaction needs to be sustained by heat transfer from the oxidation reaction, its temperature is limited by that of the oxidation reactor. Therefore the feasible region is to the right of B in Figure 3-4 and the maximum efficiency corresponds to the thermally balanced operating point defined by line B. Note, however, that the profile of the efficiency curve in Figure 3-4 is a function of the value defined for ε. If ε = 1, the expression for efficiency will correspond to equation 3.8 and maximum efficiency values will occur both at B $\left(\frac{T_{red}}{T_{ox}} = 1\right)$ and at the left end of the plot $\left(\frac{T_{red}}{T_{ox}}\right)_{min}$. The region to the left of A is characterized by low temperatures and consequently slower reactions. Closer to $\left(\frac{T_{red}}{T_{ox}}\right)_{min}$, the temperature may also fall below the feasible equilibrium limit for many common oxygen carriers. For example, for nickel, the equilibrium reduction temperature for reaction with methane corresponds to $\frac{T_{red}}{T_{ox}} \cong 0.3$ and the reaction rate at A is about 500 times slower than the rate at B. Therefore, it is preferable to operate towards the right side of region A-B, and the maximum efficiency point lies at the B-boundary, where the oxidation and reduction reactor temperatures are equal.

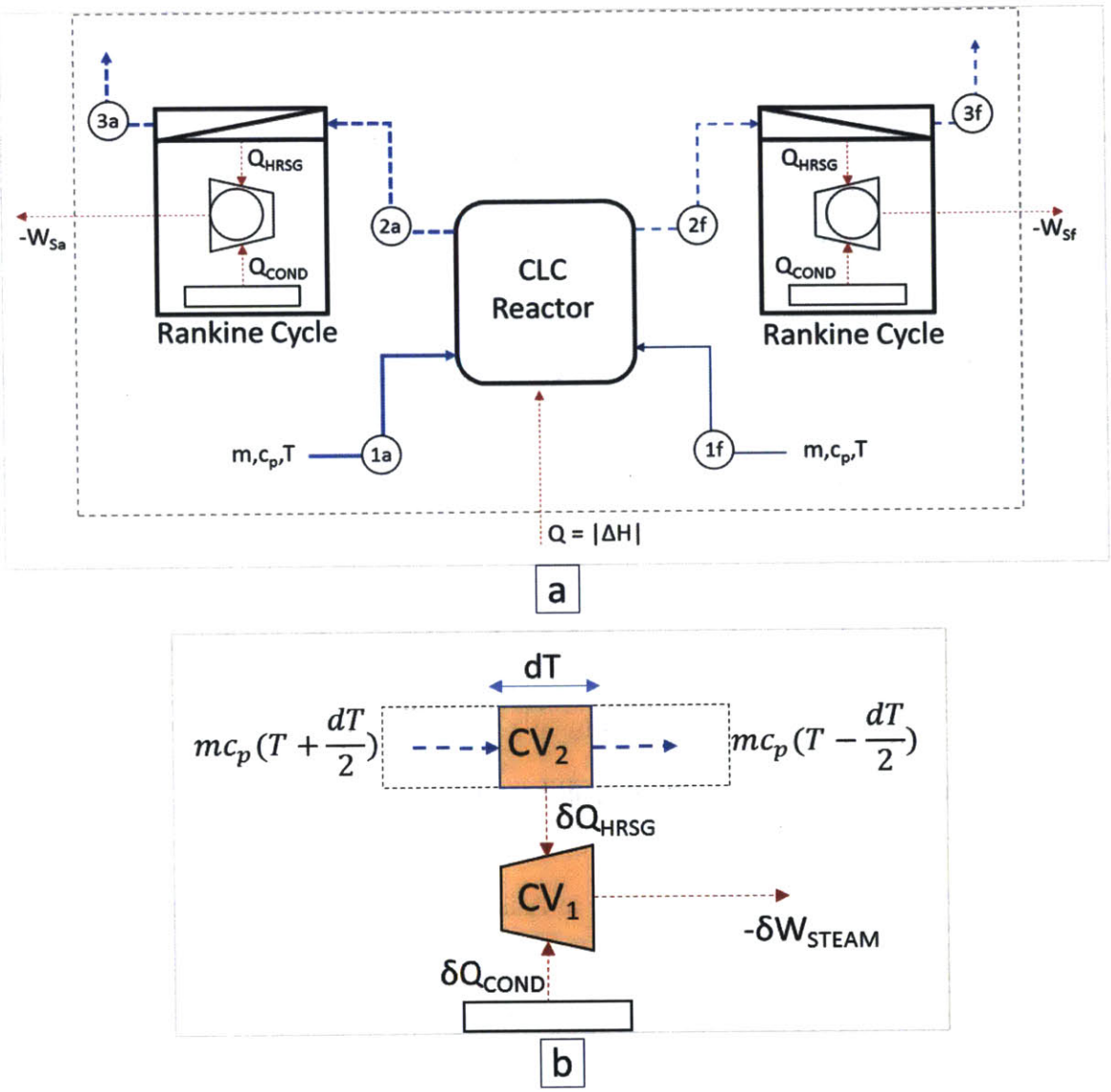

Figure 3-3: Ideal CLC steam cycle.
(a) Schematic diagram for idealized cycle; (b) Ideal steam (Rankine) engine model.

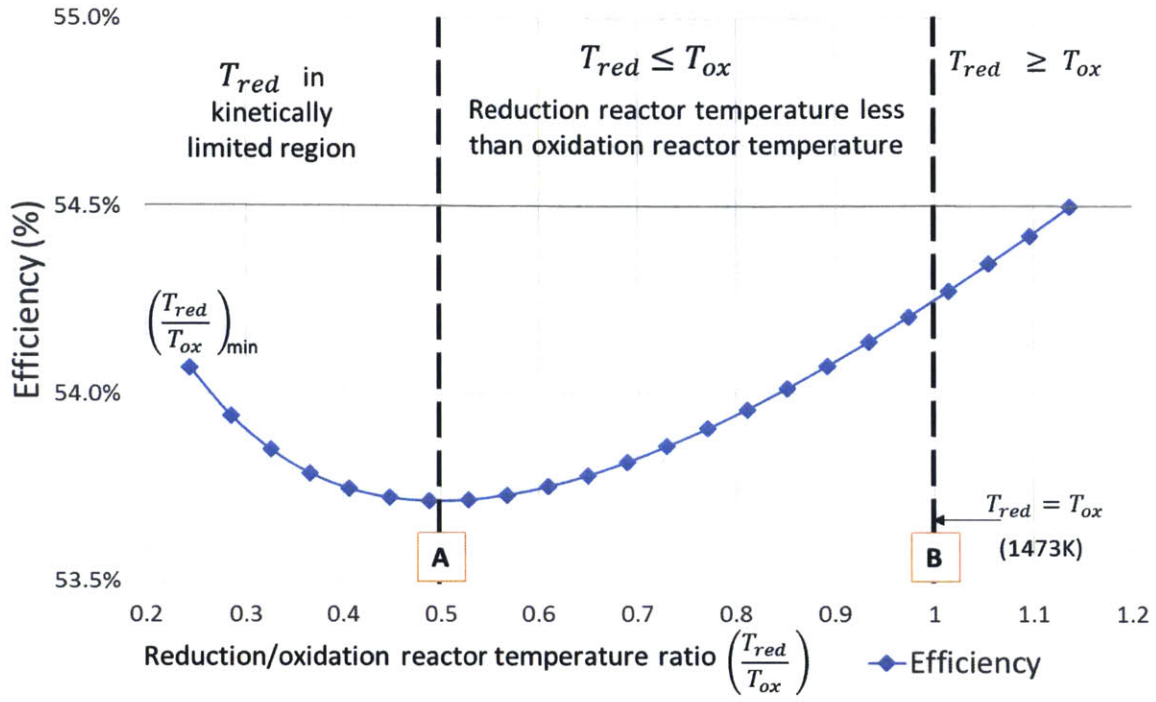

Figure 3-4: Impact of reactor thermal balance on efficiency for a simple steam CLC cycle.

3.2.4. Combined CLC cycle

Here, the foregoing analysis is extended to a simplified model of a combined CLC cycle, sketched in Figure 3-5. Details of the derivation can be found in Appendix 3C. The efficiency for the combined CLC cycle is given by

$$\eta = -\frac{(W_{Ba} + W_{Bf}) + (W'_{Sa} + W'_{Sf})}{Q} \tag{3.9}$$

$(W_{Ba} + W_{Bf})$ represents the net work output from the Brayton cycles, equivalent to equation 3.5 (equation 3-C2 in Appendix 3C) while $(W'_{Sa} + W'_{Sf})$ represents the net work output from the bottoming steam (Rankine) cycles, equivalent to a modified form of equation 3.5 (equation 3-C3 in Appendix 3C) and Q is the overall reaction heat release. Neglecting steam cycle, turbine and compressor irreversibilities, equation 3.9 simplifies to

$$\eta = 1 - \frac{Ln\left(\frac{\beta_a}{\pi^{\alpha}}\right)}{\beta_a - \pi^{\alpha}} + \frac{m_f c_{pf} T_1}{Q}\left(\frac{\beta_a Ln\left(\frac{\beta_a}{\pi^{\alpha}}\right)}{\beta_a - \pi^{\alpha}}\left(\left(\frac{T_{red}}{T_{ox}}\right) - 1\right) - Ln\left(\frac{T_{red}}{T_{ox}}\right)\right) \quad (3.10)$$

Where π is the compressor pressure ratio, $\beta_a = \frac{T_{ox}}{T_1}$ and $\left(\frac{T_{red}}{T_{ox}}\right)$ is the reactor temperature ratio. Similar to the case for the steam cycle, the combined CLC cycle efficiency in equation 3.9 is plotted against the reduction/oxidation reactor temperature ratio in Figure 3-6 for selected compressor pressure ratios, using the same parameter values as in the Brayton and Steam cycle plots. The range of $\left(\frac{T_{red}}{T_{ox}}\right)$ for each plot is defined such that $T_{red} > T_1 \pi^{\alpha}$.

Exothermic reduction reaction: For each pressure ratio, the profile is similar to that described for the simple Rankine cycle (which corresponds to $\pi = 1$) and so, the same arguments apply; material considerations typically preclude the region to the right of B, therefore maximum feasible efficiency occurs at the thermally balanced operating point (B) where $T_{red} = T_{ox}$.

Endothermic reduction reaction: Similar to the case for the simple steam cycle, the feasible operating region lies to the left of B and fast kinetics favors operation in the region A-B. Within this region, the Maximum efficiency occurs at the B where $T_{red} = T_{ox}$.

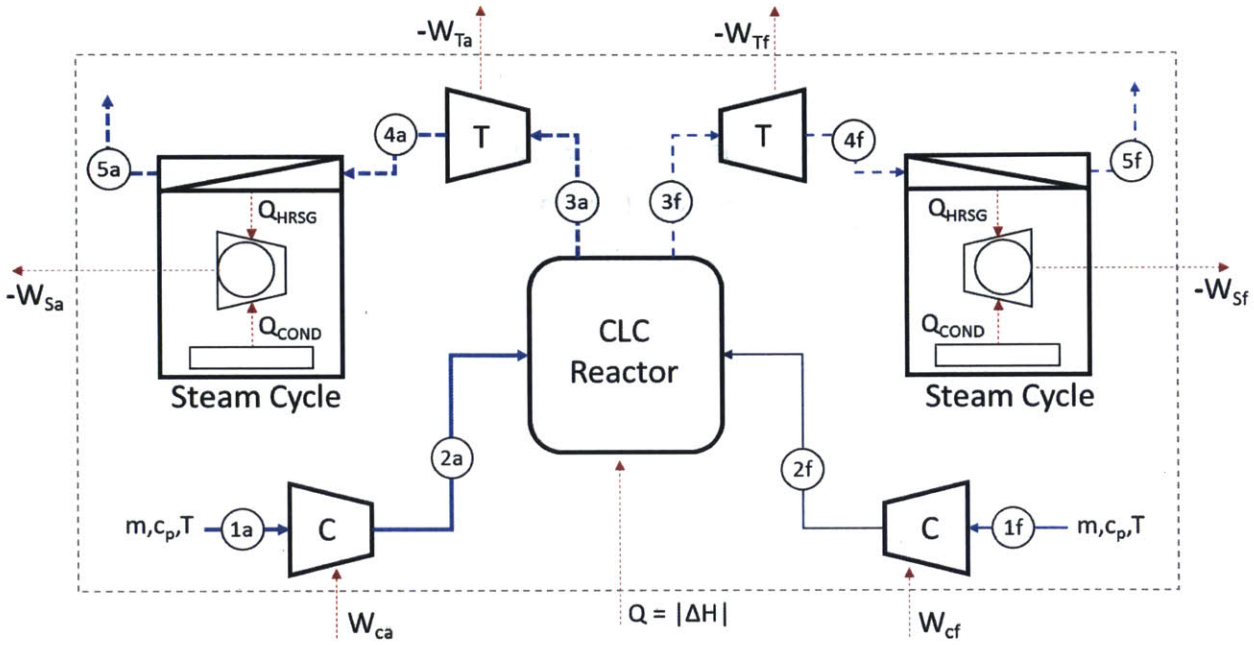

Figure 3-5: Schematic for idealized combined CLC cycle.

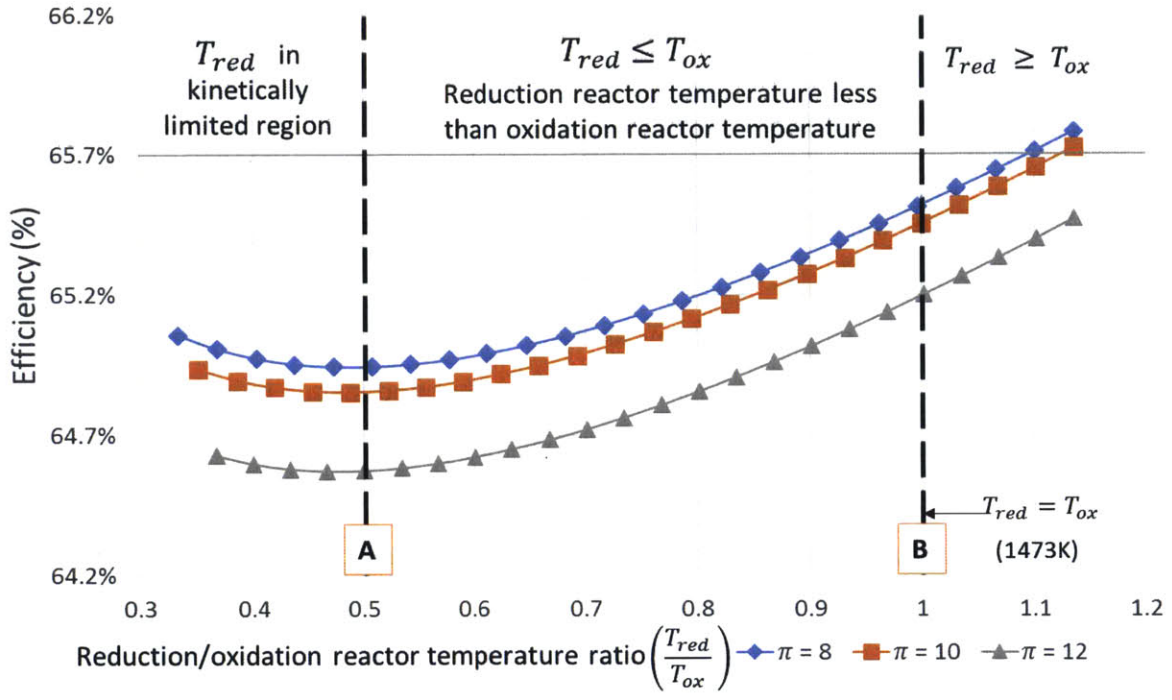

Figure 3-6: Analyzing impact of reactor thermal balance on efficiency for a combined CLC Cycle.

To summarize, simplified thermodynamic models for the Brayton CLC cycle, the simple steam CLC cycle and the combined CLC cycles have been used to analyze the impact of thermally balanced reactor operation on cycle efficiency. The main conclusion is that when oxygen carrier material properties, process material constraints and kinetic considerations are taken into account, the optimal performance is obtained when both reactors are in thermal equilibrium. These conclusions are summarized in Table 3.1.

Table 3.1: Summary table for non-ideal Brayton, steam cycle and combined cycle analysis

Reduction reaction	**Condition for maximum efficiency**	
	Thermodynamic constraints only	Thermodynamic and material constraints
Endothermic	$T_{red} = T_{ox}$	$T_{red} = T_{ox}$
Exothermic	$T_{red} > T_{ox}$	$T_{red} = T_{ox}$

3.3. Detailed flow sheet models

Section 3.2 examined the impact of reactor thermal coupling on the efficiency of the ideal Brayton, steam and combined CLC cycles. The results showed that when thermodynamic, kinetic and material constraints in practical CLC systems are factored in, thermally balanced reactor operation is preferred for optimizing system efficiency. Since the thermodynamic models used to arrive at this conclusion involved simplifying idealizations that may not capture some important constraints that exist in real systems, the current section uses the more detailed Aspen Plus® flow sheet models to assess the impact of thermal coupling on the different cycle configurations.

3.3.1. Cycle description

As discussed in chapter 1, the existence of two reactor exhaust streams creates up to n^2 possible configurational combinations for producing power compared to any n for a conventional system.

The challenge then is to select an optimal combination of power generation strategies that would maximize performance. From the 16 possible CLC cycle options listed in Figure 1-5 from chapter 1, this study will avoid an intractable enumeration of all feasible cycle combinations and select representative cycle arrangements for analysis. The configurations selected include the all the identical cycles – combined CLC cycle, recuperative CLC cycle, simple Brayton CLC cycle and simple steam CLC cycle – and some hybrid cycles – combined-recuperative CLC cycle, combined-steam CLC cycle and recuperative-steam CLC cycle. The naming convention omits the fuel-side cycle name when the two are identical, and concatenates the air and the fuel-side cycle names for the hybrid configurations. These configurations will be used to illustrate the main ideas from this study.

3.3.1.1. The combined CLC cycle

This configuration has received the most attention in CLC literature because of the high efficiencies associated with combined cycle systems. Cycle efficiencies reported in literature for single and multi-stage CLC reactors with methane fuel and complete CO_2 separation range from 47 – 53.5 % [11], [13]–[15], [31]. The combined CLC cycle uses a combined cycle layout on both the air and fuel sides to produce work from each reactor exhaust stream, as shown in Figure 3-7. On the air side, the inlet air stream is first compressed, then sent to the rotary reactor, where it reacts exothermically with the oxygen carrier. Compression without intercooling is utilized to maximize the temperature of the reactor inlet stream. The air zone exhaust, which consists of a mixture of depleted air from the air sector and steam from the air purge sector, is first expanded in a turbine to produce power before flowing into the HRSG to generate steam for the bottoming steam cycle. Power is produced in the steam cycle from the high and low pressure steam turbines and the cool HRSG exhaust is released into the atmosphere. The fuel side follows an almost identical process up to the HRSG. Some of the CO_2 from the fuel-side HRSG exhaust is recycled to the fuel inlet where it serves as a diluent gas for the fuel. The rest is dried and compressed in the CO_2 compression unit. Air and fuel sector purge steam are extracted from intermediate pressure turbines in the respective steam cycles, reheated in the HRSG and then sent to the rotary reactor.

3.3.1.2. Simple CLC cycles

The simple cycles refer to the Brayton and steam CLC cycles. The layouts are similar to that described for the combined cycle except that for the simple steam cycle, there are no gas turbines or compressors, and for the Brayton cycle, there are no bottoming steam cycles on either the fuel or air side.

3.3.1.3. Hybrid cycles

Hybrid configurations are motivated by the need to achieve some performance/complexity/cost tradeoff between cycle options. Hybrid cycles selected for this study include the combined-recuperative cycle (combined cycle on the air side, recuperative cycle on the fuel side), combined-steam cycle (combined cycle on the air side, steam cycle on the fuel side) and recuperative-steam cycle (recuperative cycle on the air side, steam cycle on the fuel side). In the combined-steam and the recuperative-steam cycles, the CO_2-rich reactor exhaust is used directly in a heat recovery steam generator without expansion in a gas turbine. This way, they reduce CO_2 compression energy penalty. The schematic of the Aspen flow sheet for the combined-recuperative cycle is shown in Figure 3-8. It adapts the combined CLC cycle design by replacing the fuel-side combined cycle with a recuperative cycle. The recuperative cycle layout was been described in detail in chapter 2. The recuperator in the combined-recuperative CLC cycle offers a less complex and probably more cost effective alternative to installing a bottoming steam turbine engine on the fuel side.

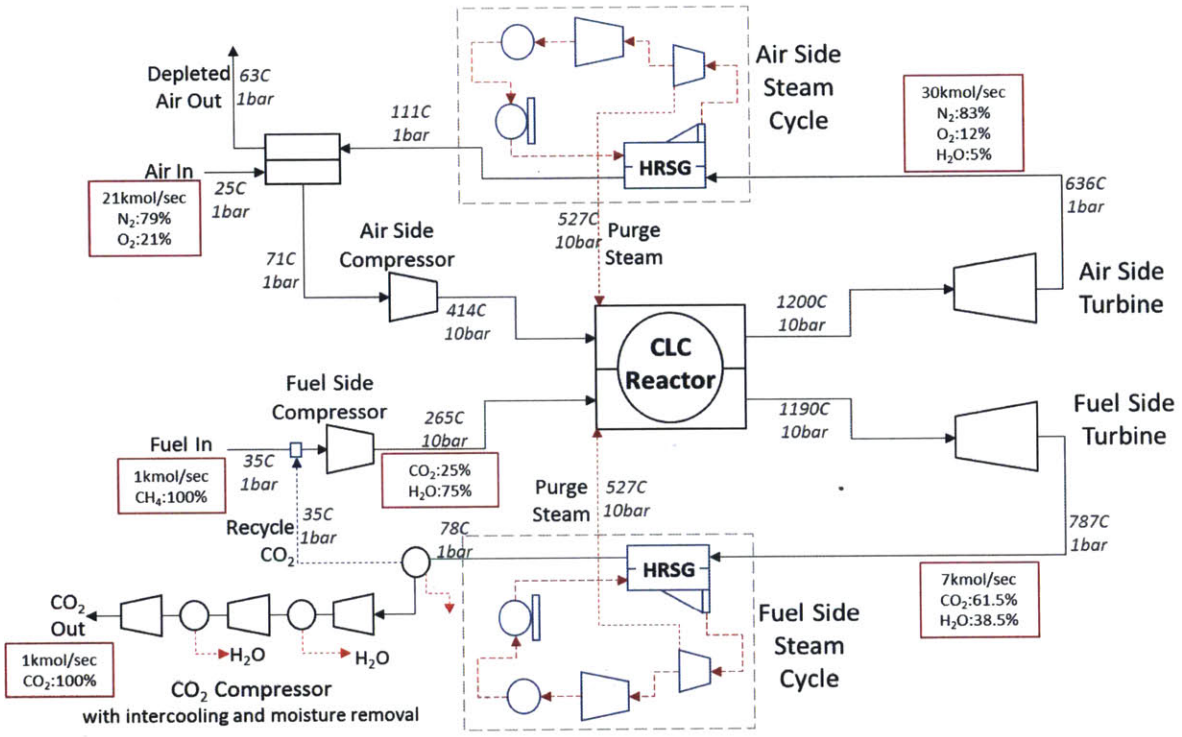

Figure 3-7: Aspen Plus® flowsheet schematic for the combined CLC cycle.

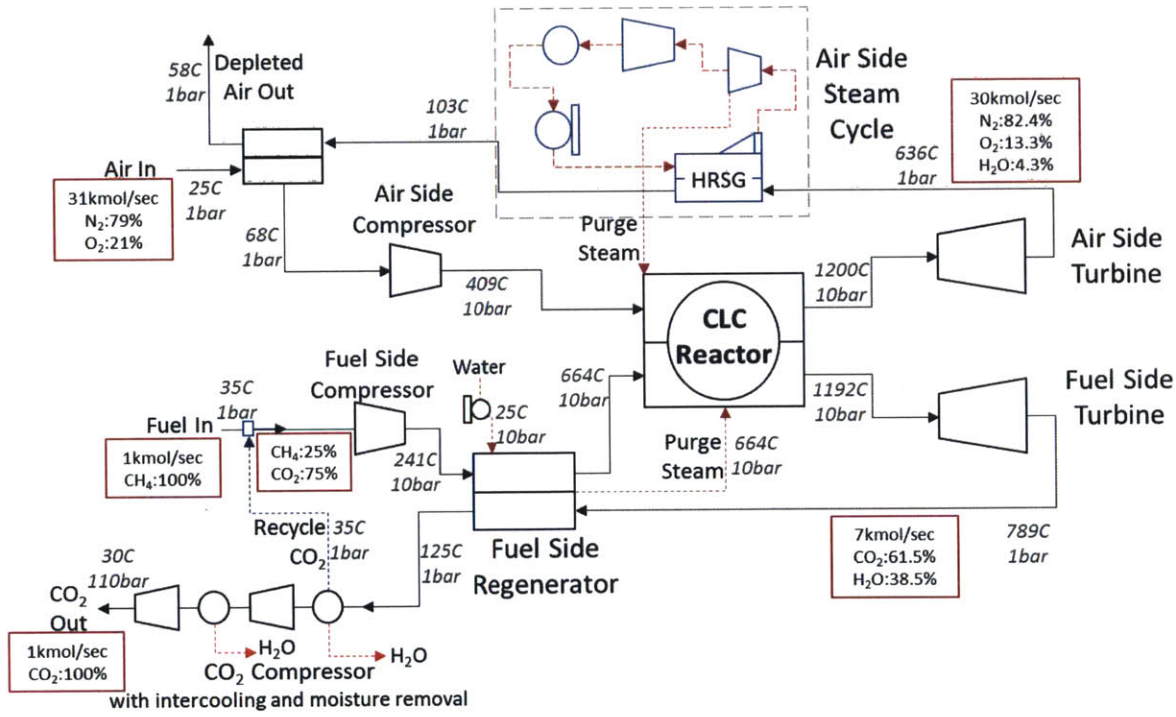

Figure 3-8: aspen plus® flowsheet schematic for the combined-recuperative CLC cycle.

3.3.2. Rotary reactor model

The rotary reactor, described in detail in [4], [27]–[29], is essentially a solid wheel with a matrix of micro channels whose walls provide structural integrity and thermal management for the entire reactor. The Aspen Plus® setup for the reactor model has been described in chapter 2. It accommodates the twofold objective of achieving quasi-thermally balanced operation and accounting for the air and fuel sector purge steam generation.

3.3.2.1. Model specifications

The modeling assumptions and specifications used in developing the Aspen Plus® system models are summarized in Table 3.2 and Table 3.3. For the reactor model, nickel is used as the oxygen carrier with boron nitride as the support material. The base case reactor temperature was set at 1200C. A base case compressor pressure ratio of 10 is used and reactor pressure drop is neglected since the value is very small for the rotary reactor [27].

Table 3.2: Simulation specifications for base case models

Item	Units	Value
General		
Air reactor temperature	C	1200
Ambient temperature	C	25
Pressure ratio[1]		10
Gas compressor isentropic efficiency	%	90%
Gas turbine isentropic efficiency	%	90%
Sequestration CO_2 compression pressure	bar	110
Reactor pressure	bar	10
Oxygen carrier (MeO / Me)		NiO / Ni
Recuperative heat exchanger minimum internal temperature approach	C	25

Steam cycle		
Pump efficiency	%	75%
HRSG exit steam temperature[2]	C	560
High pressure turbine inlet steam pressure	bar	180
Steam cycle condenser pressure	bar	0.04
Steam turbine isentropic efficiency	%	90%
HRSG minimum internal temperature approach	C	25
Inlet streams		
Fuel type		Methane
Inlet fuel flow rate	kmol/sec (kg/sec)	1 (16.04)
Inlet air N_2 composition	fraction	0.79
Inlet air O_2 composition	fraction	0.21
Recycled CO_2 / CH_4 composition in inlet stream	ratio	3 : 1
Oxidation reactor purge steam rate	kmol/sec	1
Reduction reactor purge steam rate	kmol/sec	0.5
Variable design/operating parameters		
Inlet air flow rate	Varied to control the oxidation reactor temperature	
Boron nitride (bulk support material) circulation rate	Varied to control reduction reactor temperature	

1. Does not apply to the ambient pressure simple steam cycle
2. For sensitivity studies, when exhaust gas inlet temperatures are lower (e.g. high pressure ratio cases), the value is freed and allowed to vary subject to the specified pinch value.

Table 3.3: Base case configuration-specific design strategy

Specification	Air compressor intercooling	Fuel compressor intercooling	Air reactor purge steam source	Fuel reactor purge steam source
Steam cycle	Yes	None	Air side steam cycle	Fuel side steam cycle
Simple brayton cycle	None	None	Air side recuperator	Fuel side recuperator
Combined cycle	Yes	None	Air side steam cycle	Fuel side steam cycle
Combined-recuperative cycle	None	None	Fuel side recuperator	Fuel side recuperator
Combined-steam cycle	None	None	Fuel side recuperator	Fuel side recuperator
Recuperative-steam cycle	Yes	None	Fuel side recuperator	Fuel side recuperator

3.3.3. Results

3.3.3.1. The Brayton CLC cycle configuration

Figure 3-9 shows a slight negative correlation between the efficiency and the reduction/oxidation reactor temperature ratio $\left(\frac{T_{red}}{T_{ox}}\right)$ at the lower pressure ratios (10 and 14). This contrasts with the results from the idealized cycle analysis, mostly because thermally balanced reactor operation results in a higher fuel-side exhaust enthalpy which is lost to the environment as there is no exhaust heat recovery in the Brayton Cycle. However, at higher pressure ratios -when the turbine exhaust temperatures are closer to ambient and exhaust availability loss is low - the trend reverses and efficiency positively correlates with $\left(\frac{T_{red}}{T_{ox}}\right)$ as shown in Figure 3-9 for pressure ratios of 40 and 50.

3.3.3.2. The steam and the combined CLC cycle configurations

The efficiency of both the steam cycle and the combined cycle increase with increasing reactor temperature ratio, as shown in Figure 3-10 and Figure 3-11. This trend is consistent with the

suggestion from the preceding theoretical analysis in section 3.2. Note from Figure 3-11 that the relationship between efficiency and reactor temperature ratio for the combined CLC cycle is not linear; it levels off as reactor temperature ratio approaches unity. This is a consequence of the externally constrained maximum steam temperature for the bottoming steam cycle. Thermally balanced reactor operation increases the reduction reactor temperature, creating a higher temperature gas turbine exhaust stream. Since the maximum permissible steam temperature remains at 560C, HRSG entropy generation increases with increasing reduction reactor exhaust gas temperature. This creates an increasingly inefficient bottoming steam cycle, partly eroding the advantage that derives from having a higher temperature fuel-side exhaust stream.

3.3.3.3. The hybrid CLC configurations

The hybrid configurations show mixed results. The combined-recuperative cycle in Figure 3-12 behaves consistently with the expectations from the theoretical analysis. On the other hand, the steam-based hybrid cycles exhibit a reverse trend as shown the same figure. The reason is because the 560C steam temperature cap leads to larger entropy generation in the HRSG as the reduction reactor temperature increases. Thus, the larger enthalpy in the fuel-side exhaust stream is much more inefficiently converted in the fuel-side steam cycle. Therefore, the additional fuel-side work output does not make up for the corresponding air-side loss. This conclusion is also supported by the analysis carried out by Hammers et al. for an IGCC plant integrated with a downstream combined-steam CLC cycle [42].

Therefore, in order to benefit from thermally balanced reactor operation, the fuel-side cycle must be a high efficiency design capable of taking advantage of the resulting increase in the availability of the reduction reactor exhaust stream. Cycles like the combined CLC cycle, the recuperative CLC cycle or the combined-recuperative hybrid cycle can exploit this advantage and are therefore ideal for integration with the thermally coupled rotary reactor.

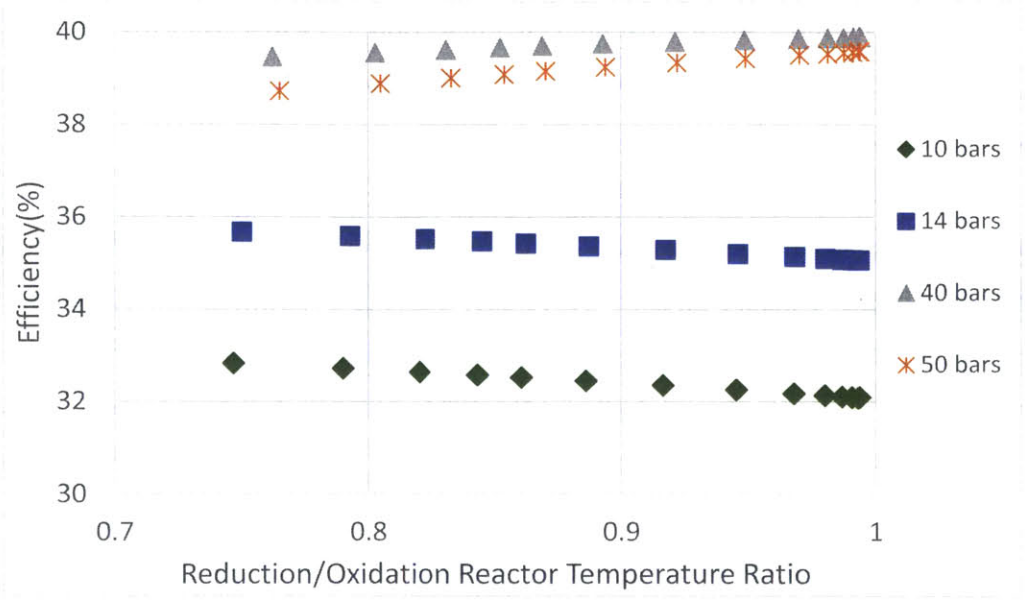

Figure 3-9: Fuel/Air reactor temperature ratio sensitivity for Brayton CLC cycle. At low operating pressures, thermally balanced reactor operation results in increased fuel-side exhaust enthalpy loss to the environment, hence, the drop in efficiency. At higher operating pressures, exhaust enthalpy loss is minimized, resulting in increased efficiency.

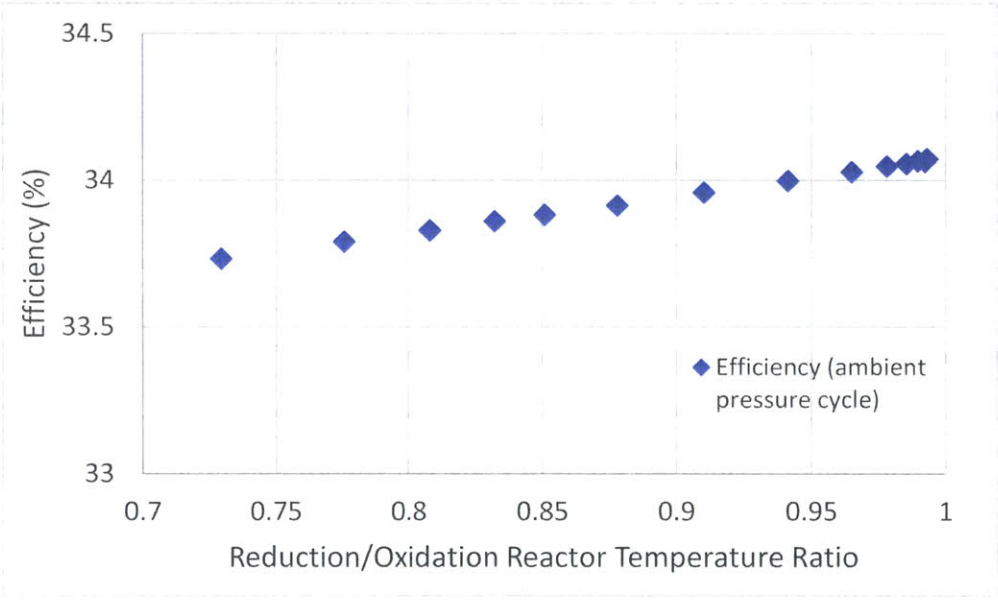

Figure 3-10: Fuel/Air reactor temperature ratio sensitivity for simple CLC steam cycle. Efficiency appears to be positively correlated to reactor thermal balance.

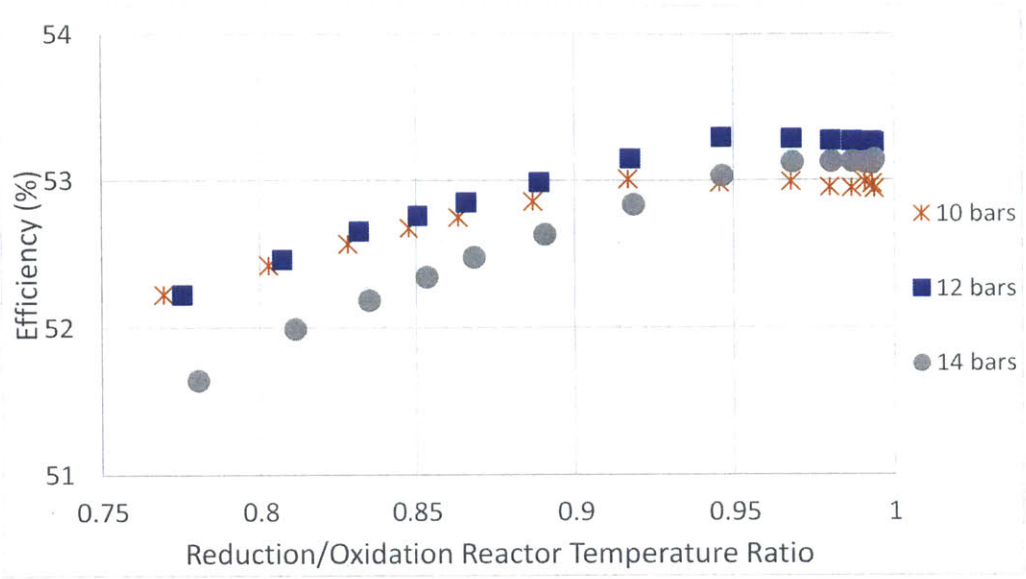

Figure 3-11: Fuel/Air reactor temperature ratio sensitivity for combined CLC cycle. Efficiency is generally positively correlated to degree of reactor thermal balance.

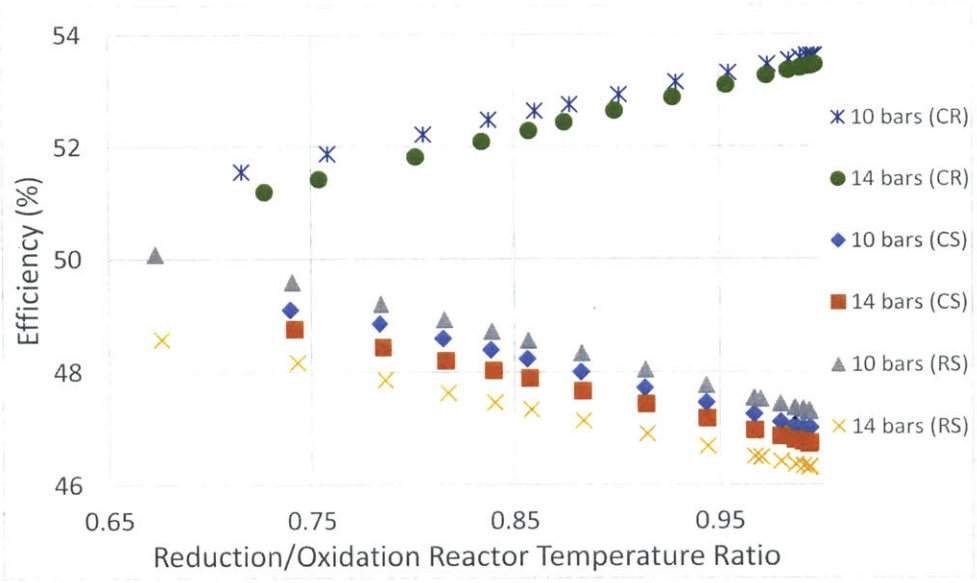

Figure 3-12: Fuel/Air reactor temperature ratio sensitivity for the hybrid CLC cycles. Thermally balanced reactor operation increases efficiency for combined-recuperative (CR) cycle but decreases in the case of the combined-steam (CS) and recuperative-steam (RS) cycles because the maximum temperature constraint on the bottoming steam cycle increases availability loss as reduction reactor temperature increases.

3.4. Parametric studies

Section 3.3 identified the combined cycle and combined-recuperative cycles as suitable cycle configurations for integrating with the rotary reactor. The analysis of the recuperative CLC cycle in chapter 2 also demonstrated its suitability for the rotary reactor. The objective of the parametric studies then is to characterize and compare how key design and operating parameters impact the efficiency of these rotary reactor-based power plant configurations. The design and operating parameters examined in this study are cycle pressure ratio, CO_2 fraction in the inlet fuel feed stream, purge steam generation strategy and purge steam demand. For the pressure sensitivity study, the system pressure ratio was varied from 2 to 20 for each cycle configuration while for the feed stream CO_2 fraction study, the CO_2 fraction was varied from around 0.3 to 0.9 by adjusting the exhaust CO_2 recycle ratio. All other design specifications are fixed at the base case values. The Pressure-TIT study is used to analyze how the efficiency/pressure profile varies with varying turbine inlet (or reactor) temperature. The steam generation study is used to compare the impact of steam requirement, as well as steam generation strategy, on system performance.

3.4.1. Pressure ratio study

The cycle pressure ratio has a significant impact on the efficiency of rotary reactor CLC-based systems. Figure 3-13 shows the variation of efficiency with pressure ratio (π) for the different cycle configurations. The profiles for combined cycle and the combined-recuperative CLC cycle configurations are similar because for both configurations, the air-side combined cycle is the dominant contributor to net work output. The maximum efficiency for either cycle occurs between 11 and 13 pressure ratio range with values of 53.3% and 53.8% for the combined and the combined-recuperative CLC cycles respectively. The dip in efficiency beyond $\pi = 15$ is caused mainly by the drop in steam cycle power output as the temperature of the turbine exhaust falls. There is also some penalty associated with the fact that the current cycle setup is not optimized for high pressure ratios. The recuperative cycle on the other hand peaks at the lower pressure ratio of around 3 with approximately 56% efficiency. Based solely on performance considerations, the recuperative configuration operating at low pressures appears to be the most attractive. However, lower pressures imply higher volumetric gas flow rates, which in turn may require larger

recuperators and reactors, and probably, higher costs. The combined-recuperative cycle offers a tradeoff that is slightly more efficient than the combined cycle and avoids the large equipment sizes that the lower pressure recuperative cycle requires.

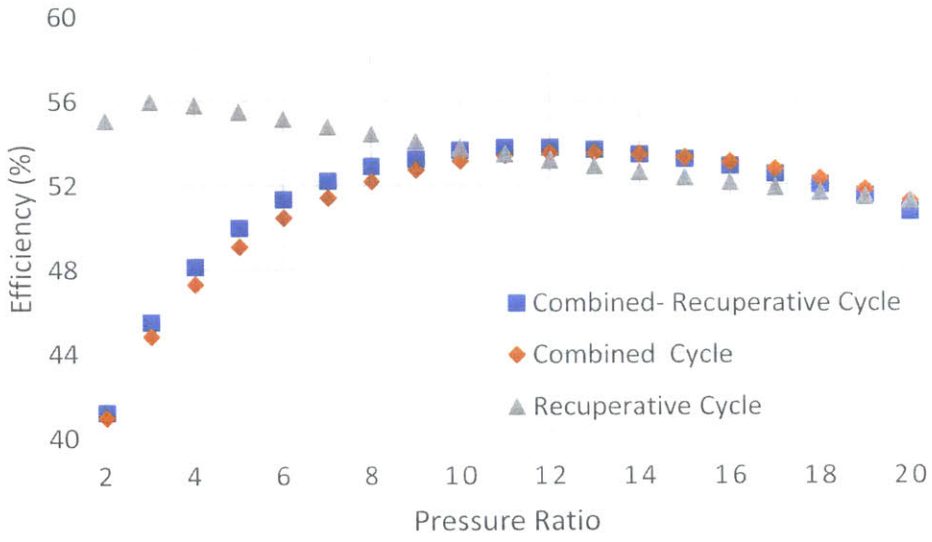

Figure 3-13: Comparing the impact of compressor pressure ratio on efficiency for combined, recuperative and combined-recuperative cycle configurations.

3.4.2. Pressure ratio – turbine inlet temperature (TIT) study

This study identifies and compares the optimal efficiency region in the space defined by pressure ratio and turbine inlet temperature (TIT) for the combined, recuperative and combined-recuperative cycles. The results are shown in Figures 3.14-3.16.

From Figure 3-14, the optimal pressure ratio for the combined CLC cycle is seen to be a strong function of TIT; it varies from 6 at 1000C (48.6% efficiency) to 14 at 1250C (54.3% efficiency). A similar trend is observed for the combined-recuperative CLC cycle (Figure 3-15) which varies from 6 at 1000C (48.5%) to 13 at 1250C (55%). In contrast, the optimal pressure ratio for the recuperative CLC cycle is not a strong function of TIT, changing only from 3 to 4 as TIT varies from 1000C (51%) to 1250 (57%), as illustrated in Figure 3-16. Thus for the combined and

combined-recuperative cycles, the optimal point lies in the high pressure, high TIT region while for the recuperative cycle, it lies in the low pressure, high TIT region.

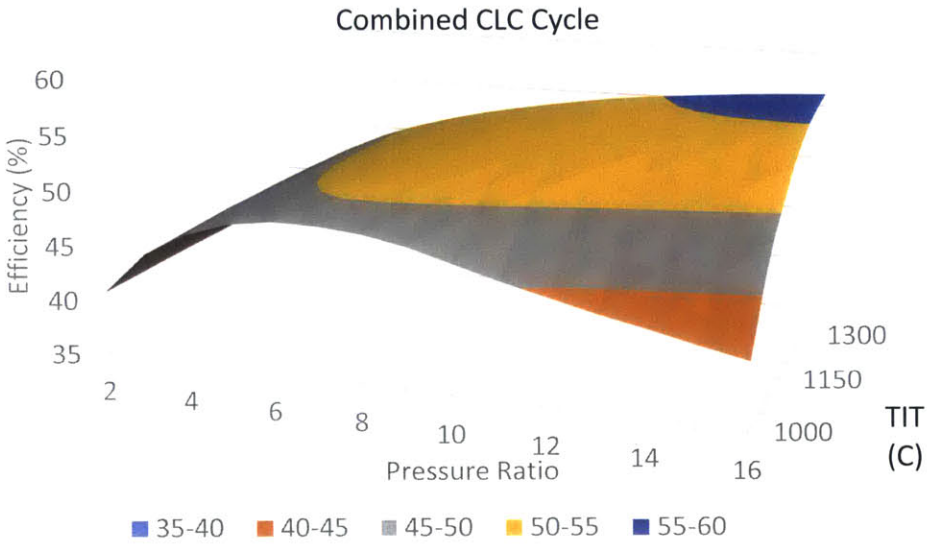

Figure 3-14: Pressure/TIT multivariable analysis result for the combined CLC cycle. Optimal conditions in the high pressure and high TIT region.

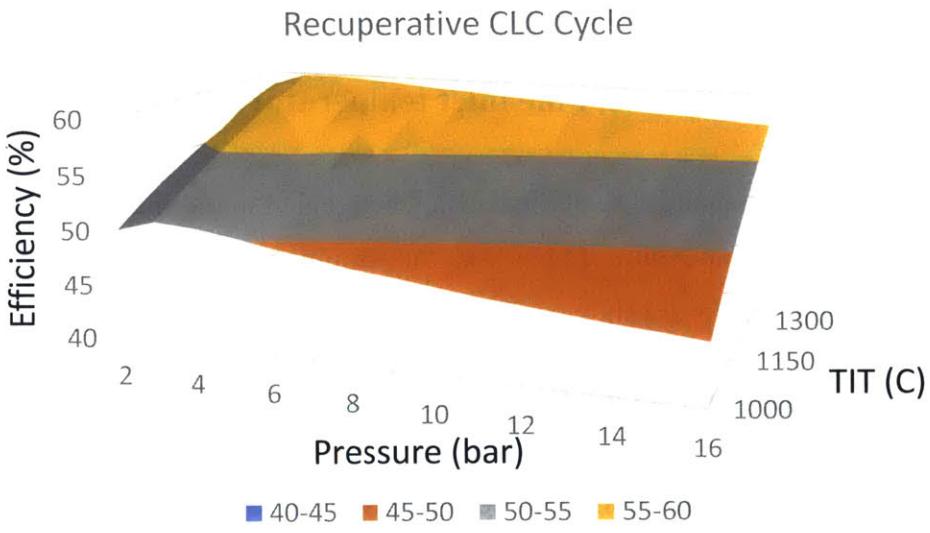

Figure 3-15: Pressure/TIT multivariable analysis result for the recuperative CLC cycle. Optimal conditions in the low pressure and high TIT region

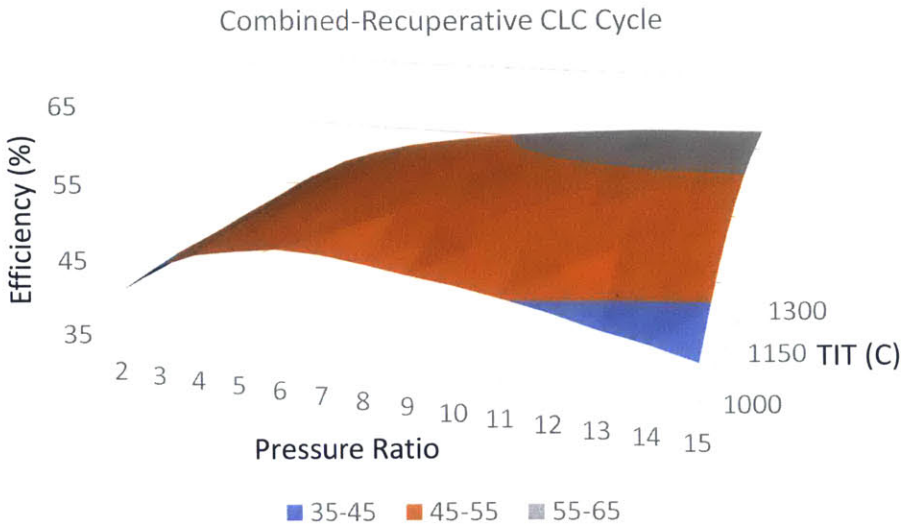

Figure 3-16: Pressure/TIT multivariable analysis result for the combined-recuperative CLC cycle.
Optimal conditions in the high pressure and high TIT region

3.4.1. CO_2 fraction sensitivity

Recycled CO_2 is used as the carrier or diluent gas for the fuel supply to the reactor. In fluid bed reactor designs, the amount of CO_2 recycle is determined by fluidization requirements. Since the rotary reactor does not require fluidization, the impact on efficiency provides an alternative criteria for determining the optimal CO_2 diluent fraction. The result for this study is shown in Figure 3-17. The profiles for the recuperative and combined-recuperative configurations are very similar since they both have a recuperative engine on the fuel side and therefore show identical responses to CO_2 recycle. Moreover, at $\pi = 10$, the efficiencies of the two designs are very similar. For both cases, higher CO_2 fraction increases cycle efficiency. On the other hand, increasing CO_2 recycle reduces efficiency for the combined CLC cycle and the reason for this trend is explained as follows: Since the fuel-side turbine exhaust temperature is higher than that on the air-side - though both have the same HRSG steam temperature constraint - the fuel-side combined cycle engine experiences larger irreversibility in the HRSG and ends up the less efficient engine. Since

increasing CO_2 recycle reduces air flow required for reactor temperature control, the net effect is moving more flue gas to the less efficient, fuel-side engine and thus, a resulting drop in efficiency. Therefore, the combined cycle performs better with lower fractions. The optimal CO_2 fraction will have to be determined from a tradeoff between cycle efficiency and the impact on reactor size and performance. These results are valid for the base case pressure ratio of 10.

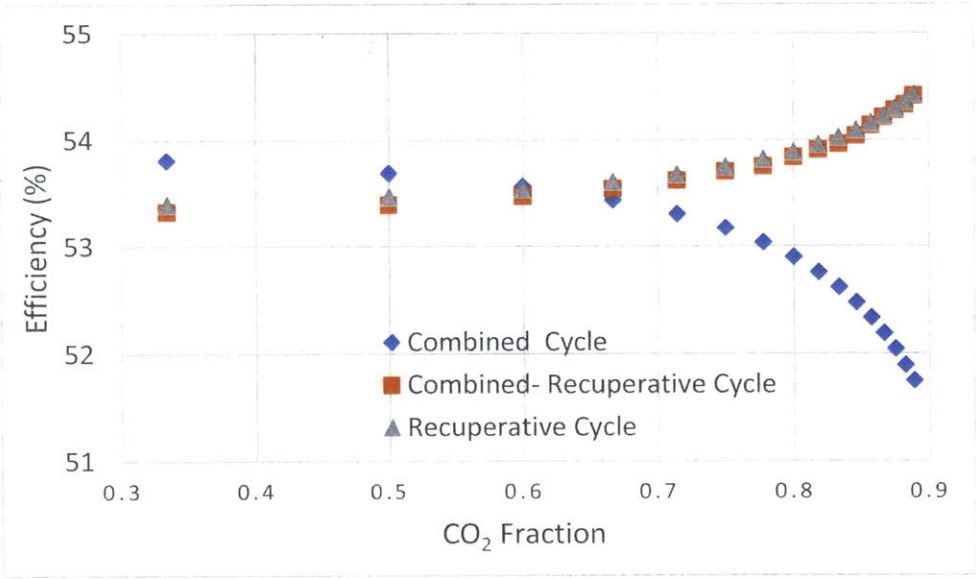

Figure 3-17: Comparing the impact of feed stream CO_2 fraction on efficiency for combined, recuperative and combined-recuperative CLC cycle configurations.

3.4.2. Purge steam generation strategy

Purge steam is required in the rotary reactor to avoid gas leakage between the reduction (fuel) and the oxidation (air) zones of the rotary reactor. Nonetheless, providing purge steam for the reactor purging could constitute a net parasitic power demand on the system. For this reason, care has to be taken in selecting the optimal amount of, as well as the least costly approach to, steam generation. Depending on the cycle configuration, there are a number of options for generating the required purge steam. These include direct steam generation from the air and fuel-side recuperative heat exchangers, and steam extraction from the air and fuel-side steam cycles. The strategy adopted

affects the overall efficiency of the system. To illustrate this, each of the cycles are simulated with steam supplied entirely from the air-side or fuel-side cycle. Figure 3-18 presents the efficiency obtained for each case. The efficiency for the recuperative and the combined-recuperative configurations drop when steam generation is switched from the fuel-side to the air-side cycle while that for the combined-CLC cycle does not change much. To understand why this happens, consider the fuel-side recuperator temperature-duty profile in Figure 3-19a and Figure 3-19b. In Figure 3-19a, the fuel-side recuperator is used to generate steam and the profile shows that the heat recovery process is efficient. Figure 3-19b shows the profile for the same exchanger when there is only fuel preheating and no steam generation. In this case, the thermal capacity of the hot exhaust stream is significantly higher than that of the cold fuel inlet stream. This creates an unbalanced heat exchanger with hot side pinch and substantial sensible enthalpy loss to the environment. Thus, there is a greater opportunity for exhaust enthalpy recovery on the fuel side, which can be exploited by generating all the purging steam from corresponding recuperative heat exchanger.

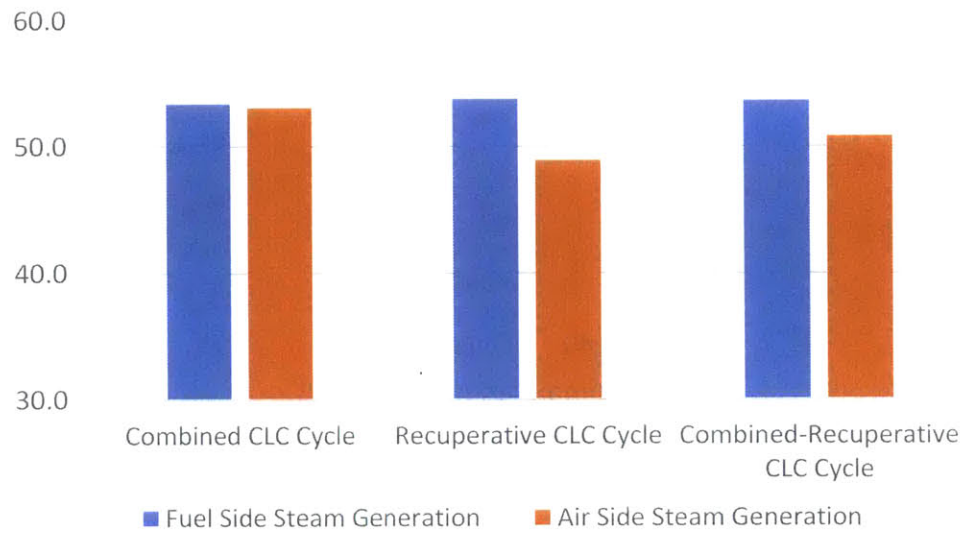

Figure 3-18: Impact of steam generation strategy.
Choice of steam generation strategy could impact efficiency by as much as 2% points for the recuperative cycles. The combined cycle is much less sensitive. Results obtained at $\pi = 10$ and 1.5 kmol/sec steam demand.

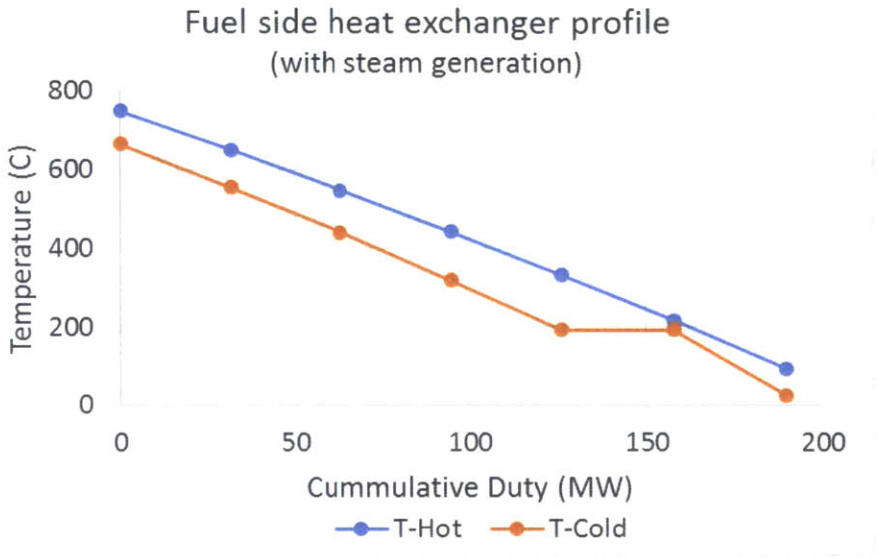

a

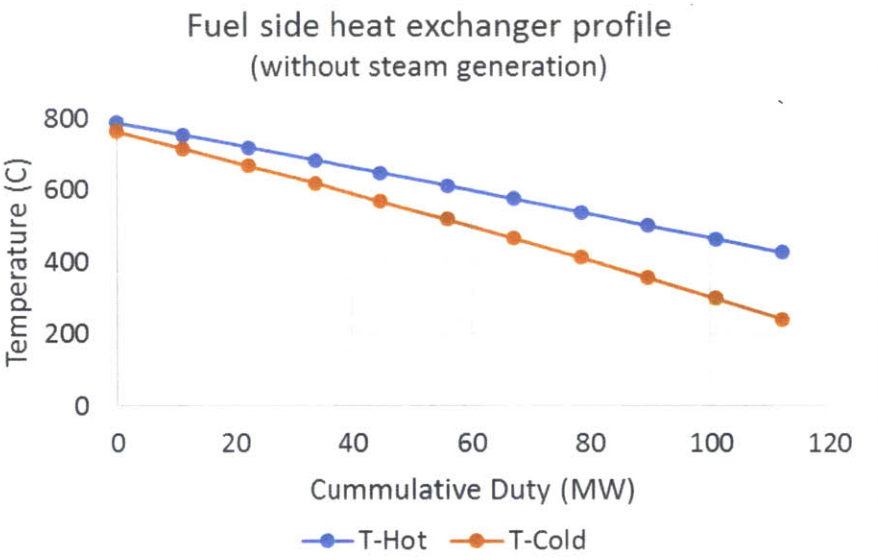

b

Figure 3-19: Fuel side recuperator temperature profile for the combined-recuperative CLC cycle configuration.
(a) With steam generation– shows substantial exhaust heat recovery; (b) Without steam generation – shows significant exhaust sensible heat lost to the environment

3.4.3. Purge steam generation requirement

Figure 3-20 illustrates the sensitivity of cycle efficiency to the required amount of purge steam generation for the three cycle configurations. The net effect of steam addition is a balance between the energetic cost of producing steam, the additional power output from increased exhaust flow and the resulting change in exhaust heat recovery. Steam generation constitutes a net efficiency penalty for the combined cycle in the range considered because the steam is extracted from an intermediate pressure turbine in the steam cycle instead of being further expanded to produce more power. For the recuperative and the combined-recuperative cycles, the net effect is positive up to about twice the fuel flow rate because in this range, generating steam also improves exhaust heat recovery. Beyond this point, additional steam generation deteriorates exhaust heat recovery; the energetic cost of steam generation becomes dominant and the net impact on efficiency is negative. This impact is more dramatic for the recuperative cycle because the combined-recuperative cycle can extract additional steam from the steam cycle, which at this point has become less costly than additional steam production in the recuperator.

Purge steam demand depends primarily on the reactor temperature, pressure and oxygen carrier type. Highly reactive oxygen carriers like nickel need smaller purge steam flow while oxygen carriers with slower reduction reaction rate like iron have much higher purge steam demand. For example, considering the rotary reactor simulation results from Zhao et al. [29], a particular design for a nickel-based rotary reactor at 10 bar and 1180C can achieve ~99% CO_2 separation efficiency steam demand at a little over twice the fuel flow rate while an iron-based reactor could require 6 x the fuel flow rate. Therefore, steam generation requirement should be an important oxygen carrier selection criteria, given the potential impact on cycle efficiency. The optimal efficiency map in Figure 3-21 presents a summary of the key results from the preceding parametric analysis.

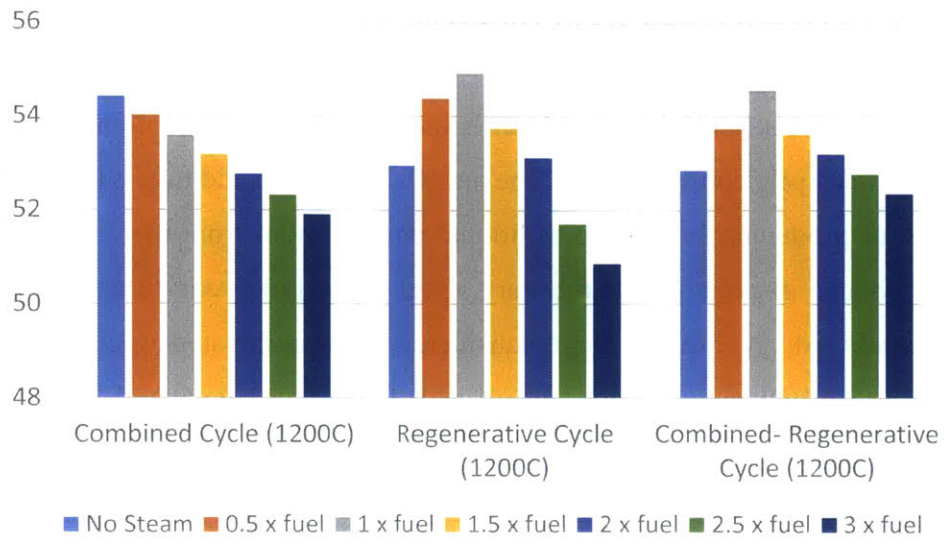

Figure 3-20: Impact of purge steam demand on efficiency.
The effect of purge steam generation on efficiency is mostly a balance between steam generation energy penalty, additional work output from larger exhaust flow and change in exhaust enthalpy recovery. This balance is also a function of the required steam flow rate. Results obtained at $\pi = 10$; fuel flow is 1kmol/sec.

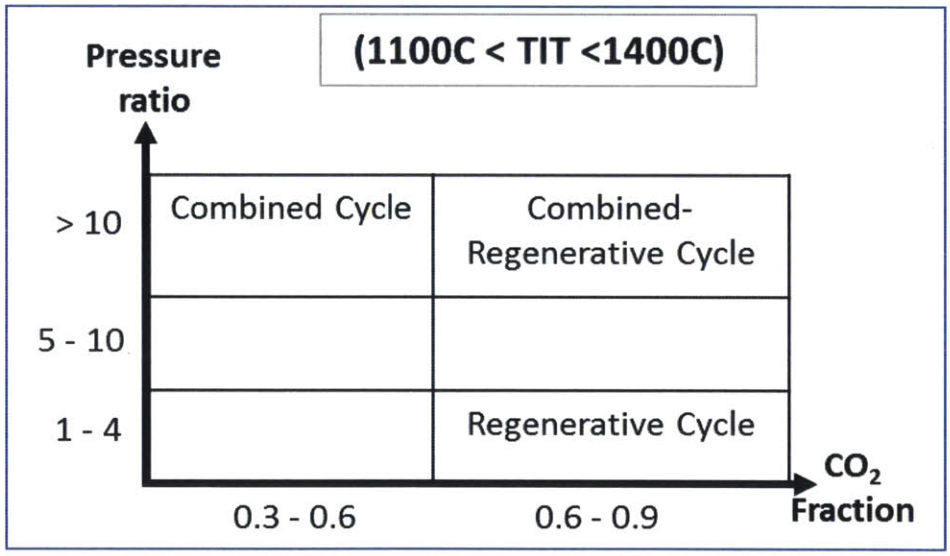

Figure 3-21: Optimal efficiency map summarizing the results from the parametric analysis.

3.5. Summary

In this study, the integration of the thermally coupled redox rotary reactor with energy conversion systems was examined in some detail. Conceptual and more detailed thermodynamic analyses demonstrate that the thermally balanced reactor operation creates the potential for higher cycle efficiencies. This potential, however, can only be actualized by high efficiency cycle configurations that are capable of exploiting the resulting increase in the reduction reactor exhaust enthalpy. Therefore, the recuperative, combined and hybrid combined-recuperative cycles are the recommended configurations for integration with the rotary reactor.

The key design and operating parameters that define system performance include allowable turbine inlet temperature, compressor pressure ratio and feed stream CO_2 fraction. An analysis of the sensitivity of cycle thermal efficiency to these parameters is used to map out the optimal performance region for each configuration. Of the three configurations compared, the recuperative cycle has the highest efficiency in the parameter space covered in this study. Another advantage of the recuperative cycle over the combined cycle is that the recuperators provide a means for sufficiently preheating the reactor inlet streams. Higher reactor inlet stream temperatures support faster reactions and minimize temperature gradients in the reactor; faster reactions mean smaller reactors while low temperature gradients minimize thermal stresses and improve operational stability. The main drawback for the recuperative cycle is that its optimal operating point is at a low pressure ratio. This means larger recuperators, and other equipment to handle the large volumetric gas flows. The combined-recuperative cycle offers a useful tradeoff; like the recuperative cycle, the fuel-side recuperator preheats the inlet fuel stream; since the oxidation reaction with nickel is highly exothermic, the inlet air stream is quickly heated up and does not significantly disrupt the thermal profile in the reactor; it operates optimally at elevated pressures and so, unlike the recuperative cycle, does not need to handle excessively large volumetric flows; finally, it can support larger purge steam demands with lower associated energy penalty than the other CLC cycles.

Another important factor to consider in rotary reactor-based system design is the purge steam generation strategy. The impact of the rotary reactor purge steam on efficiency depends on the amount of steam required and on the steam generation strategy. Purging steam requirement

depends on the type of oxygen carrier. Oxygen carriers with fast reduction reactions like nickel have lower purging steam requirements. Low purge steam requirement can increase efficiency in recuperative and combined-recuperative CLC cycles when it provides a means for improved exhaust heat recovery. It constitutes an energetic penalty when the purge steam has to be extracted from a steam turbine, like in the case for a combined CLC cycle. This makes purge steam demand is a very important criteria for selecting oxygen carriers, specifying optimal reactor design parameters and choosing an appropriate cycle configuration.

3.6. Appendices

3.6.1. Appendix 3A

$$T_{1f} = T_{1a} = T_1 \quad \text{(i)}$$

$$T_{ox} = T_{3a} \quad \text{(ii)}$$

$$T_{red} = T_{3f} \quad \text{(iii)}$$

A schematic representation of the simple Brayton CLC cycle is shown in Figure 3-1. Applying energy balance to the air-side components, fuel-side components and the reactor gives

Air Side Balance:

$$W_{Ba} = W_{turb_a} + W_{comp_a} = m_a c_{pa} T_1 \frac{(\pi^{\alpha}-1)}{\eta_c}\left(1 - \frac{\beta_a \eta_T \eta_c}{\pi^{\alpha}}\right) \quad \text{(3-A1)}$$

Fuel Side Balance

$$W_{Bf} = W_{turb_f} + W_{comp_f} = m_f c_{pf} T_1 \frac{(\pi^{\alpha}-1)}{\eta_c}\left(1 - \frac{\beta_a \eta_T \eta_c}{\pi^{\alpha}}\left(\frac{T_{red}}{T_{ox}}\right)\right) \quad \text{(3-A2)}$$

Reactor Balance:

$$m_a = \frac{Q\eta_c - m_f c_{pf} T_1 \left(\beta_a \eta_c \left(\frac{T_{red}}{T_{ox}}\right) - \pi^{\alpha} + 1 - \eta_c\right)}{c_{pa} T_1 \left(\beta_a \eta_c - \pi^{\alpha} + 1 - \eta_c\right)} \quad \text{(3-A3)}$$

Therefore, the efficiency of the system is given by

$$\eta = -\frac{W_{Ba} + W_{Bf}}{Q}$$

$$= \frac{\pi^{\alpha}-1}{\pi^{\alpha}}\left(\frac{\beta_a \eta_T \eta_c - \pi^{\alpha}}{\beta_a \eta_c - \pi^{\alpha} + 1 - \eta_c}\right) - \frac{\pi^{\alpha}-1}{Q\eta_c \pi^{\alpha}}\left(\frac{m_f c_{pf} T_1 \beta_a}{\beta_a \eta_c - \pi^{\alpha} + 1 - \eta_c}\right)\left(\eta_T \eta_c (1-\eta_c) + \eta_c \pi^{\alpha}(1-\eta_T)\right)\left(1 - \left(\frac{T_{red}}{T_{ox}}\right)\right) \quad \text{(3-A4)}$$

For the ideal case where $\eta_c = \eta_T = 1$, equation 3-A4 reduces to the classical expression for the ideal Brayton cycle efficiency

$$\eta = \frac{\pi^{\alpha}-1}{\pi^{\alpha}} \quad \text{(3-A5)}$$

3.6.2. Appendix 3B

$$T_{1f} = T_{1a} = T_1 \quad \text{(i)}$$

$$T_{ox} = T_{2a} \quad \text{(ii)}$$

$$T_{red} = T_{2f} \quad \text{(iii)}$$

A schematic representation of the simple Steam CLC cycle and the thermodynamic representation of the Rankine engine is shown in Figure 3-3. Applying the laws of thermodynamics to the air-side components, fuel-side components and the reactor gives

Air Side Balance

$$-W_{Sa} = m_a c_{pa} T_1 \eta_{sa} (\beta_a - 1 - \ln(\beta_a)) \quad \text{(3-B1)}$$

Fuel Side Balance

$$-W_{Sf} = m_f c_{pf} T_1 \eta_{sf} \left(\beta_a \left(\frac{T_{red}}{T_{ox}}\right) - 1 - \ln\left(\beta_a \left(\frac{T_{red}}{T_{ox}}\right)\right)\right) \quad \text{(3-B2)}$$

Reactor Balance

$$m_a = \frac{Q - m_f c_{pf} T_1 \left(\beta_a \left(\frac{T_{red}}{T_{ox}}\right) - 1\right)}{c_{pa} T_1 (\beta_a - 1)} \quad \text{(3-B3)}$$

Therefore, the efficiency of the system is given by

$$\eta = -\frac{W_{Sa} + W_{Sf}}{Q}$$

$$= \eta_{2sa}\left(1 - \frac{\ln(\beta_a)}{\beta_a - 1}\right) + \frac{m_f c_{pf} T_1}{Q}\left(\beta_a \frac{T_{red}}{T_{ox}} - 1\right)\left(\eta_{2sf}\left(1 - \frac{\ln\left(\beta_a \frac{T_{red}}{T_{ox}}\right)}{\beta_a \frac{T_{red}}{T_{ox}} - 1}\right) - \eta_{2sa}\left(1 - \frac{\ln(\beta_a)}{\beta_a - 1}\right)\right) \tag{3-B4}$$

The approximate steam cycle 2nd law efficiencies can be defined such that

$$\eta_{2sa}\left(1 - \frac{T_1}{T_{ox}}\right) = 1 - \frac{T_1}{T_{sa}} \tag{3-B5}$$

$$\eta_{2sf}\left(1 - \frac{T_1}{T_{red}}\right) = 1 - \frac{T_1}{T_{sf}} \tag{3-B6}$$

Assuming that $T_{sa} = \varepsilon T_{ox}$ and $T_{sf} = \varepsilon T_{ox}$ for $0 < \varepsilon \leq 1$ and $\beta_a \geq 1$, then

$$\eta_{2sa} = \frac{\varepsilon\beta_a - 1}{\varepsilon(\beta_a - 1)} \tag{3-B7}$$

$$\eta_{2sf} = \frac{\varepsilon\beta_a\left(\frac{T_{red}}{T_{ox}}\right) - 1}{\varepsilon\left(\beta_a\left(\frac{T_{red}}{T_{ox}}\right) - 1\right)} \tag{3-B8}$$

Assuming ideal process ($\eta_{sa} = \eta_{sf} = 1$), equation 3-B4 reduces to

$$\eta = 1 - \frac{Ln\beta_a}{\beta_a - 1} + \left(\frac{m_f c_{pf} T_1}{Q}\right)\left(\frac{\beta_a Ln\beta_a}{\beta_a - 1}\left(\left(\frac{T_{red}}{T_{ox}}\right) - 1\right) - Ln\left(\frac{T_{red}}{T_{ox}}\right)\right) \tag{3-B9}$$

For a thermally balanced reactor $\left(\frac{T_{red}}{T_{ox}} = 1\right)$, equation 3-B9 simplifies to the classical expression for an ideal steam cycle power plant efficiency

$$\eta = 1 - \frac{Ln\beta_a}{\beta_a - 1} \tag{3-B10}$$

3.6.3. Appendix 3C

$$T_{1f} = T_{1a} = T_1 \quad \text{(i)}$$

$$T_{ox} = T_{3a} \quad \text{(ii)}$$

$$T_{red} = T_{3f} \quad \text{(iii)}$$

A schematic representation of the combined CLC cycle is shown in Figure 3-5. It can be seen that the efficiency of the combined cycle is the sum of components from the Brayton cycle and the bottoming steam (Rankine) cycle. Therefore,

$$\eta = -\frac{(W_{Ba}+W_{Bf})+(W'_{Sa}+W'_{Sf})}{Q} \quad \text{(3-C1)}$$

Similar to equation 3-A8

$$\frac{(W_{Ba}+W_{Bf})}{Q} = \frac{\pi^{\alpha}-1}{\pi^{\alpha}}\left(\frac{\beta_a\eta_T\eta_c-\pi^{\alpha}}{\beta_a\eta_c-\pi^{\alpha}+1-\eta_c}\right)-\frac{\pi^{\alpha}-1}{Q\eta_c\pi^{\alpha}}\left(\frac{m_f c_{pf}T_1\beta_a}{\beta_a\eta_c-\pi^{\alpha}+1-\eta_c}\right)\left(\eta_T\eta_c(1-\eta_c)+\eta_c\pi^{\alpha}(1-\eta_T)\right)\left(1-\left(\frac{T_{red}}{T_{ox}}\right)\right) \quad \text{(3-C2)}$$

Similar to equation 3-B4,

$$\frac{(W'_{Sa}+W'_{Sf})}{Q} = \eta'_{sa}\left(1-\frac{\ln(\beta'_a)}{\beta'_a-1}\right)+\frac{m_f c_{pf}T_1}{Q}\left(\beta'_a\frac{T_{red}}{T_{ox}}-1\right)\left(\eta_{sf}\left(1-\frac{\ln\left(\beta'_a\frac{T_{red}}{T_{ox}}\right)}{\beta'_a\frac{T_{red}}{T_{ox}}-1}\right)-\eta'_{sa}\left(1-\frac{\ln(\beta'_a)}{\beta'_a-1}\right)\right) \quad \text{(3-C3)}$$

Where

$$\beta'_a = \beta_a(1-\eta_T+\eta_T\pi^{-\alpha}) \quad \text{(3-C4)}$$

Equation 3-C4 captures the fact that the hot gas inlet temperature to the steam cycle HRSG is the turbine exhaust temperature and not the reactor exhaust, as in the case for the simple steam cycle. Thus,

$$\eta'_{2sa} = \frac{\varepsilon\beta'_a-1}{\varepsilon(\beta'_a-1)} \quad \text{(3-C5)}$$

$$\eta'_{2sf} = \frac{\varepsilon\beta'_a\left(\frac{T_{red}}{T_{ox}}\right)-1}{\varepsilon\left(\beta'_a\left(\frac{T_{red}}{T_{ox}}\right)-1\right)} \quad \text{(3-C6)}$$

For an ideal process($\eta'_{2sa} = \eta'_{2sf} = \eta_c = \eta_T = 1$), equation 3-C1 simplifies to

$$\eta = 1 - \frac{Ln\left(\frac{\beta_a}{\pi^\alpha}\right)}{\beta_a - \pi^\alpha} + \frac{m_f c_{pf} T_1}{Q}\left[\frac{\beta_a Ln\left(\frac{\beta_a}{\pi^\alpha}\right)}{\beta_a - \pi^\alpha}\left(\left(\frac{T_{red}}{T_{ox}}\right) - 1\right) - Ln\left(\frac{T_{red}}{T_{ox}}\right)\right] \quad \text{(3-C7)}$$

For a thermally balanced reactor $\left(\frac{T_{red}}{T_{ox}} = 1\right)$, equation 3-C7 simplifies to the following expression for an ideal combined cycle power plant efficiency

$$\eta = 1 - \left(\frac{Ln\left(\frac{T_{ox}}{T_1 \pi^\alpha}\right)}{\left(\frac{T_{ox}}{T_1}\right) - \pi^\alpha}\right) \quad \text{(3-C8)}$$

4. Reduced fidelity chemical looping combustion reactor model

4.1. Introduction

Zhao et al. [4], [27]–[29] presented a one-dimensional model that simulates the periodic performance of the rotary reactor by analyzing a single channel. The basis for this approach follows from the fact that the entire drum moves at a constant angular velocity and thus, each individual channel experiences identical cyclic conditions. They demonstrated the feasibility of continuous reactor operation with complete fuel conversion and very high CO_2 separation for copper, nickel and iron-based oxygen carriers. Though appropriate for simulating reactor performance, this detailed model is computationally expensive for studies like parametric and uncertainty analyses or optimization studies that require multiple model evaluations, especially when a high level of accuracy is not essential. In addition, it is not very practical to integrate it with a system model; this is particularly important because one of the primary objectives of the rotary reactor development effort is to assess its integration in an energy conversion system.

In this chapter, a reduced fidelity model of the rotary reactor that significantly reduces the computational cost of the model evaluation while achieving relatively accurate reactor design predictions is described. A unique feature of this reduced model is that it also has a structure that enables it to find an optimal combination of reactor specification parameters that satisfy design and operating requirements. A detailed discussion of the development of the model, validation results as well as results from further analysis using the reduced model are also presented.

Section 4.2, discusses the methodology for developing the reduced rotary reactor model, starting with a summary of the detailed reference model of Zhao et al. and proceeding to cover the simplifying assumptions, model formulation and implementation. The section ends by validating the reduced model and comparing the required computational cost against that of the detailed model. Next, a reactor optimization study is presented in section 4.3 and the analysis is extended to study cases that illustrate various optimization and design applications of the reduced model.

Section 4.4 then uses the reduced model to perform parametric analysis on the rotary reactor in order to determine the sensitivity of the optimal reactor design to selected operating and kinetic parameters. Section 4.5 concludes this discussion.

4.2. Reduced fidelity reactor model (RFM)

4.2.1. Motivation

The objective for developing the reduced fidelity model (RFM) for the rotary reactor is to reduce the complexity and cost of evaluating the higher dimensional detailed model while maintaining reasonable predictive accuracy. This is especially useful for reactor optimization and sensitivity analysis, where the computational cost of using the detailed model will be too high. It is also ideal for system level studies where the reactor represents a single component in the integrated energy conversion system, and the detailed resolution of the internal thermodynamic state of the reactor is unnecessary.

Besides these primary motivations, there are other advantages that the reduced model presented in this work offers, compared to either the detailed reactor model or the simple equilibrium model used in the system level studies of chapters 2 and 3. For the detailed rotary reactor model, reactor design parameters such as diameter and sector sizes are determined manually for given operating conditions, whereas the proposed reduced model can automatically determine these values following an internal optimization logic. When integrated with a power generation cycle, the reduced model captures important feedback interactions that impact overall performance - like actual purge steam demand - which elude the simpler equilibrium reactor model.

To maintain predictive integrity, it must be ensured that the model reduction strategy adequately represents important linear and non-linear characteristics of the original model. Therefore, the RFM strategy described in this section combines a good grasp of the underlying physics, order of magnitude approximations, and insights from the detailed model predictions, to develop an approximation that satisfies the rotary reactor design objectives.

4.2.2. Detailed (reference) reactor model

Zhao et al. simulated the periodic stationary state performance of the rotary reactor using a one-dimensional plug flow model of a single channel [27], [29]. Since the entire reactor drum moves with the same angular velocity, each channel experiences an identical sequence of events as it moves across the different sectors. Therefore, the model solves for the reactive flow within one channel, with changing inlet conditions marking the transitions between the different sectors. For every point along the channel, the model solves 1-D mass and energy conservation equations for gas and solid phases and predicts the cyclic stationary state axial profiles for the gas phase compositions, oxygen carrier conversion, gas and solid temperature at each time step.

In this model, kinetic parameter values proposed by Abad et al. [5] were used to describe the heterogeneous reactions. These parameters were obtained from analysis of thermogravimetric measurements for temperatures ranging from 773K – 1073K for copper and 873 to 1223K for iron and nickel. The studied pressure range covered atmospheric to 30 bars [5], [49], [50]. The values of these parameters for copper, nickel and iron can be found in Table 4.1. Given the channel aspect ratio, plug flow was assumed within each channel; axial diffusion resistance, radiation heat transfer and pressure drop were neglected. The solid phase was modeled as a dense fin with uniform temperature at each cross-section and the thermal properties of the bulk support layer were used for solid energy balance since the porous OC layer is much thinner than the support layer.

Table 4.1: Oxygen carrier properties

Oxygen Carrier	CuO/Cu		NiO/Ni		Fe_2O_3/Fe_3O_4	
	Oxidation	Reduction	Oxidation	Reduction	Oxidation	Reduction
Melting point	1446C / 1085C		1955C / 1455C		1565C / 1597C	
Apparent density $kg\ m^{-3}$	1800		3446		3257	
Porosity	0.57		0.36		0.3	
Rate constant	$2.04\ x\ 10^4$	$1.13\ x\ 10^6$	$9.31\ x\ 10^3$	$3.09\ x\ 10^6$	$3.58\ x\ 10^3$	$9.23\ x\ 10^3$

$K_0 m^{3n-3} mol^{1-n} s^{-1}$						
Reaction order, n	1	0,4	0.2	0.8	1	1.3
Pressure coefficient, a	0.68	0.83	0.46	0.93	0.84	1.03
Activation energy, E $KJ\ mol^{-1}$	15	60	7	78	14	49
Reactions						
Reduction			Oxidation			
$CH_4 + 4CuO \rightarrow CO_2 + 2H_2O + 4Cu$ $CH_4 + 4NiO \rightarrow CO_2 + 2H_2O + 4Ni$ $CH_4 + 12Fe_2O_3 \rightarrow CO_2 + 2H_2O + 8Fe_3O_4$			$O_2 + 2Cu \rightarrow 2CuO$ $O_2 + 2Ni \rightarrow 2NiO$ $O_2 + 4Fe_3O_4 \rightarrow 6Fe_2O_3$			

The ensuing one dimensional plug-flow reference model solves the species and energy conservation equations for an individual channel as it traverses a complete cycle. The governing equations are described in equations 4.1-4.4.

Energy balance (gas)

$$A_c \frac{\partial \hat{E}}{\partial t} + A_c \frac{\partial (uH)}{\partial z} = P_c h(T_s - T_g) + \sum_i P_c \hat{h}_{s,i} \omega_{i,j} \quad (4.1)$$

Energy balance (solid)

$$A_s \frac{\partial \hat{E}_s}{\partial t} = A_s \frac{\partial}{\partial z}\left(k_s \frac{\partial T_s}{\partial z}\right) - P_c h(T_s - T_g) - \sum_i P_c \hat{h}_{s,i} \hat{\omega}_{i,j} \quad (4.2)$$

Species balance (solid)

$$A_{oc} \frac{\partial [(1-\varepsilon_g) C_{oc,j}]}{\partial t} = P_c \hat{\omega}_{oc,j} \quad (4.3)$$

Species balance (gas):

$$A_p C_{tot} \frac{\partial x_i}{\partial t} + A_p C_{tot} \frac{\partial (u x_i)}{\partial z} = P_c \hat{\omega}_{i,j} \; i = CH_4, CO_2, H_2O, \; j = reduction/oxidation \quad (4.4)$$

Here, the total concentration, $C_{tot} = \frac{P}{RT}$ (ideal gas law); $P, R, T_g, T_s, u, \widehat{\omega}, and\ x$ are the pressure, universal gas constant, gas temperature, solid temperature, gas velocity, conversion rate for gas species and species mole fraction. $P_c, C_{oc,j}, \hat{h}_{s,i}\ and\ \widehat{\omega}_{oc,j}$ are the channel perimeter, oxygen carrier molar concentration, molar enthalpy of species i, and oxygen carrier conversion rate. $A_c, A_s, and\ A_{oc}$ are respectively the channel, bulk support and oxygen carrier cross-sectional areas while ε_g defines the porosity of the oxygen carrier layer. Oxygen carrier oxidation takes place in the air sector while reduction takes place in the fuel and fuel purge sectors. The purge steam velocity in the fuel purge sector is determined to allow sufficient time for conversion of fuel carried over from the fuel sector. The simulation runs for repeated cycles until it arrives to a periodic stationary state. Simulation results validated the applicability of the rotary design to the CLC process with high conversion and separation efficiency, as shown in Table 4.2.

Table 4.2: Detailed (reference) reactor model predictions

Oxygen Carrier	CuO/Cu	NiO/Ni	Fe_2O_3/Fe_3O_4
Fuel conversion (%)	100	100	99.1
Location of 99% conversion (m)	0.7	0.49	1.44
Carbon separation efficiency (%)	98.06	100	96.89
Operating pressure	10 bar		

However, this model requires several repeated cycles before the periodic stationary state performance is achieved. For instance, the computational effort ranged from 200 to 500 cycles for the different oxygen carriers, with each cycle requiring about 500 CPU seconds. Though adequate for detailed simulation of the rotary reactor performance, it is less suited for analysis that involve multiple runs to study the reactor response to a range of parameter variations, particularly when these studies can trade some accuracy for quicker design predictions. In addition, both the setup and the computational cost of the detailed reactor model make it unsuitable for integration with steady state flow sheet models used for overall system sizing and analysis.

4.2.3. Reduced model formulation

The reduced fidelity model replaces the detailed cyclic stationary state (reference) model with a simplified quasi-steady state approximation that determines design variables/parameters that meet key rotary reactor design criteria and requirements while satisfying conservation principles using adequate approximations. The primary design and operational variables that specify the rotary reactor include the sector sizes, feed stream velocities, cycle period (rotational speed) of the reactor drum, reactor diameter and channel length for complete fuel conversion, as given in equation 4.5 and illustrated in Figure 4-1.

$$x = \left[\theta_i,\ u_i, l, D, T\left(\frac{1}{\omega}\right)\right] \tag{4.5}$$

Where θ_i = sector size, u_i = sector feed gas velocity, l = reactor channel length, D = reactor diameter, T = cycle period, ω = reactor drum rotational speed, i = fuel, fuel purge, air and air purge sectors

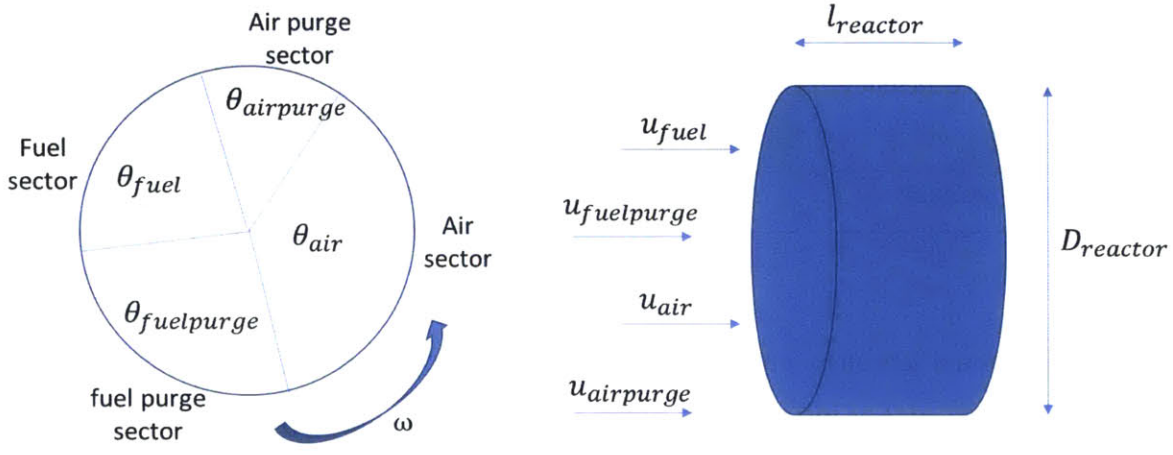

Figure 4-1: Reactor design variables.

4.2.3.1. Simplifying assumptions

To simplify the governing energy and species equations, insights from analyzing predictions from the detailed model are applied. The primary model reduction assumptions are listed below:

I. Reactor is adiabatic with negligible pressure drop
II. The reactor operates at cyclic stationary state; a steady state approximation is assumed for all the governing equations
III. There is gas-solid thermal equilibrium in each channel; a single average temperature is assumed for the gas and solid at any point within the reactor channel
IV. There is no temperature fluctuation between the different sectors; the solid temperature is uniform in the radial and circumferential directions across all sectors of the reactor
V. The reactor channel axial temperature distribution can be approximated by a quadratic profile with appropriate boundary conditions applied
VI. Reactor temperature at inlet is equal to the inlet gas stream temperature

The basis for these assumptions as well as the strategy for applying them are presented in the following discussion.

4.2.3.2. Energy

In the rotary reactor, the high thermal conductivity and heat capacity support layer thermally couples the entire reactor, distributing the heat produced by the exothermic reaction throughout the reactor and to the bulk gas flow. The results in Figure 4-2a and Figure 4-2b, obtained from the detailed model simulation, show that this thermal coupling minimizes local temperature fluctuation as the channel traverses the different reactor sectors [29]. Figure 4-2a also demonstrates that the gas temperature profile closely matches that of the solid. These support assumptions III and IV.

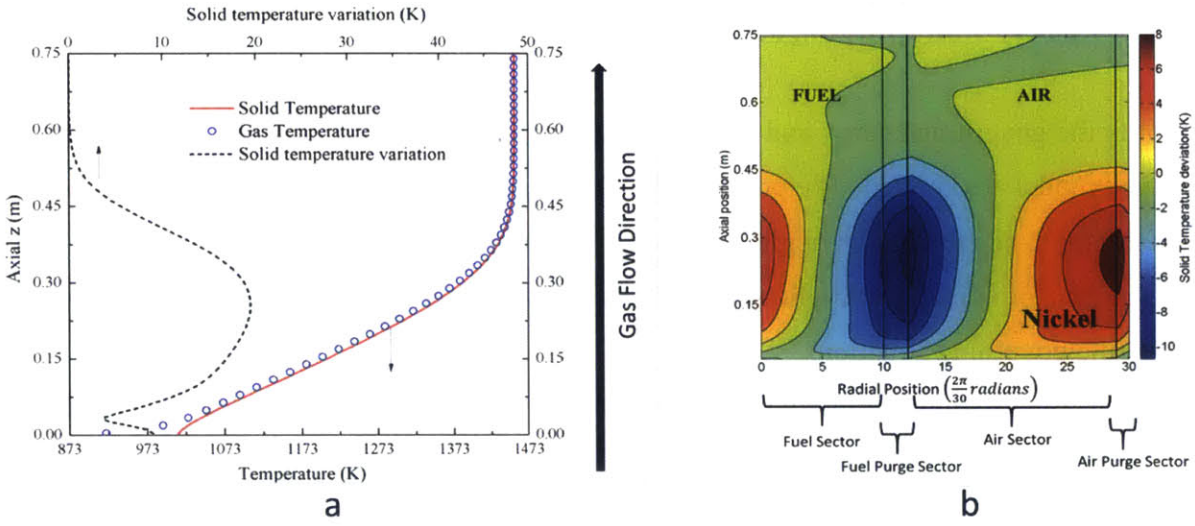

Figure 4-2: Rotary reactor thermal performance plots.
(a) solid-gas equilibrium within the channels; (b) small solid temperature fluctuation across all the sectors of the rotary reactor [29].

Assumptions II, III, IV and V allow the model to be simplified by substituting the numerical solution of the detailed gas and solid energy equations 4.1 and 4.2 with an integral method approximation to solve for the temperature distribution in the reactor channel. The setup for the integral method solution is illustrated in Figure 4-3. It shows a control volume that extends $from\ z = 0\ to\ z = z_{99}$, the location that corresponds to 99% fuel conversion. Based on observations of predicted temperature profiles from the detailed reference model, a quadratic temperature profile for use in the integral approximation is selected, as expressed in equation 4.6

$$T = Ay^2 + By + C \tag{4.6}$$

$$\left[boundary\ conditions: (i) at\ y = 0, T = T_0; (ii) at\ y = 1, \frac{dT}{dy} = 0; (iii) at\ y = 1, T = T_{ad}\right]$$

Here, T = reactor temperature profile, T_0 = inlet temperature, T_{ad} = adiabatic reaction temperature, y = normalized reactor length, A, B, C = constants. Three boundary conditions are stipulated. Since each channel is considered adiabatic, the first two conditions specify that the temperatures at the inlet and exit boundaries correspond to the inlet and the adiabatic combustion temperatures respectively. The third boundary condition specifies that the axial temperature

gradient at the reactor exit is zero. Substituting these boundary conditions and solving, the following channel temperature profile is obtained

$$T = T_0\left(1 + 2\left(\frac{(T_{ad} - T_0)}{T_0}\right)y - \left(\frac{T_{ad} - T_0}{T_0}\right)y^2\right) \tag{4.7}$$

Equation 4.7 can then be integrated to obtain the average channel temperature.

$$T_{av} = \int_0^1 T\, dy = T_{ad} - \frac{T_{ad} - T_0}{3} \tag{4.8}$$

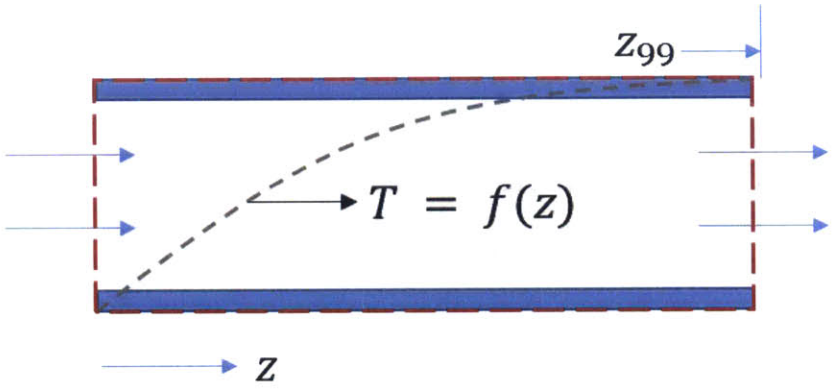

Figure 4-3: Control volume for integral method approximation of the temperature profile.

4.2.3.3. Solid species

The oxygen carrier species equation 4.3 can be reformulated as

$$A_{oc}\frac{\partial}{\partial t}(\varepsilon_s \rho_s X) = P_c \hat{\omega}_{oc,j} \tag{4.9}$$

ε_s is the solid fraction on the porous oxygen carrier layer, X is the fractional oxygen carrier conversion, defined as $X = \frac{C_{oc,oxidized}}{C_{oc,oxidized} + C_{oc,reduced}}$, ρ_s is the oxygen carrier molar density. Therefore

$$\delta_{oc}\varepsilon_s \rho_s \frac{\partial[X]}{\partial t} = \hat{\omega}_{oc,j} \tag{4.10}$$

Here, $\delta_{oc} = \left(\frac{A_{oc}}{P_c}\right)$ is the thickness of the oxygen carrier layer.

Similar to the detailed model, the reaction mechanism used to describe the heterogeneous reactions in this model is derived from the overall one-step kinetics proposed by Abad & Co [5], [49], [50] and based on the unreacted shrinking core model, which assumes a reaction front progressing towards the core of each grain of metal oxide and leaving behind a reacted product layer. The combination of oxygen carrier choice, layer thickness and channel dimension ensures a low Damkohler number process such that it is fair to assume that the active metal/metal oxide is exposed to the bulk species concentration. The resulting oxygen carrier conversion rate is given by

$$\frac{\partial[X]}{\partial t} = \frac{\vartheta_{oc,j}}{\rho_s} k_p C_{i,j}^n |X_0 - X|^\beta \tag{4.11}$$

$k_p = k_0 \left(\frac{P}{P_0}\right)^{-a} e^{-\frac{E}{RT}}$, $C_{i,j}$ is the gaseous reactant i concentration in reaction j, j refers to reduction/oxidation, ρ_s = molar density of the metal/metal oxide grain, ν_{oc} = stoichiometric coefficient of the oxygen carrier, k_0 = Arrhenius constant, n = order of the reaction, X = non-dimensional average oxygen carrier conversion, X_0 = the reference conversion state, β = geometry coefficient that accounts for structural differences in active metal oxide grains in the oxygen carrier, $\left(\frac{P}{P_0}\right)^{-a}$ = pressure inhibition coefficient that captures the effect of pressure on reaction rate, E is the activation energy and R is the universal gas constant.

For the reduction reaction in the fuel and fuel purge sector, $X_0 = 0$, therefore

$$\frac{\partial X}{\partial t} = \frac{\vartheta_{oc,j}}{\rho_s} k_p C_{i,j}^n X^\beta \tag{4.12}$$

While for the oxidation reaction, $X_0 = 1$, and the OC oxidation rate is given by

$$\frac{\partial X}{\partial t} = \frac{\vartheta_{oc,j}}{\rho_s} k_p C_{i,j}^n (1 - X)^\beta \tag{4.13}$$

4.2.3.4. Gas species

Now, for the heterogeneous reaction in the rotary CLC reactor,

$$\frac{\hat{\omega}_{oc,j}}{\vartheta_{oc,j}} = \frac{\hat{\omega}_{i,j}}{\vartheta_i} \tag{4.14}$$

$\vartheta_i, \vartheta_{oc,j}$ are the stoichiometric coefficients for the gas species and oxygen carrier reactants. Substituting 4.10 and 4.11 into 4.14 and rearranging,

$$\frac{\widehat{\omega}_{i,j}}{\vartheta_i} = \frac{\delta_{oc}\varepsilon_s\rho_s}{\vartheta_{oc,j}}\frac{\partial[X]}{\partial t} \tag{4.15}$$

$$\widehat{\omega}_{i,j} = \vartheta_i\delta_{oc}\varepsilon_s\, k_p\, C_{i,j}^n\, |X_0 - X|^\beta \tag{4.16}$$

4.2.3.4.1. Reduction (fuel conversion)

Consider the oxygen carrier reduction reaction of the form

$$C_mH_n + zMeO \rightarrow mCO_2 + \frac{n}{2}H_2O + zMe \tag{4.17}$$

Steady state approximation (assumption I) simplifies gas species balance equation 4.4 to

$$A_pC_{tot}\frac{d(ux_i)}{dz} = P_c\widehat{\omega}_i \tag{4.18}$$

Here, i represents the gas phase species (C_mH_n, CO_2, H_2O) and $\widehat{\omega}_i$ is the species conversion rate for the reduction reaction. The overall mass conservation for the bulk flow can be obtained by summing over the species

$$A_pC_{tot}\frac{du}{dz} = P_c\sum_i\widehat{\omega}_i \tag{4.19}$$

Given that for the gas phase reactant species,

$$\frac{\widehat{\omega}_{C_mH_n}}{\vartheta_{C_mH_n}} = \frac{\widehat{\omega}_{CO_2}}{\vartheta_{CO_2}} = \frac{\widehat{\omega}_{H_2O}}{\vartheta_{H_2O}} \tag{4.20}$$

The conversion rates for CO_2 and H_2O in terms of the fuel, C_mH_n can be expressed as

$$\widehat{\omega}_{CO_2} = \left(\frac{\vartheta_{CO_2}}{\vartheta_{C_mH_n}}\right)\widehat{\omega}_{C_mH_n} \tag{4.21}$$

$$\widehat{\omega}_{H_2O} = \left(\frac{\vartheta_{H_2O}}{\vartheta_{C_mH_n}}\right)\widehat{\omega}_{C_mH_n} \tag{4.22}$$

Substituting 4.17, 4.21 and 4.22 into 4.19

$$A_p C_{tot} \frac{du}{dz} = P_c \hat{\omega}_{c_m H_n} \left(1 + \frac{\vartheta_{CO_2}}{\vartheta_{c_m H_n}} + \frac{\vartheta_{H_2O}}{\vartheta_{c_m H_n}} \right) \tag{4.23}$$

$$\frac{du}{dz} = \frac{P_c}{A_p C_{tot}} \left(1 - m - \frac{n}{2} \right) \hat{\omega}_{c_m H_n} \tag{4.24}$$

Also, for $i = C_m H_n$, from equation 4.18

$$\frac{d(u x_{c_m H_n})}{dz} = \frac{P_c}{A_p C_{tot}} \hat{\omega}_{c_m H_n} \tag{4.25}$$

Multiplying 4.25 by $\left(1 - m - \frac{n}{2} \right)$ and subtracting from 4.24 gives

$$\frac{d}{dz} \left(u \left[1 - \left(1 - m - \frac{n}{2} \right) x_{c_m H_n} \right] \right) = 0 \tag{4.26}$$

Integrating gives

$$u = \frac{\alpha_0}{\left[1 - \left(1 - m - \frac{n}{2} \right) x_{c_m H_n} \right]} \tag{4.27}$$

α_0 is the integration constant. Let $1 - m - \frac{n}{2} = \emptyset$; then applying the following boundary conditions: at inlet, $x_{c_m H_n} = x_{c_m H_n, 0}$; $u = u_0$ to 4.27, the expression for the integration constant can be determined

$$\alpha_0 = u_0 \left[1 - \emptyset \, x_{c_m H_n, 0} \right] \tag{4.28}$$

Substituting 4.28 into 4.27

$$u = \frac{u_0 \left[1 - \emptyset \, x_{c_m H_n, 0} \right]}{\left[1 - \emptyset x_{c_m H_n} \right]} \tag{4.29}$$

Let $w = \frac{1}{\left[1 - \emptyset x_{c_m H_n} \right]}$ (4.30)

Then

$$u = \alpha_0 w \tag{4.31}$$

Substituting 4.31 in the expression in 4.24,

$$\frac{d}{dz}(\alpha_0 w) = \frac{P_c}{A_p C_{tot}} \emptyset \omega_{c_m H_n} \tag{4.32}$$

From 4.16

$$\widehat{\omega}_{c_m H_n} = \vartheta_{c_m H_n} \delta_{oc} \varepsilon_s \, k_p \, C_{c_m H_n}^n \, X^\beta \tag{4.33}$$

Combining 4.32 and 4.33 gives

$$\frac{dw}{dz} = \frac{P_c}{\alpha_0 A_p C_{tot}} \emptyset \left(-\delta_{oc} \varepsilon_s \, k_p \, C_{tot}^n \, x_{c_m H_n}^n \, X^\beta \right) \tag{4.34}$$

From 4.30

$$x_{c_m H_n} = \frac{1-w}{\emptyset w} \tag{4.35}$$

Therefore,

$$\frac{dw}{dz} = \frac{-P_c \delta_{oc} \varepsilon_s \, k_p}{\alpha_0 A_p} C_{tot}^{n-1} \left(\frac{1}{\emptyset}\right)^{n-1} \left(\frac{1-w}{w}\right)^n X^\beta \tag{4.36}$$

$$\left(\frac{w}{1-w}\right)^n dw = \frac{-P_c \delta_{oc} \varepsilon_s \, k_p C_{tot}^{n-1} X^\beta}{\emptyset^{n-1} \alpha_0 A_p} \, dz \tag{4.37}$$

$$\text{Let } \varphi = \frac{-P_c \delta_{oc} \varepsilon_s \, k_p C_{tot}^{n-1} \, X^\beta}{\emptyset^{n-1} \alpha_0 A_p} \tag{4.38}$$

Then

$$\left(\frac{w}{1-w}\right)^n dw = \varphi \, dz \tag{4.39}$$

4.2.3.4.2. Oxidation

The oxygen concentration profile in the channel is required to determine the average oxidation reaction rate defined by equation 4.13. Since the flow time scale is much smaller than the reaction time scale in the air sector as excess air is supplied for thermal regulation, oxygen concentration along the channel in the air sector changes very little and is therefore assumed to have an average value equal to the inlet concentration.

$$C_{O_2} = constant \tag{4.40}$$

4.2.3.5. Design and operating requirements

The reactor design requirements constitute the governing equations for the reduced model. The key requirements include (1) fuel conversion, (2) CO_2 separation, (3) reactor energy balance, (4) oxygen carrier conservation (5) other reactor design specifications.

4.2.3.4.1. Fuel conversion

The primary reactor performance criterion is the extent of fuel conversion at the channel exit. Fuel conversion is controlled by the reduction reaction between the fuel and the metal oxide on the channel wall. This reaction is governed by the local fuel concentration, temperature and the extent of oxygen carrier conversion. Whereas the detailed model solves equation 4.3 and 4.4 to obtain an accurate profile for fuel consumption and oxygen carrier conversion, the reduced model assumes a reactive plug flow with an average oxygen carrier fraction along the channel, which can be solved analytically to approximate fuel conversion in the reactor. To obtain the channel length required for a specified extent of fuel conversion, equation 4.39 is integrated to give

$$z = \frac{1}{\varphi} \int_{w(0)}^{w(z)} \left(\frac{w}{1-w}\right)^n dw \tag{4.41}$$

For example, the channel length required for 99% fuel conversion (z_{99}) will corresponds to $w(z) = 0.99$ and the required length can be obtained by substituting $w(z) = 0.99$ in equation 4.41. Thus, the model's criteria for fuel conversion is that the reactor channel length should be greater than or equal to the length required for 99% conversion. i.e.

$$L_{reactor} \geq (1 + k)\, z_{99} \tag{4.42}$$

Here, k is an adjustable safety factor.

4.2.3.4.2. Carbon separation

To ensure that there is no carry-over of CO_2 from the fuel sector to the air sector, the residual gas inside the channel should be purged with steam as it passes through the fuel purge sector. Similarly, the air purge sector ensures that air does not carry-over from the air sector to the fuel sector. To achieve this separation, the specification for the design and operating parameters should satisfy criterion that channel residence time in the fuel or air purge sectors should be longer than the effective gas residence time in the respective channels. In other words,

$$\int_0^{l_{reactor}} \frac{dz}{u_k} \leq \frac{\theta_k}{\omega} \tag{4.43}$$

where k = fuel purge or air purge sector, ω = angular velocity of rotary drum, θ = sector size, and u = purge steam velocity.

4.2.3.4.3. Energy balance

The energy balance determines the reactor sector flow rates that achieve the specified maximum reactor exit temperature. For the adiabatic reactor, energy balance requires that the difference between the inlet and exit stream enthalpies be equal to zero. This balance is solved to determine the air flow velocity required to achieve the specified exit temperature. In other words

$$\sum n_k \hat{h}_k(T_{in,k}) - \sum n_z \hat{h}_z(T_{ad}) = 0 \tag{4.44}$$

Here n_k = molar flow rate of sector k, a function of sector inlet velocities, k = air, air purge, fuel and fuel purge sectors, n_z = molar flow rate of zone z, z = air and fuel zones, $\hat{h}$ = stream enthalpy, T_{ad} = (adiabatic) reactor exit temperature.

By design, rotary reactor drum is sized by specifying the target thermal size, $\dot{W}_{thermal}$. Thus the reactor should satisfy the following thermal sizing target

$$n_f LHV = \dot{W}_{thermal} \tag{4.45}$$

$$n_f = \theta_{fuel} C_{CH_4 fuel} u_{fuel} (1 - \varepsilon_{solid}) A_{rxt} \tag{4.46}$$

Here n_f = molar fuel flow rate, k = air, air purge, fuel and fuel purge sectors, LHV = lower heating value of the fuel, equivalent to the net reaction enthalpy, ε_{solid} = solid fraction of reactor cross-section, A_{rxt} = reactor cross-sectional area given by $A_{rxt} = \frac{\pi D^2}{4}$ where D is the reactor diameter.

Therefore, the diameter of the rotary reactor can be related to the thermal size by substituting for n_f from 4.46 into 4.45:

$$D^2 = \frac{4\dot{W}_{thermal}}{LHV\, C_{tot}\, x_{fuel}\, u_{fuel}\, \theta_{fuel}(1-\varepsilon_{solid})\, \pi} \tag{4.47}$$

4.2.3.4.4. Oxygen carrier conservation

The relative sizes of the fuel and air sectors are determined primarily by the rates of the oxidation and reduction reactions. For steady state operation, the amount of oxygen carrier reduced in the fuel reactor should not be more than that oxidized in the air sector. Oxygen carrier conversion is equal to the product of rate of the equivalent redox reaction and the time spent in the sector. Thus,

$$\left(\frac{dX}{dt}\right)^{-1}_{reduction}\left(\frac{\theta_{fuel}}{\omega}\right) \leq \left(\frac{dX}{dt}\right)^{-1}_{oxidation}\left(\frac{\theta_{air}}{\omega}\right) \tag{4.48}$$

where $\left(\frac{dX}{dt}\right)_{reduction}$ is derived from equation 4.12 with $j = reduction$ and $\left(\frac{dX}{dt}\right)_{oxidation}$ is derived from equation 4.13 with $j = oxidation$. The inequality accommodates some oxygen carrier reduction that takes place in the fuel purge sector, whose significance depends on the oxygen carrier type as well as the reactor operating condition.

4.2.3.4.5. Reactor design specifications

In general, the sector design should provide sufficient residence time for reduction in the fuel sector, oxidation in the air sector, and gas removal from the channel in the purging sectors. However, the sector sizes should be selected to avoid complete conversion of the oxygen carrier, particularly in the fuel sector where the fuel conversion rate drops significantly as the oxygen carrier approaches a fully reduced state. In addition, residual metal oxide helps mitigate carbon deposition risk in the fuel sector. Consequently, the fuel sector size should satisfy the following condition

$$\frac{\theta_{fuel}}{\omega} \leq \left(\frac{dX}{dt}\right)^{-1}_{reduction} \tag{4.49}$$

where $\left(\frac{dX}{dt}\right)^{-1}_{reduction}$ is the time (in seconds) required for complete reduction of the oxygen carrier, derived from equation 4.12.

Also, since the air flow rate is determined by the energy balance requirement for achieving the specified reactor temperature, a lower-bound condition should be imposed such that the air supply to the reactor is always greater than or equal to the stoichiometric air flow required for the target fuel conversion. Based on the overall fuel conversion reaction

$$C_mH_n \; + \; p(O_2 \; + \; 3.75N_2) \rightarrow mCO_2 \; + \frac{n}{2}H_2O \; + (p - m - \frac{n}{4})O_2 \; + \; 3.75pN_2 \tag{4.50}$$

Stoichiometry will require that the airflow rate be at least 4.75p times the fuel flow rate. In other words,

$$(4.75p)u_{fuel}\theta_{fuel}x_{fuel} \leq \; u_{air}\theta_{air} \tag{4.51}$$

Another important design specification is the fuel purge velocity. Since there is unreacted fuel still in the channel leaving the fuel sector, the purge steam velocity should be such that there is sufficient time for the unreacted fuel to be converted before leaving the channel. For this reason, the fuel purge velocity is specified to be similar to that in the fuel sector to achieve the desired fuel conversion

$$(1 + \lambda)u_{fuel} \; = \; u_{fuelpurge}\,, \;\; \lambda_{min} \leq 0 \leq \; \lambda_{max}, \; |\lambda_{min}\,, \lambda_{max}| \ll 1 \tag{4.52}$$

Here λ is an adjustment factor, which can range from a little below zero to a little above zero. On the other hand, there is no such restriction for the air purge sector. The air purge velocity should simply be enough to flush out all the air from the channel before it enters the fuel sector. It is desirable but not required that the air purge sector inlet velocity be similar to the air sector inlet velocity.

A constraint that requires that the fractional sector sizes sum up to unity is included to ensure a feasible solution for the sector sizes.

$$\sum \theta_i = 1, \qquad i = air, air\ purge, fuel\ \&\ fuel\ purge\ sectors \tag{4.53}$$

4.2.4. Implementation

The reduced fidelity rotary reactor model was implemented for copper, nickel and iron-based oxygen carriers, which are considered among the most promising oxygen carrier choices for CLC applications [51]–[54]. CH_4 was selected as the fuel in this study because of its widespread use in power generation applications. The key physical, chemical and thermodynamic properties of these metal oxides, as well as their redox reaction equations, are summarized in Table 4.1. Relevant reactor design and operating parameters are specified in Table 4.3. To maintain consistency with the reference detailed model, identical values for operating pressure, feed temperatures and diluent gas fractions as in Zhao et al. [29] are used.

Table 4.3: Reactor design and operating parameters

OC	CuO/Cu	NiO/Ni	Fe_2O_3/Fe_3O_4
Size			
Reactor thermal size (MW_{th})	1	1	1
Design			
Oc layer thickness, δ_{oc} (μm)	50	50	50
Channel width, d (mm)	2	2	2
Support layer thickness, δ_{bulk}(mm)	210	210	210
Fuel sector size (%)	50	33	27
Fuel purge sector size (%)	20	7	50
Air sector size (%)	23	57	20
Air purge sector size (%)	7	3	3
Operation			
Inlet temperature, T_{in} (k)	823	823	823
Operating pressure, p (atm)	10	10	10
Fuel sector inlet fuel fraction (vol%)	15	25	50
Fuel sector inlet velocity (m/s)	0.09	0.25	0.07

Fuel purge sector inlet velocity (m/s)	0.11	0.30	0.06
Air sector inlet velocity (m/s)	0.70	1.00	1.00
Air purge sector inlet velocity (m/s)	0.70	1.00	1.20
Cycle period (sec)	30	30	30

The reactor exit temperature for the reduced model is specified as an input parameter and matches the predicted value from the corresponding detailed model. The model is implemented in Matlab®. The thermal properties of the gas mixtures are calculated using correlations from the NIST thermo-physical property database.

4.2.5. Validation

In the preceding section, the formulation for a reduced fidelity model of the rotary CLC reactor, including discussions on the underlying assumptions and model setup was presented. Since the goal of this exercise is to develop a simplified but credible representation of the more detailed model, the predictions of the reduced model are first validated against those of the reference detailed model. The predicted conversion length is used as the basis for comparing the two models.

For the validation study, the reduced model is run with the reactor variables fixed at the reference detailed model values for the three operating pressures (5, 10 and 20 bars) in Zhao et al. [29]. To implement this, the reduced model is modified by adding design constraints of the form in equation 4.54 to the formulation in section 4.2.3.5.

$$x_{i\neq j} - a_{i\neq j} = 0,\ i = reactor\ variable\ indices, j = conversion\ length\ index \qquad (4.54)$$

Here, x = the set of reactor variable parameters (equation 4.5) while a = a corresponding set of fixed parameter values from [29]. For iron and copper, the exact set of the reference parameters from the detailed model were not always feasible in the space defined by the reduced model constraints. This is a consequence of some of the simplifying approximation incorporated in the reduced model and also the fact that unlike the detailed model, the reduced model has a rigid 100% carbon separation requirement. To accommodate this and ensure feasibility, the equality criteria

in 4.54 is relaxed for some parameters, ending up with slightly different input parameter values. The adjusted input parameter values with more than 1% deviation from the reference are listed in Table 4.4.

The validation results are presented in Table 4.5, Figure 4-4, Figure 4-5 and Figure 4-6 for copper, nickel and iron-based oxygen carriers. The conversion length predicted by the reduced model for copper closely follows that of the detailed model, with the difference ranging from 12% at 20 bars to 20 % at 5 bars. The predictions for the nickel-based oxygen carrier match more closely, with a maximum deviation of about 6% at 5 bars. This better prediction suggests that the quadratic profile assumption for the reactor temperature is a very good approximation for nickel-based oxygen carriers. The predictions for iron are also comparable for both models with a maximum deviation of 12% occurring at 5 bar. There are three main factors that account for the differences in prediction between the two models: firstly, where the reduced model uses an averaged reactor temperature, the detailed model uses the more accurate, spatially resolved temperature profile to compute OC conversion within each reactor channel; secondly, there is the contribution from the adjusted input parameters, as indicated in Table 4.4; thirdly, whereas the reduced model designs for 100% carbon separation, this criteria was not strictly required for the detailed model predictions.

Table 4.4: Adjusted input parameters for validation study

Copper						
Pressure (bar)	5		10		20	
	RFM	Detailed	RFM	Detailed	RFM	Detailed
Fuel sector velocity (m/s)	Same		0.093	0.090	0.047	0.045
Fuel purge sector velocity (m/s)	0.199	0.220	0.139	0.110	0.057	0.045
Nickel						
Pressure (bar)	5		10		20	
	RFM	Detailed	RFM	Detailed	RFM	Detailed
Fuel sector velocity (m/s)	Same		Same		0.126	0.130
Iron						

Pressure (bar)	5		10		20	
	RFM	Detailed	RFM	Detailed	RFM	Detailed
Reactor diameter (m)	Same		Same		1.53	1.50
Air sector size (%)	Same		19.1	20.0	16.1	16.7
Air purge sector size (%)	2.7	2.5	4.2	3.3	3.9	3.3
Fuel sector velocity (m/s)	0.140	0.125	Same		Same	
Fuel purge sector velocity (m/s)	0.185	0.123	0.101	0.060	0.048	0.030
Air sector velocity (m/s)	1.26	1.15	0.86	1.00	0.42	0.52

Table 4.5 Comparing predicted results for the reduced and detailed reactor models

Copper						
Pressure (bar)	5		10		20	
	RFM	Detailed	RFM	Detailed	RFM	Detailed
Predicted reactor length (m)	0.59	0.46	0.82	0.7	1.13	1.01
Fuel conversion efficiency (%)	100	100	100	100	100	100
Co_2 separation efficiency (%)	100	100	100	98	100	95
Nickel						
Pressure (bar)	5		10		20	
	RFM	Detailed	RFM	Detailed	RFM	Detailed
Predicted reactor length (m)	0.46	0.4	0.53	0.49	0.61	0.65
Conversion efficiency (%)	100	100	100	100	100	100
Co_2 separation efficiency (%)	100	100	100	100	100	99
Iron						
Pressure (bar)	5		10		20	
	RFM	Detailed	RFM	Detailed	RFM	Detailed
Predicted reactor length (m)	1.48	1.68	1.51	1.44	1.3	1.32
Conversion efficiency (%)	100	99	100	99	97	99
Co_2 separation efficiency (%)	100	96	100	97	100	96

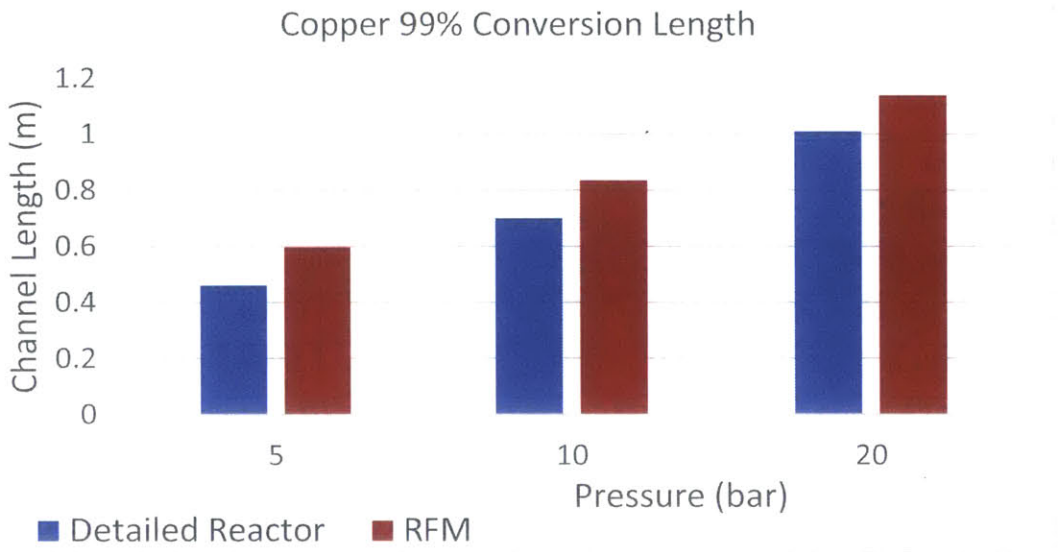

Figure 4-4: Reduced fidelity model validation for copper-based oxygen carrier. Reduced fidelity model prediction closely matches that for the detailed model for copper; notice that the reduced model consistently slightly over-predicts the detailed model.

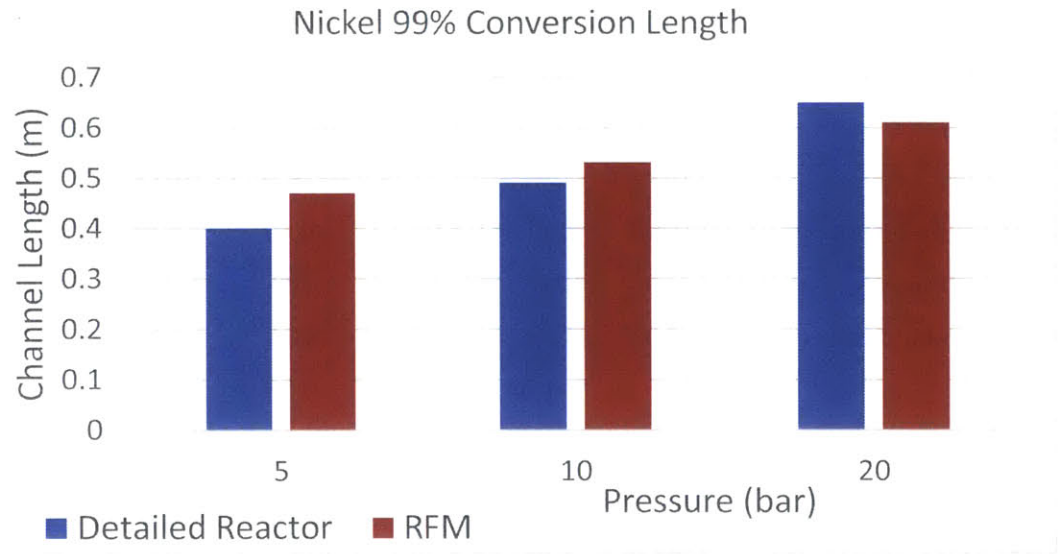

Figure 4-5: Reduced fidelity model validation for nickel-based oxygen carrier. Reduced fidelity model prediction closely matches that for the detailed reactor model for a nickel-based oxygen carrier.

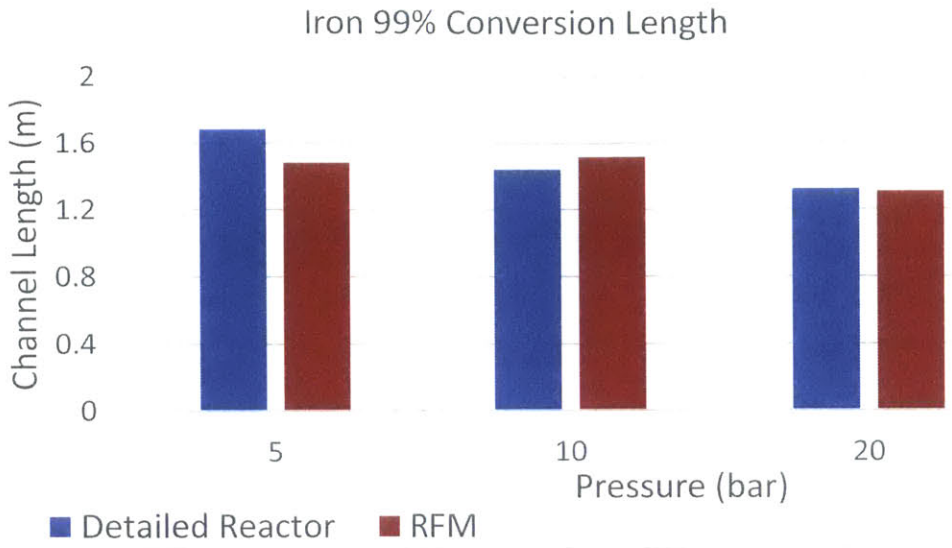

Figure 4-6: Reduced fidelity model validation for iron-based oxygen carrier.
The reduced fidelity model reasonably matches the predictions from the detailed model for iron. The difference between the two model predictions is in part due to the difference in fuel purge feed velocity required to achieve a feasible solution in the reduced model, as shown in Table 4.5.

4.2.6. Computational cost

So far, it has been demonstrated that the performance of the reduced model is comparable to that of the detailed model in representing the rotary reactor at a level of precision adequate for first order, component-level analysis. However, the most interesting feature of the reduced model is that it is able to achieve this degree of accuracy at significantly less computational effort compared to the detailed model. This fact is illustrated using Figure 4-7, which shows that the CPU time required for solving the reduced model is about four orders of magnitude smaller than that for the detailed model. This feature makes the reduced model ideal for parametric studies where multiple evaluations at different design and operating conditions are required, and where there is more tolerance for error.

Besides the significantly lower computational cost, the structure of the reduced model makes it suitable for determining an optimal reactor configuration for any given design objective. It also automates the reactor specification process, replacing the manual approach used in specifying the inputs to the detailed model. As will be shown later in section 4.3.5, the flexibility inherent in the

model structure also means that the model can be setup to deal with a range of design and optimization problems by adding constraints and modifying the objective function as needed.

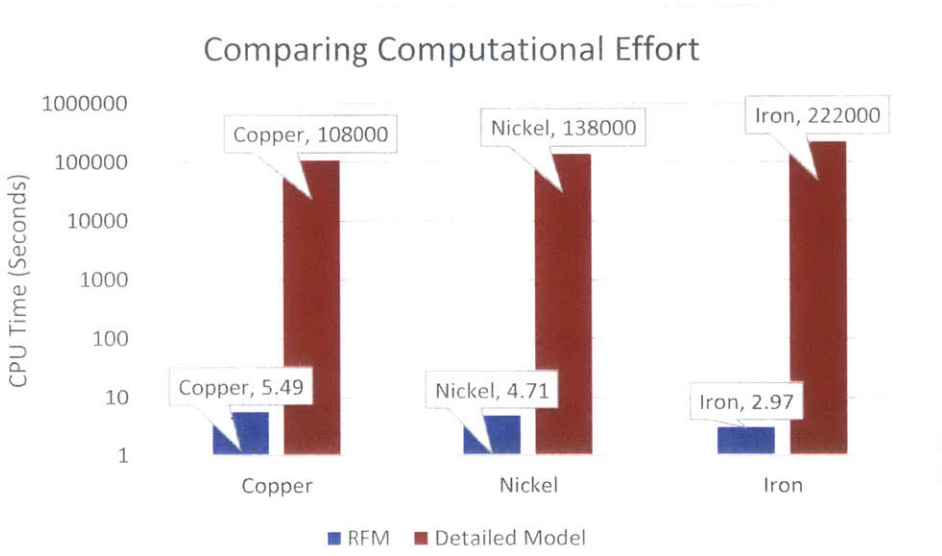

Figure 4-7: Plots comparing CPU time for the reduced and detailed models.
The CPU time required for solving the reduced model is about 4 orders of magnitude smaller than that for the detailed model for all three oxygen carriers. The CPU time axis is presented on a log scale. Results are for a sample case.

4.3. Optimization

4.3.1. Optimization problem structure

The rotary reactor design is specified by variables and parameters connected by physical and geometric relationships which satisfy a set of design requirements, operating requirements and conservation equations. Consequently, the proposed formulation for the reduced fidelity reactor model identifies an optimal combination of these reactor variables and parameters that minimize a defined cost function, where the design and operating requirements are specified as model constraints. Thus the reactor model structure is represented by the following optimization problem:

Minimize $f(x)$

$[Reactor\ Cost\ Function]$

Subject to

$H(x) = 0$

$[equality\ constraints\ that\ satisfy\ reactor\ design\ and\ operational\ requirements]$

$G(x) \leq 0$

$[inequality\ constraints\ that\ satisfy\ reactor\ design\ and\ operational\ requirements]$

$x_{\min} \leq x \leq x_{max}$

$[variable\ bounds]$

$\gamma(x)$

$[physical\ properties, modeling\ assumptions, parameter\ specifications]$

(4.55)

Here $G(x)$ and $H(x)$are constraints corresponding to the relations described in section 4.2.3.5, as well as equation 4.54, and define the feasible space of the optimization problem; x is the vector of optimization variables for the rotary reactor, given in equation 4.5.

4.3.2. Optimization cost function

The setup for the reactor model allows the designer to choose any objective function of interest, which is minimized within the feasible space defined by the design requirements. This cost function can represent anything from component costs to the performance of an integrated energy conversion system. Focusing primarily on the reactor, an option for the objective function is the cost of the reactor, which for now can be assumed proportional to the size of the reactor. In this case, the objective function to be minimized would be the solid volume of the reactor, defined in equation 4.56:

$$F(x) = \pi \epsilon_{solid} \frac{D^2 l}{4} \tag{4.56}$$

Where ϵ_{solid} = solid fraction of reactor cross-sectional area. A different choice of objective function derives from considering the reactor as a component of an integrated energy conversion system. It was demonstrated in chapter 3 that large purging steam flow could negatively impact overall thermal efficiency [45]. Therefore, another useful choice for the cost function is the purge steam requirement:

$$F(x) = \pi(1 - \epsilon_{solid})\frac{D^2}{4}(\sum u_k \theta_k) \tag{4.57}$$

Where k = air purge and fuel purge sectors. The decision to use either of the above cost functions depends on the objective of the analysis. This study defaults to the purge steam cost function of equation 4.57, but will also present optimized results for minimizing the reactor volume using the function in equation 4.56.

4.3.3. Implementation

The optimization problem was solved using the sequential quadratic programming (SQP) algorithm implemented in one of Matlab®'s nonlinear programing solver, fmincon. Since the solution is only guaranteed to be a local minimum, the model is run from several starting points randomly selected from a predefined parameter range to increase confidence in the solution. Equation 4.54 is added only for j = fuel and air purge velocities.

4.3.4. Results and discussion

The optimization results are summarized in Table 4.6. These reactor design predictions are obtained by minimizing the reactor purge steam requirement. These predictions are first validated by using the predicted values from Table 4.6 (except reactor length) as input in the detailed reference model, solving for the reactor length using the detailed model and then comparing the lengths predicted by both models.

Table 4.6: Optimized reduced fidelity model predictions

	Copper			Iron			Nickel		
Pressure (bar)	5	10	20	5	10	20	5	10	20
Diameter (m)	1.63	1.60	1.76	1.65	1.98	2.05	1.11	0.86	0.94
Length (m)	0.60	0.81	1.08	1.06	0.87	0.41	0.39	0.50	0.65
Fuel sector	55%	57%	47%	29%	20%	19%	26%	43%	36%
Fuel purge sector	8%	17%	46%	40%	56%	61%	2%	5%	10%
Air sector	36%	24%	2%	29%	21%	18%	72%	49%	52%
Air purge sector	1%	2%	5%	2%	2%	2%	1%	3%	2%
Fuel velocity (m/s)*	0.18	0.09	0.05	0.10	0.05	0.03	0.50	0.25	0.12
Fuel purge velocity (m/s)	0.19	0.09	0.05	0.10	0.05	0.03	0.52	0.26	0.13
Air velocity (m/s)	1.42	1.03	2.48	1.34	0.45	0.21	1.31	1.52	0.57
Air purge velocity (m/s)*	1.40	0.70	0.45	2.70	1.20	0.75	1.37	1.00	0.60
Cycle period (s)	39	50	50	25	30	25	50	50	50

*fixed

Figure 4-8, Figure 4-9 and Figure 4-10 compare the optimized reactor conversion lengths predicted by the reduced and the detailed reference rotary reactor models. Similar to the case for the previous validation exercise, the reduced model results for copper and nickel match the predictions of the detailed model well. The most significant deviation occurs for iron at 5bar, but in general, the results obtained provide a measure of confidence in the performance of the reduced model.

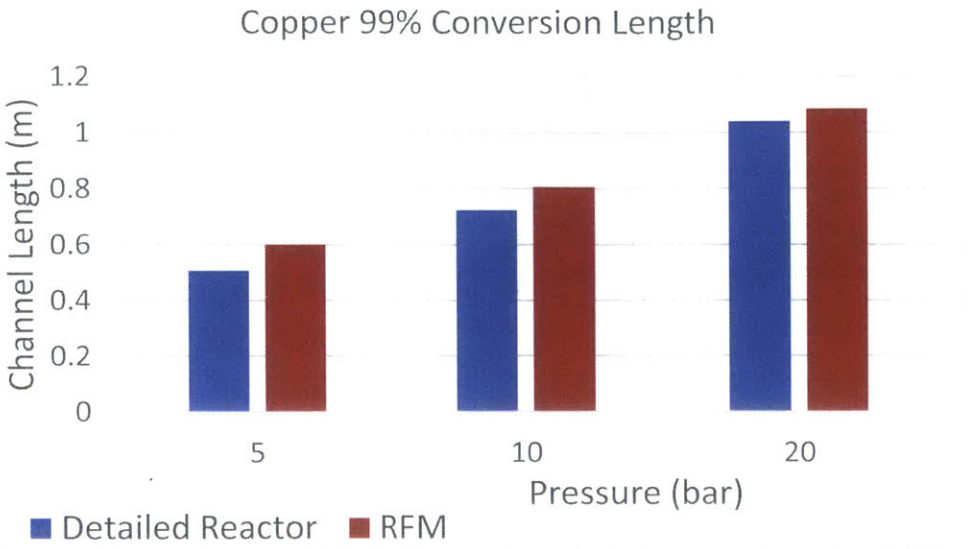

Figure 4-8: Plots comparing optimized RFM results and corresponding detailed reactor predictions for copper.
The predicted reactor length at 5 and 20 bars are comparable for the two models with deviation typically under 12% across the three pressure points.

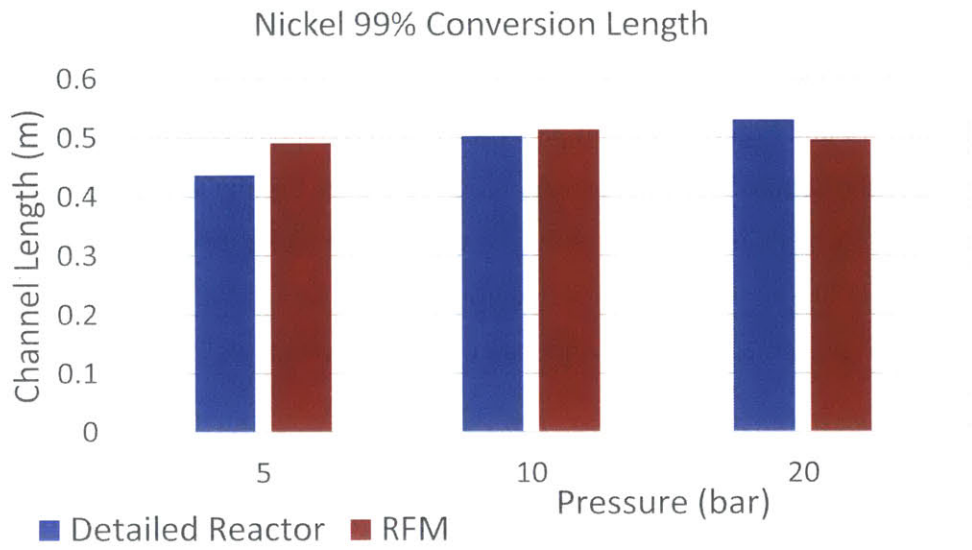

Figure 4-9: Plots comparing optimized RFM results and corresponding detailed reactor predictions for nickel.
The detailed model prediction closely matches the results from the reduced fidelity model for Nickel.

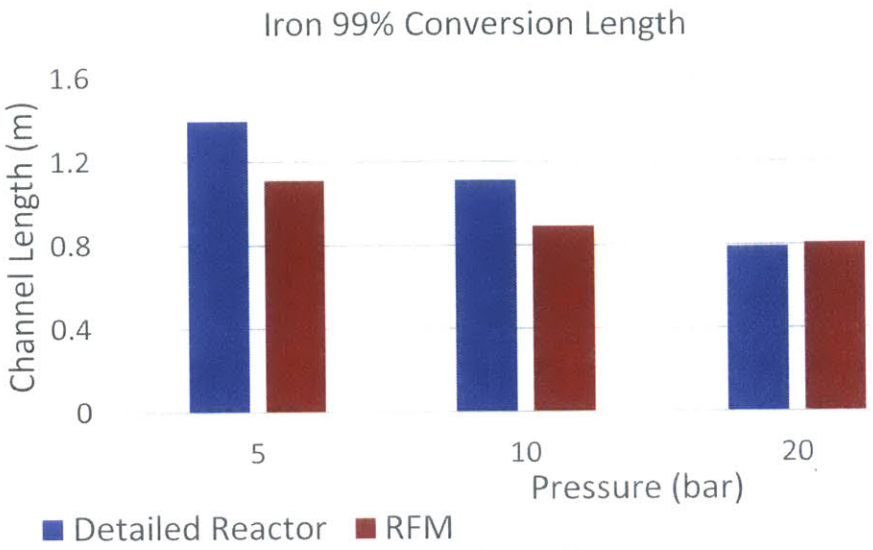

Figure 4-10: Plots comparing optimized RFM results and corresponding detailed reactor predictions for iron.

Of the three oxygen carriers, the deviations for iron are the most pronounced between the two models. Better results could be obtained by refining the temperature profile approximation, improving the energy balance equation and matching the carbon separation target.

Earlier, purge steam flow and reactor volume were identified as possible objective functions to be minimized in the reactor optimization exercise, though the model can be set up to minimize any other function of the optimization variables. The foregoing discussion has so far been based on results from the first case, which minimizes purge steam demand. In order to assess the improvement in the objective for both optimization cases, an additional optimization case, which minimizes the reactor volume, is run. The minimized reactor volume and computed steam demand from this run are compared with the corresponding values from the first case. Figure 4-11 compares the purge steam demand while Figure 4-12 does the same for reactor volume for all three oxygen carriers. As shown in Figure 4-11, optimization decreases purging steam demand for copper and nickel by about 60%, which is significant, considering the potential energetic cost of steam generation. Very little improvement was observed for iron, suggesting that purging steam for this oxygen carrier is not a strong function of the optimized variables, for the current set of constraints. For the reactor volume case, optimization achieved some reduction for all three oxygen carriers, with gains of 26%, 3% and7% for copper, iron and nickel respectively.

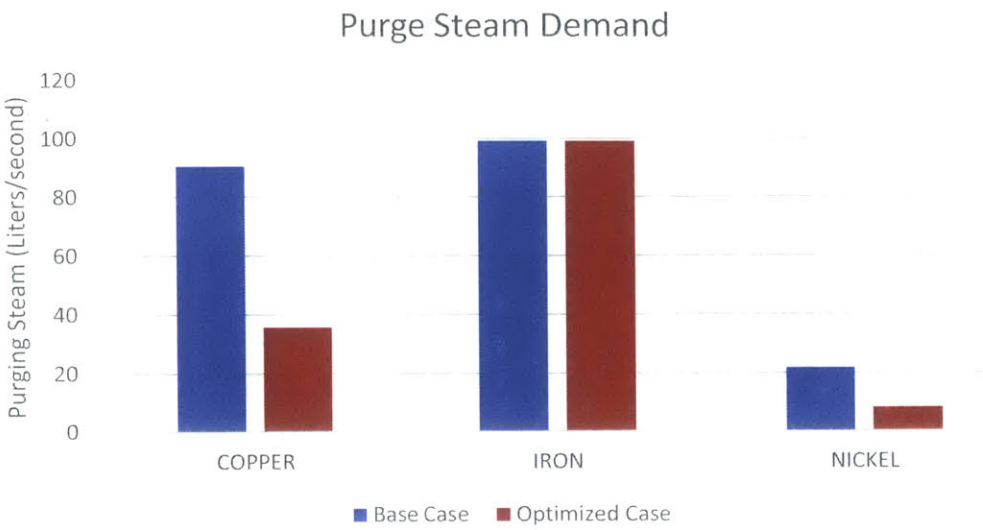

Figure 4-11: Purge steam demand plots for cases minimizing reactor volume and steam demand respectively.

The optimized purge steam demand achieves approximately 60% decrease from the un-optimized value for copper and nickel. There is no improvement for iron, for which steam demand appears to be mostly a function of the extent of fuel conversion and carbon separation.

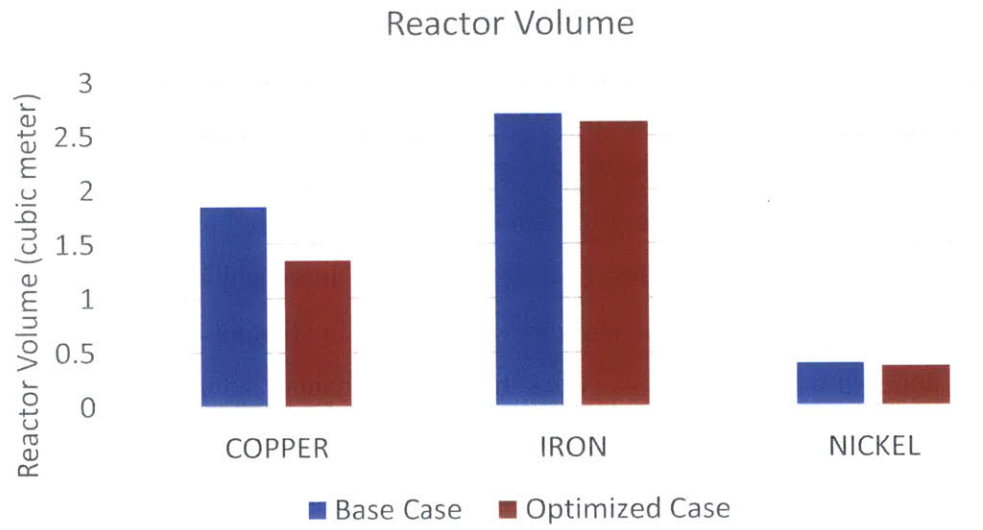

Figure 4-12: Reactor size plots for cases optimizing reactor volume and steam demand respectively.

Minimizing the reactor volume generally predicts a smaller reactor, with relative decreases of 26% for copper, 3% for iron and 7% for nickel.

4.3.5. Design-oriented case study

This case study demonstrates the application of the reduced model in a more design-oriented analysis. The preceding sections optimized for reactor geometry given a target thermal power capacity (1MW) and some other fixed parameters. However, in some scenarios, the designer may be faced with a different set of constraints and design objectives. For example, in a situation where space is limited, the reactor dimensions might be constrained and the designer then has to maximize for thermal power capacity. How can this reduced model be applied in such a case?

An example that describes three cases where the overall reactor dimension is fixed and the reactor is subjected to different sets of additional constraints, will be used to answer this question. The objective now is to maximize the reactor thermal power capacity given different extents of geometric and operating constraints. For all three cases, the reactor volume (diameter and length) are fixed while the cycle period is allowed to vary. In case A, the flow velocities are also fixed while in case C, the sector sizes are fixed instead. These specifications are listed in Table 4.7 and are applied to the model using equation 4.54. Next, the model is updated by removing the thermal size equation 4.47 from the constraint list, rearranging it to the form in equation 4.58 and replacing the default objective function with it.

$$-\dot{W}_{thermal} = \frac{-\pi D^2 LHV\, C_{tot}\, x_{fuel}\, u_{fuel}\, \theta_{fuel}(1-\varepsilon)}{4} \tag{4.58}$$

The results of this exercise is illustrated in Figure 4-13 for a reactor with copper-based oxygen carrier. The plots show how different sets of constrained reactor parameters lead to different thermal power capacities for the same reactor volume. Comparing the results for case C with those of A and B indicates that increasing the model's degrees of freedom creates the potential for achieving an improved optimum - in this case, up to 45% increase in the reactor thermal power. The more the degrees of freedom, the more the problem shifts from design to optimization, as reflected in the improved thermal power capacity objective in Figure 4-13.

Table 4.7: Parameter specifications for the design case example

Parameter	**Specification condition**		
	Case A	Case B	Case C
Volume	Fixed	Fixed	Fixed
Cycle period	Free	Free	Free
Fuel sector size	Free	Free	Fixed
Fuel purge sector size	Free	Free	Fixed
Air sector size	Free	Free	Fixed
Air purge sector size	Free	Free	Fixed
Fuel velocity	Fixed	Free	Free
Fuel purge velocity	Fixed	Free	Free
Air velocity	Fixed	Free	Free
Air purge velocity	Fixed	Free	Free

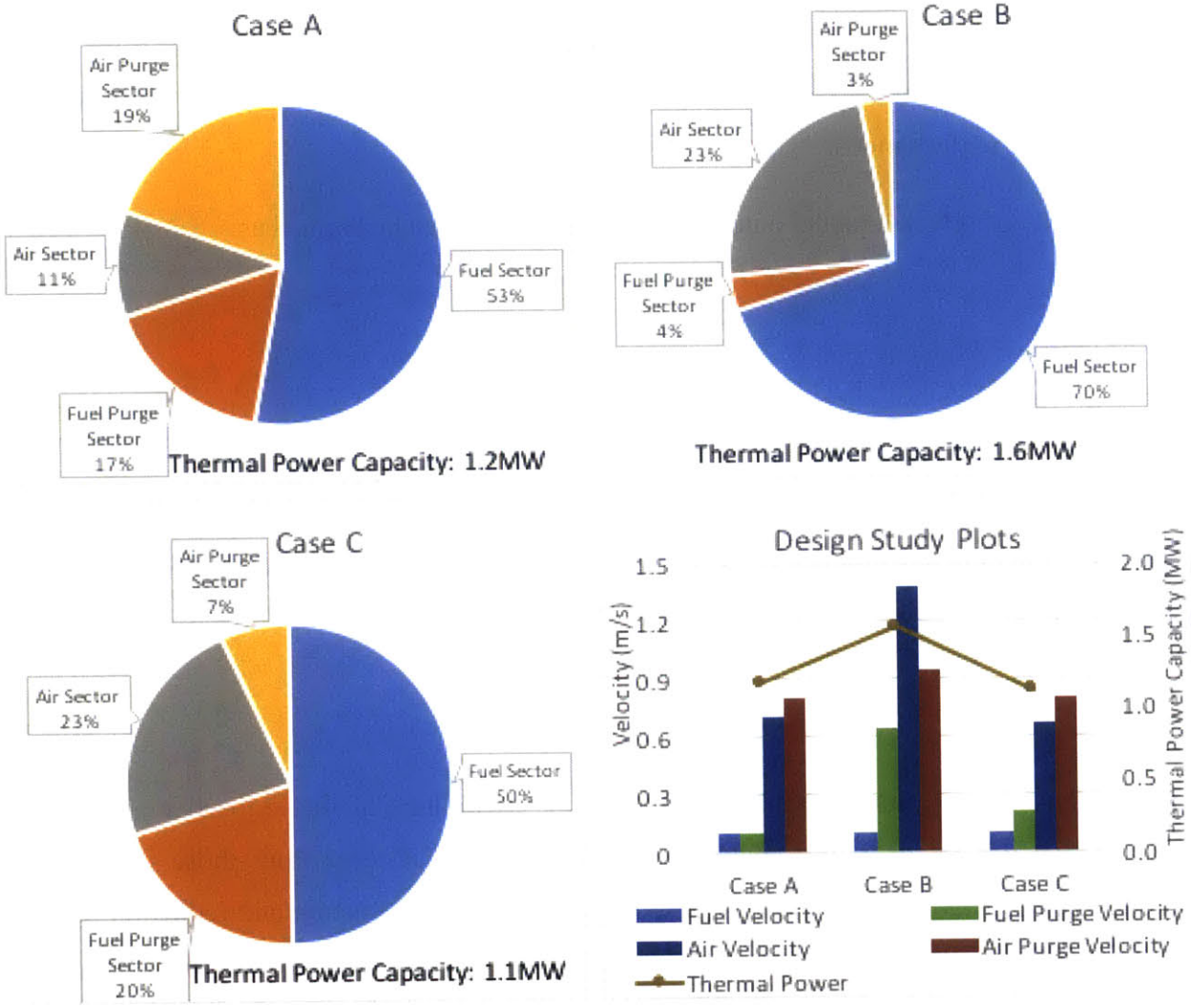

Figure 4-13: Predicted sector sizes and optimized thermal power capacity for a copper-based rotary reactor subject to different sets of constraints.
Case B is the least constrained and unsurprisingly converges to a thermal size 33% and 45% larger than cases A and C respectively by increasing the reactor fuel utilization. Notice the increase in air velocity for case B to make up for the higher oxygen carrier reduction due to increased fuel consumption.

4.4. Sensitivity analysis

The purpose of the sensitivity analysis in this section is to evaluate how the optimized rotary reactor configuration responds to changes in selected design, operating and materials related

parameters. Furthermore, this study identifies which parameters have the largest impact on the reactor behavior and how this impact varies with oxygen carrier type. It also provides some insight into how the reduced model's internal logic adjusts the optimized variable values in response to input parameter perturbations.

The sensitivity of selected model outputs to specified inputs can be defined as:

$$S_{Y\to X} = \frac{\left(\frac{\Delta Y}{Y}\right)}{\left(\frac{\Delta X}{X}\right)} \tag{4.59}$$

Here, $S_{y\to x}$ is the sensitivity of output (Y) to input (X), $\frac{\Delta Y}{Y}$ is the fractional change in output while $\frac{\Delta X}{X}$ is the fractional change in input. In section 4.2, the fuel conversion rate in the rotary reactor was defined as a function of a number of design, operating parameters and reactivity, summarized here in equation 4.60.

$$\omega = \omega\left(\left(\frac{P}{P_0}\right)^{-a},\ e^{-\frac{E}{R*T}},\ C_{fuel}^{n} \right) \tag{4.60}$$

To keep the analysis simple, while illustrating the capabilities of the reduced model, a few representative design, operating and kinetic parameters are selected from those identified in equation 4.60: operating pressure, reactor temperature, feed fuel fraction and reduction reaction activation energy. Reactor pressure, temperature and feed fraction have been shown to be important contributors to overall cycle thermal efficiency in chapters 2 and 3 [44], [45], which makes it useful to understand their impact on the optimal reactor capacity. Activation energy sensitivity provides a means of assessing the effect of the kinetic parameter uncertainty on optimal reactor design. The chosen simulation outputs of interest are the total purge steam flow (default objective function) and the reactor volume. These outputs were chosen because they relate directly to performance, space utilization and cost, all of which are important considerations in designing a rotary reactor-based power plant.

For the sensitivity study, the input parameters are varied over a specified range above and below the corresponding base values. For each run, only one input is varied while the rest remain at their base values. The following plots show the sensitivity of the selected outputs for a given change in individual input parameters for a copper, nickel and iron-based rotary CLC reactor. The input

parameter ranges and base values, as well as the output parameter base values are listed in Table 4.8. To maintain some consistency in predictions across the three different oxygen carriers, the cycle period, fuel velocity and air purge velocities are fixed at the base values from Table 4.3, while the air velocity, sector sizes, reactor length and diameter are free to vary.

Table 4.8: Input and base case parameters for sensitivity studies

Copper				
Input			Output	
Parameter	Base value	Range	Parameter	Base value
Pressure (bar)	10	± 20%	Conversion length (m)	0.8
Temperature (k)	1314	±10%	Reactor diameter (m)	1.6
Reduction activation energy (kj)	60	±10%	Purge steam flow (l/s)	35
Feed fuel fraction (%)	15%	±10%		
Nickel				
Input			Output	
Parameter	Base value	Range	Parameter	Base value
Pressure (bar)	10	± 20%	Conversion length (m)	0.5
Temperature (k)	1450	±10%	Reactor diameter (m)	0.9
Reduction activation energy (kj)	78	±10%	Purge steam flow (l/s)	8
Feed fuel fraction (%)	25%	±10%		
Iron				
Input			Output	
Parameter	Base value	Range	Parameter	Base value
Pressure (bar)	10	± 20%	Conversion length (m)	0.9
Temperature (k)	1465	±10%	Reactor diameter (m)	2
Reduction activation energy (kj)	49	±10%	Purge steam flow (l/s)	99
Feed fuel fraction (%)	50%	±10%		

For the pressure and temperature sensitivity studies, the specified gas feed velocities are scaled with temperature and pressure in such a way as to maintain similar molar flow rate within each

channel for different operating conditions. Thus for each sensitivity case, the new feed velocity is related to the base case value by the following expression

$$v_{new} = \left(\frac{P_{base}}{P_{new}}\right)\left(\frac{T_{new}}{T_{base}}\right) v_{base} \tag{4.61}$$

Here $v, P,$ and T refer to velocity, pressure and temperature respectively. Results from the sensitivity analysis are summarized in Figures 4.14 to 4.17.

4.4.1. Purge steam sensitivity

4.4.1.1. Temperature

Figure 4-14a shows a very strong dependence of purge steam demand on reactor exit temperature for copper and nickel, with significant increase in purging steam for a given temperature drop. This happens because lower temperature reduces reactivity, requiring longer channels, more channels or both to provide complete fuel conversion. The resulting change in reactor geometry produces an increase in the purging steam demand. A curious case is encountered with iron, where the optimal purge steam demand is insensitive to temperature. It is likely that this is a consequence of the nature of the feasible space defined by the constraints and parameter values for the iron-based oxygen carrier, such that the model is able to find the same minimum (purge steam) for any reactor temperature within the defined range.

4.4.1.2. Pressure

The pressure sensitivity profiles are illustrated in Figure 4-14b. In general, pressure impacts reactivity by modifying the value of the pressure factor, $\left(\frac{P}{P_o}\right)^{-a}$, and the concentration, $C_{fuel}^{n} \propto \left(\frac{P}{RT}\right)^{n}$ in the reaction rate expression. Thus the effective contribution from pressure derives from the combined effect of these two parameters, conveyed in the expression, P^{n-a}. $'n'$ and $'a'$ are the reaction order and the pressure inhibition exponent respectively. Thus when $n > a$, increasing pressure enhances reactivity, as seen for copper and nickel. Changing the reactor pressure resulted in a proportional change in purge steam requirement for copper. The change for nickel is

approximately half to one-third that for copper. Once again, steam demand for iron does not appear to be sensitive to pressure, even though an inverse relationship with pressure is expected since $n < a$. As explained for temperature, it is likely that the feasible space for iron is such that the model is able to find an optimal combination of flow and geometric parameters that achieve the same minimum purge steam flow. This behavior highlights the fact that the converged solution for the reactor model is not unique, and multiple feasible solutions that attain the same minimum are possible.

4.4.1.3. Reduction reaction activation energy

From Figure 4-14c, the observed trend for the sensitivity of copper and nickel-based carriers to activation energy is the reverse of that for temperature, which is expected, given the form of the exponential function in the reaction rate expression. Very much like in the case for temperature, copper exhibits the highest sensitivity to variations in the value of the activation energy, underscoring the importance of the uncertainty in the value of this parameter to reactor geometry and performance.

4.4.1.4. Fuel sector inlet fuel fraction

The fuel sector inlet fraction, x_{fuel}, affects the value of the concentration term in the expression for fuel conversion, since $C_{fuel} \propto x_{fuel}$. From Figure 4-14d, the purge steam flow is, in general, only slightly sensitive to fuel feed fraction for the 3 oxygen carriers, with less than 2% change in purge steam for a 10% change in fuel fraction of the fuel sector inlet stream.

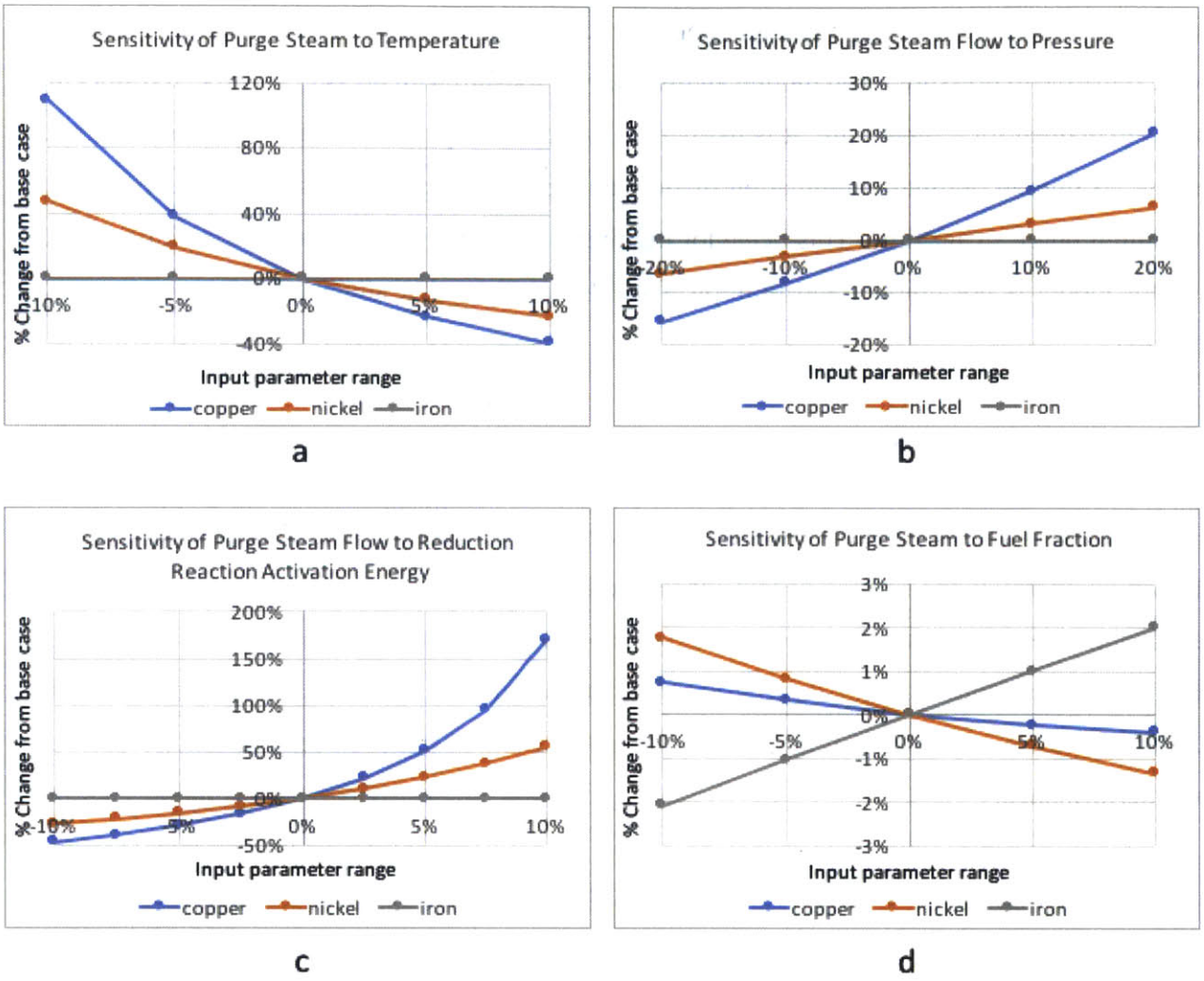

Figure 4-14: Purge steam sensitivity.

The negative impact of pressure on reactivity results in larger reactor dimensions that cause the required purging steam flow to increase for copper and nickel. Higher temperature increases reactivity, reducing reactor dimension and required purging steam while activation energy has the reverse effect. Iron shows no sensitivity to pressure , temperature or activaton energy because the net changes in reactor length, diameter and relative sector sizes accommodate consequent the variations in steam demand. All three oxygen carriers have very little sensitivity to feed fuel fraction.

4.4.2. Reactor volume sensitivity

The sensitivity results for reactor volume summarized in Figure 4-15a to Figure 4-15d are identical to those for purge steam. The primary reason is that like purge steam, the reactor size depends on the same flow and geometric parameters, such that the predicted response to parameter perturbations for both cases are proportional. Note that the sensitivity profiles presented depend on the model setup. Changing the objective function, parameter bounds or constraint sets can modify the feasible space for the solution and lead to different minima. Also, the optimal configurations achieved for each run is not necessarily unique, so there can be multiple feasible solutions that converge to the same minimum for the objective function. For this reason, it is very important to apply design experience and good engineering judgment when setting up the model.

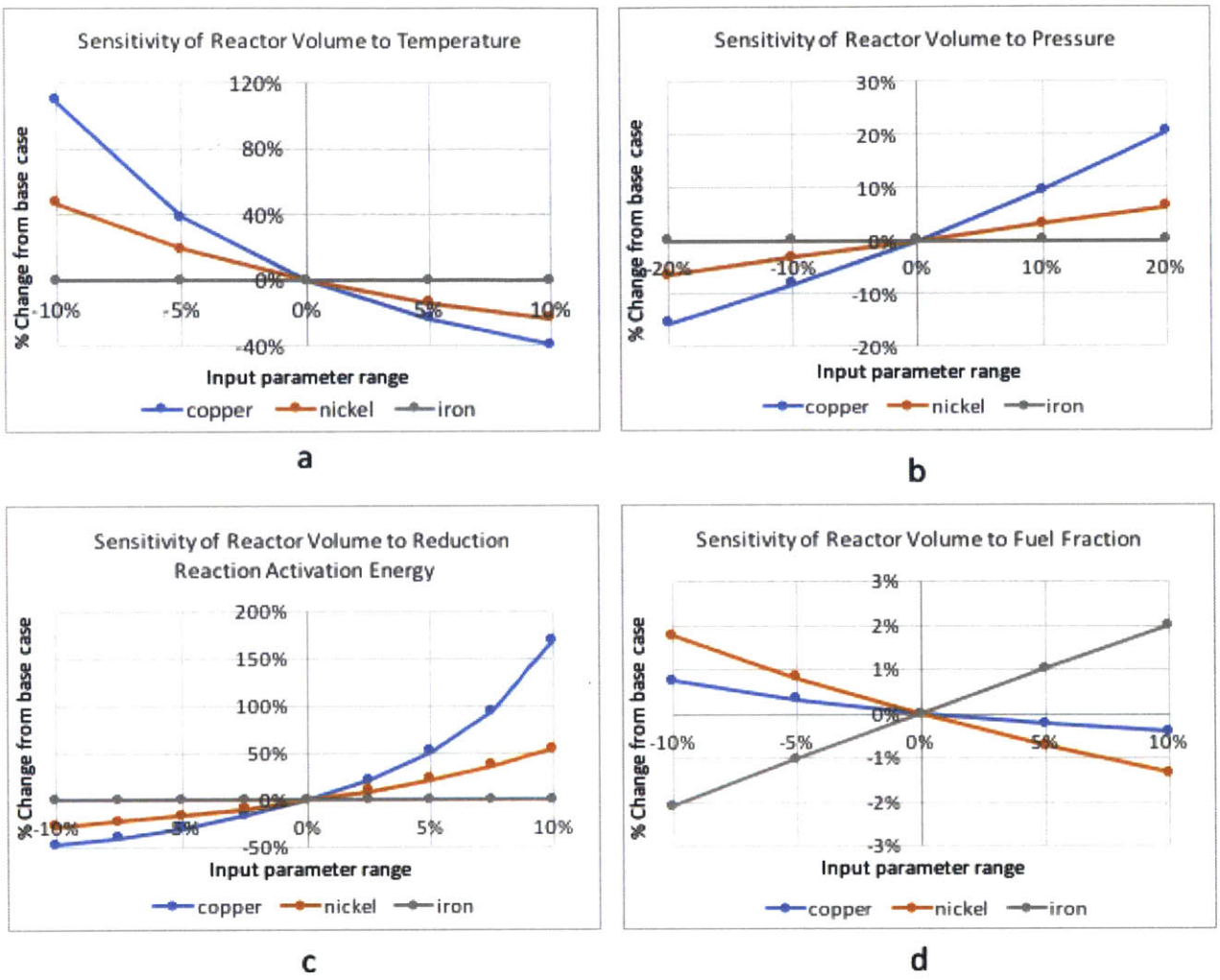

Figure 4-15: Reactor Volume sensitivity.

The sensitivity of reactor volume temperature, pressure, activation energy and fuel fraction is identical to that for purge steam since purge steam flow and reactor volume depend on the same geometric parameters. Copper displays a higher sensitivity to temperature and activation energy than nickel and iron.

4.4.3. Comparing sensitivities

To wrap up the foregoing discussion, combined sensitivity plots that provide a direct comparison of the relative importance of each sensitivity parameter on the optimal reactor design is presented in Figure 4-16 and Figure 4-17. Figure 4-16 shows that both purge steam demand and reactor volume are most sensitive to reduction activation energy and the reactor temperature. It can also

be concluded from Figure 4-16 that they are not very sensitive to fuel feed fraction. Figure 4-17 provides some insight on the observed sensitivity behavior for iron. Since the model has the freedom to vary the reactor length and diameter – in addition to sector sizes and flow velocities – in search of a minimum for the objective function, an increase in diameter tends to be accompanied by a corresponding decrease in reactor length (and vice-versa) for iron. Thus, despite significant changes in internal reactor configuration, the overall value of the purge steam or reactor volume objective stayed the same.

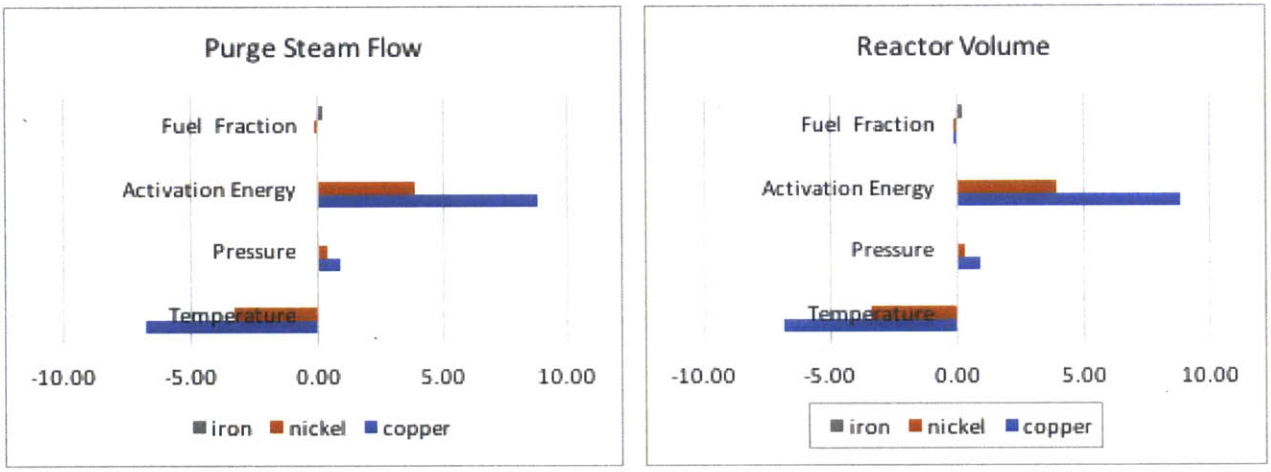

Figure 4-16: Comparing the sensitivity of the purge steam flow and reactor size to selected kinetic parameters and operating conditions for the three oxygen carriers.

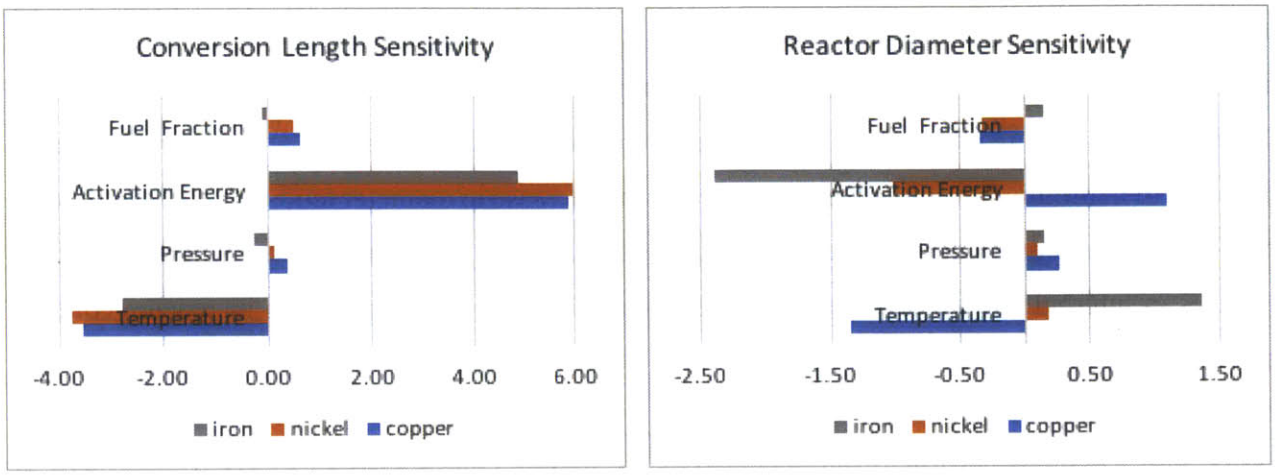

Figure 4-17: Comparing the sensitivity of conversion length and reactor diameter to selected kinetic parameters and operating conditions for the three oxygen carriers.
Notice that particularly for iron, diameter sensitivity is the reverse of that for length, which mostly explains the net zero sensitivity of seen in Figure 4-14 and Figure 4-15.

4.5. Summary

In this study, a reduced fidelity model of a rotary reactor was presented. This model predicts the reactor configuration and performance with reasonable accuracy and at a significantly reduced computational cost compared to the higher dimensional detailed model presented earlier by Zhao et al. [4], [27]–[29]. This reduced model is based on a quasi-steady state approximation of the 1-D plug flow reactor of Zhao et al. It simplifies the energy and continuity equations of the detailed reactor model, then incorporates additional carbon separation criteria and reactor design constraints. The reduced reactor model is structured as an optimization problem that minimizes a cost function given a set of defining constraints and parameter bounds and was adapted to evaluate reactor designs for copper, nickel and iron-based oxygen carriers.

One of the most attractive features of this reduced model is that its evaluation time is about four orders of magnitude lower than that for the detailed model. In addition, each run automatically determines an optimal reactor configuration for any number of specified design and operational constraints. The reduced model's low computational effort and modular structure also make it ideal

for integration with a system level model for analyzing rotary reactor-based energy conversion systems.

Subsequent to prediction validation, the reduced model was used to carry out reactor optimization, and to analyze the sensitivity of the optimal reactor configuration to perturbations in selected operational and kinetic parameters. The optimization study demonstrated how the model can easily be modified to minimize any objective that is a function of the optimization variables. In addition, converting the model from an optimization to a design tool becomes simply a matter of reducing the model degrees of freedom by fixing previously variable parameters. The sensitivity analysis considered the impact of pressure, temperature, reduction reaction activation energy and feed fuel fraction on reactor purge steam flow and volume. Sensitivity results showed that the optimal reactor configuration is most sensitive to activation energy and temperature.

There are three key factors which account for the differences in predictions between reduced model and the detailed model. The first is the error introduced by the average temperature approximation in the reactor channel. The second is that the reduced model assumes gas/solid thermal equilibrium within each channel and thus, neglects both conduction and convection heat transfer limitations that may occur for cases with both high flow rate and low inlet stream temperatures. The third factor is the strict requirement for 100% CO_2 separation, which may not be feasible under certain conditions, especially for iron-based oxygen carriers. One way of improving reactor temperature estimate is to break up the reactor into a number of segments and use scaled average temperatures in each segment. To address the feasibility problem, the carbon separation constraints can be relaxed to allow for gas carryover between the sectors, and perhaps modify the objective function to penalize incomplete CO_2 separation. These could be addressed in future studies.

5. System integration for simultaneous optimization

5.1. Introduction

This chapter presents a strategy for directly integrating the system-level model with the reactor model developed in chapter 4. The idea is to develop a tool for system analysis which captures important feedback interactions between the reactor and the overall system. Such a tool can then be used for the simultaneous optimization of the integrated system while keeping computational costs to a minimum. To this end, it treats the flowsheet as a collection of interconnected sub models - reactor, recuperative heat exchangers, turbines and compressors - and simultaneously solves for the reactor geometry while optimizing the overall flowsheet. Though demonstrated here for the recuperative cycle, it can also be applied to other cycle configurations integrated with the rotary reactor. The chapter is divided into two broad sections; section 5.2 covers the description of the model and presents the mathematical formulation of the different sub-models that represent the power generation cycle components; section 5.3 analyzes simulation results and compares the performance of rotary reactor-based systems using copper, nickel and iron-based oxygen carriers.

5.2. Integrated model development

5.2.1. Motivation

In chapters 2 and 3, theoretical availability models, simple thermodynamic cycle models and detailed flowsheet models were used to analyze rotary CLC reactor-based energy conversion systems. Specifically, the rotary reactor was successively represented by thermal reservoirs in the availability models, simple enthalpy balance in the ideal cycle models and equilibrium reactors in the detailed flowsheet models. Thus, each successive representation progressively relaxed the idealized modeling assumptions, increasing the reactor model complexity to provide higher fidelity predictions of the integrated system performance, as illustrated in Table 5.1. Most of the system-level analysis in literature stop at this third phase, making use of an equilibrium or similarly

simplified reactor model for system analysis and confining the detailed reactor design to a subsequent stage of the design process, completely independent of the system analysis.

Table 5.1: Degrees of idealization in earlier reactor representation

Availability models	**Ideal cycle models**	**Detailed cycle models**
Chapter 2	Chapter 2,3	Chapter 2,3
CLC reactor modeled as interacting thermal reservoirs.	CLC reactor modeled as energy conservation for a control volume with heat input equivalent to reaction enthalpy.	CLC reactor modeled as interacting equilibrium (or complete combustion) reactors.

This chapter presents an alternative approach that directly combines a higher resolution reactor model with the detailed system-level model. This is done by integrating the system-level model with the reduced fidelity reactor model developed in chapter 4, which was shown to significantly reduce computational cost compared to the detailed model of Zhao et al. [28], [29] while maintaining reasonable predictive accuracy. This integrated modeling approach has a number of advantages that make it preferable to alternative strategies. Firstly, it combines a high-level system view with a sufficiently detailed component-level view of the reactor, simultaneously computing both the thermodynamic state of the overall system and the associated reactor geometry. It is robust enough to generate sufficiently accurate predictions at both the system and reactor-level. Secondly, it captures important feedback interactions between the reactor and the rest of the system that impact overall performance. This is particularly consequential when it comes to predicting the actual purge steam demand, which is a function of both oxygen carrier kinetic properties and operating conditions (e.g., reactor inlet temperature and pressure) defined by the system. The studies presented in chapters 2 and 3 assumed a fixed value for purge steam, which is an inadequate specification, given the potentially significant impact of purge steam on system performance. Lastly, in response to the desired application, the integrated model can be easily switched from an optimization tool to a design tool.

5.2.2. The recuperative cycle model structure

In chapter 3, the recuperative cycle was identified as a suitable configuration for integration with the rotary reactor because it combines high efficiency with the capacity to sufficiently preheat the reactor inlet streams. This is important, because higher inlet stream temperatures support faster reactions in the reactor, which reduce both the reactor size and steam demand. Therefore, this study will implement the integrated model for a recuperative CLC cycle configuration. This integrated modeling tool can also be applied to other cycle configurations, where such an exercise becomes a matter of replacing the recuperative cycle sub-models with those for the other cycle configuration.

A high-level schematic of the recuperative CLC cycle highlighting the key sub-components is shown in Figure 5-1. For both the fuel-side and air-side streams, the primary sub-components are: 1) the compressor, for raising the inlet stream to the system pressure, 2) the recuperator, for preheating the inlet stream using exhaust stream enthalpy, 3) the reactor and 4) the turbine, for power generation. Figure 5-1 also includes short descriptions of each sub-model in the integrated flowsheet. The turbine and compressor are represented by enthalpy conservation with specified isentropic efficiency to account for irreversibilities; the recuperator is modeled as a multi-stream heat exchanger and the rotary reactor model from chapter 4 represents the CLC redox reaction. Each of these sub-models is described in more detail in the following sections.

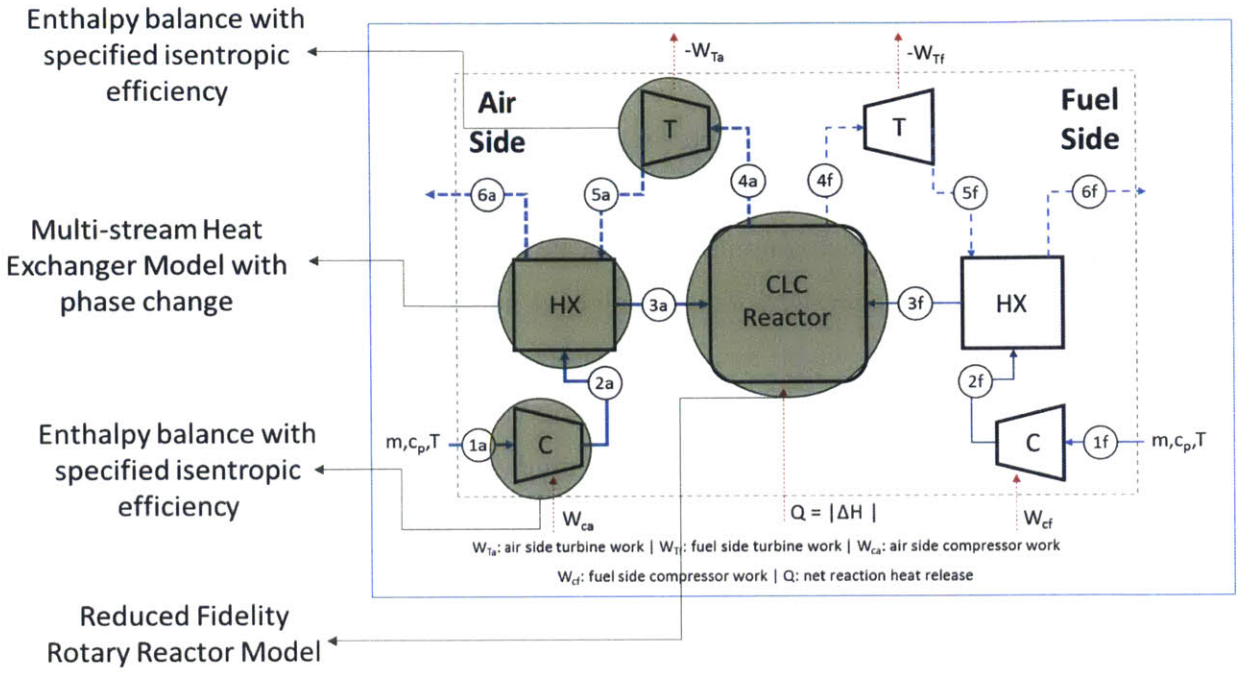

Figure 5-1: Schematic of the recuperative CLC cycle showing key sub models.

5.2.3. The recuperator (multi-stream heat exchanger) model

5.2.3.1. Overview

The demand for purge steam in the rotary reactor requires steam generation which, in the case of the recuperative cycle, takes place in the recuperators. Since this heat exchanger is also used to preheat the inlet air stream, the recuperator unit is modeled as a multi-stream heat exchanger (MHEX) that allows simultaneous exchange of heat from multiple hot and cold streams. MHEXs are typically analyzed using the pinch method, which minimizes the heat integration driving force, consistent with the laws of thermodynamics [55]–[58]. This method is traditionally used to analyze heat exchanger networks using composite curves, and is based on the fact that on either side of the pinch (point of minimum temperature difference, $\Delta T_{\min}$), the hot stream enthalpy change must match that of the cold stream. The pinch approach usually assumes a constant heat capacity for the exchanger streams, which is not the case where some of the streams can change phase. In addition, since the heat exchanger could be embedded in an outer optimization problem, the phase and thermodynamic state of the heat exchanger streams are not necessarily known a priori. This is

because the stream compositions, flow rates and temperatures are also variables in the optimization process.

To deal with this problem, this study adopts the method proposed by Kamath et al., based on the Duran Grossmann minimum utility model [59], [60]. The Duran Grossman model defines a set of heat integration constraints which automatically locate the pinch point that minimizes the utility requirement for a heat exchanger network. Kamath et al. adapted this model to MHEXs by setting the utility requirement to zero, which forces the heat integration constraints to match the enthalpy change of the hot and cold streams while still satisfying the minimum driving force criterion. The resulting model subsequently embedded in the larger flowsheet by simply adding the heat integration constraints to the overall flowsheet constraints.

5.2.3.2. The heat integration model

As mentioned earlier, pinch-based heat integration cannot be applied directly to streams with phase change because of the non-linear variation of heat capacity across the phases. Failure to take this into consideration will result in the use of incorrect thermodynamic properties and lead to temperature cross-overs near the phase boundaries, which violate the 2nd law of thermodynamics. However, within each phase, it can be assumed that the heat capacity flow rate is constant. For a generic MHEX with multiple streams, the adopted model classifies the streams into two mutually exclusive sets: those that do not change phase and those capable of changing phase. The streams capable of phase change are further subdivided into superheated (sup), two-phase (2p) and sub-cooled (sub) sub-streams. Each of these sub-streams are treated as independent streams with associated heat loads, but they all inherit the same flow-rate from the parent stream. This heat integration modification is represented in Figure 5-2 for the recuperator in this study. Since the cold H_2O streams are capable of traversing the three phases and the hot-side exhaust could have water condensation, the original three physical streams are now replaced with six heat integration streams.

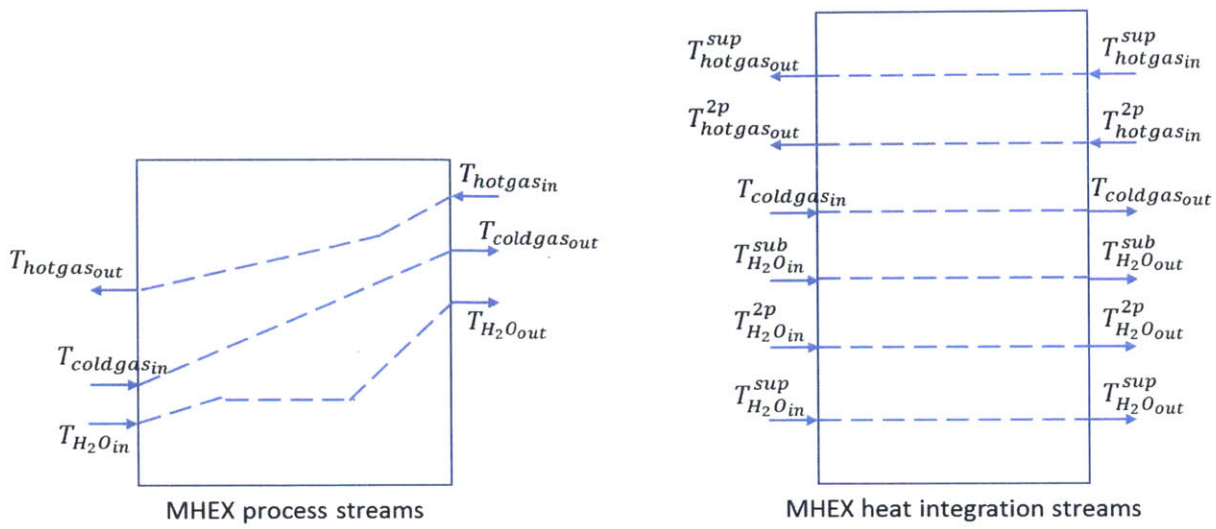

Figure 5-2: Integrated multi-stream heat exchanger model accounting for streams capable of phase change.
This represents the model used for both the air-side and fuel-side recuperators.

The heat integration constraints for this MHEX are composed of a set of energy and pinch balance equations derived from the modified stream set. The model is thus represented by the following optimization problem:

Minimize φ^{obj}

s.t.

Energy balance:

$$\sum_{i\in Hot} F_i^{ph}\left(T_i^{in} - T_i^{out}\right) + \sum_{j\in Cold} F_j^{ph}\left(T_j^{in} - T_j^{out}\right) = 0$$

Pinch balance:

$$\aleph_C^p - \aleph_H^p \leq \varepsilon\,; p \in \overline{P}$$

$$\aleph_H^p = \sum_{i\in Hot} F_i^{ph}\left(\max\{0, T_i^{in} - T^p\} - \max\{0, T_i^{out} - T^p\}\,; p \in \overline{P}\right)$$

$$\aleph_C^p = \sum_{j\in Cold} F_j^{ph}\left(\max\{0, T_j^{out} - [T^p - \Delta T_{min}]\} - \max\{0, T_j^{in} - [T^p - \Delta T_{min}]\}\;; p \in \overline{P}\right)$$

Other:

Parameter values, variable bounds, etc (5.1)

Here φ^{obj} is the objective function which may correspond to the MHEX or the outer flowsheet model; ε is a conditioning tolerance factor; F_k^{ph} is the thermal capacity rate of hot/cold stream (k) for phase (ph); $T_i^{in} = \left[T_{hotgas_{in}}^{sup}, T_{hotgas_{in}}^{2p} \right]$; $T_i^{out} = \left[T_{hotgas_{out}}^{sup}, T_{hotgas_{out}}^{2p} \right]$; $T_j^{in} = \left[T_{coldgas_{in}}, T_{H_2O_{in}}^{sub}, T_{H_2O_{in}}^{2p}, T_{H_2O_{in}}^{sup}, \right]$; $T_j^{out} = \left[T_{coldgas_{out}}, T_{H_2O_{out}}^{sub}, T_{H_2O_{out}}^{2p}, T_{H_2O_{out}}^{sup} \right]$; $\overline{P}$ is the set of pinch point candidates whose temperatures are defined as $T^p = [T_i^{in}, T_j^{in} + \Delta T_{min}]$; $ph = \{sup, 2p, sub\}$; These pinch point candidates represent the inlet and phase transition temperatures where the minimum temperature approach between hot and cold stream can occur. As the max function in equation 5.1 is not differentiatable at $T = T^p$, it is replaced with the following smooth approximation equation of Balakrishna et al. [61]

$$\max\{0, f(x)\} = \frac{1}{2}\left((f(x)^2 + \beta^2)^{\frac{1}{2}} + f(x) \right) \tag{5.2}$$

where β is a smoothing factor whose value can be fine-tuned to improve convergence. The above formulation applies to both the air-side and fuel-side recuperators.

5.2.3.3. Phase detection

Given that the MHEX is to be integrated with the rest of the flowsheet for analysis and optimization, the temperature and composition of the different streams are optimization variables and it is not known a priori whether or not the streams will traverse the two-phase region. To track phase change, this model compares the inlet and exit temperature of the parent stream with the dew and bubble point temperatures which are calculated during flowsheet integration. In the MHEX heat integration analysis, the heat load corresponding to the parent stream depends on the actual phases traversed, and assigning the proper heat loads can be accomplished by combinatorial decision-making using disjunctions. The set of disjunction constraints for the hot and cold streams are illustrated in Figure 5-3

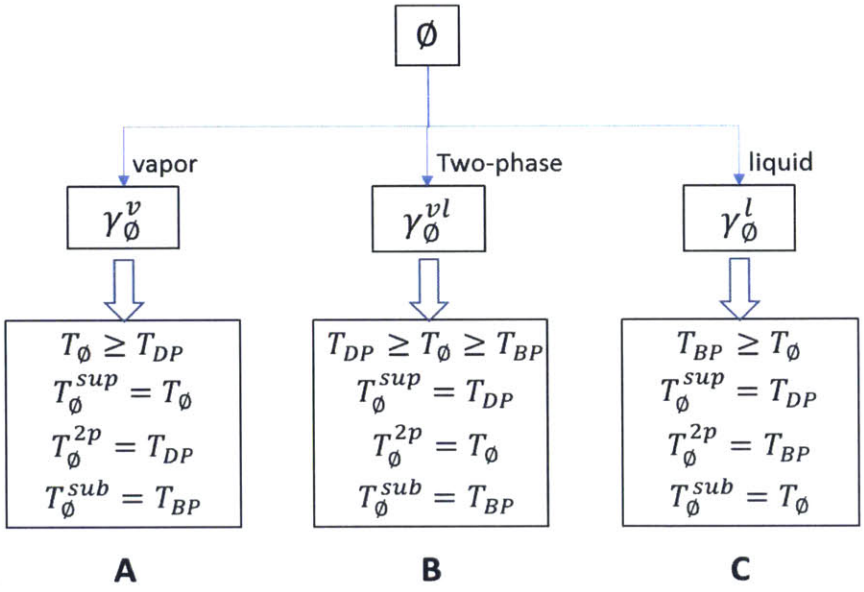

Figure 5-3: disjunction logic for assigning constraints.
When a decision variable is true, the corresponding inequality in the top row of the bottom box is satisfied and the subsequent equality assignments are enforced.

$\emptyset$ represents inlet/exit stream; DP, BP represent dew and bubble points; $sup, 2p, sub$ refer to superheated, 2-phase and subcooled states; $\gamma^{v}, \gamma^{vl}, \gamma^{l}$ are the mutually exclusive Boolean decision variables whose truth is defined by the inequality in the top row of the boxed relations. The equality relations handle the substream temperature assignment and are enforced when the corresponding decision variable is true. So if an inlet stream is in the superheated state, γ_{in}^{v} becomes true and the corresponding assignments in box 'A' are enforced. A corresponding set of logic statements can written for this case as follows

$$\gamma_{in}^{V} \veebar \gamma_{in}^{VL} \veebar \gamma_{in}^{L} \tag{5.3a}$$

$$\gamma_{in}^{V} \rightarrow \gamma_{out}^{V} \veebar \gamma_{out}^{VL} \veebar \gamma_{out}^{L} \tag{5.3b}$$

This means that for a superheated inlet stream, the outlet could be exclusively in the vapor, vapor-liquid or liquid states. Following this approach, the disjunction relation represented in Figure 5-3 can be expressed as logic propositions relating the truth values of the decision variables. These can then be transformed into a set of linear constraints for both the cold and hot streams. The complete set of constraints for the recuperator streams are listed in Table 5.2.

Table 5.2: Disjunction logic represented as logic constraints for MHEX model

Cold H_2O inlet (air / fuel side)	Cold H_2O outlet (air / fuel side)
$\gamma_{in}^{V} + \gamma_{in}^{VL} + \gamma_{in}^{L} - 1 \leq 0$	$\gamma_{out}^{V} + \gamma_{out}^{VL} + \gamma_{out}^{L} - 1 \leq 0$
$\gamma_{in}^{V} - \gamma_{out}^{V} \leq 0$	$\gamma_{out}^{L} - \gamma_{in}^{L} \leq 0$
$\gamma_{in}^{VL} - \gamma_{out}^{VL} - \gamma_{out}^{V} \leq 0$	$\gamma_{in}^{V} + \gamma_{in}^{VL} + \gamma_{out}^{V} - \gamma_{in}^{L} - 2 \leq 0$
$\gamma_{in}^{VL} + \gamma_{out}^{VL} + \gamma_{out}^{V} - 2 \leq 0$	$\gamma_{in}^{V} - \gamma_{in}^{VL} + \gamma_{in}^{L} + \gamma_{out}^{V} - 2 \leq 0$
$\gamma_{in}^{L} + \gamma_{out}^{L} + \gamma_{out}^{VL} - \gamma_{out}^{V} - 2 \leq 0$	$\gamma_{in}^{L} + \gamma_{in}^{VL} - \gamma_{in}^{V} + \gamma_{out}^{V} - 2 \leq 0$
$\gamma_{in}^{L} + \gamma_{out}^{L} - \gamma_{out}^{VL} + \gamma_{out}^{V} - 2 \leq 0$	$\gamma_{out}^{V} - \gamma_{in}^{L} - \gamma_{in}^{VL} - \gamma_{in}^{V} \leq 0$
$\gamma_{in}^{L} - \gamma_{out}^{L} + \gamma_{out}^{VL} + \gamma_{out}^{V} - 2 \leq 0$	$\gamma_{out}^{VL} - \gamma_{in}^{VL} - \gamma_{in}^{L} \leq 0$
$\gamma_{in}^{L} - \gamma_{out}^{L} - \gamma_{out}^{VL} - \gamma_{out}^{V} \leq 0$	$\gamma_{out}^{VL} + \gamma_{in}^{VL} + \gamma_{in}^{L} - 2 \leq 0$
Hot gas inlet (air / fuel side)	Hot gas out (air / fuel side)
$\gamma_{in}^{V} + \gamma_{in}^{VL} - 1 \leq 0$	$\gamma_{out}^{V} + \gamma_{out}^{VL} - 1 \leq 0$
$\gamma_{in}^{V} - \gamma_{out}^{V} - \gamma_{out}^{VL} \leq 0$	$\gamma_{out}^{V} - \gamma_{in}^{V} \leq 0$
$\gamma_{in}^{V} + \gamma_{out}^{VL} + \gamma_{out}^{V} - 2 \leq 0$	$\gamma_{out}^{VL} - \gamma_{in}^{V} - \gamma_{in}^{VL} \leq 0$
$\gamma_{in}^{VL} - \gamma_{out}^{VL} \leq 0$	$\gamma_{out}^{VL} + \gamma_{in}^{V} + \gamma_{in}^{VL} - 2 \leq 0$

5.2.3.4.1. Reformulating the phase detection disjunctions

Rather than having to solve a non-linear mixed-integer programming problem, Kamath et al. [56] reformulated the disjunctions to allow for the use of continuous variables. This was done by introducing an inner minimization function defined in piecewise smooth domains whose solution sets the value of the Boolean decision variable from the disjunction to be 0 or 1, depending on whether the inlet or exit temperature of the stream lies in the interval defined for that disjunction term. This then takes the form of a mathematical problem with complementarity constraints, and is embedded in the outer problem by including its optimality conditions as additional constraints. The optimality conditions for either the inlet or exit of the fuel/air-side exhaust and H_2O streams take the following form:

$$\gamma^{V} + \gamma^{VL} + \gamma^{L} - 1 = 0 \tag{5.4}$$

$$-(T - T_{DP}) - \mu^{V} + \lambda = 0 \tag{5.5}$$

$$-(T_{DP} - T)(T - T_{BP}) - \mu^{VL} + \lambda = 0 \tag{5.6}$$

$$-(T_{BP} - T) - \mu^{L} + \lambda = 0 \tag{5.7}$$

$$0 \leq \gamma^{V} \perp \mu^{V} \geq 0 \tag{5.8}$$

$$0 \leq \gamma^{VL} \perp \mu^{VL} \geq 0 \tag{5.9}$$

$$0 \leq \gamma^{L} \perp \mu^{L} \geq 0 \tag{5.10}$$

γ, μ are the vector of multipliers for the inner minimization function. For example, if $T \in [T_{DP}, T_{BP}]$, (5.6) ensures that γ^{VL} is set to 1 and from (5.4), γ^{V}, γ^{L} are set to zero. The complementarity constraints (5.8-5.10) are handled by applying the following penalty formulation to the objective function [62]–[64]

$$Minimize\ \varphi^{obj} + \rho\gamma^{T}\mu \tag{5.11}$$

where ρ is the penalty parameter whose value can be adjusted to improve convergence.

5.2.3.4. Flash calculations

To determine the state of the parent stream at the MHEX inlet and outlet, the parent stream temperature is compared with the corresponding dew and bubble point temperatures. For vapor-liquid equilibrium (VLE),

$$y_i = K_i x_i \tag{5.12}$$

Where $K_i = \frac{P_i^{sat}(T)}{P}$ from Raoult's law for an ideal mixture; $K_i = \frac{H_i}{P}$ for a dilute mixture; y_i, x_i are the vapor and liquid phase mole fractions for component i; $P_i^{sat}(T)$ is the vapor pressure of component i at temperature, T and P, H_i are the total pressure and Henry constant. $P^{sat}(T)$ and H can be computed from the extended Antoine and Henry correlations [65]:

$$\log(P_i^{sat}) = A_1^i + \left(\frac{A_2^i}{A_3^i + T}\right) + A_4^i T + A_5^i Log(T) + \left(A_6^i T^{A_7^i}\right) \tag{5.13}$$

$$\log(H_i) = H_1^{i-j} + \frac{H_2^{i-j}}{T} + H_3^{i-j} Log(T) + H_4^{i-j} T + H_5^{i-j} T^2 \tag{5.14}$$

where j represents the solvent component. H_k^{i-j} and A_k^i are respectively the Henry and Antoine correlation coefficients.

5.2.3.4.1. Bubble point calculation

At the bubble point, the computed sum of the component fractions in the just-formed vapor bubble is equal to 1 [66]:

$$\sum y_i = \sum \frac{P_i^{sat}(T)}{P} x_i = 1 \tag{5.15}$$

For example, for the single component H_2O purge stream, $x_{H_2O} = 1$ and equation 5.15 becomes

$$P = p_{H_2O}^{sat}(T) \tag{5.16}$$

The bubble point temperature for H_2O can then be obtained by substituting equation 5.13 into (5.16) with $i = H_2O$ and P = overall stream pressure. The Antoine parameters for H_2O are listed in Table 5.8.

5.2.3.4.2. Dew point calculation

Similar to the bubble point analysis, at dew point, the sum of the component fractions of the first liquid bubble is equal to 1 [66]:

$$\sum x_i = P \sum \frac{y_i}{P_i^{sat}(T)} = 1 \tag{5.17}$$

For the single component H_2O stream, $y_{H_2O} = 1$ and the dew point temperature is found to be identical to the bubble point temperature. For the flue gas dew point, there are two options for estimating the dew point temperature. The first option is to assume that the other gas phase components (mostly CO_2 and any unspent fuel) are non-condensable, and only water vapor moves to the liquid phase. For this case, equation 5.17 becomes:

$$\frac{y_{H_2O}}{P_{H_2O}^{sat}(T)} = \frac{1}{P} \tag{5.18}$$

The other option is to consider all the gas phase components. This case assumes that for the multicomponent exhaust streams, the liquid phase will contain only dilute amounts of the other

gases. So, for example, since the fuel-side exhaust condensate could contain some CO_2 and unspent fuel, the vapor pressure defined in equation 5.13 can be replaced with the Henry constant defined equation 5.14 for these components so that equation 5:17 becomes:

$$\frac{y_{H_2O}}{P^{sat}_{H_2O}(T)} + \frac{y_{CO_2}}{H_{CO_2}(T)} + \frac{y_{fuel}}{H_{fuel}(T)} = \frac{1}{P} \tag{5.19}$$

For the typical conditions in this study, both estimates predict nearly identical dew points so the simpler equation 5.18 was used. The Henry parameter values are listed in Table 5.7.

5.2.3.4.3. Two-phase calculations

When the parent stream temperature is between the dew and bubble point, it contains both vapor and liquid phases. Therefore, flash calculations are required to determine the amounts and compositions of the vapor/liquid fractions. This is necessary for accurate computation of the corresponding enthalpies. The vapor - liquid split can be obtained using the Rachford-Rice flash and flow conservation expressions:

$$\sum_i \frac{z_i(K_i-1)}{1+\frac{V}{F}(K_i-1)} = 0 \tag{5.20}$$

$$F = V + L \tag{5.21}$$

Where z_i is the composition of the feed stream; F, V, L are the feed flow, vapor split and liquid split.

5.2.3.4.4. The flash model

To avoid discontinuities due to runtime decision making for VLE calculations, a formulation that integrates flash calculations with the disjunctions is used. This formulation is designed to be applicable, irrespective of whether or not the two-phase region is traversed [59]. Thus, if only vapor or liquid outlet exists, this pressure-temperature (P-T) flash model forces the flash to be evaluated at the dew or bubble point conditions of the parent stream, and calculates the heat duty as an output value from enthalpy balance. The flow rate and composition data are derived from the parent stream while the associated flash temperature and duty are calculated as follows:

$$H_{flash_{in}} = H(T_{IN}) - H_v\left(T_{in}^{sup}\right) + H(T_{DP}) + H(T_{BP}) - H_L\left(T_{in}^{sub}\right) \quad (5.22)$$

$$T_{flash} = T_{out}^{2p} \quad (5.23)$$

$$Q_{flash} = VH_v\left(T_{flash}, y\right) + LH_L\left(T_{flash}, x\right) - H_{flash_{in}} \quad (5.24)$$

where $H(T)$ is the enthalpy of the parent stream at temperature, T; T_{flash} is the temperature for flash calculation; H_v, H_L explicitly refer to the enthalpy correlations corresponding to the vapor and liquid phases and Q_{flash} is the calculated heat duty. To illustrate how this works, consider a superheated hot inlet stream for which the outlet is in the two-phase region. For this case, γ_{in}^{v} *and* γ_{out}^{vl} from Figure 5-3 become true, and the corresponding constraints apply. Substituting into equations 5.22 and 5.23 gives:$H_{flash_{in}} = H_{DP}$; $T_{flash} = T_{OUT}$. If the exit were sub-cooled, then $H_{flash_{in}} = H_{BP}$; $T_{flash} = T_{BP}$. If the exit were at the two-phase boundary, then $H_{flash_{in}}$ and T_{flash} will correspond to either the dew point or bubble point conditions.

Having calculated the heat duty, the corresponding heat load for the flue gas and H_2O sub-streams can be determined using the following equations:

Air/Fuel-side exhaust stream

$$Q_{flue}^{sup} = m\left(H_{v,flue}\left(T_{in}^{sup}\right) - H_{v,flue}\left(T_{out}^{sup}\right)\right) \quad (5.25)$$

$$Q_{flue}^{2p} = -m\, Q_{flash,flue} \quad (5.26)$$

$$Q_{flue}^{sub} = m\left(H_{v,flue}\left(T_{in}^{sub}\right) - H_{v,flue}\left(T_{out}^{sub}\right)\right) \quad (5.27)$$

Air/Fuel-side H_2O stream

$$Q_{flue}^{sup} = m\left(H_{v,H_2O}\left(T_{out}^{sup}\right) - H_{v,H_2O}\left(T_{in}^{sup}\right)\right) \quad (5.28)$$

$$Q_{flue}^{2p} = m\, Q_{flash,H_2O} \quad (5.29)$$

$$Q_{flue}^{sub} = m\left(H_{v,H_2O}\left(T_{out}^{sub}\right) - H_{v,H_2O}\left(T_{in}^{sub}\right)\right) \quad (5.30)$$

Notice that if the hot flue outlet were in the two phase region, $T_{in}^{sub} = T_{out}^{sub} = T_{BP}$ and the subcooled heat load from equation 5.27 becomes zero.

5.2.3.5. Simplification

The formulation described above for the MHEX model is not a very tractable nonlinear programming problem to solve and usually requires special care both in the choice of solvers and in the specification of parameter values. Since this model will be embedded in an outer system-level model for the analysis of the overall energy conversion system, it is useful to apply modifications that reduce the size of the MHEX model without significantly impacting prediction accuracy. The proposed simplifications rid the model of the need to evaluate the disjunctions and are based on the following assumptions

I. Only superheated steam is allowed for purging at the reactor inlet; therefore, the heat exchanger exit steam vapor fraction must be equal to 1.
II. The heat exchanger inlet purge H_2O stream is always sub-cooled.
III. Heat duty from condensation from the air and fuel hot exhaust streams is negligible.

Assumptions I and II are practical requirements for operating the reactor. Assumption III is valid for the depleted air exhaust stream, which has a relatively low H_2O fraction. It is also mostly valid for the fuel-side exhaust stream, as simulations show that the exhaust temperature is typically above the corresponding dew point. These assumptions invariably fix the values of the disjunction variables so that the set of constraints from Figure 5-3 that apply for the MHEX streams are known a priori. This makes it possible to eliminate the disjunction and logic constraints in Table 5.2 and the reformulations of equations 5.4 to 5.11 from the model. These simplifications lead to significant reduction in computational complexity.

5.2.4. The reactor model

In chapter 4, the formulation for the reduced fidelity model of the rotary CLC reactor was described in detail. The reduced model was developed as a steady-state approximation of the detailed reactor model from [28], [29] and is represented by the following optimization model:

$Minimize\ \varphi^{obj}$

s.t.

$H(x) = 0$

$$G(x) \leq 0$$

$$x_{\min} \leq x \leq x_{\max}$$

$$\gamma(x) \qquad \text{ref: (4.55)}$$

where $H(x), G(x)$ are equality and inequality constraints that satisfy reactor design requirements; $x_{\min}, x_{\max}$ are variable bounds and $\gamma(x)$ represents other model parameters and specifications. Like the case for the MHEX model, the objective function, φ^{obj} may correspond to the reactor or to the outer flowsheet model. The key reactor variables are given in equation 5.31:

$$x = \left[\theta_i,\ u_i, l, D, T\left(\frac{1}{\omega}\right)\right] \tag{5.31}$$

where θ_i = sector size, u_i = sector feed gas velocity, l = reactor channel length, D = reactor diameter, T = cycle period, ω = reactor drum rotational speed, i = fuel, fuel purge, air and air purge sectors. The reactor design requirements constitute the governing equations for the reduced model and are represented by constraints that govern fuel conversion, CO_2 separation, reactor energy balance, oxygen carrier conservation and other reactor specifications. These governing equations are summarized here, but the full derivation and validation can be found in chapter 4.

5.2.4.1. Fuel conversion

The channel length required for a specified extent of fuel conversion is determined by assuming a reactive plug flow within each channel, with the conversion rate controlled by the reduction reaction between the fuel and the metal oxides on the channel wall. Thus the conversion criteria requires that the reactor channel length be greater than or equal to the required fuel conversion length

$$\int_0^{l_{reactor}} dz \geq (1+k)\ \frac{1}{\varphi}\int_{w(0)}^{w(z)} \left(\frac{w}{1-w}\right)^n dw \tag{5.32}$$

Where $l_{reactor}$ is the reactor channel length; k is an adjustable safety factor; $w = \frac{1}{[1-\emptyset x_{c_m H_n}]}$; $\emptyset = 1 - m - \frac{n}{2}$ for a reduction reaction of the form, $C_mH_n + zMeO \rightarrow mCO_2 + \frac{n}{2}H_2O + zMe$; $\varphi = \frac{-P_c \delta_{oc} \varepsilon_s k_p C_{tot}^{n-1} X^{\beta}}{\emptyset^{n-1} \alpha_0 A_p}$; $k_p = k_0 \left(\frac{P}{P_0}\right)^{-a} e^{-\frac{E}{RT}}$; $k_0, n, X \text{ and } \beta$ are the Arrhenius constant, order of

reaction, non-dimensional OC conversion and OC geometry coefficient; $\left(\frac{P}{P_0}\right)^{-a}$ = pressure inhibition coefficient, $E, R, P_c, \delta_{oc}, \varepsilon_s \; and \; C_{tot}$ are the activation energy, universal gas constant, channel perimeter, oxygen carrier layer thickness, oxygen carrier solid fraction and total gas concentration within the channel respectively. The kinetic coefficients and parameters are derived from the kinetics proposed by Abad et al. for copper, iron and nickel-based oxygen carriers [5], [49], [50].

5.2.4.2. Carbon separation

The carbon separation criteria prevents gas carry-over between the fuel and air sectors by requiring that the channel residence time in the fuel or air purge sectors be longer than the effective gas residence time in the respective channels:

$$\int_0^{l_{reactor}} \frac{dz}{u_k} \leq \frac{\theta_k}{\omega} \tag{5.33}$$

Here k = fuel purge and air purge sector, ω = angular velocity of rotary drum, θ = sector size, and u = purge steam velocity.

5.2.4.3. Energy balance

For the adiabatic rotary reactor, the net enthalpy change of the reactor streams should be equal to zero. This energy balance is used to determine the required air flow for reactor thermal regulation.

$$\sum n_k \hat{h}_k(T_{in,k}) - \sum n_z \hat{h}_z(T_{ad}) = 0 \tag{5.34}$$

Here n_k = molar flow rate of sector k, a function of sector inlet velocities, k = air, air purge, fuel and fuel purge sectors, n_z = molar flow rate of zone z, z = air and fuel zones, $\hat{h}$ = stream enthalpy, T_{ad} = (adiabatic) reactor exit temperature. The rotary drum size is related to the specified reactor thermal size by the following expression

$$D^2 = \frac{4\dot{W}_{thermal}}{LHV \; C_{tot} \; x_{fuel} \; u_{fuel} \; \theta_{fuel}(1-\varepsilon_{solid}) \; \pi} \tag{5.35}$$

Here LHV = lower heating value of the fuel, equivalent to the net reaction enthalpy, ε_{solid} = solid fraction of reactor cross-section, D is the reactor diameter.

5.2.4.4. Oxygen carrier conversion

For cyclic stationary operation, the amount of oxygen carrier (OC) oxidized in the air sector should be greater than or equal to the amount of OC reduced in the fuel sector. The inequality accommodates some OC conversion in the fuel purge sector

$$\left(\frac{dX}{dt}\right)_{reduction}^{-1}\left(\frac{\theta_{fuel}}{\omega}\right) \leq \left(\frac{dX}{dt}\right)_{oxidation}^{-1}\left(\frac{\theta_{air}}{\omega}\right) \tag{5.36}$$

Where $\left(\frac{dX}{dt}\right)_j = \frac{\vartheta_{oc,j}}{\rho_s} k_p C_{i,j}^n \left(X_0 - X^\beta\right)$; j = reduction/oxidation; $C_{i,j}$ is the gaseous reactant i concentration in reaction j; X_0 = the reference OC conversion state.

5.2.4.5. Other reactor specifications

The sector sizes should be selected to avoid complete OC consumption, particularly in the fuel sector where residual metal oxide helps mitigate carbon deposition risk.

$$\frac{\theta_{fuel}}{\omega} \leq \left(\frac{dX}{dt}\right)_{reduction}^{-1} \tag{5.37}$$

where $\left(\frac{dX}{dt}\right)_{reduction}^{-1}$ is the time (in seconds) required for complete reduction of the oxygen carrier. Also, the air supply to the reactor should always be greater than or equal to the stoichiometric air flow required for the target fuel conversion. In other words,

$$(\Omega)u_{fuel}\theta_{fuel}x_{fuel} \leq u_{air}\theta_{air} \tag{5.38}$$

Where Ω = air/fuel mole ratio. Since reduction reactions take place in the fuel purge sector, the purge steam velocity should allow sufficient time for carried-over fuel to be completely converted before leaving the channel. For this reason, the fuel purge velocity is specified to be similar to that in the fuel sector to achieve the desired fuel conversion

$$(1+\lambda)u_{fuel} = u_{fuelpurge}, \quad \lambda_{min} \leq 0 \leq \lambda_{max}, \ |\lambda_{min}, \lambda_{max}| \ll 1 \tag{5.39}$$

Here λ is an adjustment factor. To ensure a feasible solution for the sector sizes, the constraint that the fractional sector sizes sum up to unity is applied:

$$\sum \theta_i = 1, \qquad i = air, air\ purge, fuel\ \&\ fuel\ purge\ sectors \tag{5.40}$$

The equality and inequality constraints of equations 5.31 to 5.40 constitute the rotary reactor model and can be incorporated into the system-level model either directly or as an independent sub-model, depending on whether and equation oriented or sequential modular approach is used in flowsheet programming.

5.2.5. Pressure change models

5.2.5.1. Turbine

The turbine model is formulated from energy conservation defined for a control volume around the turbine. For steady-state, adiabatic turbine operation,

$$W_T + \dot{m}h(T_{in}, x) - \dot{m}h(T_{out}, x) = 0 \tag{5.41}$$

W_T is the turbine power output; $\dot{m}$ is the molar flow rate; h is the specific molar enthalpy; x refers to the component mole fractions. For the ideal isentropic turbine, there is no heat flow across the system boundary and the outlet temperature is related to the inlet temperature by the following ideal isentropic relation

$$\hat{T}_{out} = T_{in}\, \hat{\pi}^{-\alpha} \tag{5.42}$$

Here $\hat{\pi} = \frac{P_{in}}{P_{out}}$ is the turbine pressure ratio; $\alpha = \frac{\frac{c_p}{c_v} - 1}{\frac{c_p}{c_v}}$; c_p, c_v are respectively the specific heat capacity at constant pressure and volume; $\hat{T}_{out}$ is the isentropic outlet temperature. An isentropic efficiency, $\acute{\eta}_{isen}$, is applied to account for irreversibilities in a real turbine:

$$\acute{\eta}_{isen} = \frac{h(T_{in}) - h(T_{out})}{h(T_{in}) - \hat{h}(\hat{T}_{out})} = \frac{T_{in} - T_{out}}{T_{in} - \hat{T}_{out}} \tag{5.43}$$

Therefore, the turbine exit temperature can be obtained by rearranging equation 5.43

$$T_{out} = T_{in} - \acute{\eta}_{isen}\left(T_{in} - \hat{T}_{out}\right) \tag{5.44}$$

5.2.5.2. Compressor

Similar to the formulation for the turbine, the compressor model can be represented with the following equations:

$$W_c + \dot{m}_{in}h(T_{in},x) - \dot{m}_{out}h(T_{out},x) = 0 \quad (5.45)$$

$$\hat{T}_{out} = T_{in}\,\hat{\pi}^{\alpha} \quad (5.45)$$

$$\dot{\eta}_{isen} = \frac{h(T_{in}) - \hat{h}(\hat{T}_{out})}{h(T_{in}) - h(T_{out})} = \frac{T_{in} - \hat{T}_{out}}{T_{in} - T_{out}} \quad (5.47)$$

$$T_{out} = T_{in} - \frac{(T_{in} - \hat{T}_{out})}{\dot{\eta}_{isen}} \quad (5.48)$$

$T_{in}, T_{out}, \dot{\eta}_{isen}$ *and* $\hat{\pi}$ are the inlet temperature, compressor exit temperature, compressor isentropic efficiency and compressor pressure ratio, respectively. The compressor model allows for the flexibility of choosing multistage compression with intercooling, in which case an intercooling temperature, T_0, is specified as the inlet temperature for each intermediate stage, and the inter-stage pressure ratio is defined as

$$\hat{\pi}_i = \hat{\pi}^{\frac{1}{n}} \quad (5.49)$$

Where n is the number of compressor stages.

5.2.5.3. CO_2 pump

For the CO_2 train, there are two phases of the compression process. The first phase is the gas compression phase, where the CO_2 is compressed up to its critical pressure. The compressor model for this phase is the same as already described. The second phase is the pumping phase, where the supercritical CO_2 is then pumped from the critical pressure to the sequestration pipeline pressure. For this phase, the compression power input is given by the following relation

$$W_p = \frac{\dot{m}_{in}}{\rho_{CO2}}\left(\frac{\Delta P}{\dot{\eta}^{p}_{isen}}\right) \quad (5.50)$$

$\dot{m}_{in}$ is the mass flow rate in kg/sec; ρ_{CO2} is the average density of supercritical CO_2 in kg/m^3 [67]; $\dot{\eta}^{p}_{isen}$ is the pump isentropic efficiency and ΔP is the pump pressure difference in Pascals.

5.2.6. System integration

So far, the component sub-models that have to be combined to represent the integrated rotary reactor-based power plant have been defined. The process representation of the integrated plant is in reality a system of linear and non-linear algebraic constraints of the form:

$$F(x) \leq 0 \tag{5.51}$$

Where F is the vector of functions and x is the vector of process variables. Indeed, F and x could represent individual process unit blocks or the overall flowsheet. The former typically falls under a class of flowsheet analysis strategy known as sequential modular programming while the latter case corresponds to the equation oriented programming. This study used the equation oriented approach for flowsheet optimization. With each flowsheet component defined as a mathematical model with a set of equations and variables, the equation oriented approach assembles these sub-models into one grand system of equations and solves them simultaneously [68]–[70]. Figure 5-4 illustrates the strategy employed for the simultaneous optimization of the integrated recuperative cycle. The system of mathematical formulations that relate the variables and specifications of each sub-model, as well as implicit connecting stream identities and variable bounds, are pooled together to form a set of equality and inequality constraints that define the feasible space for the entire system. Thus the overall solution structure optimizes for efficiency or some surrogate function, subject to the assembled constraints and variable bounds.

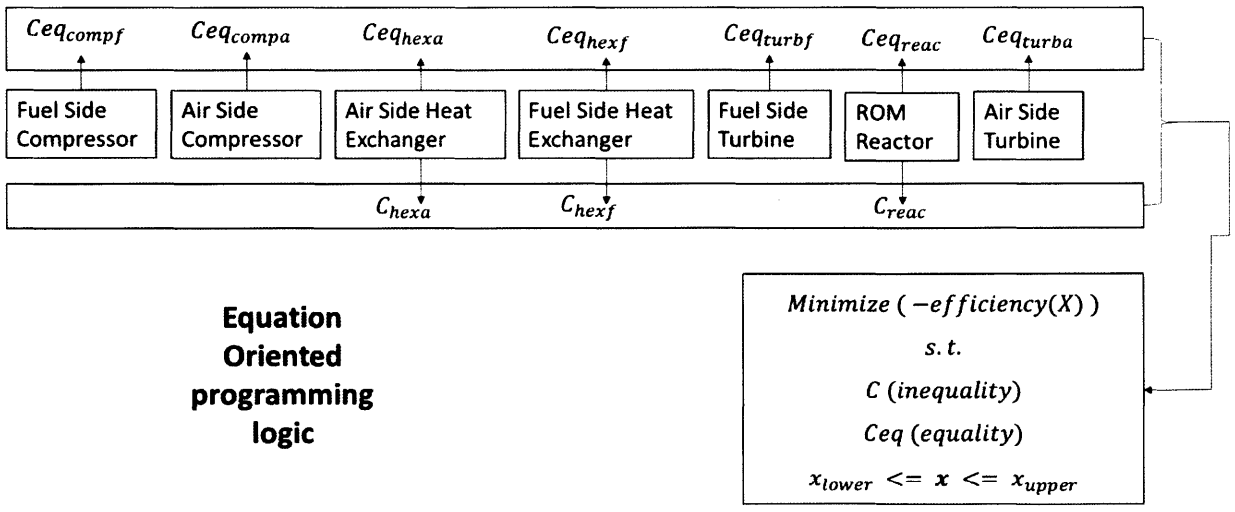

Figure 5-4: Equation oriented setup for the integrated recuperative cycle model.

5.2.7. Specifications and implementation

The integrated rotary CLC reactor-based power plant model was implemented in Matlab® for nickel, copper and iron-derived oxygen carriers. The non-linear constrained minimization solver, fmincon, which uses sequential quadratic programming algorithm, was used for flowsheet optimization. The oxygen carrier properties are listed in Table 5.3. Table 5.4 and Table 5.5 contain the base case input specifications and key variable bounds for the reactor. Table 5.6 lists important system-level specifications. The reactor exit temperature for copper is about 150K lower than those for nickel and iron because of the limitation imposed by the low melting point of copper. CH_4 is selected as the fuel for these studies and the corresponding redox reaction equations can be found in Table 5.3. A single reactor with thermal size capacity of 25MW is modeled in this study. The required fuel flow rate is calculated by dividing this value by the fuel LHV.

Table 5.3: Oxygen carrier property data

Oxygen Carrier	**CuO/Cu**		**NiO/Ni**		**Fe_2O_3/Fe_3O_4**	
	Oxidation	Reduction	Oxidation	Reduction	Oxidation	Reduction
Melting point	1446C / 1085C		1955C / 1455C		1565C / 1597C	
Apparent density $kg\ m^{-3}$	1800		3446		3257	
Porosity	0.57		0.36		0.3	
Rate constant $K_0 m^{3n-3} mol^{1-n} s^{-1}$	$2.04\ x\ 10^4$	$1.13\ x\ 10^6$	$9.31\ x\ 10^3$	$3.09\ x\ 10^6$	$3.58\ x\ 10^3$	$9.23\ x\ 10^3$
Reaction order, n	1	0,4	0.2	0.8	1	1.3
Pressure coefficient	0.68	0.83	0.46	0.93	0.84	1.03
Activation energy, E $KJ\ mol^{-1}$	15	60	7	78	14	49

Table 5.4: Reactor base case specification

OC	CuO/Cu	NiO/Ni	Fe_2O_3/Fe_3O_4
Size			
Reactor thermal size (MW_{th})	25	25	25
Design			
OC layer thickness, δ_{oc} (μm)	50	50	50
Channel width, d (mm)	2	2	2
Support layer thickness, $\delta_{bulk}(mm)$	210	210	210
Operation			
Fuel sector inlet stream fuel fraction ($vol\%$)	15	25	50
Reference fuel sector inlet velocity (m/s)	0.09	0.25	0.065
Cycle period (sec)	30	30	30
Fuel conversion efficiency (%)	95	95	95

Table 5.5: Variable bounds

Variable group	**Upper bound**	**Lower bound**	**Comments**
Gas velocities (m/s)	4	0.01	An upper bound of 2 is set for fuel and fuel purge velocities
Sector sizes	0.8	0.03	
Reactor length (m)	4	0.1	The limiting consideration is reactor pressure drop, which is desired to be below 1%
Reactor diameter (m)	6	0.3	The upper bound defines the maximum single reactor diameter desired for this thermal capacity range
Period (sec)	48	12	60% variation from a reference value of 30
Temperatures (K)	1800	288	

Flow rates (mol/sec)	500 x fuel flow	0.1 x fuel flow	This allows scaling the flows based on the fuel flow rate
Gas Compositions	1	0	

Table 5.6: Integrated system base case specifications

Item	Units	CuO/Cu	NiO/Ni	Fe_2O_3/Fe_3O_4
Reactor exit temperature	K	1314	1473	1473
Ambient temperature	K	288	288	288
Ambient pressure	bar	1	1	1
Compressor pressure ratio		5	5	5
Turbine isentropic efficiency	%	90	90	90
Compressor isentropic efficiency	%	90	90	90
Mechanical efficiency	%	100	100	100
Transport co_2 compression pressure	bar	110	110	110
Recuperator minimum pinch	K	25	25	25
Intercool temperature	K	303	303	303
Bulk support layer material		Boron nitride		
Fuel		CH_4		
Ch_4 lower heating value (LHV)	kJ/mol	802.4		
Inlet air N_2 composition	%	79		
Inlet air O_2 composition	%	21		
Number of air-side compressor stages		1, 3		
Number of fuel-side compressor stages		2		
Number of CO_2 compressor stages		9		

Table 5.7: Henry parameters

$\log(H_i) = H_1^{i-j} + \frac{H_2^{i-j}}{T} + H_3^{i-j} Log(T) + H_4^{i-j} T + H_5^{i-j} T^2$					
Component pair	H_1^{i-j}	H_2^{i-j}	H_3^{i-j}	H_4^{i-j}	H_5^{i-j}
N_2 / H_2O	176.507	-8432.77	-21.558	-8.44E-3	0
O_2 / H_2O	155.921	-7775.06	-18.3974	-9.44E-03	0
CO_2 / H_2O	170.7	-8477.7	-21.95	0.00578	0

Table 5.8: Antoine parameters

$\log(P_i^{sat}) = A_1^i + \left(\frac{A_2^i}{A_3^i + T}\right) + A_4^i T + A_5^i Log(T) + \left(A_6^i T^{A_7^i}\right)$							
Component	A_1^i	A_2^i	A_3^i	A_4^i	A_5^i	A_6^i	A_7^i
H_2O	72.55	-7206.7	0	0	-7.1385	4.406E-06	2

The thermal properties of the gas mixtures are calculated using correlations from the NIST thermo-physical property database [71]. Steam data is obtained using the Matlab XSteam implementation of the IAPWS IF97 standards formulation [72]. For gas compression, a two-stage compressor on the fuel-side and a three-stage compressor on the air side are used for the base case simulation. However, the model allows the selection of any number of compressor stages. The power requirement for CO_2 compression is computed using a 5-stage intercooled compressor for the gas compression side, and a pump for the supercritical fluid side. There is no guarantee that either the fuel or air-side exhaust enthalpy is sufficient to generate the steam needed in the corresponding reactor sector. For this reason, a splitter is introduced upstream of the recuperator to redistribute the feed water flows to both recuperators. The split fraction is thus included as a free variable to be solved for during the flowsheet optimization. The CO_2 compression unit delivers supercritical CO_2 at 110 bars and 30C to an external CO_2 pipeline. Water is condensed out in the intercoolers during the compression process.

The model was run from several starting points randomly selected from a pre-defined parameter range, since the optimal solution is not unique and each solution is only guaranteed to be a local minimum. The different starting points were determined as follows:

$$x_{0_i} = x_{0_{lower}} + \left(x_{0_{upper}} - x_{0_{lower}}\right) * \tilde{\varphi}_{rand,i} \tag{5.52}$$

$x_{0_{upper}}, x_{0_{lower}}$ represent the lower and upper initial vector ranges; $\tilde{\varphi}_{rand,i}$ is a random parameter generated for simulation run i. To improve the gas velocity initial estimates for cases with different operating conditions, the velocity values are scaled to maintain similar molar flow within each channel using the following expression:

$$v_{new} = \left(\frac{P_{ref}}{P_{new}}\right)\left(\frac{T_{new}}{T_{ref}}\right) v_{ref} \tag{5.53}$$

Here v, P, and T refer to velocity, pressure and temperature respectively.

5.3. Results and discussion

5.3.1. Base case results

The flowsheets showing simulation results for the integrated cycle for nickel, copper and iron-based rotary reactors are presented in Figure 5-5, Figure 5-6 and Figure 5-7. These results show the thermodynamic states, compositions and flow rates of the process streams at the inlets and exits of each major component. Input specifications are in regular font while computed values are highlighted. These results are optimized values for the given base case operating conditions and system specifications. Note that unlike the results presented in chapters 2 and 3, the purge steam flow rates are computed by the model in response to the actual steam requirement in the reactor and not simply supplied as input parameters. Also, since the model optimizes for steam generation strategy, the purge steam for the base case conditions are mostly generated in the fuel-side recuperator. This is because the air-side flow is comparatively balanced while on the fuel side, the hot exhaust thermal capacity is significantly larger than that of the cold gas stream. Thus,

generating steam in this fuel-side recuperator creates a more thermally balanced flow which improves exhaust enthalpy recovery.

One of the consequences of the difference in purge steam demand between the three oxygen carriers is the average reactor inlet stream temperature. The nickel-based systems, which requires lower purge steam, has higher fuel-side inlet temperature than iron. This feature has a compounding effect, because the lower inlet temperature for iron leads to slower overall reduction reaction which results in a larger reactor. On the other hand, as discussed in chapters 2 and 3, increased purge steam flow up to a certain value, may constitute a net positive contribution to overall cycle efficiency. To put things in perspective, the pressure sensitivity results in Chapter 2 use a value of 1.5 for the ratio of the purge steam to fuel flow rate for the entire pressure range. However, the actual optimized value at base case compressor ratio, ($\pi = 5$) , was 1.9, and varied from 1.8 to 2.4 over the entire pressure range.

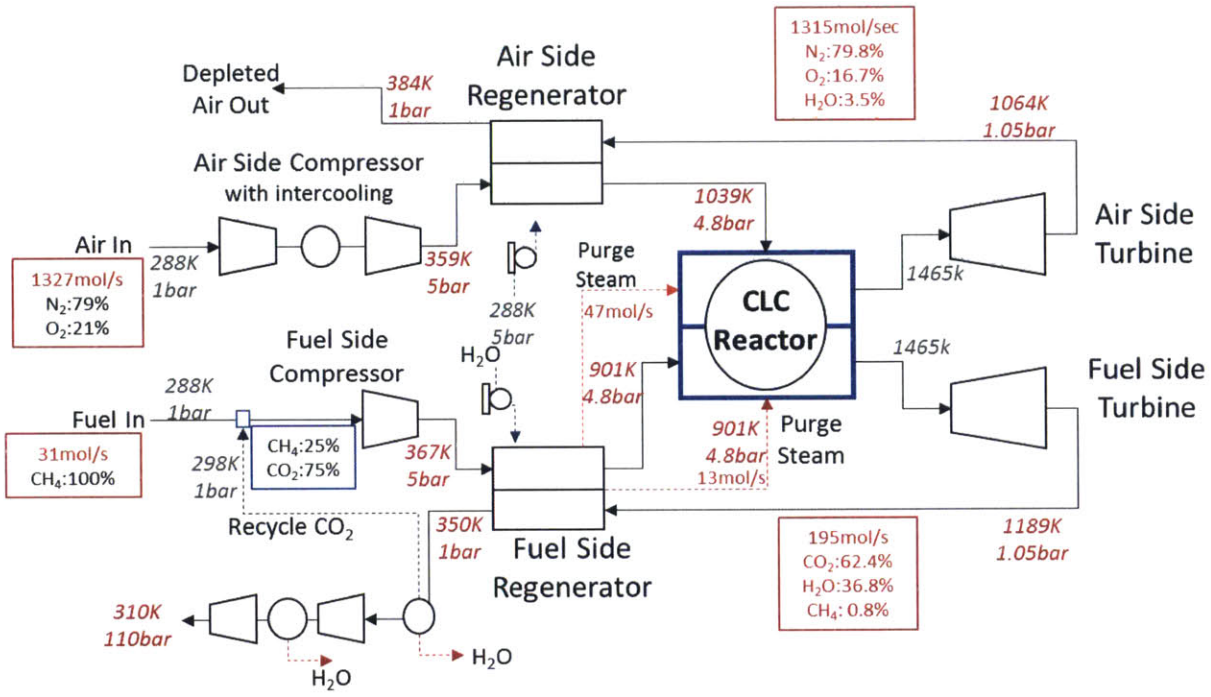

Figure 5-5: Optimized base case flowsheet results for the integrated nickel-based system.

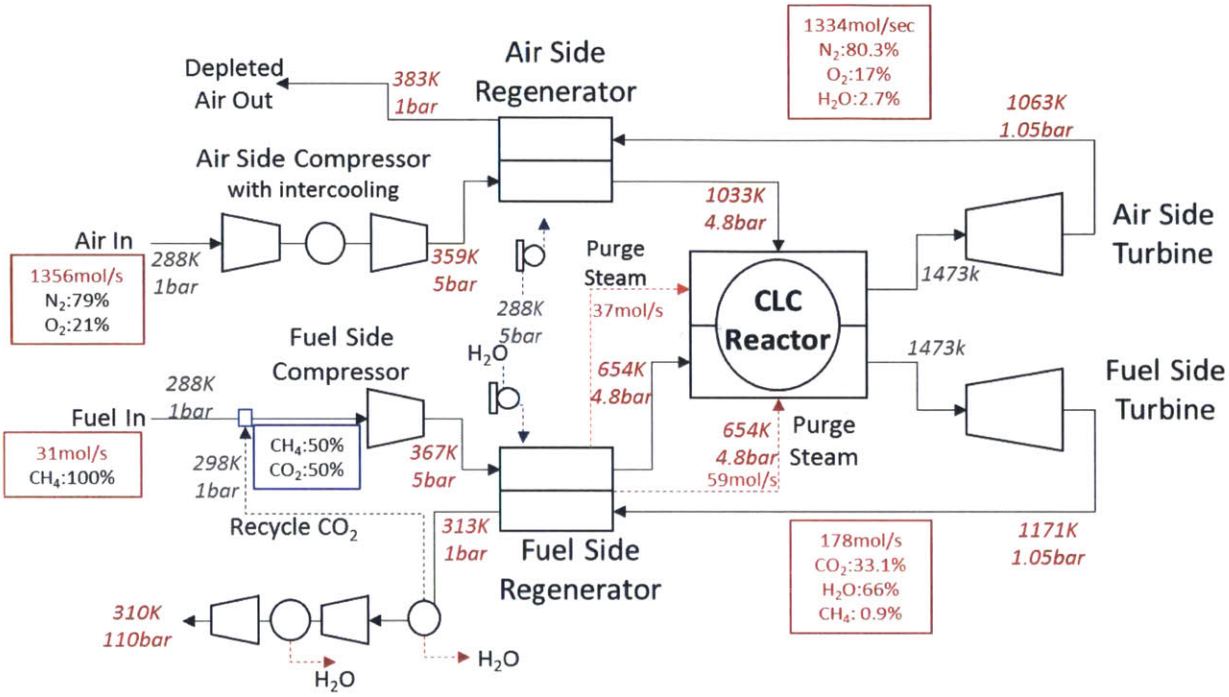

Figure 5-6: Optimized base case flowsheet results for the integrated iron-based system.

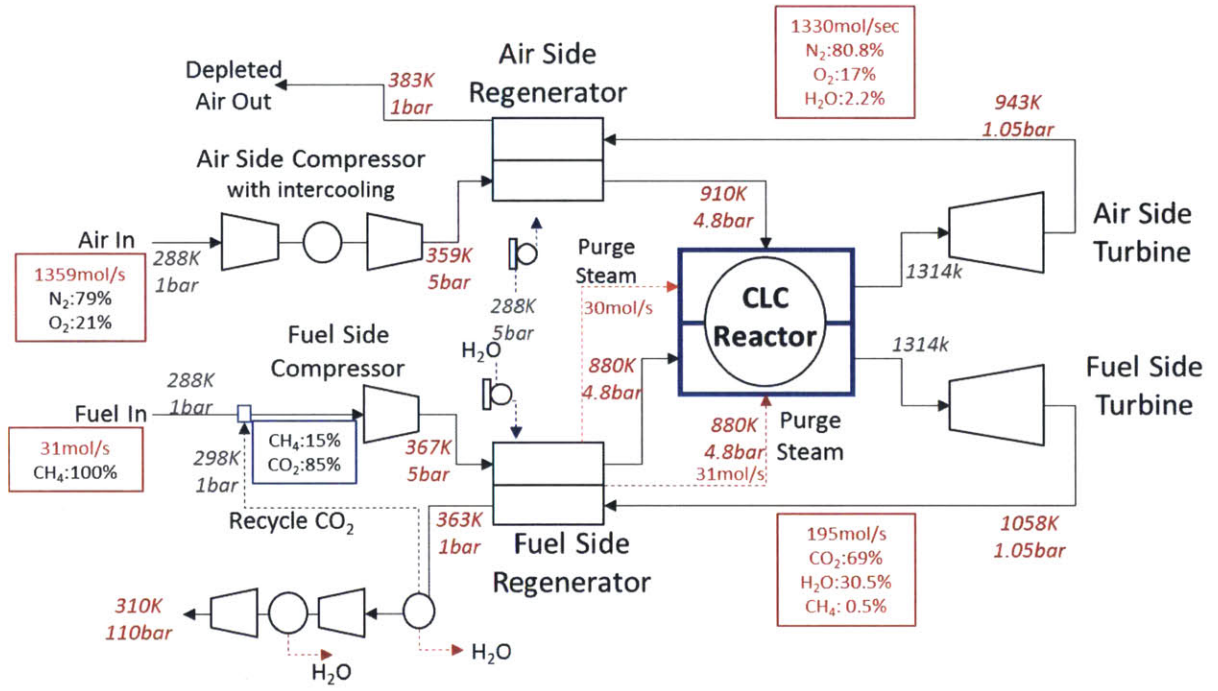

Figure 5-7: Optimized base case flowsheet results for the integrated copper-based system.

Figure 5-8, Figure 5-9 and Figure 5-10 show reactor configurations that correspond to each of the optimized flowsheets for nickel, iron and copper-based systems. These optimal reactor configuration solutions are not unique, as there are multiple combinations of geometry and flow conditions that will achieve the same efficiency objective defined at the system-level. However, it illustrates an important feature of the integrated model, which allows for the simultaneous optimization of the reactor and the rest of the integrated system for any desired objective. Comparing Figure 5-8, Figure 5-9 and Figure 5-10, it can be seen that the nickel-based system requires the smallest reactor while iron-based reactor is the largest. These differences are mostly explained by the difference in reactivity of the oxygen carriers, particularly the reduction reaction, with nickel being the most reactive and iron the least. However, since the conversion criteria only specifies a lower bound, other contributors like CO_2 separation criteria, parameter bounds, or even the quest of the model to increase efficiency by improving exhaust thermal recovery in the recuperator, also affect the optimized reactor geometry and operating conditions.

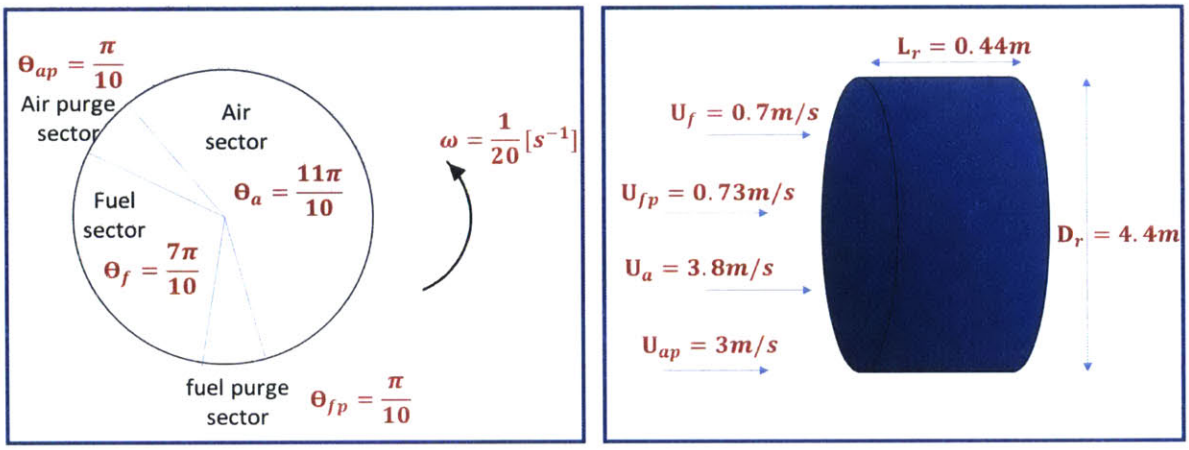

Figure 5-8: Reactor geometry and operating results at the optimized base case conditions for nickel-based carrier.

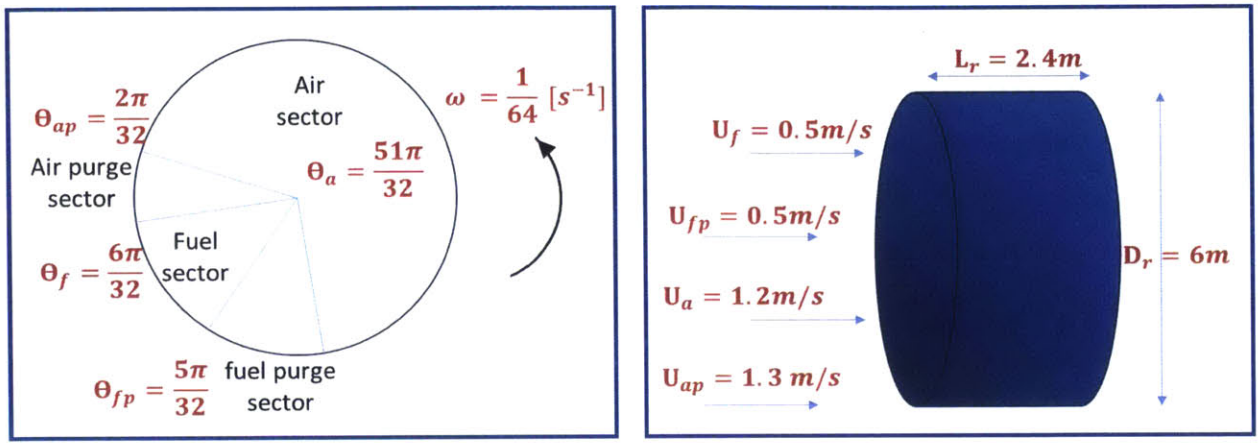

Figure 5-9: Reactor geometry and operating results at the optimized base case conditions for iron-based carrier.

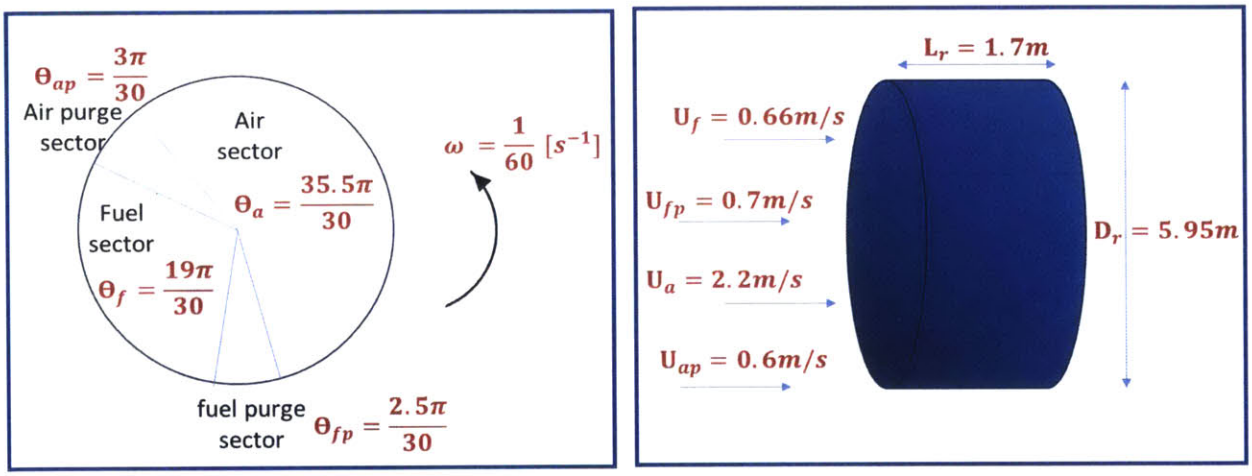

Figure 5-10: Reactor geometry and operating results at the optimized base case conditions for copper-based carrier

Table 5.9: Base case power plant performance data

	Nickel	**Iron**	**Copper**
Fuel side compressor power (w)	601,638	301,150	1,002,297
Air side compressor power (w)	6,357,318	6,581,638	6,583,385
Fuel side turbine power (w)	2,927,221	2,569,112	3,929,556
Air side turbine power (w)	18,633,550	19,149,901	16,919,566
CO_2 compression unit power (w)	406,983	406,983	406,983
With CO_2 Compression			
Net cycle power output (w)	14,194,832	14,429,242	12,856,457
Efficiency (%)	56.8%	57.7%	51.4%
Without CO_2 Compression			
Net cycle power output (w)	14,601,816	14,836,225	13,263,440
Efficiency	58.4%	59.3%	53.1%

Figure 5-11 compares the thermal efficiencies of the different oxygen carrier-based systems at base case conditions with and without exhaust CO_2 compression. The thermal efficiency for copper is constrained by its relatively low melting point. This material limit constrains the maximum reactor temperature to a little over 1300K for the copper-based oxygen carrier, compared to 1473K for nickel and iron-based carriers. The plot also shows almost 1% point higher efficiency for iron compared to nickel. This is primarily due to the difference in purge steam flows for the two systems at this base case condition. Table 5.9 provides a breakdown of the contributors to overall thermal efficiency for the three carriers. The difference in fuel-side compressor power is primarily a function of the CO_2 feed fraction in the fuel-side feed stream which is used as a carrier gas for the fuel. CO_2 fraction in the copper-based system is 85% compared to 50% in the iron-based system. The appropriate fraction for each case will ultimately be determined as tradeoff between thermal efficiency, reactor pressure drop, fuel conversion rate and plant economics. Table 5.9 also shows that CO_2 compression for sequestration typically results in about 2% point drop in efficiency (4-5% penalty).

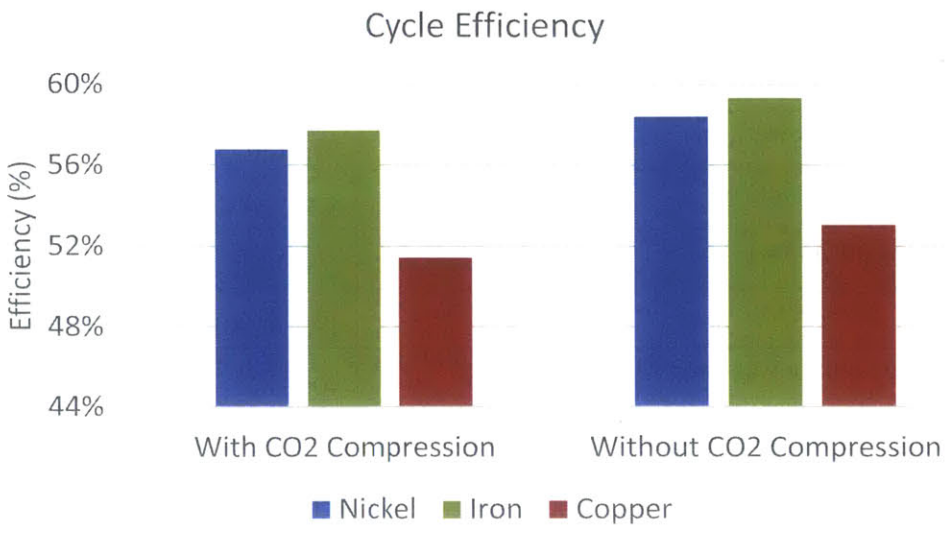

Figure 5-11: Comparing cycle efficiencies for different oxygen carriers.
Note that the turbine inlet temperature for the copper-based system is limited by its low melting point. Iron requires more purge steam than nickel which, for these conditions, results in a better exhaust enthalpy recovery in the recuperator and consequently, a higher efficiency.

Figure 5-12 and Figure 5-13 provide a more detailed comparison of the purge steam demand, reactor size and pressure drop for the three systems. In Figure 5-12, the purge steam demand distribution between the air and fuel sectors of the reactor is shown. On the fuel side, purge steam demand is lowest for nickel and highest for iron, which is a reflection of the respective reduction kinetics. This is the case because slower reduction reaction kinetics requires a larger oxygen carrier surface for complete conversion and the channel size and purge steam flow must provide sufficient residence time for complete fuel conversion in the purge sector. On the air side, however, the minimum requirement is simply that all the air is purged out before the channel enters the fuel sector. What then determines the final purge steam flow is the efficiency objective, which explains why nickel has a higher air-side purge steam flow than the other oxygen carriers. Note also that, since the maximum system temperature is lower for copper, it places a limitation on the capacity for steam generation in the recuperator compared with either the nickel or iron-based system.

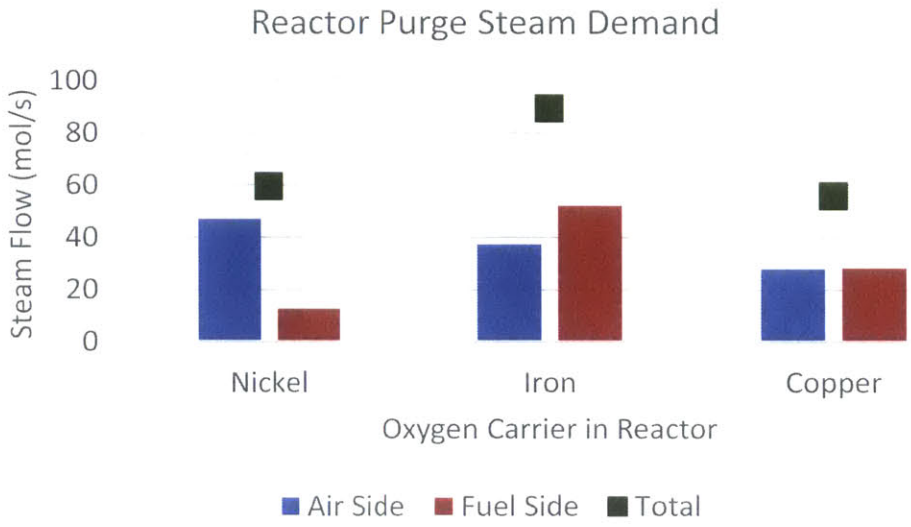

Figure 5-12: Comparing purge steam flows for the different OCs.
The fuel-side purge steam demand is a function of the rate of the OC reduction reaction and follows the expected trend. The larger Air-side purge steam for nickel results from the model attempting to optimize for efficiency, and is larger than is strictly needed for reactor purging.

Figure 5-13 compares the reactor sizes at the optimized solution for the three oxygen carrier-based systems. There are two important observations from this result. First is that in general, the observed trend is expected because the nickel-based oxygen carrier is more reactive than iron and copper-based systems at the operating conditions specified in this analysis. The second important fact is that this solution is not unique. Since efficiency is the objective, the model simply ensures that the reactor design criteria are satisfied at the optimal solution and does not have any incentive to necessarily minimize the size of the reactors. This means that it is possible to obtain a different reactor geometry and size that still achieves the same efficiency objective. This factor suggests that rather than efficiency, a more appropriate objective function would be the cost of electricity, which, to some extent, combines efficiency and economic criteria in optimizing the system. Figure 5-13 also shows that the estimated reactor pressure drop for each of the three oxygen carriers is generally less than 1% for the given operating conditions and as such can be justifiably neglected in simulating the integrated system performance.

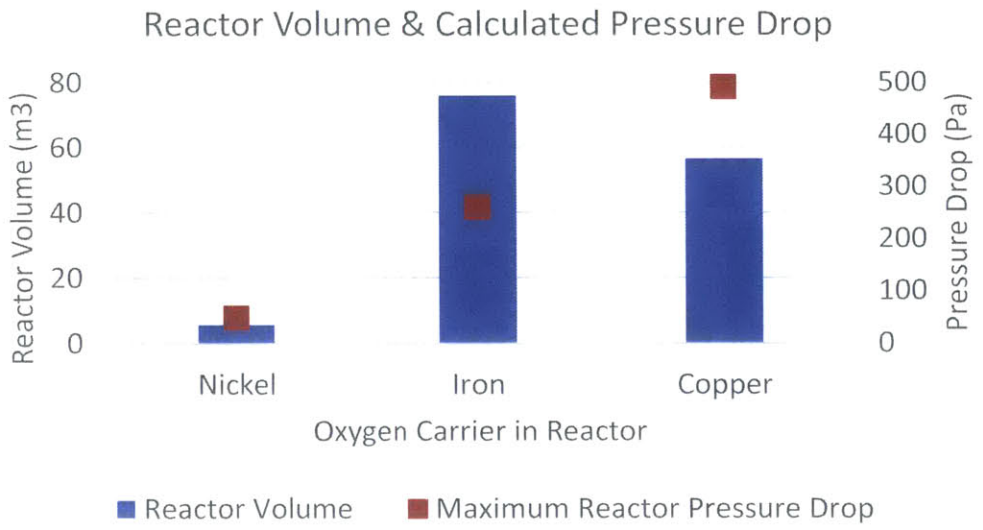

Figure 5-13: Reactor volume and pressure drop plots.
The reactor volume is generally a function of the overall reactivity of the oxygen carriers. Nickel is the most reactive and thus has the least volume. The channel pressure drops for each OC are is negligible compared to the overall reactor pressure.

5.3.2. Parametric studies

The objective of the parametric study is to determine the response of the optimal solution to changes in certain operating conditions and specifications. Due to the coupling between the reactor and the rest of the integrated system, it also provides insight into the nature and relevance of the feedback between the two in response to parameter changes. Four parameters are considered in this study: compressor pressure ratio, fuel conversion efficiency, CO_2 feed fraction and recuperator pinch. Each parameter is varied over a specific range above and below the base case values while the rest remain unchanged. The parameter variation range varies for each case but are set wide enough to capture important trends.

5.3.2.1. Pressure

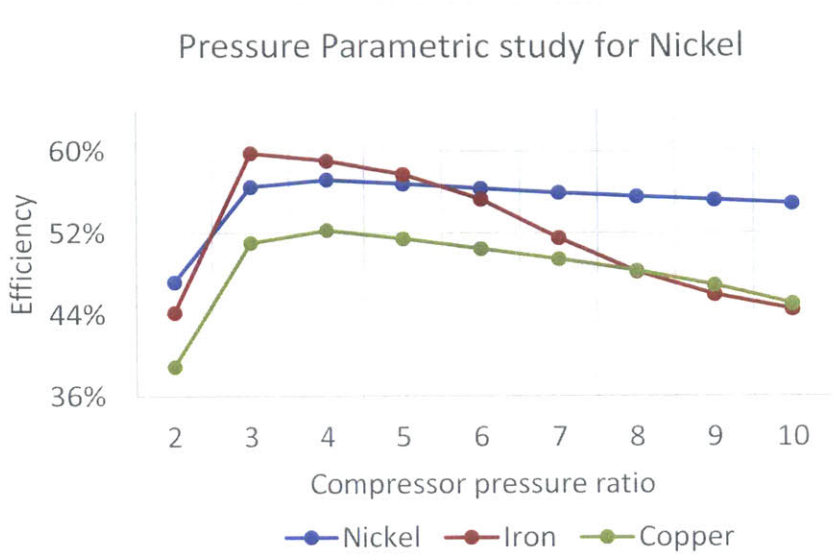

Figure 5-14: Pressure parametric study.
The larger drop of efficiency with pressure ratio for nickel is a function of the impact of increasing steam demand as reactivity has a negative proportionality to pressure.

To study the effect of pressure on the optimal cycle efficiency, the integrated system is simulated for compressor ratios (π) ranging from 2 to 10 for the different oxygen carriers. The results for this study are presented in Figure 5-14. For the iron-based system, efficiency peaks at around 59% ($\pi = 3$) while copper and nickel peak near $\pi = 4$) with 52% and 57% efficiencies respectively. However, as the pressure ratio increases, the efficiency for the iron-based system drops off considerably faster than for nickel and copper, leading to almost the same efficiencies for iron and copper-based systems at a ratio of 9. The reason for this sharp decline is explained in Figure 5-15 to Figure 5-17. As the compressor ratio increases from the base case value of 5 up to 7, Figure 5-15 shows only about 4% increase in total purge steam for the nickel-based system compared to about 50% for iron in the same range (Figure 5-16). This large increase in steam demand ends up penalizing recuperator thermal recovery and leads to lower reactor inlet temperatures, both of which end up penalizing efficiency.

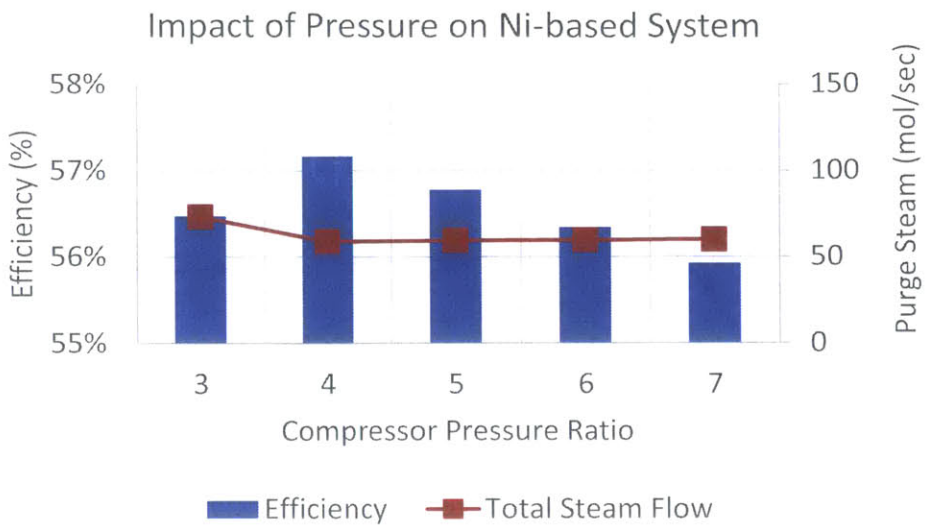

Figure 5-15: Relationship between compressor pressure ratio, efficiency and purge steam demand for a nickel-based system.

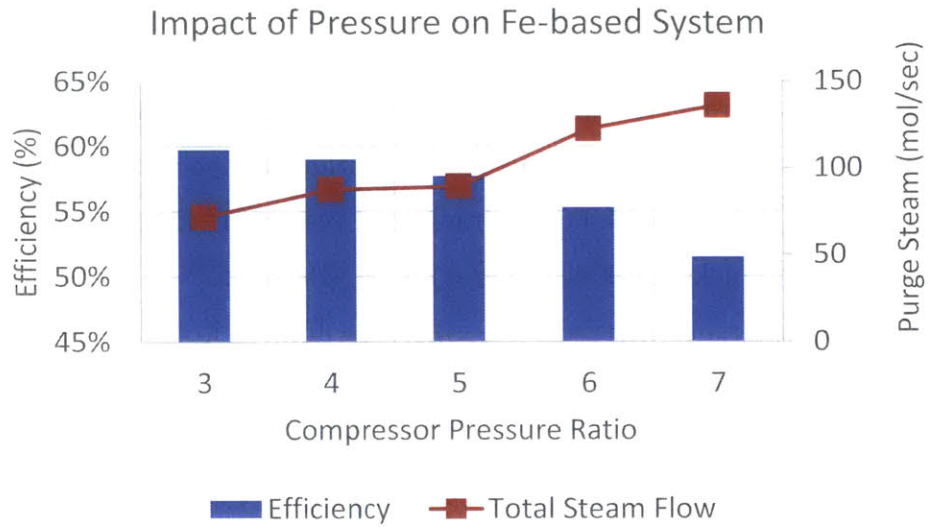

Figure 5-16: Relationship between compressor pressure ratio, efficiency and purge steam demand for an iron-based system.

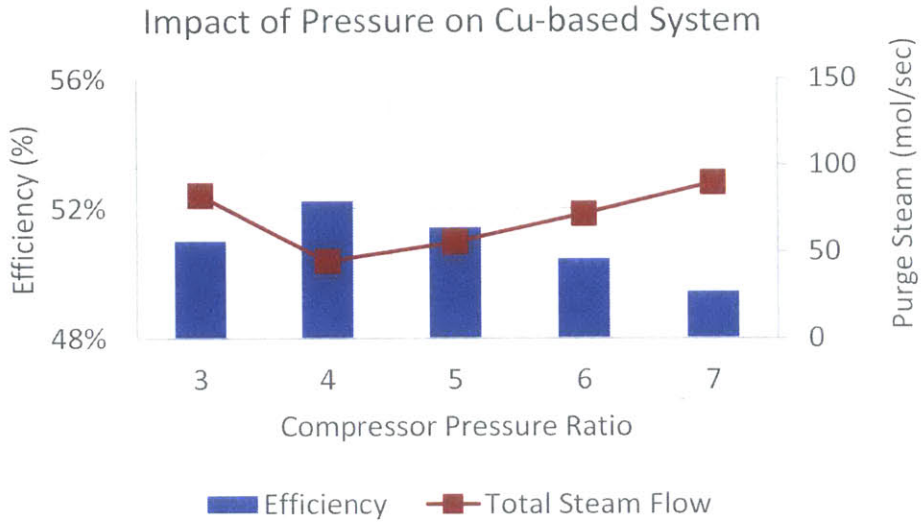

Figure 5-17: Relationship between compressor pressure ratio, efficiency and purge steam demand for a copper-based system.

However, comparing Figure 5-16 to Figure 5-17, one sees a similar increase in purge steam demand for copper as for the iron-based system, yet the drop in efficiency for iron is steeper than that for copper. One factor that explains this difference is simply the absolute amount of steam generation demand, which is larger for iron than for copper. The other factor has to do with the resulting difference in purge steam generation strategy, as illustrated in Figure 5-18. Given that the enthalpy in the fuel or air-side turbine exhaust stream might not be sufficient to meet the steam demand in the corresponding reactor sector, the model is setup to automatically assign the steam generation loads between the two recuperators in a manner that optimizes efficiency. It does this by determining the steam split fraction, which is defined as the fraction of the total steam demand that is generated in the air-side recuperator. Figure 5-18 shows a steam split fraction of zero for nickel over the entire range and for copper over most of the compressor pressure ratio range. This means that all the steam is generated on the fuel-side recuperator. Yet, for iron, the air-side steam generation is zero only up to compressor ratio of 5, and increases to around 60% at a ratio of 9. Recall that the CO_2 ratio in the fuel feed stream for iron is 50% compared to 85% for copper. Therefore, the copper-based system has a higher fuel-side exhaust flow and can thus handle more steam generation in the fuel-side recuperator. Since the fuel-side steam generation capacity is lower for iron, it is forced to switch to the air-side recuperator. Since the air-side capacity flow

rates were nearly balanced without steam generation, adding steam generation now upsets this balance, resulting in a less efficient steam generation and consequently, larger efficiency penalties as steam demand increases. Comparing Figure 5-18 and Figure 5-16, one can see that the sharper drop in efficiency beyond compressor ratio of 5 in Figure 5-16 corresponds to the ramp up in steam split fraction in Figure 5-18.

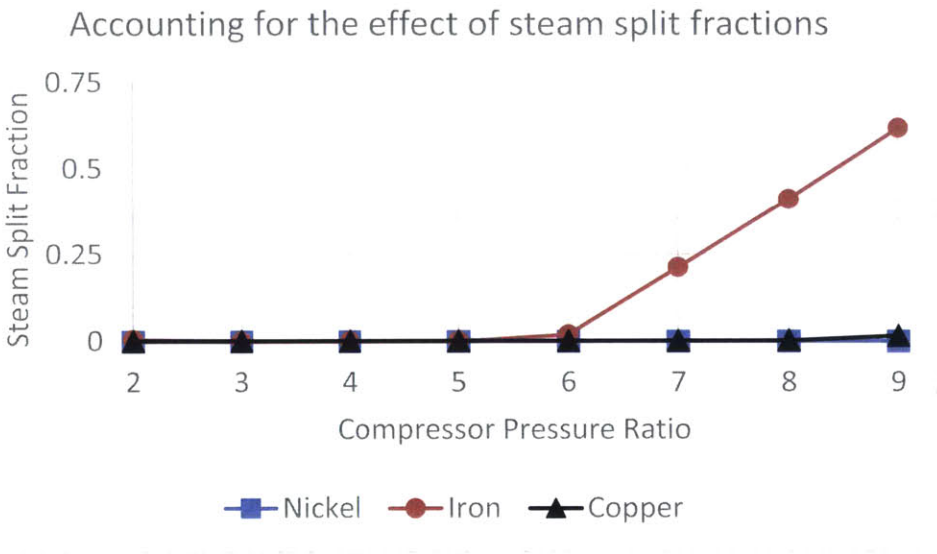

Figure 5-18: Comparing purge steam generation strategy for the three oxygen carriers over the pressure parametric study range.

5.3.2.2. Fuel conversion

Figure 5-19 compares the effect of increasing fuel conversion target on thermal efficiency for the three oxygen carriers. The copper and nickel-based systems exhibit a linear dependence as efficiency monotonically increases with fuel conversion, which is expected. The surprising result occurs with the iron-based system, where efficiency significantly drops as the specification on fuel conversion is tightened. To understand the mechanism behind this behavior, the relationship between fuel conversion, thermal efficiency and purge steam demand is plotted for copper, nickel and iron in Figure 5-20, Figure 5-21 and Figure 5-22. In Figure 5-20 and Figure 5-22, as fuel conversion efficiency specification increased from 95% to 99%, purge steam demand increased

by about 3% and 8% respectively for nickel and copper. On the other hand, the increase for the iron-based system as shown in Figure 5-21 is close to 50%, which ultimately constitutes an important penalty on the cycle thermal efficiency. Such behavior derives from the kinetic parameters for iron redox reactions, for which the reaction rate is a very strong function of the fuel mole fraction. Thus as the fuel mole fraction tends towards zero, the reduction reaction rate substantially slows down, requiring longer and/or more channels to provide sufficient oxygen carrier surface to convert the fuel, which pushes up purge steam demand.

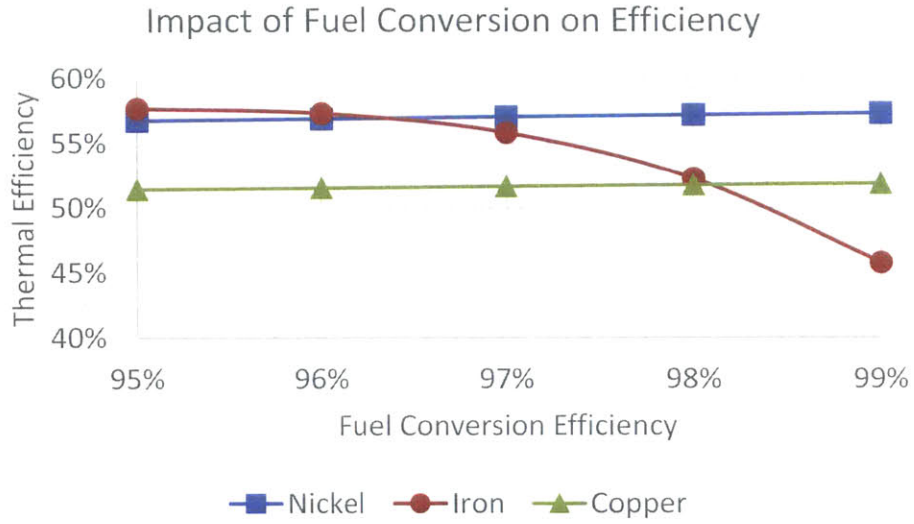

Figure 5-19: Impact of specified extent of fuel conversion on thermal efficiency.

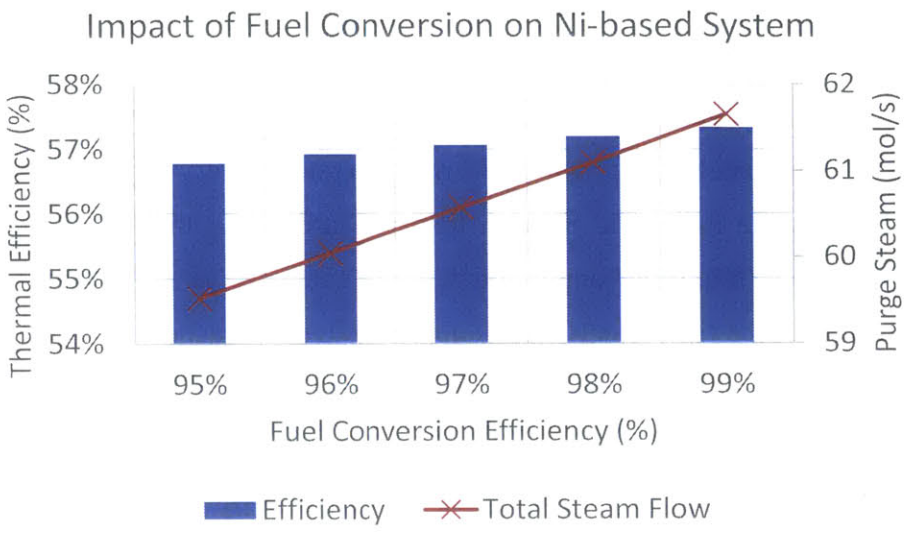

Figure 5-20: Relationship between fuel conversion, thermal efficiency and purge steam demand for a nickel-based system.

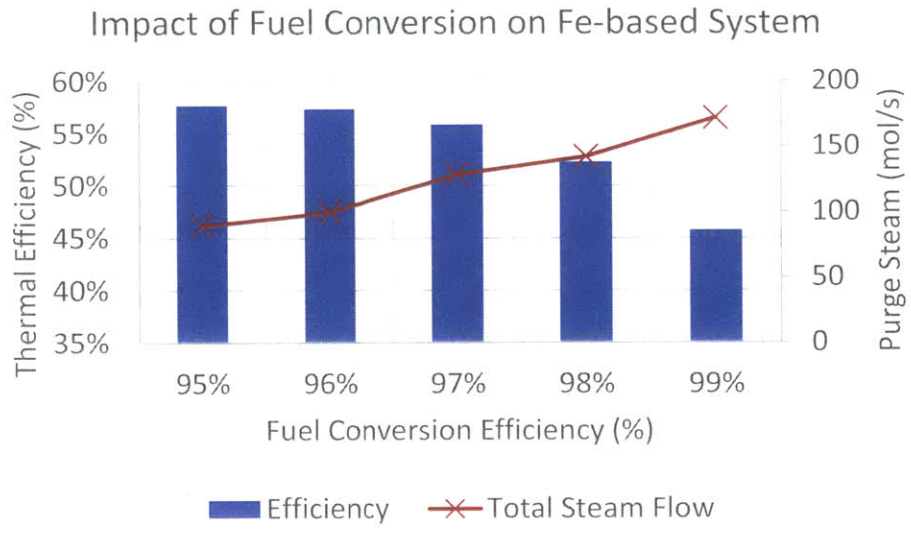

Figure 5-21: Relationship between fuel conversion, thermal efficiency and purge steam demand for an iron-based system.

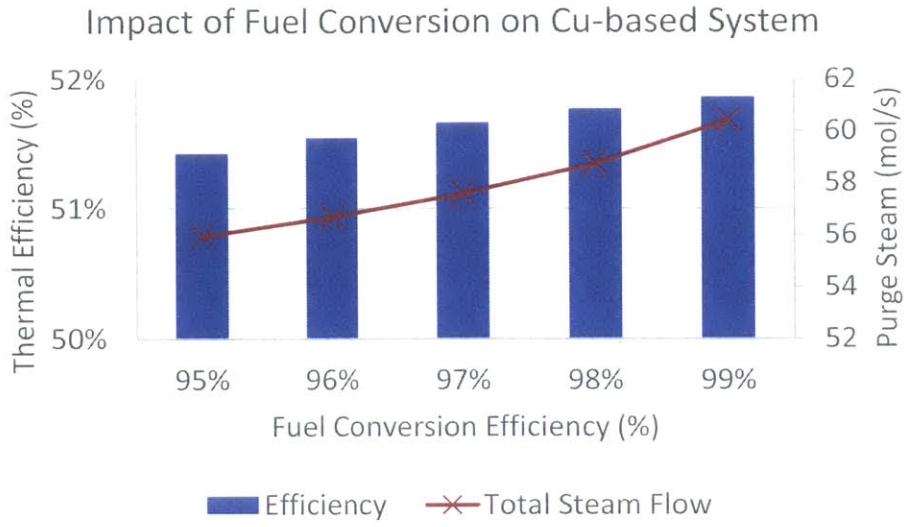

Figure 5-22: Relationship between fuel conversion, thermal efficiency and purge steam demand for a nickel-based system.

5.3.2.3. CO_2 fraction

Figure 5-23 illustrates the relationship between the optimized efficiency value for the integrated system and the CO_2 fraction in the feed fuel stream. This CO_2 is obtained by recycling some CO_2 from the exhaust stream back into the reactor. In literature, exhaust recycle (~50%) is primarily used for particle fluidization and for controlling carbon deposition [32], [33]. However, for carbon deposition control, steam, rather than CO_2, is the more important control agent. The plots in Figure 5-23 were obtained by varying the fuel fraction in the feed stream by 40% above and below the base case value and plotting the results against the corresponding CO_2 fraction. Figure 5-23 shows that at the base case compressor pressure ratio, the optimal efficiency is negatively correlated with CO_2 fraction. These profiles are specific to the current compressor ratio and change as pressure ratio increases, as was shown in chapter 2. Thus, for this compressor ratio, reducing the CO_2 feed fraction by 20% increases efficiency by about 1.5% for copper and nickel and 0.5% for iron.

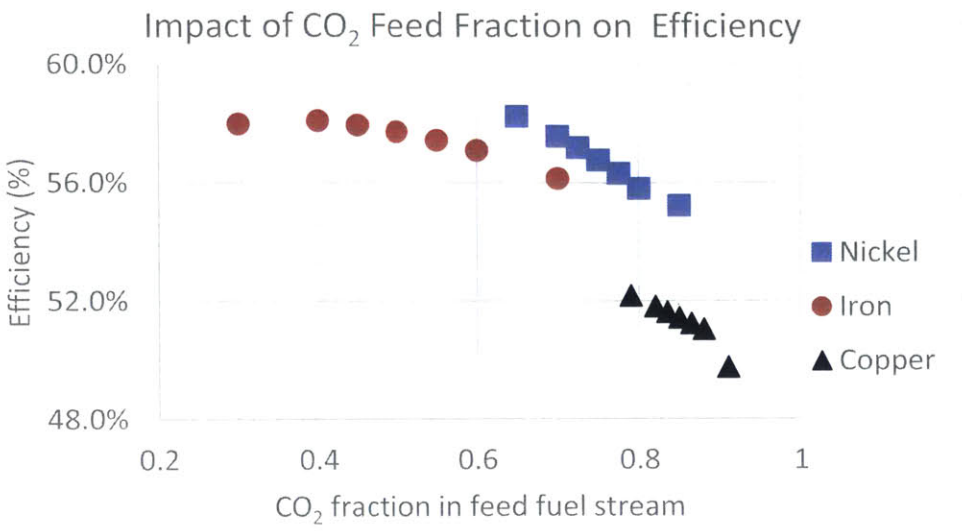

Figure 5-23: Comparing impact of CO_2 feed fraction on optimal efficiency for the three oxygen carriers.
CO_2 feed fraction is negatively correlated to the optimal efficiency of the integrated system at the base case compressor ratio. The base CO_2 fractions for nickel, iron and copper are 75%, 50% and 85% respectively.

5.3.2.4. Recuperator pinch

This study addresses one of the major obstacles to adopting the recuperative cycle, even in conventional systems. In practice, there is usually no effort at minimizing the heat recovery pinch in the recuperator because the overriding objective is usually to keep the recuperator compact. It is evident from Figure 5-24 that loosening the target pinch temperature difference from 20K to 60K penalizes efficiency by at least 4% points (the pinch specification for this study was set at a minimum of 25K). Tighter pinch values typically require larger exchangers which add to the capital cost of the plant, but the benefit in efficiency gains could be a strong motivation for designing exchangers that meet more a stringent pinch temperature difference.

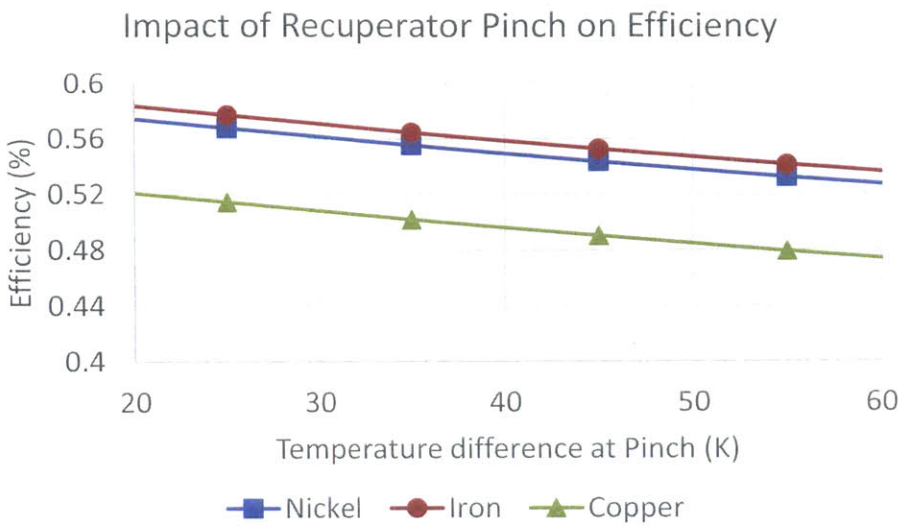

Figure 5-24: Impact of recuperator pinch on efficiency.
Pinch specification is strongly correlated with efficiency. The strong negative correlation between efficiency and pinch temperature difference probably explains why recuperative cycles have not been widely implemented.

5.4. Summary

This chapter presented a model formulation that integrates the reduced fidelity rotary reactor model from chapter 4 with a system-level power generation cycle model. The recuperative cycle was selected to illustrate the implementation of the model integration, though it can be applied to any other cycle configuration. Unlike the simpler models presented in chapters 2 and 3, this integrated model is able to capture important feedback interactions between the reactor and the rest of the system which impact overall performance.

The integrated system model was set up as an optimization problem in which the models of the system sub components are defined as the optimization constraints and solved using an equation oriented approach to flowsheet programming. This allows the simultaneous optimization of the integrated flowsheet and predicts both the thermodynamic state of the system at optimal solution as well as the reactor geometry and operating parameters at this optimum. This integrated model was used to

compare the performance of power generation cycles integrated with reactors using three different oxygen carriers – nickel, iron and copper. The objective of this comparative study was to examine the relationship between oxygen carrier properties, operating specifications and the overall system performance. Such a study provides relevant criteria for selecting an appropriate oxygen carrier in energy conversion system applications.

The simulation results show that in general, nickel and iron-based oxygen carriers are preferable to those based on copper for use in power generation applications because of they can support higher temperatures, resulting in higher system thermal efficiencies. The parameter that captures the most important feedback interaction between the reactor and the rest of the system is the purge steam demand. Because purge steam demand is a strong function of the oxygen carrier reactivity, the amount of purge steam required plays an important role in exhaust heat recovery in the recuperator. At lower values, it tends to improve exhaust heat recovery while beyond a certain point, it simply constitutes an efficiency penalty for the recuperative cycle.

The parametric studies presented show how this parameter plays a role in differentiating the selected oxygen carriers. Whereas iron-based systems demonstrate higher efficiencies at low compressor ratios, the efficiency rapidly falls off as pressure increases compared to nickel. This is because nickel maintains a high reactivity at elevated pressures while for iron, the reactivity drops, requiring longer reactors and thus, larger purge steam flows. The larger steam demand reduces the average reactor inlet temperature, leading to still slower overall reactions, creating a negative feedback loop that penalizes efficiency. Another interesting result captures the relationship between fuel conversion, purge steam demand and overall cycle thermal efficiency. For oxygen carriers, like iron, whose conversion rates strongly depend on fuel mole fraction, an inverse trend is observed between fuel conversion efficiency and cycle thermal efficiency as the fuel fraction tends towards zero.

It is evident that the accuracy of the system-reactor interaction presented depends on the accuracy of the kinetic data on which the reactor model is based. This underscores the importance of refining and validating the CLC kinetic parameter values. However, the key contribution of this study is to develop a framework for modeling a rotary reactor-based energy conversion system and a tool that implements this framework for the recuperative cycle. Improving simulation prediction therefore becomes simply a matter of updating the input parameters to the integrated model.

6. Economic analysis & optimization of the integrated system

This chapter develops an economic model which is used to assess the economic performance of rotary reactor-based power generation cycles. The objective is to optimize the energy conversion cycle and to select the best oxygen carrier from an electricity cost stand point. A primary motivation for developing the rotary reactor technology was to overcome the efficiency and cost barriers which have so far prevented the large-scale deployment of CO_2 capture in power plants. In chapter 5, the integrated system model was used to optimize the efficiency of the rotary reactor-based system, and the simulation results demonstrated high efficiencies for systems based on selected oxygen carriers. However, the decision to build a power plant is ultimately an economic one, so a high efficiency by itself does not provide sufficient motivation.

For this reason, this chapter considers the levelized cost of electricity (LCOE) as an alternative metric for optimizing the rotary reactor-based plant. By accounting for both the capital and operating costs over the lifetime of the plant, the LCOE also captures the impact of system efficiency since operating costs are primarily determined by the rate of fuel consumption. Consequently, rotary reactor-based plants using Ni/NiO, Cu/CuO or Fe_3O_4/Fe_2O_3 oxygen carriers are optimized based on LCOE.

This chapter is divided into 3 sections: section 6.1 discusses the cost estimation methodology for the major equipment; section 6.2 outlines the economic model leading up to the determination of LCOE; and section 6.3 presents an analysis of the optimization results.

6.1. Equipment cost evaluation

This study employed a bottom-up approach for determining the overall plant costs. This approach starts with the estimation of the capital cost of each major piece of equipment, based on the results of the cycle optimization. The equipment costs (in US dollars) were evaluated using a combination of data and correlations from literature, vendor data and standard equipment cost estimation tools. The capital cost estimation strategy for each major piece of equipment is presented next.

6.1.1. Air-side compressor

The base air compressor cost was evaluated using a power-law correlation derived by fitting equipment cost data from Pauschert et al. [73] as a function of the net power output excluding CO_2 compression:

$$C_{aircomp}^{base} = 109800\ (KW_{Net-air})^{0.2133} \tag{6.1}$$

Here, KW_{Net} is the net air-side power output in kW ($5000 \leq KW_{Net} \leq 150{,}000$). The total compressor cost is given by:

$$C_{aircomp}^{final} = (F_{int})(F_{CI}^{2008})\ C_{aircomp}^{base} \tag{6.2}$$

where F_{int} is a factor that modifies the compressor cost to account for intercooling. It was determined by fitting the ratio of compressor capital costs with and without intercooling as predicted using Aspen Economic Analyzer™; F_{CI}^{2008} is the cost index factor that accounts for the difference in equipment price between the current year and 2008, on which Pauschert's prices were based. The indices for the respective years were obtained from producer price index tables published by the US Bureau of Labor Statistics [74]. The cost index factor has the following form:

$$F_{CI}^{2008} = \frac{Cost\ Index\ current\ year}{Cost\ Index\ 2008} \tag{6.3}$$

The values of the different cost adjustment factors and relevant cost indices can be found in Table 6.1.

6.1.2. Fuel-side compressor

The fuel-side compressor is essentially a CO_2 compressor since the fuel feed stream is mostly made up of recycled CO_2. Therefore, the compressor cost is estimated using the correlation proposed by McCollum and Ogden [67] for a CO_2 compression train:

$$C_{fuelcomp}^{base} = m_{kg}\ \left[\left(130000\ m_{kg}^{-0.71}\right) + \left(0.0000014\ m_{kg}^{-0.6}\log(\pi)\right)\right] \tag{6.4}$$

Here m_{kg} is the mass flow rate in kilograms per second, and π is the compressor pressure ratio. These costs were determined based on 2006 prices, so the updated cost for the compressor is given by:

$$C_{fuelcomp}^{final} = (F_{CI}^{2006})\, C_{fuelcomp}^{base} \tag{6.5}$$

where F_{CI}^{2006} is the cost index factor with 2006 as the reference year. The values of the different cost adjustment factors and relevant cost indices are listed in Table 6.1.

6.1.3. Air-side turbine cost

The air-side turbine cost was derived using a similar power-law, fitted to data from Pauschert et al. [73]:

$$C_{airturb}^{base} = 7778\, (KW_{Net-air})^{0.7035} \tag{6.6}$$

Since the turbine cost provided by Pauschert included the cost of the combustor, their cost estimates was adjusted to only represent the turbine. Assuming that the combustor is responsible for roughly 20% of the stated turbine cost, the actual cost is given by:

$$C_{airturb}^{final} = (\, F_{NC})(F_{CI}^{2008})\, C_{airturb}^{base} \tag{6.7}$$

where the "no combustor" adjustment factor, F_{NC}, is equal to 0.8. The values of the different cost adjustment factors and relevant cost indices are listed in Table 6.1.

6.1.4. Fuel-side turbine cost

The fuel-side turbine base cost was determined using the same correlation for the air-side turbine:

$$C_{airturb}^{base} = 7778\, \left(KW_{Net-fuel}\right)^{0.7035} \tag{6.8}$$

Since CO_2 turbines would have different material and flow characteristics, the final cost was additionally modified by a factor, F_{CO2}, that accounts for the competing effects of higher material costs and lower volumetric flow rates that arise from handling the CO_2-rich working fluid:

$$C_{fuelturb}^{final} = (F_{CO2})(F_{NC})(F_{CI}^{2009})\, C_{airturb}^{base} \quad (6.9)$$

Table 6.1 contains the values used for the different cost adjustment factors and relevant cost indices.

6.1.5. Air-side and fuel-side recuperators

In the absence of component cost data, an indirect approach was adopted to estimate the cost of the recuperators. The cycle thermal analysis considered the recuperator as a multi-stream heat exchanger for both preheating the inlet gas stream and generating steam for reactor purging. However, to provide a conservative estimate of the heat exchanger unit cost, two separate exchangers are considered here for gas pre-heating and steam generation. Aspen Economic analyzer® is used to size the corresponding heat exchangers over a range of thermal duties and independent cost curves were developed for each heat exchanger type as a function of heat exchange duty. A quadratic function was determined to be the best fit for the steam generator while a linear profile was adequate for the gas heat exchanger. The following correlations were obtained for the steam and gas heat exchangers:

$$C_{steam}^{base} = 0.0001454\,(\Delta H_{steam})^2 + 5.125\,(\Delta H_{steam}) + 12370 \quad (6.10)$$

$$C_{gas}^{base} = 15.09\,(\Delta H_{gas}) - 2847 \quad (6.11)$$

where the net steam generation duty is defined for the range: $70 \leq \Delta H_{steam} \leq 31000$, and the net gas duty is defined for the range: $500 \leq \Delta H_{gas} \leq 145000$ (both in kW). For the fuel-side recuperator, a material factor, F_{HXMat}, is applied to both the gas and steam exchangers to account for the impact of changing the shell-and-tube material from carbon steel to stainless steel [75]. Similarly for the air-side recuperator, a corresponding tube material conversion factor is applied to the steam exchanger, resulting in the following modified costs:

$$C_{gas,k}^{mod} = F_{HXMat,k} C_{gas}^{base} \quad (6.12)$$

$$C_{steam,k}^{mod} = F_{HXMat,k} C_{steam}^{base} \quad (6.13)$$

Where k refers to the fuel or air-side heat exchanger. The total heat exchanger cost is then simply the sum of these two component costs:

$$C_{hex,k}^{final} = C_{gas,k}^{mod} + C_{steam,k}^{mod} \quad (6.14)$$

The values of the different cost adjustment factors and relevant cost indices can be found in Table 6.1.

6.1.6. Reactor cost

The rotary reactor is a new technology and therefore one cannot find explicit reactor cost data available in literature. Estimating the cost of the reactor involved combining information about material costs with those on the cost of the ceramic honeycomb regenerators published by vendors. These cost data can be found in Table 6.1. The reactor cost is estimated by first determining the ratio of module-to-material cost for the commercial ceramic honeycomb regenerators. Then assuming that the same ratio applies to the rotary reactor, the corresponding module cost is determined based on the substrate (boron nitride) material cost. The channel structure used in modeling the rotary reactor consists of a thin, porous layer covering the inner walls of the channel passage. For the purpose of costing, it is assumed that the entire channel is filled with the porous oxygen carrier-support structure with an upward-adjusted porosity. This approach provides a conservative estimate of the material requirements but does highlight one of the possible strategies for constructing the porous layer. The cost of the reactor module is then estimated based on the costs of the oxygen carrier, substrate and binder materials associated with the porous layer. These costs are combined with the energy costs and adjusted by a contingency factor as described in the following steps:

I. Determine commercial ceramic regenerator module-to-material cost ratio:

$$C_{ceram}^{mat} = V_{reac}\, \rho_{ceram}\, C_{ceram}^{kg} \quad (6.15)$$

$$C_{ceram}^{base} = C_{unit}^{m3} * V_{reac} \quad (6.16)$$

$$F_{mat}^{mod} = \frac{C_{ceram}^{base}}{C_{ceram}^{mat}} \tag{6.17}$$

where V_{reac}, ρ_{ceram}, C_{ceram}^{kg} are the rotary reactor volume, commercial regenerator ceramic material density and cost-per-kg of ceramic material; C_{ceram}^{mat}, C_{ceram}^{base}, C_{unit}^{m3} are the total material cost, total module cost and cost per cubic meter of the regenerator module; F_{mat}^{mod} is the module-to-material cost ratio.

II. Determine the rotary reactor module cost

$$C_{substrate}^{mat} = C_{substrate}^{kg} V_{reac} \rho_{substrate} \varepsilon_{reac} \tag{6.18}$$

$$C_{reac}^{base} = C_{substrate}^{mat} F_{mat}^{mod} \tag{6.19}$$

where $\rho_{substrate}$ is the density of the substrate material; ε_{reac} is the solid-to-passage ratio of reactor cross-section; $C_{substrate}^{kg}$, $C_{substrate}^{mat}$ are the cost-per-kg and total cost of the substrate material; and C_{reac}^{base} is the base rotary reactor module cost. Note that the reactor framework is made from the solid substrate material.

III. Determine the porous layer cost

$$\mathrm{V}_i^{\mathrm{Porous}} = V_{reac}(1 - \varepsilon_{reac}) F_p (1 - \varphi) X_p^i \tag{6.20}$$

$$C_i^{porous} = C_i^{kg} \rho_i \mathrm{V}_i^{\mathrm{Porous}} \tag{6.21}$$

$$C_{\mathrm{total}}^{porous} = \sum_i C_i^{porous} \tag{6.22}$$

where $V_{reac}(1 - \varepsilon_{reac})$ is the total channel volume; ρ_{oc}, φ, X_p^{oc} represent the oxygen carrier density, porosity and oxygen carrier loading within the porous layer; F_p is the porosity enhancement factor; C_i^{porous} refers to the corresponding costs; and $C_{\mathrm{total}}^{porous}$ is the total cost. The index i represents the oxygen carrier, substrate and binder materials in the porous layer.

IV. Determine associated energy costs

The associated energy cost is estimated as the unit cost of energy multiplied by the total energy required by the system:

$$C_{\text{total}}^{Energy} = E_{total}\, C_{energy}^{KWH} \tag{6.23}$$

where C_{energy}^{KWH} is the unit cost of energy per kWh, and E_{total} is the sum of the following energy loads (all in kWh):

- the energy required to heat up the entire reactor mass from room temperature to furnace temperature
- the energy required to maintain the furnace at temperature for 24 hours (assuming a 5% heat loss)
- the energy required to burn off all the binder material, which is assumed to be equivalent to the heat required to evaporate the same mass of binder material

V. Determine final cost

The final cost of the reactor is then given by multiplying the sum of the base, porous material and energy costs by a contingency factor to account for uncertainties in the reactor construction:

$$C_{reac}^{final} = F_{con}\left(C_{reac}^{base} + C_{\text{total}}^{porous} + C_{\text{total}}^{Energy}\right) \tag{6.24}$$

All of the values for the estimation parameters used in this process are listed in Table 6.2.

6.1.7. CO_2 compressor cost

The cost of the CO_2 compression train is estimated using the correlations proposed by McCollum and Ogden [67]. There are two phases to this compression train: 1) compressing the CO_2 gas stream up to its critical point, and 2) pumping the supercritical CO_2 up to sequestration pipeline pressure (110bar). The cost correlation for the first phase is given by:

$$C_{CO2comp}^{base} = \dot{m}_{kg}\left[\left(130000\, m_{kg}^{-0.71}\right) + \left(0.0000014\, \dot{m}_{kg}^{-0.6}\log(\pi_c)\right)\right] \tag{6.25}$$

where $\dot{m}_{kg}$ is the mass flow rate in kilograms per second and π_c is the critical-to-ambient pressure compressor pressure ratio. The correlation for the second phase is given by:

$$C_{CO2pump}^{base} = 1{,}110{,}000\left(MW_{CO_2}\right) + 70{,}000 \tag{6.26}$$

where MW_{CO_2} is the CO_2 pump work in MW. The final cost is the sum of the pump and compression train costs multiplied by a cost index conversion factor from 2006 to 2016:

$$C_{CO2comp}^{final} = (F_{CI}^{2006})\left(C_{CO2comp}^{base} + C_{CO2pump}^{base}\right) \tag{6.27}$$

The values of the different cost adjustment factors and relevant cost indices are listed in Table 6.1.

Table 6.1: Equipment cost conversion factors

Factor	**Value**	**Comment**
Compressor intercool factor (F_{int})	1.11 / 1.23	2 stages / 3 stages
Cost indices (CI)	220 / 169 / 159.9	2016 / 2008 / 2006
Fuel side turbine co_2 factor (F_{CO2})	1.3 [1]	
Recuperator shell & tube material conversion factor (F_{HXMat})	2.86*	Fuel side gas and steam exchangers (shell and tube)
	1.67*	Air side steam exchanger (tube)
	1	Air side gas exchanger

*[75]

Table 6.2: Reactor cost estimation parameter values

	Unit	**Ni/NiO**	**Fe_2O_3/Fe_3O_4**	**Cu/CuO**
	Commercial honeycomb regenerator			
Material		Ceramic	Ceramic	Ceramic
Material cost per kg (1)	$/kg	0.35 - 0.5	0.35 - 0.5	0.35 - 0.5

[1] Current results used a value of 1.3 for this factor (not taking into account the lower volumetric flow rates ~ 66% lower). Updated simulation results will use a value of 0.9

Density	Kg/m^3	3950	3950	3950
Module cost [2]	\$/m^3	800-5000	800-5000	800-5000
	Rotary reactor solid substrate			
Material		Boron nitride	Boron nitride	Boron nitride
Density ($\rho_{substrate}$)	Kg/m^3	2100	2100	2100
Cost per kg [3]	\$/kg	10-50	10-50	10-50
	Oxygen carrier			
Material		Ni/NiO	Fe_2O_3/Fe_3O_4	Cu/CuO
Density (ρ_{oc})	Kg/m^3	8908	5240	8960
Porous layer loading (X_p^{oc})		0.4	0.45	0.1
Porous layer porosity (φ)		0.36	0.3	0.57
Porous layer to wall thickness ratio (γ_s^p)		0.1923	0.1923	0.1923
solid-to-passage ratio (ε_{reac})		0.45	0.45	0.45
Cost per kg [4]	\$/kg	10	0.75	4
Binder				
Material		Ethylene glycol		
Density	Kg/m^3	1,110		
Cost per kg[5]	\$/kg	0.967		
Porosity enhancement factor (F_p)		0.4	0.4	0.4
Energy cost	\$/KWH	0.06		
Contingency factor (F_{con})		1.33	1.33	1.33

(1) Comment: \$0.5/kg is used; source: http://minerals.usgs.gov/minerals/pubs/commodity/bauxite/mcs-2015-bauxi.pdf

(2) Comment: \$5,000 is used; source: http://www.alibaba.com/product-detail/Honeycomb-Ceramic-Monolith-Catalyst-Support_60141675444.html?spm=a2700.7724838.0.0.TZrToS&s=p

(3) Comment: \$50 is used; source: http://www.alibaba.com/product-detail/High-quality-boron-nitride-boron-nitride_1965422861.html?spm=a2700.7724857.29.59.lG0QGu

(4) Source:

a. http://www.lme.com/metals/non-ferrous/nickel/

b. http://www.alibaba.com/

c. http://www.infomine.com/investment/metal-prices/copper/5-year/

(5) http://www.statista.com/statistics/248840/ethylene-glycol-total-costs-and-potential-price-us-saudi-arabia-asia/

6.1.8. Total equipment cost

The total equipment cost is the sum of all the major component costs from equations 6.1-6.27:

$$C_{total}^{equip} = \sum_k C_k^{final} \tag{6.28}$$

This total cost accounts for the air and fuel-side compressors, turbines, and heat exchangers, as well as the rotary reactor and CO_2 compression train.

6.2. Overall plant cost model

The overall plant cost model here is based on the methodology described in the NETL cost estimation report [76]. The goal is to determine the levelized cost of electricity (LCOE), which is then used as a basis for comparing the economic effectiveness of different plant designs. The LCOE is derived from the total overnight capital cost (TOCC), which is composed of the total equipment cost, direct and indirect costs, engineering services cost, project contingencies and other escalation factors. The steps in determining the TOCC involve the evaluation of the bare erected costs (BEC), the engineering, procurement and construction costs (EPCC) and the total plant cost (TPC).

6.2.1. Bare erected cost (BEC)

BEC accounts for the costs of all the major power plant equipment as well as additional construction costs, including piping, erection of foundations and support structures, electrical installation, control and instrumentation, and other auxiliary equipment. These capital cost components were estimated by fitting the cost data reported by Pauschert et al. using correlations parameterized by the total equipment cost:

$$C_{Pipe} = 0.003596 \left(C_{total}^{equip}\right)^{1.149} \quad (6.29)$$

$$C_{Elect} = 0.0009276 \left(C_{total}^{equip}\right)^{1.173} \quad (6.30)$$

$$C_{I\&C} = 0.02446 \left(C_{total}^{equip}\right)^{0.9903} \quad (6.31)$$

$$C_{C\&S} = 0.03604 \left(C_{total}^{equip}\right)^{1.067} \quad (6.32)$$

$$C_{BoP} = 0.1111 \left(C_{total}^{equip}\right)^{0.978} \quad (6.33)$$

$$C_{BEC}^{plant} = C_{total}^{equip} + C_{Pipe} + C_{Elect} + C_{I\&C} + C_{C\&S} + C_{BoP} \quad (6.34)$$

where $C_{Pipe}, C_{Elect}, C_{I\&C}, C_{C\&S}, C_{BoP}$ are the costs associated with piping, electrical installations, instrumentation & control, civil & structural and balance of plant (general facilities); C_{BEC}^{plant} is the total bare erected plant cost.

6.2.2. Engineering, procurement and construction costs (EPCC)

This cost adjusts the bare erected plant cost to account for the costs of services provided for detailed engineering design, project execution and management, permitting costs and other costs associated with procurement, construction and installation by the contractor. These various costs are lumped into the factor, $F_{contractor}$, whose value is stated in Table 6.3.

$$C_{EPCC}^{plant} = F_{contractor}\, C_{BEC}^{plant} \quad (6.35)$$

6.2.3. Total plant cost

The total plant cost is then determined by adjusted the EPCC for both project and process contingencies according to equation 6.36:

$$C_{TPC}^{plant} = C_{EPCC}^{plant} \left(1 + F_{process} + F_{project}\right) \quad (6.36)$$

where C_{EPCC}^{plant} is the EPCC cost and $F_{process}$, $F_{project}$ are the process and project contingencies as listed in Table 6.3. The NETL guidelines recommend about 30-70% process contingency for new technologies. Although all of the equipment in this system, with the exception of the rotary reactor, are off-the-shelf components, a conservative process contingency of 55% was applied.

6.2.4. Total overnight capital cost (TOCC)

The total overnight capital cost adjusts the total plant cost for pre-production costs, inventory capital costs and other owners' costs:

$$C_{TOCC}^{plant} = C_{TPC}^{plant}\,(1 + F_{preprod} + F_{inventory} + F_{OtherOwners}) \tag{6.37}$$

where C_{TOCC}^{plant} is the total overnight capital cost, and $F_{preprod}$, $F_{inventory}$, $F_{OtherOwners}$ are factors for the pre-production, inventory capital and other owner's costs as listed in Table 6.3.

6.2.5. Levelized cost of electricity (LCOE)

The levelized cost of electricity (LCOE) can be defined as the revenue received by the operator of the power plant per net MWh during the power plant's first year of operation, assuming that the cost of electricity (COE) remains constant in nominal terms over the life of the plant. The cost of electricity is the operator's revenue per net MWh for the first year, assuming an escalation rate equivalent to the general inflation rate over the life of the plant [76]. It is a function of the sum of the capital charge, the fixed operating costs and the variable operating costs. For this study, the operational life of the plant is assumed to be 25 years and the LCOE is defined for this period. To determine the LCOE, the COE is first evaluated, then multiplied by a levelization factor. The equations for the COE and LCOE were obtained from NETL's report [76]:

$$COE = \frac{\left(F_{CC}\; C_{TOCC}^{plant}\right) + C_{fixed}^{op} + \left(F_{Cap}\; C_{var}^{op}\right)}{F_{Cap}\left(\frac{Days}{Year}\right)\left(\frac{Hours}{Day}\right)MW_{net}} \tag{6.38}$$

where F_{CC} is the capital charge factor; C_{fixed}^{op}, C_{fixed}^{op} are the fixed and variable operating costs; and F_{Cap} is the plant capacity factor. The denominator is the effective net megawatt-hour of power

generated in one year. The fixed operating cost is defined as a percentage of the EPCC costs while the variable operating cost is a function of the EPCC cost and the fuel cost:

$$C_{fixed}^{op} = F_{fixed}^{OM}\, C_{EPCC}^{plant} \tag{6.39}$$

$$C_{fixed}^{op} = \left(\left(F_{var}^{OM}\, C_{EPCC}^{plant}\right) + \left(Q_{fuel}^{MMBTU}\, C_{fuel}^{MMBTU}\right)\right) F_{cap} \tag{6.40}$$

$$Q_{fuel}^{MMBTU} = \left[\left(\frac{Days}{Year}\right)\left(\frac{Hours}{Day}\right) MW_{thermal}\right]\left(\frac{MMBTU}{MWH}\right) \tag{6.41}$$

F_{var}^{OM} , F_{fixed}^{OM} are the variable and fixed operating costs parameters; Q_{fuel}^{MMBTU} is the total fuel needed in MMBTU; C_{fuel}^{MMBTU} is the cost of natural gas in MMBTU; and $MW_{thermal}$ is the overall fuel heat rate. All parameter and conversion factors are specified in Table 6.3.

The levelized cost of electricity, LCOE, is the obtained using the following equation:

$$LCOE = (COE)(F_L) \tag{6.42}$$

where the levelization factor is given by:

$$F_L = \emptyset\left(\frac{1-\varphi^{LP}}{F_D - F_N}\right) \tag{6.43}$$

and the capital recovery factor is given by:

$$\emptyset = \frac{F_D(1+F_D)^{LP}}{(1+F_D)^{LP} - 1} \tag{6.44}$$

where $\varphi = \frac{(1+F_N)}{(1+F_D)}$, LP is the levelization period (equivalent to the plant life), F_D the discount rate (rate of return on interest) and F_N is the nominal escalation rate (equivalent to the inflation rate). The values of all these parameters can be found in Table 6.3.

Table 6.3: Cost estimation parameter values

Parameter	**Unit**	**Value**
Base year		2016
Capital expenditure period	Years	3
Plant life	Years	25

Inflation	%	3
Rate of return on interest	%	10
Capacity factor	%	90
Income tax rate	%	38
Capital charge factor	%	11.1
Contractor services cost	% of BEC	9
Process contingency	% of EPCC	55
Project contingency	% of EPCC	25
Pre-production factor	% of TPC	2
Inventory capital	% of TPC	0.5
Other owners cost	% of TPC	15
Fixed O&M	% of EPCC	3.5
Variable O&M	% of EPCC	1.5
Fuel cost	$/MMBTU	3
MMBTU/MWH		3.41214
Days/year		365
Hours/day		24

6.3. Results

6.3.1. Base case results with efficiency objective

Figure 6-1 compares the base case costs for the system simulated in chapter 5. Nickel has the lowest estimated levelized cost of electricity (LCOE) at about $105/MWH, while those for copper and iron are about 60% higher. Figure 6-2 shows that the difference in LCOE is proportional to the difference in the equipment costs for the three oxygen carriers. The cost breakdown in Figure

6-3 shows that for the analyzed systems, the reactors and the turbines constitute the most important cost elements in the rotary CLC power plant.

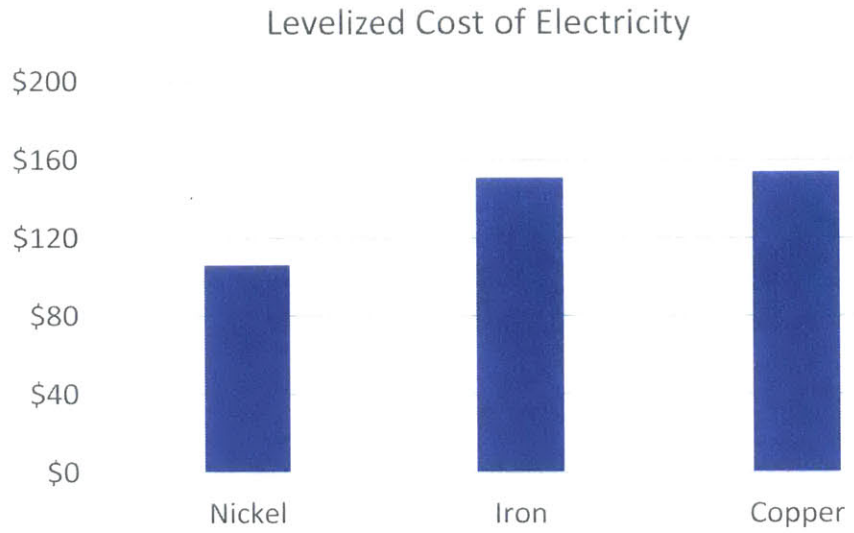

Figure 6-1: Base case plot comparing LCOE for systems with nickel, iron and copper-based carriers.
Base case levelized cost of electricity for the iron and copper-based systems are around 60% higher than that for nickel.

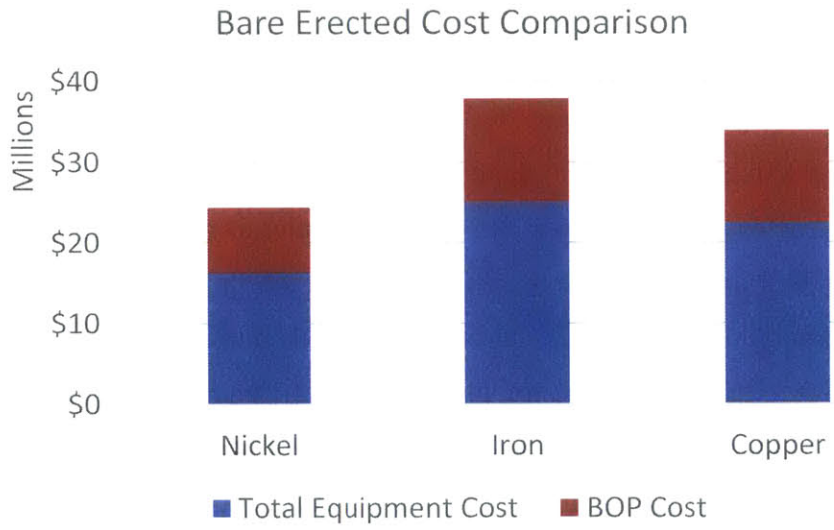

Figure 6-2: Base case plot comparing BEC for systems with nickel, iron and copper-based carriers.
The respective bare erected cost for the three oxygen carriers are the primary contributors to the observed difference in levelized cost of electricity.

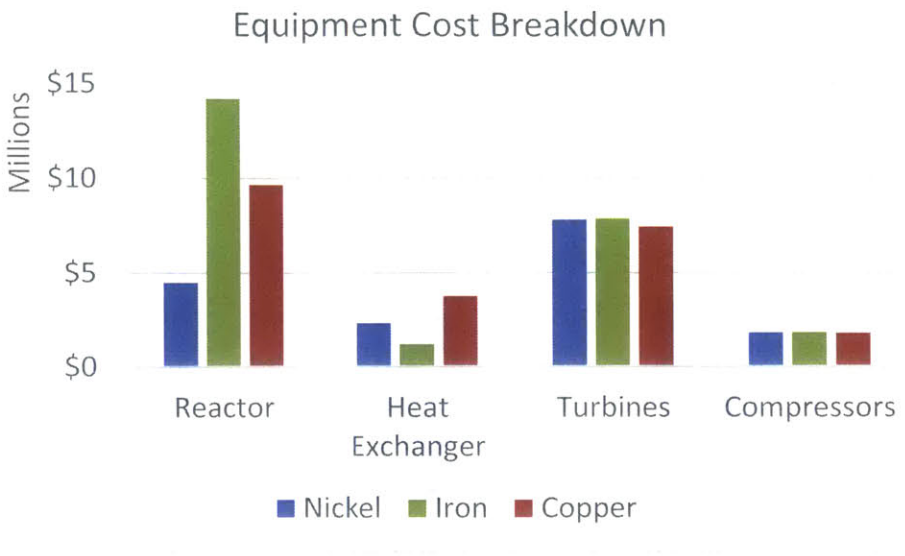

Figure 6-3: Equipment cost breakdown.
A breakdown of equipment cost shows that the difference in reactor costs was the key determinant for the predicted levelized costs.

6.3.2. Impact of LCOE objective function on system performance and cost

The results presented in Figure 6-1 to Figure 6-3 correspond to the case where the overall thermal efficiency of the respective CLC power plants were optimized. One of the limitations of this approach is that the reactor configuration at the optimal solution is not unique and could vary for different starting points. Moreover, since there is no built-in incentive to minimize costs, there is no requirement that maximum efficiency be correlated with minimum equipment cost. These factors explain the large predicted costs for the copper and iron-based reactors in Figure 6-3. Minimizing the LCOE incorporates both performance and economic criteria and is therefore a more suitable basis for contrasting the impact of using the different oxygen carriers in the reactor design. To compare these two scenarios, the integrated model was run for the same operating conditions and parameter bounds, but with the objective function changed from efficiency to LCOE.

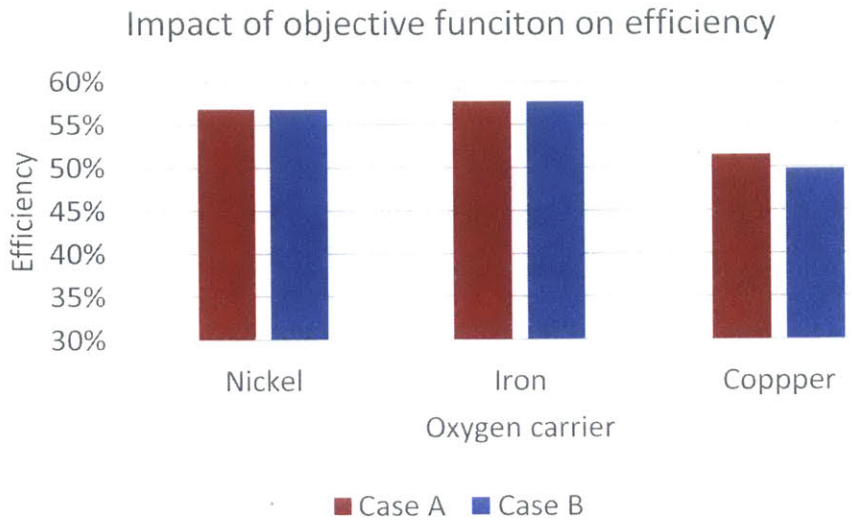

Figure 6-4: Plot comparing efficiency and LCOE objective functions.
At the base case compressor ratio, using the levelized cost of electricity as the objective function converges to nearly the same efficiency optimum as the case with 'thermal efficiency' as objective function. *[Case A: Efficiency objective; Case B, LCOE objective].*

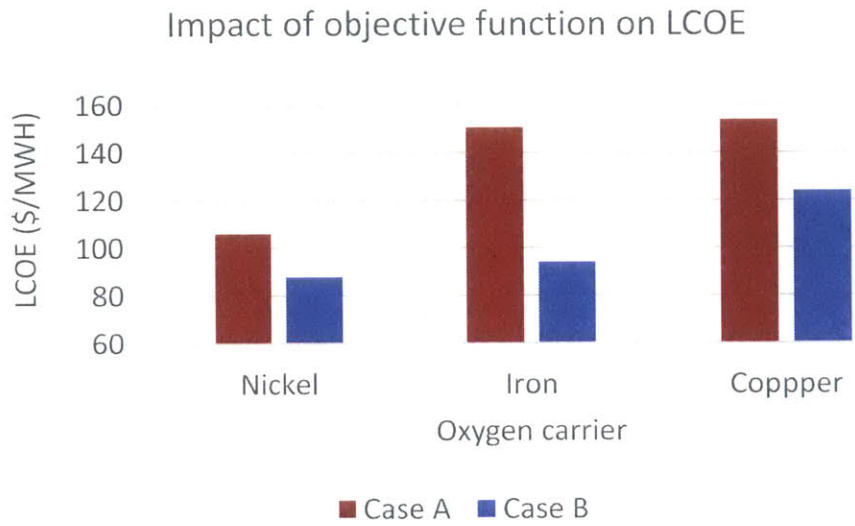

Figure 6-5: Plot comparing efficiency and LCOE objective functions.
The levelized cost of electricity is a more appropriate objective for optimizing the different cycles since it seeks for an optimal tradeoff between performance and economic targets. *[Case A: Efficiency objective; Case B, LCOE objective].*

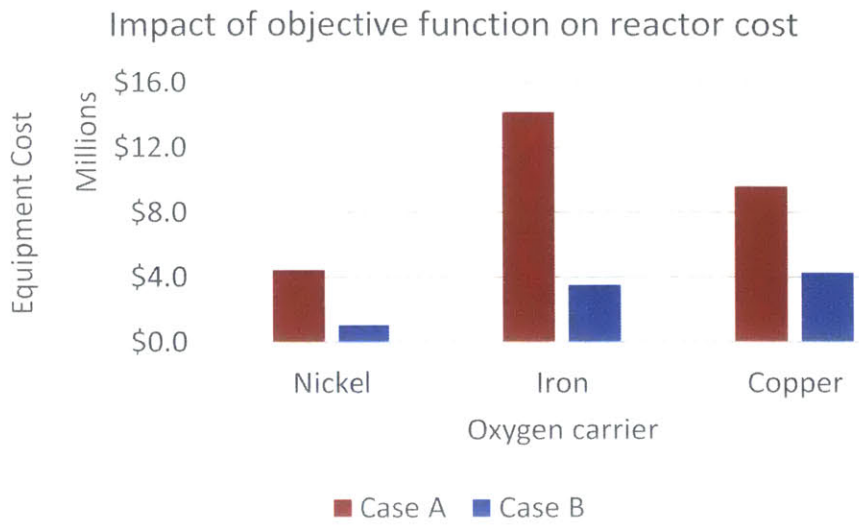

Figure 6-6: Plot comparing efficiency and LCOE objective functions.
Most of the gains in cost of electricity is achieved by selecting a more cost-optimal geometry for the reactor. *[Case A: Efficiency objective; Case B, LCOE objective].*

Table 6.4: Base case cost results

	Nickel ($1000)		**Iron($1000)**		**Copper($1000)**	
Objective function	Efficiency	LCOE	Efficiency	LCOE	Efficiency	LCOE
Reactor	4,461	1,066	14,202	3,553	9,637	4,294
Fuel-side recuperator	1,912	1,912	783	782	3,403	3,425
Air side recuperator	384	384	392	393	307	296
Fuel side turbine	1,703	1,703	1,672	1,663	2,002	1,987
Air side turbine	6,097	6,097	6,199	6,205	5,403	5,321
Fuel side compressor	279	279	214	214	330	330
Air side compressor	1,310	1,310	1,317	1,317	1,263	1,257
Co_2 compressor train	195	195	270	270	167	167
Total equipment cost	16,341	12,945	25,050	14,397	22,512	17,077
Civil/structural	1,792	1,398	2,827	1,566	2,522	1,878
Instrument/ control	340	270	519	300	467	355
Electrical	2,682	2,041	4,427	2,312	3,906	2,825
Piping	698	534	1,140	604	1,009	734
Balance of plant	1,260	1,003	1,913	1,113	1,723	1,315

Bare erected cost	24,373	19,195	37,790	21,405	33,863	25,501
LCOE ($/mwh)	106	88	150	94	154	124

Figure 6-4 to Figure 6-6 compare the simulation predictions obtained for the two objective functions. Efficiency objective is labeled as Case A while LCOE objective is labeled as Case B. From Figure 6-4, the predicted efficiency for the two cases coincide for iron and nickel-based systems, underscoring the fact that the LCOE objective factors-in the plant thermal efficiency. The copper-based system is different, which goes to show that the LCOE objective ultimately involves a tradeoff between capital and operating costs, so that the optima for the two cases do not necessarily coincide.

However, when it comes to the comparing the levelized electricity costs, there is a significant difference in the predicted results as shown in Figure 6-5. A closer look at equipment cost distribution indicates that the reduction in LCOE arises mostly as a consequence of reductions achieved in the reactor cost, as can be seen by comparing Figure 6-5 and Figure 6-6. Details of the simulation results (Table 6.4) show that the reactor costs for nickel, copper and iron drop by 55% - 75%. It appears that for nickel and iron, the LCOE objective (Case B) found smaller reactor dimensions that meet the same efficiency objective, as if the LCOE objective guided convergence towards a subset of feasible configurations for the efficiency objective (Case A), which have smaller dimensions. On the other hand, copper required a new solution that optimized the trade-off between efficiency and capital costs. It is important to point out here that the results presented here are not unique. This means that a different run from a different initial point could end up with different results for the same objective function value, though more likely for Case A than for Case B. The only thing guaranteed is that optimizing the levelized cost of electricity will always converge to an objective function value that is less than or equal to that predicted by optimizing thermal efficiency. The detailed results for Case A (efficiency objective) and Case B (LCOE objective) can be found in Table 6.4.

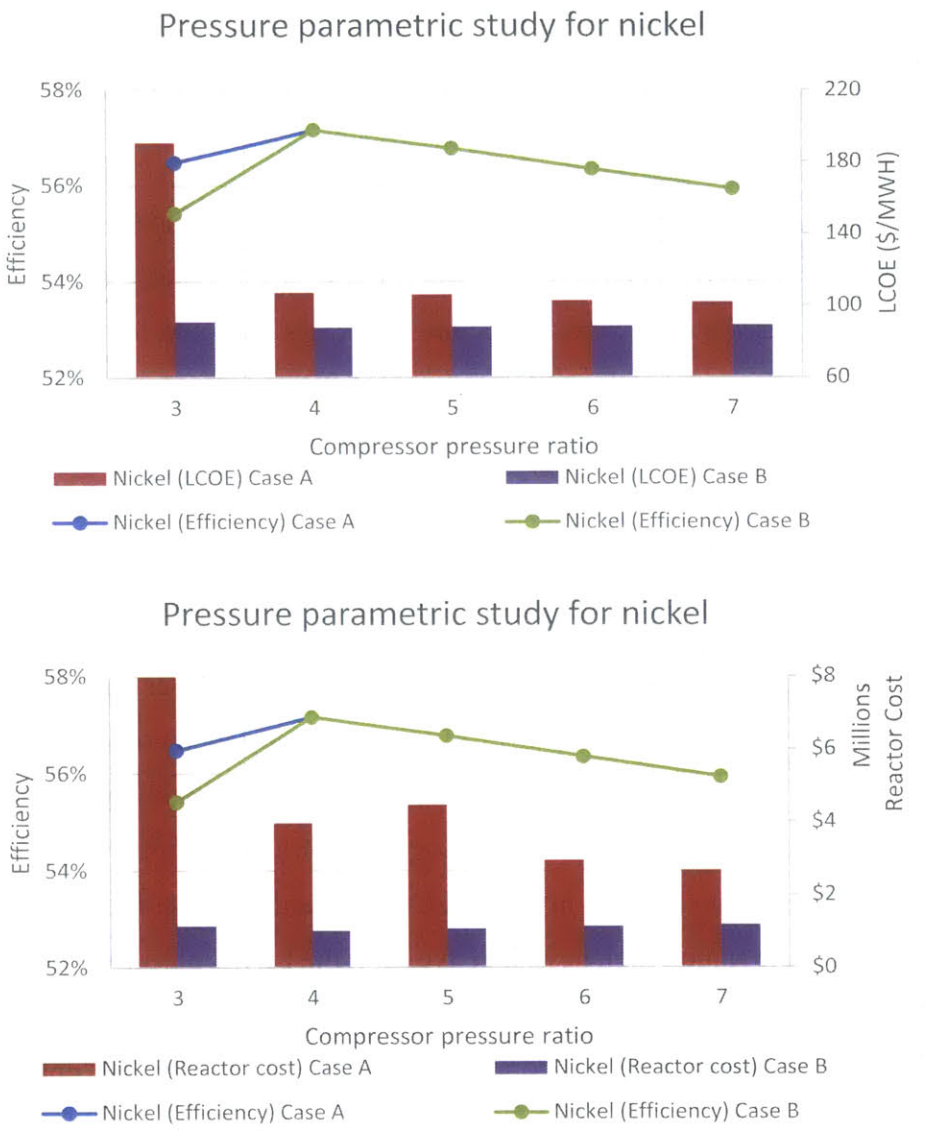

Figure 6-7: Plot comparing efficiency *(lines)* and LCOE *(bars)* objective functions-parametric study for nickel-based oxygen carrier.

The efficiency predictions for both cases mostly match over the entire pressure ratio range and the LCOE ($/MWH) profile is very much the inverse of the efficiency profile for Case B. The reduction in levelized cost of electricity achieved by switching from Case A to Case B is proportional to the reduction in reactor cost. *[Case A: Efficiency objective; Case B, LCOE objective]*.

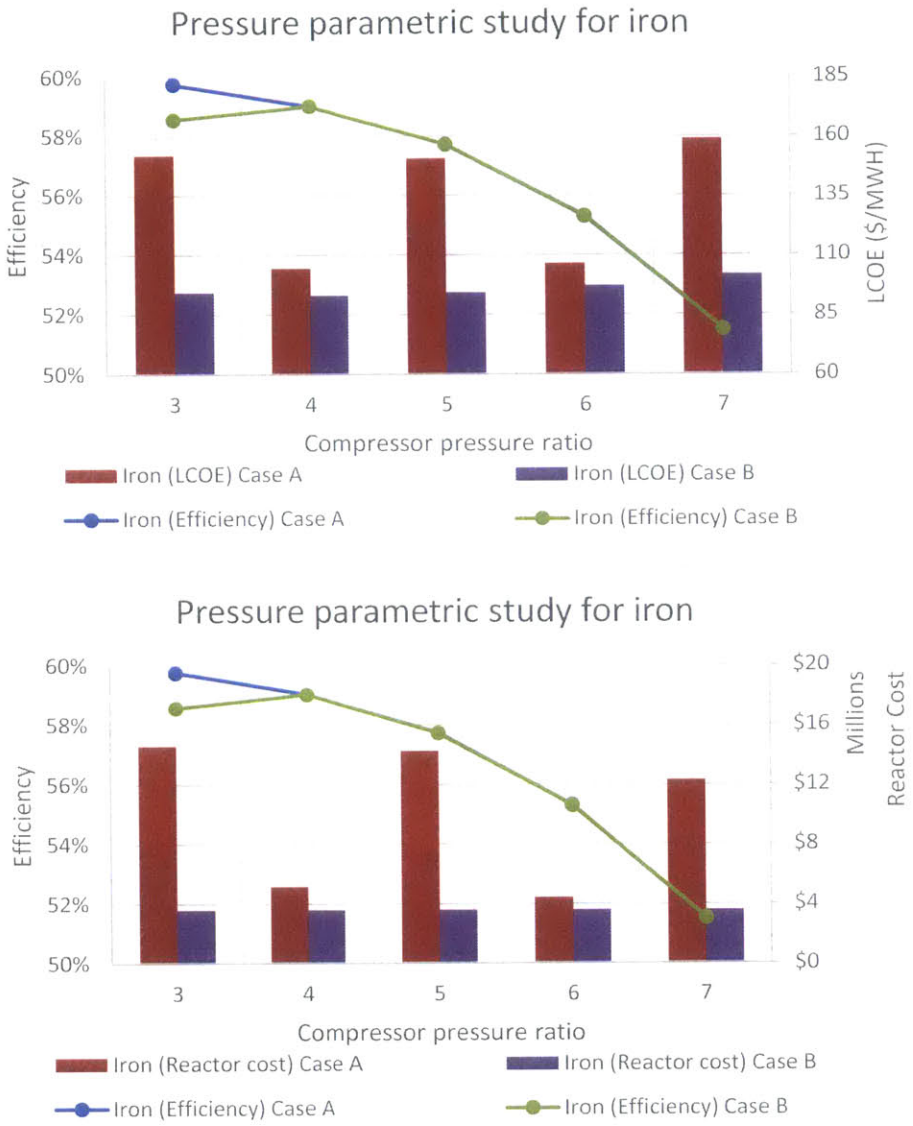

Figure 6-8: Plot comparing efficiency *(lines)* and LCOE *(bars)* objective functions: parametric study for iron-based oxygen carrier.

The behavior of the two cases for the iron-based system is similar to that for nickel, except that there is less correlation between the optimized LCOE and the corresponding reactor cost. The maximum efficiency point for Case B does not exactly tally with the minimum LCOE, though the difference in LCOE between the two points is not significant. *[Case A: Efficiency objective; Case B, LCOE objective].*

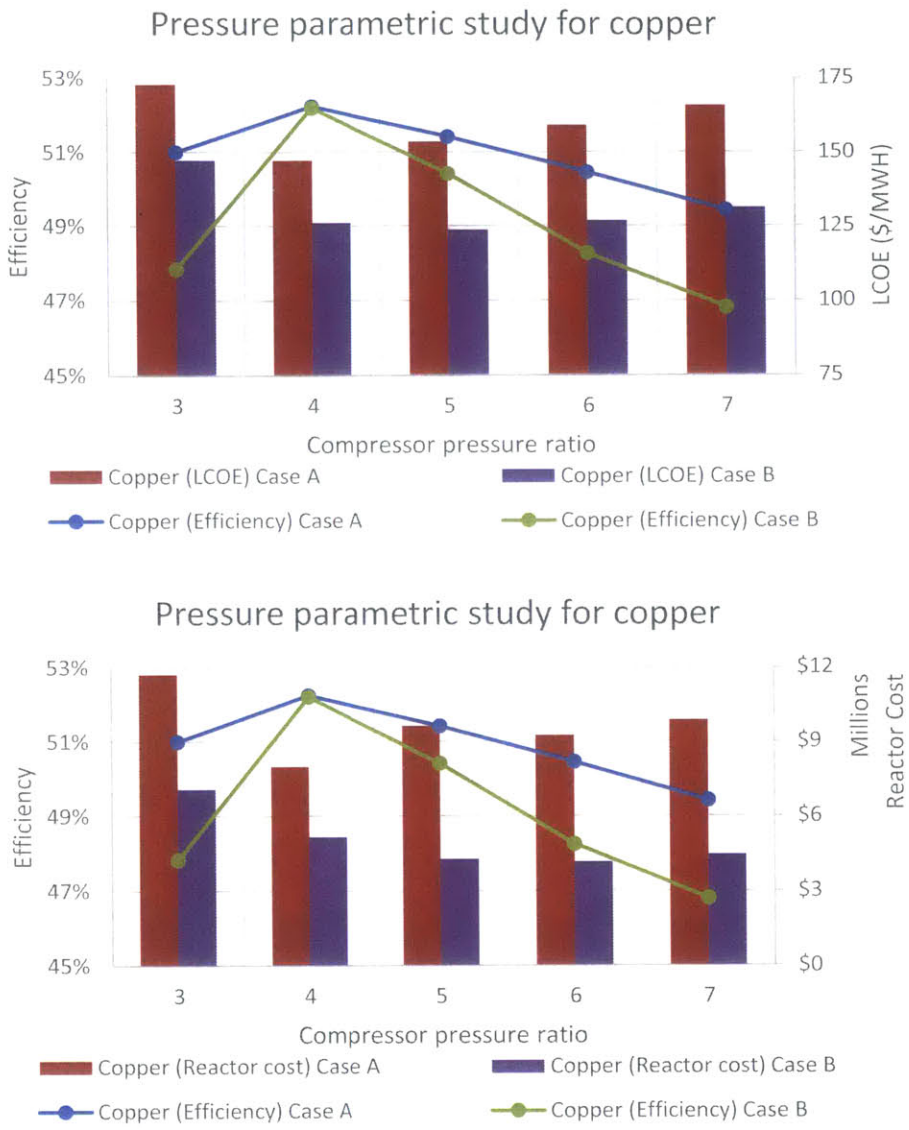

Figure 6-9: Plot comparing efficiency *(lines)* and LCOE *(bars)* objective functions: parametric study for copper-based oxygen carrier.
Unlike for nickel and iron, the LCOE objective Case B almost always under predicted efficiency compared to case A, suggesting a more pronounced cost-efficiency mismatch. Like the case for nickel, the optimized LCOE profile follows that of the corresponding reactor cost. *[Case A: Efficiency objective; Case B, LCOE objective].*

Having established the relationship between the two objective functions at the base case condition, the next step was to see how these two objective functions compare over a range of parameters. To this end, the respective models were simulated for compressor pressure ratios ranging from 3 to 7 (with other parameters fixed at the base case values). Figure 6-7 to Figure 6-9 compare the

Case B (LCOE) and Case A (efficiency) predictions over the selected pressure range for the three recuperative CLC cycles. Each data point corresponds to an optimized result, with the bar charts representing costs while the lines represent efficiencies.

Much like the base case results, minimizing the LCOE (Case B) at least guarantees a lower electricity cost compared to using the efficiency objective (Case A), and much of this reduction is accounted for by a corresponding reduction in reactor costs. For Case B in nickel, the lowest efficiency occurs at compressor ratio, $\pi = 3$ and corresponds to an LCOE of around \$91/MWH. The minimum LCOE is 3% lower than this value and occurs at $\pi = 4$. The trend is a little different for iron Case B, with a minimum LCOE of around \$93/MWH at compressor ratio $\pi = 4$ and a maximum of \$102/MWH at $\pi = 7$. Note from figure 6.8 that unlike nickel and copper, the LCOE for iron is decoupled from the reactor cost. This means that as pressure varies, the iron-based reactor adjusts the sector sizes and the corresponding flows in a way that allows it to keep the reactor size at the same minimum. This behavior is discussed in the pressure sensitivity analysis in chapter 4. The change in LCOE therefore derives from the net change in the cost of the other power plant equipment. For the nickel and iron-based oxygen carriers, however, the efficiency profiles predicted by Case A and Case B align at nearly all the parameter points. This is where copper is a little different, as the efficiencies predicted by Case B are almost always lower than those for Case A. This behavior is related to the temperature-constrained efficiency for copper and suggests that the capital cost of the plant plays a more significant role in determining the LCOE than for nickel and iron. For the copper-based system, the predicted LCOE from Case B ranges from \$124/MWH ($\pi = 5$) to \$147/MWH ($\pi = 3$).

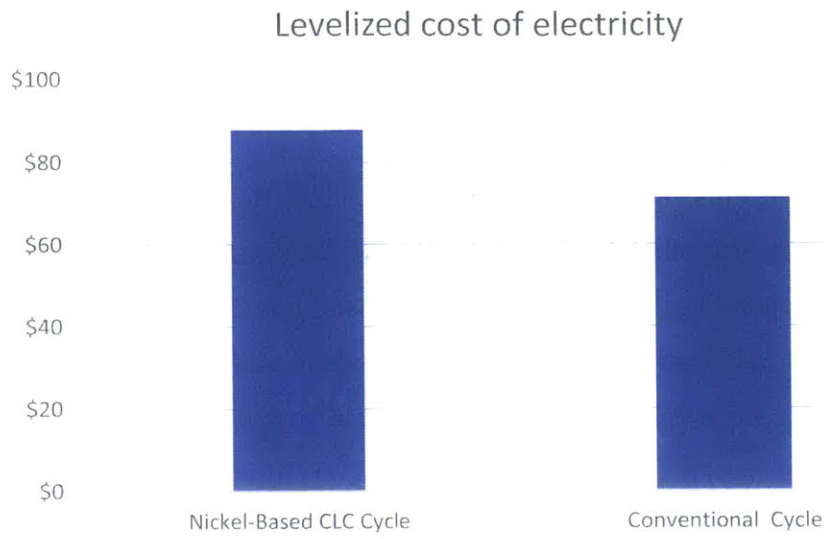

Figure 6-10: Plot comparing LCOE for conventional and rotary CLC-based plants. The levelized cost of electricity for a nickel rotary reactor-based system is about 24% higher than for an equivalent conventional recuperative cycle without CO_2 capture.

To put things in perspective, Figure 6-10 compares the levelized cost of electricity for the nickel-based cycle with that of a conventional recuperative cycle modeled with the same specifications but without CO_2 capture. The LCOE is about 24% higher for the CLC system, a difference that is partly accounted for by the high contingency factors applied to the CLC cycle. A study by Consonni et al [31] showed that retrofitting a 300-400MW_{net} plant for CLC operation (with a circulating fluidized bed system) increased electricity cost by about 50%. Therefore, though 24% is a significant increase in electricity cost, it is within a range that makes the rotary-based system a potentially viable option for sustainable electricity generation. In addition, scaling and manufacturing experience will ultimately bring down the effective electricity cost for this plant, improving its competitiveness.

6.4. Summary

This chapter presented an economic model for analyzing and optimizing the rotary reactor-based power generation plant. This model is based on the levelized cost of electricity (LCOE), which is used to compare the impact of oxygen carrier choice on the lifetime economic performance of the

plants. The LCOE was also used as the objective function in lieu of efficiency in order to predict and compare the economic optima of the three oxygen carrier cases.

A clear inference from these results is that choosing nickel as the oxygen carrier leads to the lowest LCOE compared to copper and iron. Two main factors support this finding: 1) the kinetic properties of nickel favor faster reactions, which results in smaller and therefore cheaper reactors, and 2) the most significant component of the reactor cost is the boron nitride substrate, which is several times more expensive than the different oxygen carriers. Therefore, even though nickel has a higher per unit material cost than copper or iron-based oxygen carriers, the nickel-based system is still cheaper because the savings in boron nitride material cost due to the smaller reactor offset the cost of nickel.

Comparing the LCOE of this nickel-based system with that of an equivalent conventional plant shows that the rotary reactor-based system is attractive for sustainable electricity generation from fossil fuel plants. A combination of scaling, manufacturing and operating experience will contribute to bringing down the effective cost of CO_2 capture, making this technology even more attractive from an economic perspective. It should be noted, however, that these cost evaluations admit some level of uncertainty with respect to the cost of the reactor relative to the rest of the plant. Further work is needed to quantify the different material and manufacturing costs associated with producing this novel rotary reactor in order to improve upon this preliminary economic analysis.

7. Conclusion

7.1. Summary

This thesis implemented a multiscale modeling approach for assessing the feasibility of integrating the rotary reactor technology into energy conversion systems, analyzing the behavior of the integrated system and optimizing the overall system performance. In this analysis, emphasis was placed on the impacts of reactor thermal coupling and oxygen carrier properties on system techno-economic performance. This multiscale approach used models of increasing fidelity to represent the rotary reactor and system, with the objective of capturing important feedback interactions that determine overall system behavior and performance. The integrated system model was successively represented by: 1) availability models, with the reactor modeled as interacting thermal reservoirs; 2) ideal thermodynamic cycles, with energy balance models for the reactor; 3) detailed thermodynamic cycles, with the reactor modeled as interacting equilibrium reactors; and 4) detailed thermodynamic cycles, with a reduced fidelity model of the actual rotary reactor.

Thermodynamic availability analysis showed that maximum work output can be obtained from the system when the redox reaction is in thermal equilibrium. These results were confirmed using ideal thermodynamic cycle models, which proved that thermal efficiency is proportional to the degree of thermal coupling, and that maximum efficiency occurs when the oxidation and reduction reactors are in thermal equilibrium. Subsequently, detailed cycle analysis showed that this increase in efficiency was due to the increased availability of the fuel-side reactor exhaust streams, and only efficient cycle configurations can exploit this potential. Based on this criteria, the recuperative, combined and hybrid combined-recuperative cycles were identified as ideal configurations for integration with the thermally-balanced rotary reactor.

Preliminary sensitivity analysis also revealed that purge steam demand significantly impacts efficiency. However, purge steam demand is a function of the kinetic properties of the oxygen carrier and the reactor operating conditions. The simple reactor models used thus far could neither represent the oxygen carrier kinetics nor quantify the actual purge steam demand. To overcome this limitation, a higher resolution rotary reactor model was developed.

This model simplified the governing equations of the detailed model of Zhao et al. [28], [29] and incorporated other design and operating criteria that are implicitly satisfied at cyclic stationary convergence. The result was a reduced fidelity reactor model that maintained prediction accuracy, significantly reduced computational cost, and was suitable for integration into the system level model.

The resulting integrated system model was set up as an optimization problem that allowed for the simultaneous optimization of the integrated flow sheet and the rotary reactor design parameters. This modeling tool was then used to assess the relationship between oxygen carrier kinetic properties, operating specifications and the optimal techno-economic system performance for nickel, copper and iron-based oxygen carriers. Results from this analysis provided insight into the level of coupling between the oxygen carrier reactivity and purging steam demand, which directly impact system efficiency. This analysis also elucidated the relationship between oxygen carrier reactivity, operating conditions, system specifications and optimal reactor geometry. The integrated system was optimized for levelized cost of electricity (LCOE) and the resulting comparative analysis indicated that nickel was the preferred oxygen carrier, due mostly to its high reactivity. Copper had the highest LCOE because its low melting point constrained the maximum reactor temperature and consequently, the system efficiency. Further breakdown of the economic analysis results showed that the reactor cost was dominated by the expensive boron nitride support layer. This result implies that the selection of substrate material is a critical decision in minimizing the cost of this system.

Overall the contributions of this work to the field of CLC research are as follows:

1) Developed a methodology for the rotary reactor model reduction that can be adapted to other cyclic CLC reactor configurations like rotating beds and fixed packed beds with inlet switching.
2) Created a modeling tool for design, analysis and optimization of an integrated CLC-based system and implemented it for recuperative cycles using nickel, copper and iron-based oxygen carriers. This tool is capable of simultaneously optimizing for specifications at both the system and reactor levels.
3) Investigated the complex relationship between design specifications, operating conditions and oxygen carrier kinetics in a CLC-based system.

4) Determined the optimal oxygen carrier for the rotary reactor from a techno-economic standpoint on the basis of minimizing system LCOE.

7.2. Suggested future work

7.2.1. Refining the current model

The reactor model presented in this study is based on the kinetics reported by Abad et al. for oxygen carrier particles in fluid bed reactors [5], [49], [50]. There is however some level of uncertainty in these kinetic parameters as well as their applicability to rotary reactor conditions. This is further exacerbated by the fact that oxygen carrier reactivity also depends on preparation methods and binder physical properties. For this reason, the need for more accurate kinetic data that specifically apply to the rotary reactor conditions cannot be overstated. Some of the simplifying assumptions in the reduced reactor model could also be improved upon for better prediction. For example, the current reactor model assumes a single temperature profile across the entire channel rather than applying scaled average temperatures in each segment. The model also makes ideal gas assumptions when calculating reactor inlet gas concentration, assuming equal fuel/fuel-purge and air/air-purge inlet concentrations, which could slightly over-predict efficiency. Finally, though the gas-solid equilibrium assumption is valid for most of the reactor channel length, this is not necessarily the case at the reactor inlet. Refining these assumptions would improve the prediction accuracy of both the reactor and the integrated system model. A study of the optimal materials for CO_2 and H_2O turbines is also critical to the successful operation of this system.

7.2.2. Exploring other problems

The current study used a single, 25 $MW_{thermal}$ reactor to illustrate the integration of a CLC reactor into a power generation system. As a next step, the system should be optimized for number and size of reactors given practical space, cost and electricity demand constraints. This analysis should also factor in the risk of planned and unplanned reactor shut-downs during the optimization for LCOE. Another promising application for this reactor design is the co-generation of hydrogen and

electricity. This application requires oxygen carriers (e.g. ceria) whose kinetic properties are selective towards hydrogen production. Analyzing such a system within the current model framework would involve updating the oxygen carrier kinetics for ceria, and then optimizing the system for the combined economic value of electricity and hydrogen production.

Finally, this reactor should be studied for application in systems that run on solid fuels (e.g. coal or biomass). One potential solid fuel system design, shown in Figure 7-1, integrates the CLC reactor with an upstream coal or biomass gasifier. In this configuration, the gasifier is used to produce synthesis gas that is sent as a gaseous fuel to the rotary reactor. One of the synergies of this proposed system is that the reactor fuel-side exhaust stream can be recycled to fluidize, heat and react with the solid fuels in the gasifier. Excess fuel may also be expanded in a turbine to produce more power, and the air-side exhaust can produce power in a traditional combined cycle. This system study would be a natural extension of the research conducted in this thesis, and would provide further motivation for the adoption of CLC reactor technology in fossil fuel power systems.

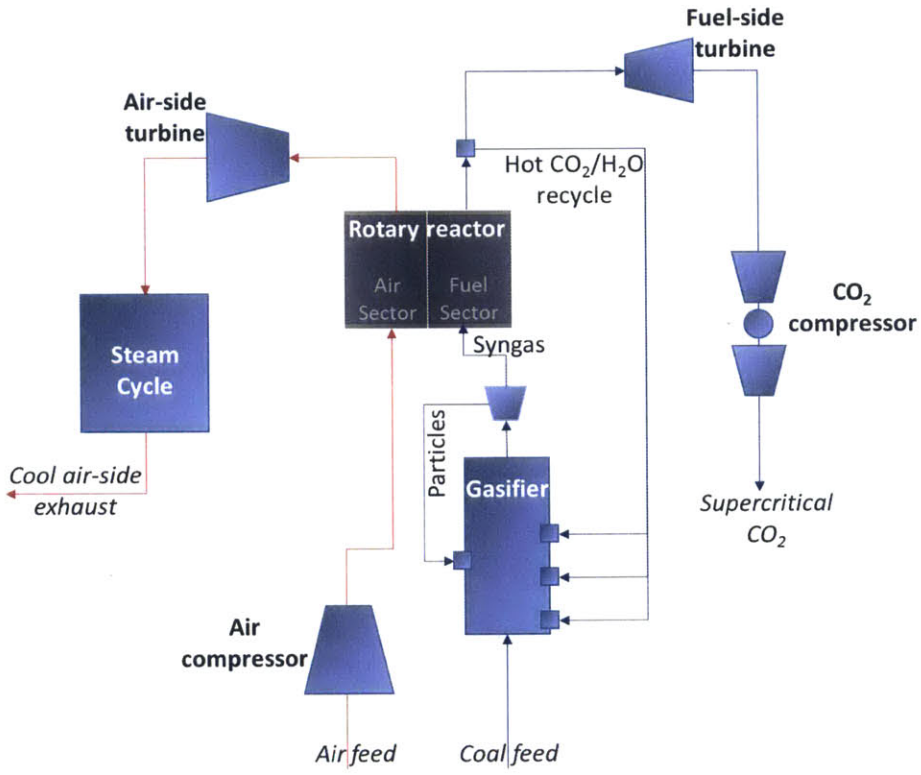

Figure 7-1: Proposed configuration for assessing rotary reactor application in solid fuel plants.

8. **Bibliography**

[1] J. R. Ritcher and K. F. Knoche, "Reversibility of Combustion Processes," *ACS Symp. Ser.*, pp. 71–85, 1983.

[2] L. Fan and L. Fanxing, *Chemical Looping Systems for Fossil Energy Conversions*. New Jersey, USA: John Wiley & Sons, Inc, 2010.

[3] J. Adanez, A. Abad, F. Garcia-Labiano, P. Gayan, and L. F. de Diego, "Progress in Chemical-Looping Combustion and Reforming technologies, Progress in Energy and Combustion Science," *Prog. Energy Combust. Sci.*, vol. 38, pp. 215–282., 2012.

[4] Z. Zhao, T. Chen, and A. F. Ghoniem, "Rotary bed reactor for chemical-looping combustion with carbon capture. Part 2: base case and sensitivity analysis," *Energy Fuels*, vol. 27, pp. 344–359, 2013.

[5] A. Abad, J. Adanez, F. Garcia-Labiano, L. F. de Diego, P. Gayan, and J. Celaya, "Mapping of the range of operational conditions for Cu-, Fe-, and Ni-based oxygen carriers in chemical-looping combustion," *Chem. Eng. Sci.*, vol. 62, pp. 533–549, 2007.

[6] J. Adanez, F. Garcia-Labiano, L. F. de Diego, P. Gayan, J. Celaya, and A. Abad, "Nickel–copper oxygen carriers to reach zero CO and H_2 emissions in chemical-looping combustion," *Ind. Eng. Chem. Res.*, vol. 45, no. 8, pp. 2617–2625, 2006.

[7] E. Jerndal, T. Mattisson, and A. Lyngfelt, "Thermal Analysis of Chemical-Looping Combustion," *Chem. Eng. Res. Des.*, vol. 84, no. 9, pp. 795–806, 2006.

[8] S. Hurst, "Production of hydrogen by the steam - iron method," *J. Am. Oil Chem. Soc.*, vol. 16, pp. 29–36, 1939.

[9] W. K. Lewis, E. R. Gilliland, and G. T. McBride, "Gasification of carbon metal oxides in a fluidized powder bed," *Ind. Eng. Chem.*, vol. 41, no. 6, pp. 1213–1226, 1949.

[10] E. R. Gilliland and W. K. Lewis, "Production of pure carbon dioxide," US2665972A, 1954.

[11] H. M. Kvamsdal, K. Jordal, and O. Bolland, "A quantitative comparison of gas turbine cycles with CO_2 capture," *Energy*, vol. 32, pp. 10–24, 2007.

[12] M. Ishida and H. Jin, "A new advanced power-generation system using chemical-looping combustion," *Energy*, vol. 19, pp. 415–422, 1994.

[13] M. Anheden and G. Svedberg, "Exergy analysis of chemical-looping combustion systems," *Energy Convers. Manag.*, vol. 39, pp. 1967–1980, 1998.

[14] R. Naqvi and O. Bolland, "Multi-stage chemical looping combustion (CLC) for combined cycles with CO_2 capture," *Int. J. Greenh. Gas Control*, vol. 1, no. 1, pp. 19–30, 2007.

[15] J. Wolf and J. Yan, "Parametric study of chemical looping combustion for tri-generation of hydrogen, heat, and electrical power with CO_2 capture," *Int. J. Energy Res.*, vol. 29, pp. 739–753, 2005.

[16] O. Brandvoll, "Chemical looping combustion fuel conversion with inherent CO_2 capture," PhD Thesis, Norwegian University of Science and Technology, Trondheim, Norway, 2005.

[17] M. Ishida, D. Zheng, and T. Akehata, "Evaluation of a chemical looping combustion power generation system by graphic exergy analysis," *Energy*, vol. 12, no. 2, pp. 147–154, 1987.

[18] A. Lyngfelt, B. Leckner, and T. Mattisson, "A fluidized-bed combustion process with inherent CO_2 separation; application of chemical-looping combustion," *Chem. Eng. Sci.*, vol. 56, pp. 3101–3113, 2001.

[19] M. M. Hossain and H. I. de Lasa, "Chemical-looping combustion (CLC) for inherent separations—a review," *Chem. Eng. Sci.*, vol. 63, no. 18, pp. 4433–4451, 2008.

[20] J. Wolf, "Mitigation in Advanced Power Cycles- Chemical Looping Combustion and Steam-Based Gasification," PhD Thesis, KTH - Royal Institute of Technology, Stockholm, Sweden, 2004.

[21] F. Li, L. Zeng, L. G. Velazquez-Vargas, Z. Yoscovits, and L. Fan, "Syngas chemical looping gasification process: Bench-scale studies and reactor simulations," *AIChE J.*, vol. 56, pp. 2186–2199, 2010.

[22] S. Noorman, M. van Sint Annaland, and H. Kuipers, "Packed Bed Reactor Technology for Chemical-Looping Combustion," *Ind. Eng. Chem. Res.*, vol. 46, no. 12, pp. 4212–4220, 2007.

[23] S. Noorman, F. Gallucci, M. van Sint Annaland, and J. A. M. Kuipers, "Experimental Investigation of Chemical-Looping Combustion in Packed Beds: A Parametric Study," *Ind. Eng. Chem. Res.*, vol. 50, no. 4, pp. 1968–1980, 2011.

[24] K. Chakravarthy, C. S. Daw, and J. A. Pihl, "Thermodynamic analysis of alternative approaches to chemical looping combustion," *Energy Fuels*, vol. 25, pp. 656–669, 2011.

[25] I. M. Dahl, E. Bakken, Y. Larring, A. I. Spjelkavik, S. F. Hakonsen, and R. Blom, "On the development of novel reactor concepts for chemical looping combustion," *Energy Procedia*, vol. 1, pp. 1513–1519, 2009.

[26] S. F. Hakonsen and R. Blom, "Chemical Looping Combustion in a Rotating Bed Reactor - Finding Optimal Process Conditions for Prototype Reactor," *Environ. Sci. Technol.*, vol. 45, pp. 9619–9626, 2011.

[27] Z. Zhao, T. Chen, and A. F. Ghoniem, "Rotary bed reactor for chemical-looping combustion with carbon capture. Part 1: reactor design and model development," *Energy Fuels*, vol. 27, pp. 327–343, 2013.

[28] Z. Zhao, C. O. Iloeje, and A. F. Ghoniem, "Design of a rotary reactor for chemical-looping combustion. Part 1: Fundamentals and design methodology," *Fuel*, vol. 121, pp. 327–343, 2014.

[29] Z. Zhao and A. F. Ghoniem, "Design of a rotary reactor for chemical-looping combustion. Part 2: Comparison of copper-, nickel-, and iron-based oxygen carriers," *Fuel*, vol. 121, pp. 344–360, 2014.

[30] O. Brandvoll and O. Bolland, "Inherent CO_2 Capture using chemical looping combustion in a natural gas fired power cycle," *J. Eng. Gas Turbine Power*, vol. 126, no. 2, pp. 316–321, 2004.

[31] S. Consonni, G. Lozza, G. Pelliccia, S. Rossini, and F. Saviano, "Chemical-loopingcombustion for combined cycles with CO_2 capture," *J. Eng. Gas Turbine Power*, vol. 128, no. 3, pp. 525–534, 2006.

[32] J. Yu, A. B. Corripio, D. P. Harrison, and R. J. Copeland, "Analysis of the sorbent energy transfer system (SETS) for power generation and CO_2 capture," *Adv. Environ. Res.*, vol. 7, no. 2, pp. 335–345, 2003.

[33] R. Naqvi, O. Bolland, O. Brandvoll, and K. Helle, "Chemical looping combustion - analysis of natural gas fired power cycles with inherent CO_2 capture," in *ASME Turbo Expo*, Vienna, Austria, 2004.

[34] X. Zhang, W. Han, H. Hong, and H. Jin, "A chemical intercooling gas turbine cycle with chemical-looping combustion," *Energy*, vol. 34, no. 12, pp. 2131–2136, 2009.

[35] T. B. Reed, "Efficiencies of Methanol Production from Gas, Coal Waste or Wood," in *Symposium on Net Energetics of Integrated Synfuel Systems*, New York, 1976, vol. 21.

[36] S. Rezvani, Y. Huang, D. McIlveen-Wright, N. Hewitt, and J. D. Mondol, "Comparative assessment of coal fired IGCC systems with CO_2 capture using physical absorption, membrane reactors and chemical looping," *Fuel*, vol. 88, no. 12, pp. 2463–2472, 2009.

[37] W. Xiang and S. Wang, "Investigation of gasification chemical looping combustion combined cycle performance," *Energy Fuels*, vol. 22, pp. 961–966, 2008.

[38] L. Fan and L. Fanxing, "Chemical Looping Technology and Its Fossil Energy Conversion Applications," *Ind. Eng. Chem. Res.*, vol. 49, no. 21, pp. 10200–10211, 2010.

[39] E. J. Sheu, E. M. A. Mokheimer, and A. F. Ghoniem, "A review of methane reforming systems," *Int. J. Hydrog. Energy*, vol. 40, no. 38, pp. 12929–12955, 2015.

[40] B. Moghtaderi, "Application of chemical looping concept for air separation at high temperatures," *Energy Fuels*, vol. 24, pp. 190–198, 2010.

[41] N. R. McGlashan, "Chemical looping combustion - a thermodynamic study," *Proc. Inst. Mech. Eng.*, vol. 222, pp. 1005–1019, 2008.

[42] H. P. Hamers, M. C. Romano, V. Spallina, P. Chiesa, F. Gallucci, and M. van Sint Annaland, "Comparison on process efficiency for CLC of syngas operated in packed bed and fluidized bed reactors," *Int. J. Greenh. Gas Control*, vol. 28, pp. 65–78, 2014.

[43] Y. Shastri, J. Salazar, and U. Diwekar, "Multi-Objective Optimization Analysis of the IGCC System with Chemical Looping Combustion, Design for Energy and the Environment," in *Foundations of Computer-Aided Process Design*, 2009, pp. 479–487.

[44] C. O. Iloeje, Z. Zhao, and A. F. Ghoniem, "Analysis of thermally coupled chemical looping combustion-based power plants with carbon capture," *Int. J. Greenh. Gas Control*, vol. 35, pp. 56–70, 2015.

[45] C. O. Iloeje, Z. Zhao, and A. F. Ghoniem, "Efficient cycles for carbon capture CLC power plants based on thermally balanced redox reactors," *Int. J. Greenh. Gas Control*, vol. 41, pp. 302–315, 2015.

[46] P. Peltola, "Analysis And Modelling of Chemical Looping Combustion Process with and without Oxygen Uncoupling," PhD Thesis, Lappeenranta University of Technology, Lappeenranta, 2014.

[47] P. Perrot, *A to Z of Thermodynamics*. Oxford, UK: Oxford University Press, 1998.

[48] A. J. Appleby and F. R. Foulkes, *Fuel Cell Handbook*, vol. 1. New York: van Nostrand Reinhold, 1989.

[49] F. Garcia-Labiano, L. F. de Diego, J. Adanez, A. Abad, and P. Gayan, "Reduction and oxidation kinetics of a copper-based oxygen carrier prepared by impregnation for chemical-looping combustion," *Ind. Eng. Chem. Res.*, vol. 43, pp. 8168–8177, 2004.

[50] F. Garcia-Labiano, J. Adanez, L. F. de Diego, P. Gayan, and A. Abad, "Effect of pressure on the behavior of copper-, iron-, and nickel-based oxygen carriers for chemical looping combustion," *Energy Fuels*, vol. 20, pp. 26–33, 2006.

[51] J. Adanez, L. F. de Diego, F. Garcia-Labiano, P. Gayan, A. Abad, and J. M. Palacios, "Selection of oxygen carriers for chemical-looping combustion," *Energy Fuels*, vol. 18, pp. 371–377, 2004.

[52] P. Cho, T. Mattisson, and A. Lyngfelt, "Comparison of iron-, nickel-, copper- and manganese-based oxygen carriers for chemical-looping combustion," *Fuel*, vol. 83, pp. 1215–1225, 2004.

[53] T. Mattisson, M. Johansson, and A. Lyngfelt, "The use of NiO as an oxygen carrier in chemical-looping combustion," *Fuel*, vol. 85, pp. 736–747, 2006.

[54] M. Johansson, T. Mattisson, A. Lyngfelt, and A. Abad, "Using continuous and pulse experiments to compare two promising nickel-based oxygen carriers for use in chemical-looping technologies," *Fuel*, vol. 87, pp. 988–1001, 2008.

[55] B. Linnhoff and J. R. Flower, "Synthesis of heat exchanger networks. Part I: systematic generation of energy optimal networks," *AIChE J.*, vol. 24, pp. 633–642, 1978.

[56] R. S. Kamath, L. T. Biegler, and I. E. Grossmann, "Modeling multistream heat exchangers with and without phase changes for simultaneous optimization and heat integration," *AIChE J.*, vol. 58, no. 1, pp. 190–204, 2012.

[57] T. Umeda, T. Harada, and K. Shiroko, "A thermodynamic approach to the synthesis of heat integration systems in chemical processes," *Comput. Chem. Eng.*, vol. 3, pp. 273–282, 1979.

[58] J. J. Klemes, P. S. Varbanov, and Z. Kravanja, "Recent Developments in Process integration," *Chem. Eng. Res. Des.*, vol. 91, pp. 2037–2053, 2013.

[59] R. S. Kamath, I. E. Grossmann, and L. T. Biegler, "Modeling of multi-stream heat exchangers with phase changes for cryogenic applications," *Comput. Aided Chem. Eng.*, vol. 27, no. C, pp. 921–926, 2009.

[60] M. A. Duran and I. E. Grossmann, "Simultaneous optimization and heat integration of chemical processes," *AIChE J.*, vol. 32, pp. 123–138, 1986.

[61] S. Balakrishna and L. T. Biegler, "Targeting strategies for the synthesis and energy integration of non isothermal reactor networks," *Ind. Eng. Chem. Res.*, vol. 31, pp. 2152–2164, 1992.

[62] B. T. Baumrucker, J. G. Renfro, and L. T. Biegler, "MPEC problem formulations and solution strategies with chemical engineering applications," *Comput. Chem. Eng.*, vol. 32, pp. 2903–2913, 2008.

[63] V. Gopal and L. T. Biegler, "Smoothing methods for complementarity problems in process engineering," *AIChE J.*, vol. 45, no. 7, pp. 1535–1547, 1999.

[64] M. Anitescu, P. Tseng, and S. J. Wright, "Elastic-mode algorithms for mathematical programs with equilibrium constraints: Global convergence and stationarity properties," *Math. Programing*, vol. 110, pp. 337–371, 2007.

[65] R. J. Wooley and V. Putsche, "Development of an ASPEN PLUS Physical Property Database for Biofuels Components," NREL, Colorado, NREL/TP-425-20685, Apr. 1996.

[66] S. Skogestad, *Chemical and Energy Process Engineering*, 1st Edition. CRC Press, 2009.

[67] D. L. McCollum and J. M. Ogden, "Techno-economic models for carbon dioxide compression, transport, and storage & correlations for estimating carbon dioxide density and viscosity," Institute of Transportation Studies, Davis, California, UCD—ITS—RR—06-14, 2006.

[68] M. Shacham, P. Macchieto, L. F. Stutzman, and P. Babcock, "Equation oriented approach to Process flowsheeting," *Comput. Chem. Eng.*, vol. 6, no. 2, pp. 79–95, 1982.

[69] C. C. Pantelides, M. Nauta, and M. Matzopoulos, "Equation-Oriented Process Modelling Technology: Recent Advances & Current Perspectives," in *5th Annual TRC- Idemitsu Workshop*, Abu Dhabi, UAE, 2015.

[70] L. T. Biegler, *Nonlinear Programming: Concepts, Algorithms, and Applications to Chemical Processes*. Philadelphia: MOS-SIAM, 2013.

[71] M. . Chase, *NIST-JANAF Themochemical Tables*, Fourth Edition., vol. Monograph 9. J. Phys. Chem. Ref. Data, 1998.

[72] M. Holmgren, "XSteam, Thermodynamic properties of water and steam," 2006. [Online]. Available: http://www.mathworks.com.

[73] D. Pauschert, "Study of Equipment Prices in the Power Sector," IBRD/The World Bank Group, Washington DC, ESMAP Technical Paper 122/09, 2009.

[74] "Producer Price Indices." US Bureau of Labor Statistics, 2016.

[75] H. P. Loh, J. Lyons, and C. W. White, "Process Equipment Cost Estimation Final Report," NETL, Pittsburgh, PA, DOE/NETL-2002/1169, 2002.

[76] NETL, "Quality guidelines for energy systems studies: cost estimation methodology for NETL assessments of power plant performance," NETL, DOE/NETL-2011/1455, 2011.